Aerodynamic Noise Reduction with Porous Materials

Aeroacoustics Investigations and Applications

Teruna, C.

DOI
10.4233/uuid:260cd874-c1ed-4155-bfdc-cf7fc3813ca6

Publication date
2022

Document Version
Final published version

Citation (APA)
Teruna, C. (2022). *Aerodynamic Noise Reduction with Porous Materials: Aeroacoustics Investigations and Applications*. [Dissertation (TU Delft), Delft University of Technology].
https://doi.org/10.4233/uuid:260cd874-c1ed-4155-bfdc-cf7fc3813ca6

Important note
To cite this publication, please use the final published version (if applicable).
Please check the document version above.

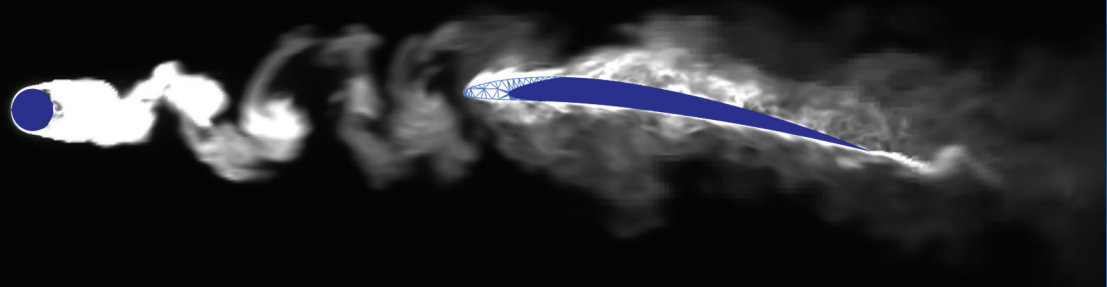

AERODYNAMIC NOISE REDUCTION WITH POROUS MATERIALS

Aeroacoustics Investigations and Applications

Christopher Teruna

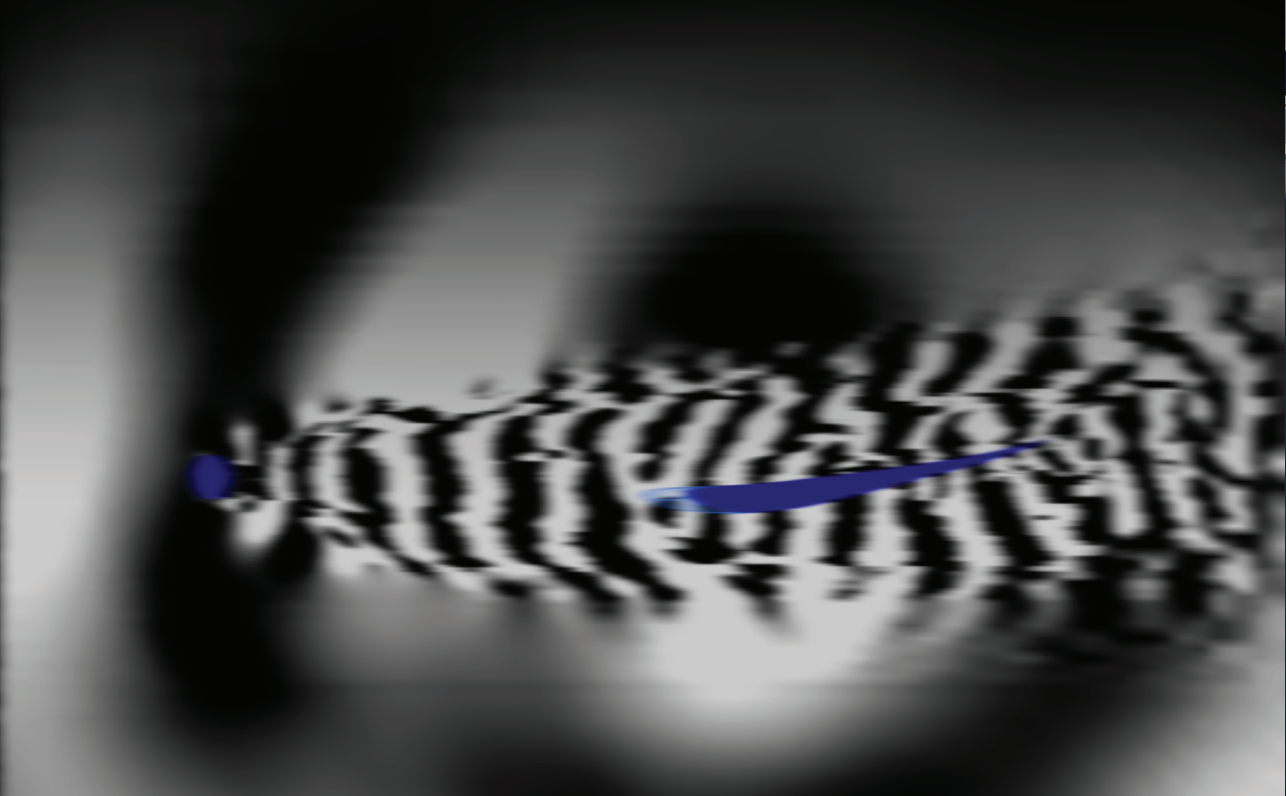


KLM
KLM

INVITATION

For attending the public defence of the thesis

Aerodynamic Noise Reduction with Porous Material

Aeroacoustics investigations and applications

By

Christopher Teruna

On

March 11th 2021

14:30 – Layman talk

15:00 – Public defence

At

Senaatzaal

Aula Congrescentrum

Mekelweg 5, Delft

Propositions

accompanying the dissertation

AERODYNAMIC NOISE REDUCTION WITH POROUS MATERIALS
AEROACOUSTICS INVESTIGATIONS AND APPLICATIONS

by

Christopher TERUNA

1. Separating the porous medium region dominated by the entrance effect from that by the bulk effect circumvents the modelling inconvenience due to the thickness dependency of porous-material resistivity for thin geometries. (*Chapter 2*).
2. Mitigation of leading/trailing-edge noise using a porous insert is the result of a pressure-release process, resulting in a gradual impedance adjustment instead of an abrupt one between a solid body and the inflow/wake (*Chapter 3 & 4*).
3. Although porous edges are more complex than serrations to design and implement, the former possess greater potential and versatility (*Chapter 3 & 4*).
4. Reducing turbulence-interaction noise using a porous edge can incur a severe aerodynamic penalty. Thus, the possibility of inflow-turbulence control should also be considered as an alternative (*Chapter 4 & 5*).
5. Turbulent kinetic energy cascade is analogous to the inequality in our society. As our economy grows (Reynolds number increases), the larger is the difference between the "Haves" (forcing range) and the "Have-Nots" (dissipation range).
6. Aviation will never be more sustainable than any ground/sea-based transportation modes since aircrafts always need to spend energy for overcoming gravity.
7. Noise emission of a mechanical system is closely related to its efficiency, and thus, performance optimisation should be the first noise-reduction approach to pursue.
8. Serious global issues would be neglected if they were deemed unprofitable to solve, although we have sufficient resources to do so.
9. Worsening of climate change is the result of psychological inertia in people and their aversion against long-term commitment.
10. Revisiting history allows one to understand present trends, and to help making a more informed decision for a better future, except in the stock market.

These propositions are regarded as opposable and defendable, and have been approved as such by the promotor prof. dr. D. Casalino.

Stellingen

AERODYNAMIC NOISE REDUCTION WITH POROUS MATERIALS

AEROACOUSTICS INVESTIGATIONS AND APPLICATIONS

door

Christopher TERUNA

1. Het scheiden van het gebied met poreus materiaal waar het *entrance effect* domineert en die waar het *bulk effect* domineert, vermijdt de modelleer moeilijkheid als gevolg van de dikte afhankelijkheid van de weerstand van poreuze materialen betreft dunne vormen. (*Hoofdstuk 2*).
2. Het verminderen van het geluid afkomstig van de *leading/trailing-edge* met behulp van een poreus inzetstuk komt door het pressure-release-process. Dit leidt tot een graduele aanpassing van impedantie in plaats van een abrupte overgang tussen een lichaam en de inkomende luchtstroom/zog (*Hoofdstuk 3 & 4*).
3. Hoewel het ontwerp en de verwerking van poreuze randen complexer zijn dan die van *serrations*, hebben de poreuze randen meer potentie en bieden meer mogelijkheden (*Hoofdstuk 3 & 4*).
4. Het verminderen van turbulentie-interactie geluid met behulp van een poreuze rand kan de aerodynamische prestaties verminderen, vandaar moet de mogelijkheid van de regeling van instroom-turbulentie ook worden overwogen (*Hoofdstuk 4 & 5*).
5. De deling van turbulente kinetische energie is analoog aan de ongelijkheid in onze samenleving. Als de economie groeit (het Reynolds getal neemt toe), wordt het verschil tussen de *Haves* (*forcing range*) en de *Have-Nots* (*dissipation range*) groter.
6. Luchtvaart zal nooit duurzamer zijn dan land/zeevervoer, aangezien vliegtuigen altijd energie moeten verbruiken om de zwaartekracht tegen te gaan.
7. De geluidsemissie van een mechanisch systeem hangt nauw samen met de efficiëntie, vandaar zou de optimalisatie van de prestaties de eerste te onderzoeken aanpak zijn voor geluidsvermindering.
8. Cruciale wereldproblemen zouden genegeerd worden als deze niet winstgevend zijn om op te lossen, ondanks dat er genoeg middelen beschikbaar zijn om ze tegen te gaan.
9. De klimaatverandering wordt verergerd door de psychologische traagheid van mensen en hun afkeer tegen lange termijn toewijding.
10. Door de geschiedenis opnieuw te bekijken kan iemand de huidige trends begrijpen en een beter geïnformeerde beslissing nemen voor een betere toekomst, dit geldt echter niet voor de aandelenmarkt.

Deze stellingen worden opponeerbaar en verdedigbaar geacht en zijn als zodanig goedgekeurd door de promotor prof. dr. D. Casalino.

AERODYNAMIC NOISE REDUCTION WITH POROUS MATERIALS

AEROACOUSTICS INVESTIGATIONS AND APPLICATIONS

AERODYNAMIC NOISE REDUCTION WITH POROUS MATERIALS

AEROACOUSTICS INVESTIGATIONS AND APPLICATIONS

Proefschrift

ter verkrijging van de graad van doctor
aan de Technische Universiteit Delft,
op gezag van de Rector Magnificus prof. dr. ir. T. H. J. J. van der Hagen,
voorzitter van het College voor Promoties,
in het openbaar te verdedigen op Donderdag 10 maart 2022 om 15:00 uur

door

Christopher TERUNA

Master of Science in Aerospace Engineering Korea Advanced Institute of Science and Technology, Zuid-Korea
geboren te Medan, Indonesië.

Dit proefschrift is goedgekeurd door de promotor:

Prof. dr. D. Casalino

Copromotor: Dr. D. Ragni
Copromotor: Dr. F. Avallone

Samenstelling promotiecommissie:

Rector Magnificus,	voorzitter
Prof. dr. D. Casalino,	Technische Universiteit Delft, promotor
Dr. D. Ragni,	Technische Universiteit Delft, copromotor
Dr. F. Avallone,	Technische Universiteit Delft, copromotor

Onanhafkelijke leden:

Prof. D. A. von Terzi,	Technische Universiteit Delft
Prof. dr. -ing. J. Delfs,	Technische Universität Braunschweig, Germany
Prof. dr. ir. C. Schram,	von Kármán Institute of Fluid Dynamics, Belgium
Dr. H. Chen,	Dassault Systèmes, United States of America
Prof. dr. S. J. Watson,	Technische Universiteit Delft, reservelid

Smart Mitigation of flow-induced Acoustic Radiation and Transmission for reduced Aircraft, surface traNSport, Workplaces and wind enERgy noise

H2020 MARIE SKŁODOWSKA-CURIE ACTIONS

Keywords: Trailing-edge noise, leading-edge noise, aeroacoustics, porous materials, lattice-Boltzmann method

Printed by: Ridderprint

Front & Back: Illustrations of wake-interaction noise and turbulent-boundary-layer trailing-edge noise. Cover design by Christopher Teruna.

ISBN 978-94-6384-309-6

An electronic version of this dissertation is available at
http://repository.tudelft.nl/.

But remember this, Japanese boy... airplanes are not tools for war. They are not for making money. Airplanes are beautiful dreams. **Engineers turn dreams into reality**.

Giovanni B. Caproni in "*The Wind Rises*" (2013)

The stars come together to perform a skit at the edge of the sky,
but its meaning is hidden by the first one with a perfect square and a perfect cube.

CONTENTS

NOMENCLATURE

Acronyms

AoA	angle of attack
APM	Acoustic Porous Medium model in PowerFLOW
BPR	turbofan bypass ratio
BTE	Boltzmann transport equation
BVI	blade-vortex interaction
CAA	computational aeroacoustics
CFD	computational fluid dynamics
CTS	wind tunnel with closed test section
DNC	direct noise computation
DNS	direct numerical simulation
EPNdB	effective perceived noise level in decibel (sometimes EPNL)
Exp.	experimental data
FW-H	Ffocws-Williams & Hawking acoustic analogy
GCI	grid convergence index
HWA	hot-wire anemometry
LBM	lattice-Boltzmann method
LE	leading edge
LES	large eddy simulation
OAPWL	overall sound power level
OGV	outlet-guide vane
OJS	wind tunnel with open-jet test section
OSPL	overall sound pressure level
PIV	particle-image velocimetry

PM	Porous Medium model in PowerFLOW
PNL	Perceived noise level
PWL	sound power level
RAC	Rod-airfoil configuration
RANS	Reynolds-averaged Navier-Stokes
RLC	Rod-linear cascade configuration
RNG	Renormalisation group (turbulence model)
SDT	NASA-Glenn source diagnostic test rig
Sim.	numerical data
SPL	sound pressure level
TE	trailing edge
TIN	turbulence-impingement noise
VLES	very-large eddy simulation

Greek letters

δ^*	displacement thickness
δ_{99}	boundary layer height where the mean velocity is 99 % of the freestream
ϵ	rate of dissipation of turbulent kinetic energy (in $k-\epsilon$ turbulence model)
η	variable based on a local strain parameter $k\lvert\boldsymbol{S}/\epsilon\rvert$
γ^2	magnitude-squared coherence
κ	collision operator
Λ	serration wavelength (e.g., distance between two serration tips)
λ	acoustic wavelength
λ_2	the second eigenvalue of a velocity gradient tensor; negative values indicate vortex core
ν	kinematic viscosity
ω	angular frequency, i.e., $2\pi f$
ω_n	weighting for particle distribution function
Φ	turbulent energy spectrum

ϕ porous medium porosity

ρ density

τ relaxation time in the collision operator

τ_w wall shear stress

θ^* momentum thickness

$\boldsymbol{\omega}$ vorticity

Latin letters

ΔP pressure drop across a porous medium sample for one-dimensional flow

$\mathbb{S}$ control surface

$\mathbb{V}$ control volume

$\mathcal{K}$ Von Kármán constant

G transfer function (e.g., Green's function)

$\boldsymbol{C}$ porous medium form coefficient vector

$\boldsymbol{K}$ porous medium permeability vector

$\boldsymbol{l}$ a small segment of the airfoil contour

$\boldsymbol{n}$ unitary vector in the normal direction relative to a surface

$\boldsymbol{R_I}$ inertial resistivity

$\boldsymbol{R_V}$ viscous resistivity

$\boldsymbol{R}$ porous medium resistivity vector

$\boldsymbol{s}$ unitary vector in the tangential direction relative to a surface

$\boldsymbol{u}$ velocity vector

$\boldsymbol{V}$ particle velocity vector in BTE

$\boldsymbol{x}$ coordinate in space

A phase angle of a cross-correlation function

a_s non-dimensional speed of sound in lattice unit

c airfoil chord length

C_d mean drag coefficient

C_f wall-friction coefficient

C_l	mean lift coefficient
C_p	mean surface pressure coefficient
D	rod diameter
d	half thickness of the airfoil trailing edge
d_c	unit-cell dimension
d_p	mean pore diameter
e	natural exponential function
F	particle distribution function in BTE
f	frequency
G	cross-spectral density
$g(\cdots)$	a parameter g as a function of $\cdots$
H	serration amplitude (e.g., distance between serration tip and root)
h	porous medium sample thickness for one-dimensional flow
h_b	the thickness of PM layer (bulk effect dominated region)
h_e	the thickness of APM layer (entrance effect dominated region)
j	complex number $\sqrt{-1}$
k	turbulent kinetic energy (e.g., in $k-\epsilon$ turbulence model)
k_c	Helmholtz number based on the airfoil chord
L	correlation length (e.g., integral length scale)
L_{E}	the chordwise extent of the porous trailing edge where the thickness is less than twice the entrance length
M	Mach number
N_{grid}	number of grid elements or voxels
p'	acoustic pressure fluctuations
q_∞	freestream dynamic pressure
R	cross-correlation function
Re_c	chord-based Reynolds number
S	power spectral density

St	Strouhal number
t	time
U	time-averaged streamwise velocity
u	fluctuating component of streamwise velocity
U^+	wall-parallel velocity normalised by the friction velocity
u_τ	friction velocity
uv	streamwise-vertical component of Reynolds stress
V	time-averaged vertical velocity
v	fluctuating component of vertical velocity
v_d	Darcian velocity (mean velocity inside the porous medium sample)
y^+	wall distance normalised by the friction velocity
T	Lighthill's stress tensor
A	law-of-the-wall parameter (a function of pressure gradient)
B	law-of-the-wall parameter (y^+ shift)
b	airfoil span

Others

$\langle\cdot\rangle$	averaging operator
$\|\|\cdots\|\|$	euclidean norm (e.g., magnitude of a vector)

Subscripts

∞	freestream variable
mean	time-averaged variable
RMS	root-mean-square of the fluctuations of a variable
c	a variable based on the airfoil chord
D	a variable based on the rod diameter
i	vector index
j	vector index
p	pressure variable
1/3	SPL in one-third octave band

pp	surface pressure fluctuations
ps	pressure side variable
SLE	straight (baseline) leading edge
ss	suction side variable
uu	streamwise velocity fluctuations
vv	vertical velocity fluctuations
WLE	serrated leading edge

SUMMARY

Turbulence-induced noise mechanisms are prevalent in many industrial applications, such as the turbulent boundary-layer trailing-edge (TBL-TE) noise on wind-turbine blades and turbulence-impingement (leading-edge/LE) noise in a turbofan fan stage. As the demands for air transport and wind energy are expected to increase in the near future, concerns surrounding noise pollution are also becoming more relevant. This trend necessitates the development of novel noise mitigation approaches beyond the capability of present technology. Within this scope, this dissertation focuses on the application of permeable (or porous) material to mitigate turbulence-induced noise mechanisms. Specifically, the present study examines the role of material permeability in modifying the aeroacoustic characteristics of the system.

Present investigations mainly employ high-fidelity numerical simulations based on the lattice-Boltzmann method to resolve the flow field surrounding and inside a porous body. It has been known that the flow inside a porous medium would encounter resistance that depends on the material properties (e.g., porosity and resistivity). The resistivity of porous materials are often reported as constant values, but this is not true for thin samples. This implies that the variation of resistivity with the material thickness needs to be taken into account for slender bodies, such as the leading/trailing edges of an airfoil. To simplify the modelling procedure, the porous medium region is divided into two regions. The outer layer has a constant thickness that is equal to or slightly larger than the entrance length, while the inner one contains the rest of the porous medium region. While the resistivity values of the two layers are different, they can be taken as constant regardless of the sample thickness. This multi-layer approach is verified by replicating a porous-material characterisation rig in the simulation, with which the pressure drop values from the experiment have been accurately predicted.

For mitigating TBL-TE noise, a porous TE insert has been used to replace the aft 20 % of a NACA 0018 airfoil. Initially the porous insert is modelled after a metal foam with a mean pore size of 0.8 mm. For several flow conditions with Reynolds numbers at the order of 1×10^5, up to 8 dB of noise reduction has been achieved, mainly in the low-frequency range. The noise sources on the porous TE tend to be distributed with out-of-phase relations. The opposite is true for the solid TE, particularly at frequencies where the airfoil is acoustically compact. As a result, the porous TE has a lower scattering efficiency compared to the solid one. Similar phenomena have been observed when the simulations are performed at higher Reynolds numbers and angle-of-attack settings, although the efficacy of the porous TE decreases. Subsequent simulations employ a fully-resolved porous insert based on a porous-cell geometry, and therefore, the porous medium model is not needed. These investigations confirm that an unobstructed flow interactivity between both sides of the porous insert is necessary to realise noise attenuation. Additionally, the segment near the porous TE tip, where the local thickness is comparable to the entrance length, has the largest noise reduction contribution. On

the aspect of aerodynamic performance, the porous inserts generally cause a minor drag increase due to the enhanced flow shear near the porous medium surface.

Porous treatments are subsequently employed in a rod-airfoil configuration (RAC) as a simplified representation of the rotor-stator interaction mechanism in a turbofan fan stage. Due to the periodic shedding of turbulent vortices by the upstream rod, the downstream airfoil experiences an unsteady forcing with combined tonal and broadband components. Two types of airfoils have been considered, the NACA 0012 from the classical rod-airfoil configuration, and the thin and cambered NACA 5406 that better represents the typical features of a turbomachinery blade. In addition to LE serrations, several porous LE concepts are examined, all of which are modelled after the same metal foam previously used for the TBL-TE noise studies. The LE modifications are applied at the first 15 % of the airfoil chord. It is found that the porous LE can produce up to 3 dB of broadband noise reduction in the mid-to-high frequency range, similar to that of the LE serrations. However, the serrations realise a significantly higher tonal noise reduction, thanks to the reduced coherence of the unsteady aerodynamic response along the airfoil span. Lacking the aforementioned benefit, the porous LE only suppresses the noise source intensity surrounding the LE. To obtain larger noise attenuation, a porous LE combined with a serration-like planform has been proposed. The poro-serrated LE produces 2 dB higher broadband noise reduction beyond that of the regular serrations while the tonal noise reduction remains similar. All of the porous treatments cause larger lift reduction and drag increase compared to the LE serrations. In particular for the NACA 5406 case, the pressure imbalance between upper and lower sides of the porous LE causes a cross-flow that significantly alters the aerodynamic characteristics of the airfoil.

The dissertation is concluded with two studies on more complex test setups. The first one is a rod-linear cascade (RLC) configuration that extends the aforementioned RAC. A blade row is used instead of an isolated airfoil to realise a high-solidity environment that resembles that in turbomachinery. The central blade in the linear cascade is positioned downstream of a rod such that it experiences aerodynamic perturbations due to the rod wake impingement. This process leads to a resonance-like behavior at the vortex-shedding frequency that is associated with Parker's beta mode. Porous and serrated LE are applied at the central blade in an attempt to attenuate the noise emission. Similarly in the RAC case, the serrated blade is found to be more effective than the porous one as the latter does not produce any attenuation on the tonal noise component. Nevertheless, the drag penalty caused by both the porous and serrated LE are relatively comparable. The second study considers the NASA-CRM airframe and NASA-SDT fan stage that have been upscaled to match their full-scale counterparts. In order to mitigate the noise arising from the fan wake impinging the outlet guide vanes (OGVs) inside the fan stage, poro-serrated treatments, which are based on metal foam with two different porosities, are implemented at the leading edge of the OGVs. The freestream, angle-of-attack, airframe configuration, and fan rotational speed have been set to an *approach* reference condition. The leading-edge treatments lead to the attenuation of the tonal noise component at the blade-passage frequency and the broadband one in the high-frequency range. However, the flow separation at the suction side of the porous OGV leads to an enhanced broadband noise level at low frequencies. Consequently, the overall source power level of the treated fan stage remains similar to the baseline one.

The porous treatment also incurs a thrust penalty to the fan stage by up to 9 percent. Nevertheless, the poro-serrations with lower porosity produce both lower excess broadband noise and milder thrust reduction.

In conclusion, this dissertation has demonstrated that permeable edge treatments are very promising for mitigating flow-induced noise. However, it is evident that further investigations are still necessary to better understand how the implementations of porosity on an aerodynamic body can be optimised. Besides, there are other practical aspects, such as manufacturing and maintenance, that also deserve closer attention. Hence, the author has summarised several open questions in the final chapter of this dissertation, which should encourage future activities on this subject.

SAMENVATTING

Turbulentie-geïnduceerd-geluid-mechanismen komen voor in veel industriële toepassingen, zoals het turbulente-grenslaag-achterrand-geluid (TBL-TE-geluid) op windturbinebladen en het inkomende-turbulentie-geluid (LE-geluid) in een turbofan. Aangezien het wordt verwacht dat de vraag naar luchtvervoer en windenergie in de toekomst zal toenemen, neemt ook de bezorgdheid over geluidsoverlast toe. Deze trend maakt de ontwikkeling van nieuwe oplossingen voor geluidsvermindering noodzakelijk die momenteel nog niet haalbaar zijn. Binnen dit onderwerp, richt dit proefschrift zich op de toepassing van permeabel- (of poreuze-) materiaal voor het verminderen van turbulentie-geïnduceerd-geluid. In dit onderzoek wordt de rol van de permeabiliteit van het poreuze-materiaal onderzocht bij het wijzigen van de aëro-akoestieke kenmerken van het systeem.

De huidige studie maakt gebruik van numerieke simulaties met hoge getrouwheid op basis van de *lattice-Boltzmann* methode om het stromingsveld rond en binnen een poreus materiaal op te lossen. Het is bekend dat de stroming in een poreus medium weerstand ondervindt die afhangt van de materiaaleigenschappen (b.v. porositeit). De weerstand van poreuze materialen wordt vaak gerapporteerd als constante getallen, maar dit is niet het geval voor dunne monsters. Dit betekent dat er rekening moet worden gehouden met de variatie van de weerstand met de materiaaldikte voor gestroomlijnde vormen, zoals de voor- en achterranden van een vleugelprofiel. Om het modelleren te vereenvoudigen, wordt het gebied van het poreuze medium in twee gebieden verdeeld. De buitenste laag heeft een constante dikte die gelijk is aan of iets groter is dan de *entrance-length*, terwijl de binnenste laag de rest van het gebied van het poreuze medium omvat. Hoewel de weerstandswaardes van de twee lagen verschillend zijn, kunnen zij als constant worden genomen, ongeacht de dikte van het monster. Deze meerlaagse methode wordt geverifieerd met behulp van een simulatie van de poreus-materiaal-karakteriserings-opstelling waarmee de drukverschil in het experiment nauwkeurig zijn voorspeld.

Om het TBL-TE-geluid te verminderen is een poreus inzetstuk gebruikt om de achterste 20 % van een NACA 0018-vleugelprofiel te vervangen. Aanvankelijk wordt de poreuze inzetstuk gemodelleerd door een metaalschuim met een gemiddelde poriegrootte van 0.8 mm. Voor verschillende stromingsomstandigheden met Reynoldsgetallen in de orde van 1×10^5 werd een geluidsvermindering tot 8 dB bereikt, voornamelijk in het lage-frequentiegebied. De geluidsbronnen op de poreuze TE hebben de neiging te worden verdeeld met out-of-phase relaties. Het tegenovergestelde vindt plaats op de massieve TE, vooral bij frequenties waar het vleugelprofiel akoestisch compact is. Dus, de poreuze TE heeft een lagere geluid-verspreidings-efficiëntie in vergelijking met de massieve TE. Vergelijkbare fenomenen zijn waargenomen wanneer de simulaties worden uitgevoerd bij hogere Reynoldsgetallen en invalshoeken, ondanks dat de doeltreffendheid van de poreuze TE lager wordt. Latere simulaties maken gebruik

van een volledig gemodelleerd poreus inzetstuk op basis van een poreuze celgeometrie, en daarom is het poreuze-medium-model niet nodig. Deze onderzoeken bevestigen dat een ongestoorde stromingsinteractie tussen beide zijden van het poreuze inzetstuk nodig is om geluiddemping te realiseren. Bovendien heeft het segment vlakbij het uiteinde van de poreuze-TE, waar de lokale dikte vergelijkbaar is met de *entrance-length*, de grootste bijdrage aan de geluidsvermindering. Wat de aerodynamische prestaties betreft, veroorzaken de poreuze inzetstukken over het algemeen een beperkte toename van de luchtweerstand ten gevolge van de verhoogde afschuiving van de stroming vlakbij het oppervlak van het poreuze medium.

De poreuze inzetstukken worden ook toegepast in een configuratie bestaande uit een cilinder en vliegtuigvleugel (RAC) als een vereenvoudigd model van het rotor-stator interactiemechanisme in een turbofan. Ten gevolge van het periodiek loslaten van turbulente wervelingen door de stroomopwaartse cilinder, ondervindt het stroomafwaartse vleugelprofiel een onregelmatige belasting met gecombineerde tonale en breedband componenten. Twee typen vleugelprofielen zijn opgenomen, de NACA 0012 van de klassieke RAC, en de dunne en gewelfde NACA 5406 die beter de typische kenmerken van een turbomachineblad benaderd. Naast de *LE-serrations* worden verschillende poreuze LE-concepten onderzocht, die alle zijn gemodelleerd met hetzelfde metaalschuim dat eerder voor de TBL-TE-geluidsstudies is gebruikt. De LE-modificaties worden aangebracht op de eerste 15 % van de koorde van het vleugelprofiel. Het blijkt dat de poreuze-LE (voorrand) in het midden- en hoge frequentiebereik een breedband-geluidsvermindering opleveren die vergelijkbaar is met die van de *LE-serrations*. De *serrations* zijn echter beter in het onderdrukken van tonaal geluid, dankzij de verminderde coherentie van de veranderlijke aerodynamische reactie langs de spanwijdte van het vleugelprofiel. Bij gebrek aan het bovenvermelde voordeel onderdrukt de poreuze LE alleen de geluidsbron-intensiteit rond de voorrand. Om een grotere geluidsdemping te verkrijgen, werd een poreuze-LE in combinatie met een *serration* planvorm ontworpen. De poro-serrated-LE behaalt 2 dB hogere breedband-geluidsvermindering dan de gewone *serrations*, terwijl de tonale geluidsvermindering gelijk blijft. Alle poreuze inzetstukken blijken een grotere draagkrachtvermindering en weerstandsverhoging te veroorzaken in vergelijking met de *LE-serrations*. Vooral in het geval van de NACA 5406 veroorzaakt het drukverschil tussen de boven- en onderzijde van de poreuze-LE een dwarsstroming die de aerodynamische eigenschappen van het vleugelprofiel aanzienlijk wijzigt.

Het proefschrift wordt afgesloten met twee studies betreft complexere testgevallen. De eerste is een cilinder-lineaire cascade (RLC) configuratie welke een uitbreiding is van de eerder genoemde RAC. Een rij bladen wordt gebruikt in plaats van een enkel vleugelprofiel om een omgeving met hoge soliditeit te realiseren die lijkt op die in turbomachines. Het centrale blad in de lineaire cascade is stroomafwaarts van een cilinder geplaatst, zodat het aerodynamische verstoringen ondervindt van het zog van de cilinder. Dit proces leidt tot een resonantie-achtig gedrag bij de werveling-loslating-frequentie die geassocieerd wordt met Parker's beta mode. Poreuze en serrated-LE worden aangebracht op het centrale blad in een poging om de geluidsemissie te verminderen. Net als het geval voor de RAC, blijkt dat de serrated-blad doeltreffender zijn dan die met de poreuze-LE, aangezien de poreuze blad geen demping

van de tonale geluidscomponent veroorzaakt. De weerstandsverhoging die veroorzaakt wordt door de poreuze-LE staat in verhouding met die van de serrated-LE . De tweede studie heeft betrekking op het NASA-CRM-luchtframe en de NASA-SDT-turbofan die zijn opgeschaald om te kunnen vergelijken met hun tegenhangers op ware grootte. Om het geluid door het zog van de fan dat de outlet-guide-vanes (OGV) raakt, zijn poro-serrated-LE aan de voorrand van de OGV's toegepast, die zijn gebaseerd op metaalschuim met twee verschillende porositeiten. Voor de vrije luchtstroom, de invalshoek, de configuratie van het vliegtuig en de draaisnelheid van de fan is gebruik gemaakt van een approach referentie-instelling. De wijzigingen aan de OGV voorrand leiden tot een vermindering van de tonale geluidscomponent bij de blade-passage frequentie en de breedband geluid in het hoge frequentiebereik. De stromingsloslating aan de aanzuigzijde van de poreuze OGV leidt echter tot een verhoogd breedbandig geluidsniveau bij lage frequenties. Bijgevolg blijft het totale bronvermogensniveau van de gewijzigde OGV gelijk aan die van de referentie. De gewijzigde OGV leidt ook tot een stuwkrachtvermindering van de turbofan met maximaal 9 %. De poreuze OGV met lagere porositeit produceert niettemin een lager breedband-geluid en een kleinere vermindering van de stuwkracht.

Tot slot, heeft dit proefschrift aangetoond dat poreuze modificaties aan de voor-/acherrand zeer veelbelovend zijn voor het verminderen van luchtstroom-geïnduceerd geluid. Het is echter duidelijk dat verder onderzoek nodig is om beter te begrijpen hoe de implementatie van porositeit op een aerodynamisch systeem kan worden geoptimaliseerd. Daarnaast zijn er andere praktische aspecten, zoals fabricage en onderhoud, die ook extra aandacht verdienen. Op basis hiervan heeft de auteur in het slothoofdstuk van dit proefschrift een aantal open vragen samengevat, die toekomstige activiteiten over dit onderwerp zouden kunnen stimuleren.

PREFACE

As a "trailing-edge" millennial, I was born in an age when the aerospace industry still had a very exciting outlook: the Space Shuttle Discovery had just deployed the Hubble Space Telescope; Boeing 777 was launched as the first airliner to be completely designed with the aid of computers; the Concorde broke the record of supersonic circumnavigation. However, the entire industry has been facing very different challenges in the last decade, such as the rising fuel prices, the growing concerns about aviation climate effects, and the increasing numbers of protests related to aircraft noise emission. Without undermining the others, the latter is particularly crucial to address as noise pollution often causes immediate annoyance.

Noise pollution concerns are not only affecting airliners, but also wind turbines, with recent studies reporting health issues suffered by residents nearby wind farms. In both industrial applications, noise is often a byproduct of the interaction between the turbulent motion of fluid and solid bodies, which is referred to as flow-induced noise mechanisms. Some of these examples include the rotor-stator interaction in a turbofan and the trailing-edge noise from a wind-turbine blade. Researchers have been working on finding different means of noise reduction, both passive and active. As a contribution towards this ongoing effort, this dissertation focuses on the application of permeable edge treatments for mitigating leading- and trailing-edge noise.

Following the quote of Oliver Wendell Holmes Jr., "*a page of history is worth a volume of logic*", the dissertation begins with an overview of aircraft noise and wind-turbine noise trends for the past several decades, including how noise emission concerns have shaped both industries. The second chapter informs the reader about the methodology employed throughout the dissertation, including the lattice-Boltzmann method. The application of permeable edge concepts for both trailing- and leading-edge noise cases are discussed afterward. Key findings are summarised in the last chapter. All of these information have been compiled from the research activities in the framework of the *SmartANSWER* project under the Horizon 2020 programme, and the author acknowledges all parties involved.

In conclusion, it cannot be stressed enough that the information provided in this dissertation are by no means exhaustive nor ground-breaking. In fact, the author hopes that this work would inspire further developments of permeable material treatments and other forms of noise mitigation technology to accelerate the realisation of sustainable aviation and the adoption of renewable energy.

Christopher Teruna
Delft, November 2021

1

INTRODUCTION

Villages and woods, meadows and chateaux, pass across the moving scene,
out of which the whistling of locomotives throws sharp notes.
These faint, piercing sounds, together with the yelping and barking of dogs,
are the only noises that reach one through the depths of the upper air.
The human voice cannot mount up into these boundless solitudes.
Human beings look like ants along the white lines that are highways;
and the rows of houses look like children's playthings.

Alberto Santos-Dumont

A page of history is worth a volume of logic.

Oliver Wendell Holmes Jr.

Turbulence-induced noise mechanisms are very relevant in many industrial applications, such as aircraft engines and wind turbines, since they are often responsible in causing airborne noise pollution. The negative implications of aircraft and wind-turbine noise on the well-being of communities surrounding wind farms and airports have been widely reported, leading to the enforcement of noise regulations. In order to comply with evermore stringent noise limits, researchers and engineers from both the industry and academia are actively looking for solutions. Recently, however, it has become clear that the "low-hanging fruits" are running out, and this situation promotes innovations and deeper investigations into novel noise mitigation approaches. One of the more promising passive noise reduction technique is the application of porous (permeable) leading-/trailing-edge, but the role of permeability in this regard is still poorly understood.

1

THE rapid growth of human population, especially in the past century, has lead to an increased demand in energy supply and mobility solutions. In order to mitigate the worsening of climate change due to the excessive usage of fossil fuel, wind turbines have been considered as a sustainable alternative for generating electricity. Unfortunately, many wind farm projects, particularly the onshore ones, have been facing resistance in many places [1]. A common reason for this is the widespread annoyance induced by wind-turbine noise. Aside from wind turbines, airborne noise pollution from civilian flights has also become a widespread issue. As a matter of fact, it has been reported that 47 major European airports have been responsible for exposing more than 2.5 million people to a noise level that is well above the recommended limit from the World Health Orgnaisation (WHO) [2]. The impact of aircraft noise pollution is expected might become worse as the number of flights continues to rise in the near future, in spite of major global events, including the COVID-19 pandemic. Therefore, noise mitigation approaches will become key elements in the development of new wind turbines and aircrafts in the near future.

1.1. AERODYNAMIC NOISE CHALLENGES IN THE INDUSTRY

1.1.1. TURBOFAN NOISE

Modern passenger airliners have enabled long-distance travel within a relatively short amount of time compared to other modes of mass transportation, such as trains and ships. This achievement can be partly attributed to the development of jet engines. Unfortunately, as soon as jetliners become more popular, reports of noise annoyance were also becoming more common. In the mid 1950s, less than a decade after the first jetliner (i.e., de Havilland Comet) had flew before, Boeing's first jet airliner, the 707, was heavily criticised for causing noise-related disturbances surrounding major airports in the United States [3]. Under the pressure from both government and general public, engineers and scholars began to investigate aircraft noise sources, and it was unsurprising that the propulsion system was one of the main culprit [4].

Early investigations into turbulence-induced sound were motivated by the emission of loud noise produced by turbojets. The unsteady velocity gradients in the shear layer of a high-speed jet play an important role in noise generation, which was confirmed mathematically by Sir James Lighthill [15, 16] through his seminal paper in 1952. He also concluded that the noise intensity scales with the eighth-power of the jet velocity, and therefore, noise reduction can be achieved by reducing the engine exhaust velocity. In order to maintain thrust, it is necessary for the engine to deliver a higher mass flow rate, which can be achieved by enlarging engine diameter. Concurrently, a wider engine operating with a lower exhaust velocity has a higher propulsive efficiency and lower specific thrust (i.e., the amount of energy spent per unit of thrust), and in turn, fuel consumption. These benefits led to the shift from turbojets to turbofans for civilian airliners in the 1960s [17].

As shown in figure 1.2, a turbofan is equipped with a fan upstream of the engine core. A portion of the air flowing through the fan is diverted into the bypass duct, while the rest undergoes combustion in the engine core. This is different from a turbojet where the entire inflow is utilised for the combustion process. The ratio between the mass flow rate

Figure 1.1: The evolving trends of jetliners. Image sources following the chronological order: [5], [6], [7], [8], [9], [10], [11], [12].

that enters the bypass duct and that into the engine core is referred to as the bypass ratio (BPR). An engine with higher BPR generally produces the majority of its thrust from the flow in the bypass duct that is accelerated by the fan. Thus, one can argue that a modern high-BPR turbofan is almost identical to a ducted fan that is powered by a gas-turbine engine at the core, similar in principle to a turboprop engine. The flow exiting the bypass duct has a lower velocity compared to that from the engine core. This realises a more gradual mixing between the exhaust from the engine core and the surrounding free stream, resulting in a weaker jet noise generation. Since aircrafts started to adopt turbofans over turbojets, their overall noise emission level has been reduced substantially, as depicted in figure 1.2. Nevertheless, the exhaust jet is not the only noise source in a turbofan. In fact, as the jet noise contribution is reduced further, other noise sources would only become more relevant .

Several major aerodynamic noise sources on a typical modern wide-body jetliner (e.g.,

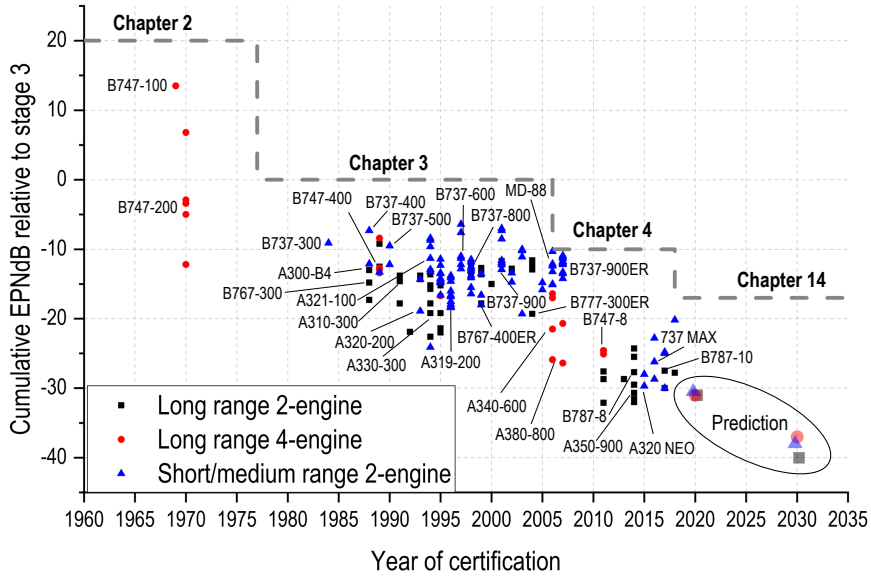

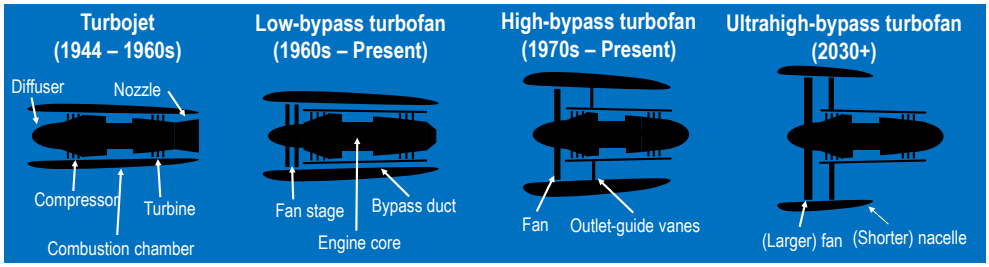

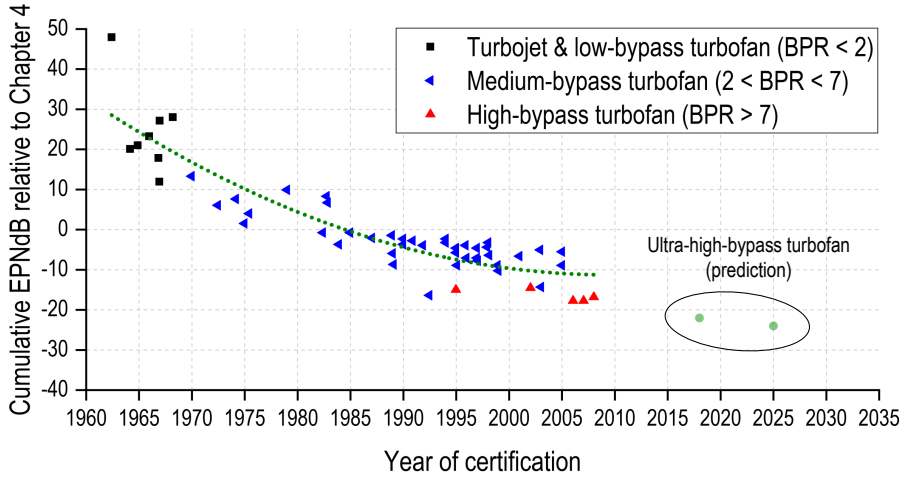

Figure 1.2: (Top) The trend of aircraft noise in term of the cumulative effective-perceived noise level in decibel (EPNdB) relative to the Stage 3 limit [13]. (Middle) Types of turbomachinery as aircraft propulsion system. (Bottom) The correlation between the aircraft noise in cumulative EPNdB relative to the Chapter 4 limit and the propulsion system [14].

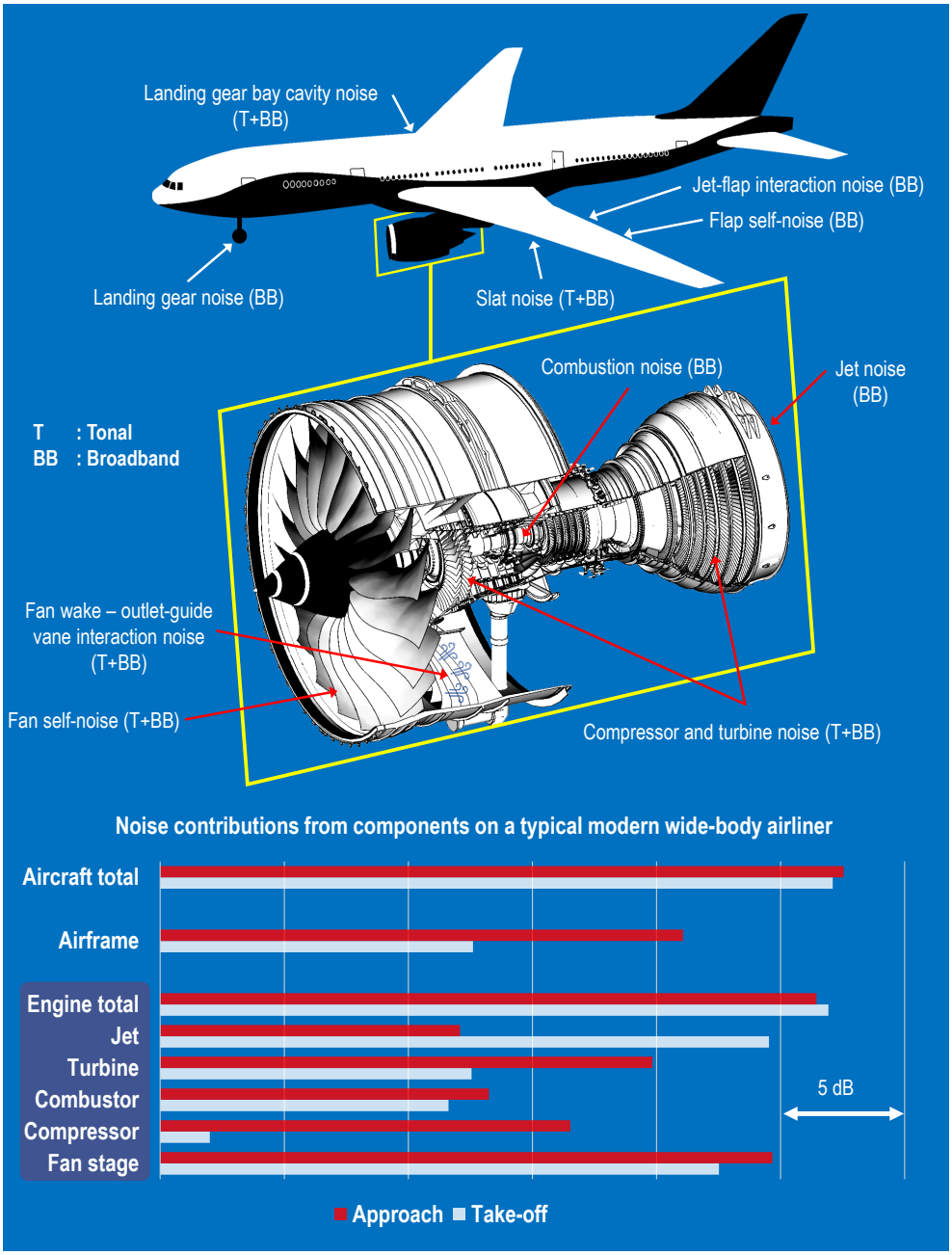

Figure 1.3: (Top) Several of the most relevant noise sources on a modern airliner, including those inside a turbofan (middle). (Bottom) A comparison between the noise contribution from engine components, airframe, and the total from the entire aircraft [18].

Boeing 787 or Airbus A350) are illustrated in figure 1.3 . The bar chart at the lower part of the figure shows the differences in noise levels between take-off and approach conditions. Spectral characteristics of each noise source are also indicated, e.g., tonal, broadband, or both. It is evident that the noise from the turbofan is still more dominant than that of the airframe (e.g., landing gear and high-lift devices).

Aside from jet noise, the turbofan itself contains multiple noise sources. Some of which are found in the fan stage, which consists of two main elements, the rotating fan (rotor) and the downstream outlet-guide vanes (OGVs / stator). The OGV helps improving the aerodynamic efficiency of the turbofan by recovering the swirl in the fan wake. The steady loading component on the fan blades produces distinct tones at the blade-passage frequency (BPF) and its harmonics, which are often referred to as rotor-locked (Gutin) noise [19]. Additional tonal and broadband noise would be generated if the fan is subject to unsteady loading due to, among others, boundary-layer ingestion or inflow distortion at the engine inlet. The fan blades also produce broadband self-noise [20] [1] as the turbulent boundary layer on each blade flows past the trailing edge. As the fan rotates, it leaves behind trails of turbulent wakes that impinge the OGVs. This process is referred to as the fan wake-OGV interaction, which has been found to be the main noise contributor in mid-to-high BPR turbofans [21]. The fan wake-OGV interaction noise is characterised by both tonal and broadband features. The former is determined by the periodicity of the fan wake impingement at the OGV, and therefore, it is related to the fan rotational speed. The latter is associated with the existence of a wide range of turbulence length scales in the fan wake.

Even though newer turbofans are equipped with higher BPR compared to their predecessors, the overall noise reduction benefit between generations is becoming smaller due to the increased contribution of the fan-stage noise. This trend can be clearly observed in figure 1.2. For a modern high BPR turbofan, as shown in figure 1.3, the fan-stage noise is almost at the same intensity as the jet noise during take-off, but the former is significantly more intense during approach. Consequently, the mitigation of fan-stage noise has become equally, if not more important than that of jet noise. Furthermore, the approach condition can also be considered more crucial than take-off in term of noise impact as the aircraft stays closer to the ground for a longer period of time [22].

In the European Union, ACARE[2] has set several goals for future aviation technologies with its *FlightPath* 2050 programme. It aims to reduce CO_2 and NO_x emissions by 75 % and 90 % respectively relative to those in the year 2000. Meanwhile, the perceived aircraft noise level is targeted to be 65 % or 4.5 dB lower, which is equivalent to an average of 0.1 dB reduction per annum. To achieve these targets, future turbofans are expected to accommodate a ultrahigh-bypass ratio (UHBPR) fan stage [23], due to which fan-stage noise mitigation efforts would become more essential.

1.1.2. WIND TURBINE NOISE

Wind energy has been considered as a very promising source of renewable energy, and its adoption has been increasing steadily over the past several decades. The wind turbine

[1] The noise due to the interaction between an aerodynamic body and the turbulence in its boundary layer.
[2] Advisory Council for Aeronautics Research in Europe

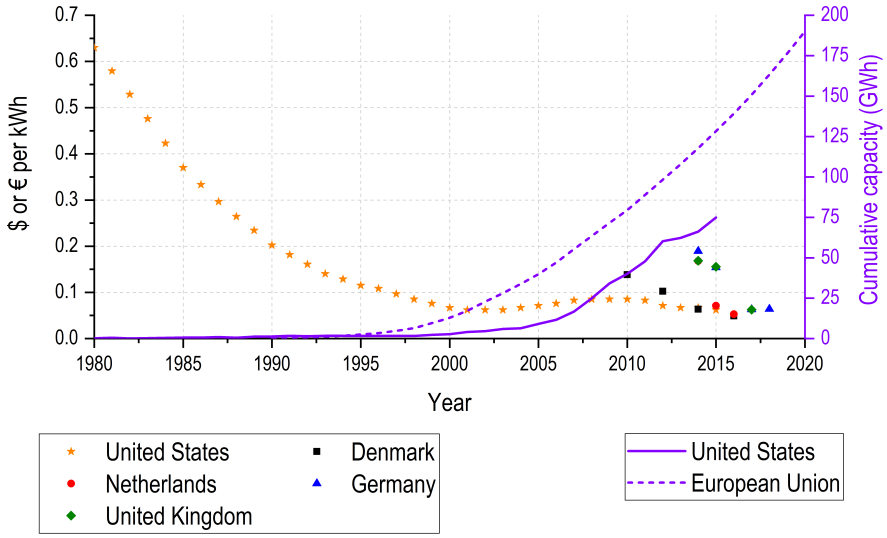

Figure 1.4: The trend of cost per unit of wind electricity and the cumulative capacity of wind energy across the global north [24, 30].

industry saw a massive growth during the 1980s, especially in the United States with the financial support of the local government [24]. During this period, the cost of wind-generated electricity dropped exponentially, as depicted in figure 1.4, although it did not last long as the public funding scheme was ended in 1985. Over the 1990s, the development of wind energy infrastructure in Europe outpaces that in the United States. By 2003, Denmark has 3 GW of wind energy capacity [25] supplied by more than 5500 turbines. Nevertheless, other developing nations are also catching up to the rest of the global north. At the time of writing [26], the International Renewable Energy Agency (IRENA) reported that China owns almost 39 % of worldwide wind capacity, followed by the European Union (27 %), United states (16 %), and India (5.3 %). It is evident that more nations around the world are considering wind energy as a renewable alternative to replace carbon-based energy sources [27], especially in an effort to reduce carbon-dioxide emission and to slow down the progress of climate change. Hence, the demand for wind energy is projected to continue growing in the near future [28, 29]. Wind energy manufacturers have responded to such demand by designing new wind turbines with higher efficiency and energy production capacity.

The maximum wind power than could be extracted by a horizontal-axis wind turbine (HAWT) P_{max} can be estimated using the actuator disk theory as in equation 1.1,

$$P_{max} = \frac{16}{27}\left(\frac{1}{2}\rho_\infty U_{wind}^3 S\right) \tag{1.1}$$

where ρ_∞ is the air density, U_{wind} is the wind velocity, and S is the actuator disk area. Since $\frac{1}{2}\rho_\infty U_{wind}^3 S$ is equal to the available power within the wind itself, one can conclude that the maximum theoretical efficiency of a HAWT is $\frac{16}{27}$ or 59.3 %. This limit was first

identified by a German physicist, Albert Betz [31], and it is subsequently referred to as the Betz's law. In equation 1.1, the wind turbine design is represented by the rotor area S. Thus, it is possible to increase the wind turbine energy output by employing a wider rotor diameter. Such design choice also has the added benefit of exposing the rotor to a faster wind at higher altitudes as it would be necessary to mount a wider rotor on a taller tower. These design choices are reflected in figure 1.5, which shows that both the rotor diameter and the tower height have been steadily increasing over the past several decades. However, these trends also bring negative implications concerning wind-turbine noise emission.

As illustrated in the upper half of figure 1.6, there are multiple aerodynamic noise mechanisms on wind-turbine blades [20]. Most of these can be suppressed or completely eliminated by improving the design of the blade profile [38]. However, the turbulent boundary-layer trailing-edge (TBL-TE) noise mechanism remains unavoidable, and it is currently the primary noise source in modern wind turbines. TBL-TE noise is generated by the scattering of pressure fluctuations beneath the turbulent boundary layer at the TE of a wind turbine blade. The source power level (PWL) of TBL-TE noise is proportional to the blade span (b) and to the fifth-power of the local incidence velocity (U_∞^5) as indicated in equation 1.2 [39]:

$$\mathrm{PWL} \propto \frac{\rho_\infty U_\infty^5 L^2 b}{a_\infty^3} \tag{1.2}$$

where L is the spanwise turbulence length scale in the boundary layer. As a consequence, there exists a direct proportionality between the radiated acoustic energy and both power output and rotor diameter as depicted in the lower half of figure 1.6 [35]. In addition to this, the low-frequency noise component is increasingly dominant for larger wind turbines, especially in the MW-class. The enhanced low-frequency noise is particularly concerning as the corresponding sound waves are able to propagate farther than the high-frequency ones in the atmosphere. The underlying mechanism of TBL-TE noise also plays a role in this regard. Although TBL-TE noise is broadband in nature, its peak intensity follows the proportionality $f \leq U_\infty/\delta^*$ [40], where δ^* is the displacement thickness of the turbulent boundary layer that is also proportional to the boundary layer thickness. Since a wind-turbine blade with a longer span and chord tends to produce a thicker turbulent boundary layer on its surface, the resulting peak noise intensity also shifts towards a lower frequency.

Public responses to wind turbine noise have been widely reported in literature. Pedersen [41] surveyed several communities in Sweden and Netherlands and subsequently found that the exposure to wind-turbine noise can induce higher stress levels and sleep disturbances. Davy *et al.* [37] performed a similar study after compiling the data gathered from a larger number of countries. The percentage of annoyed survey participants rises substantially as the perceived wind turbine noise level is comparable to or above that of the background noise, as shown in figure 1.6. To provide a perspective, the wind-turbine noise level for a rotor diameter of 100 m (e.g., 4 to 5 MW class) can still reach 40 dBA at a distance of half a kilometer away [42]. This level is equivalent to the noise emission from an average refrigerator or a microwave oven. Although such noise level is not completely unbearable, there might be certain aspects of wind turbine noise

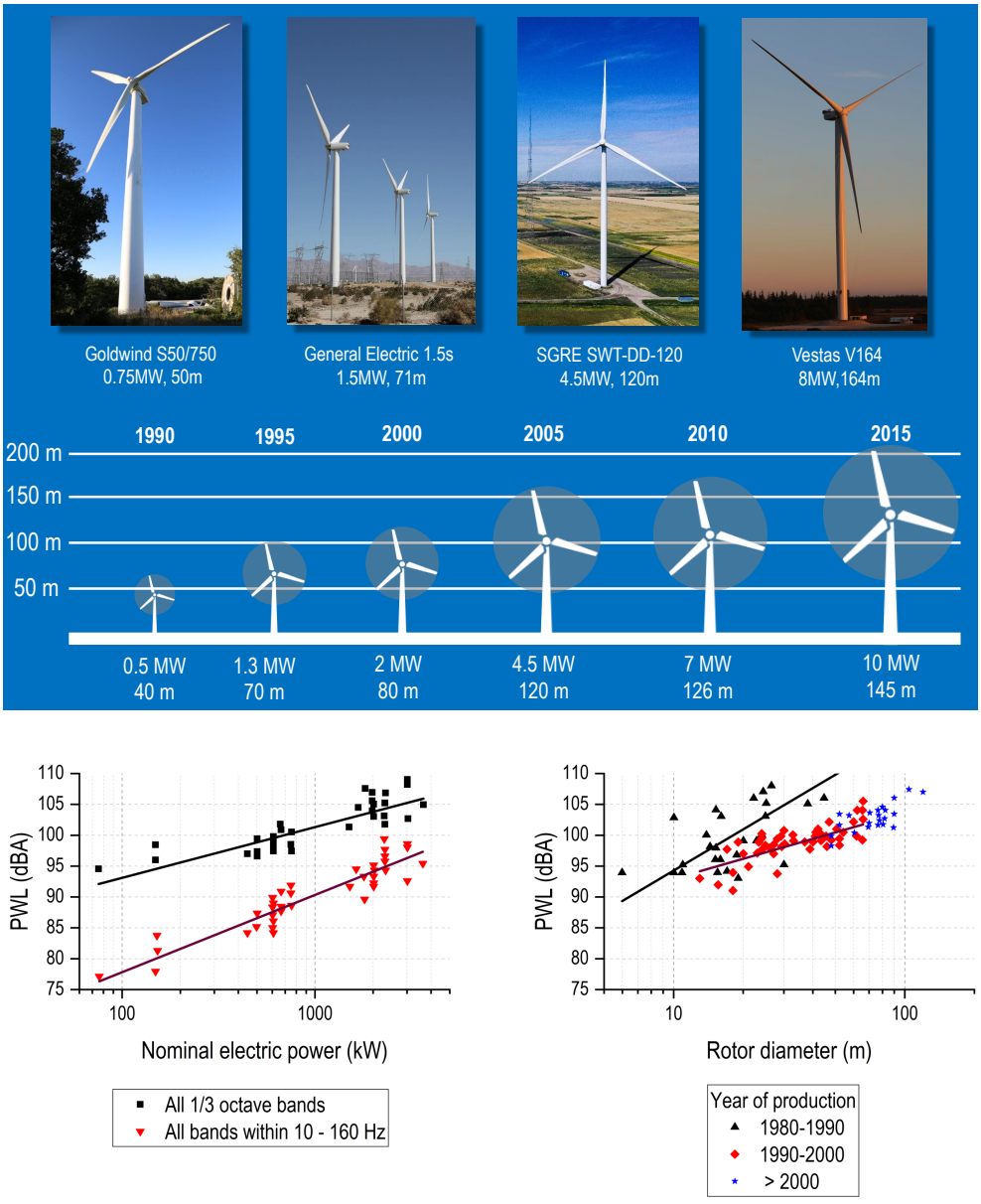

Figure 1.5: (Top) The trend of wind-turbine rotor diameter for the past 3 decades [32]; photos were taken from online databases [33], SGRE: Siemens-Gamesa Renewable Energy. (Bottom) The correlation between acoustic power level (PWL) with power output and rotor diameter [34, 35]. Logarithmic fit of the dataset is shown as solid lines.

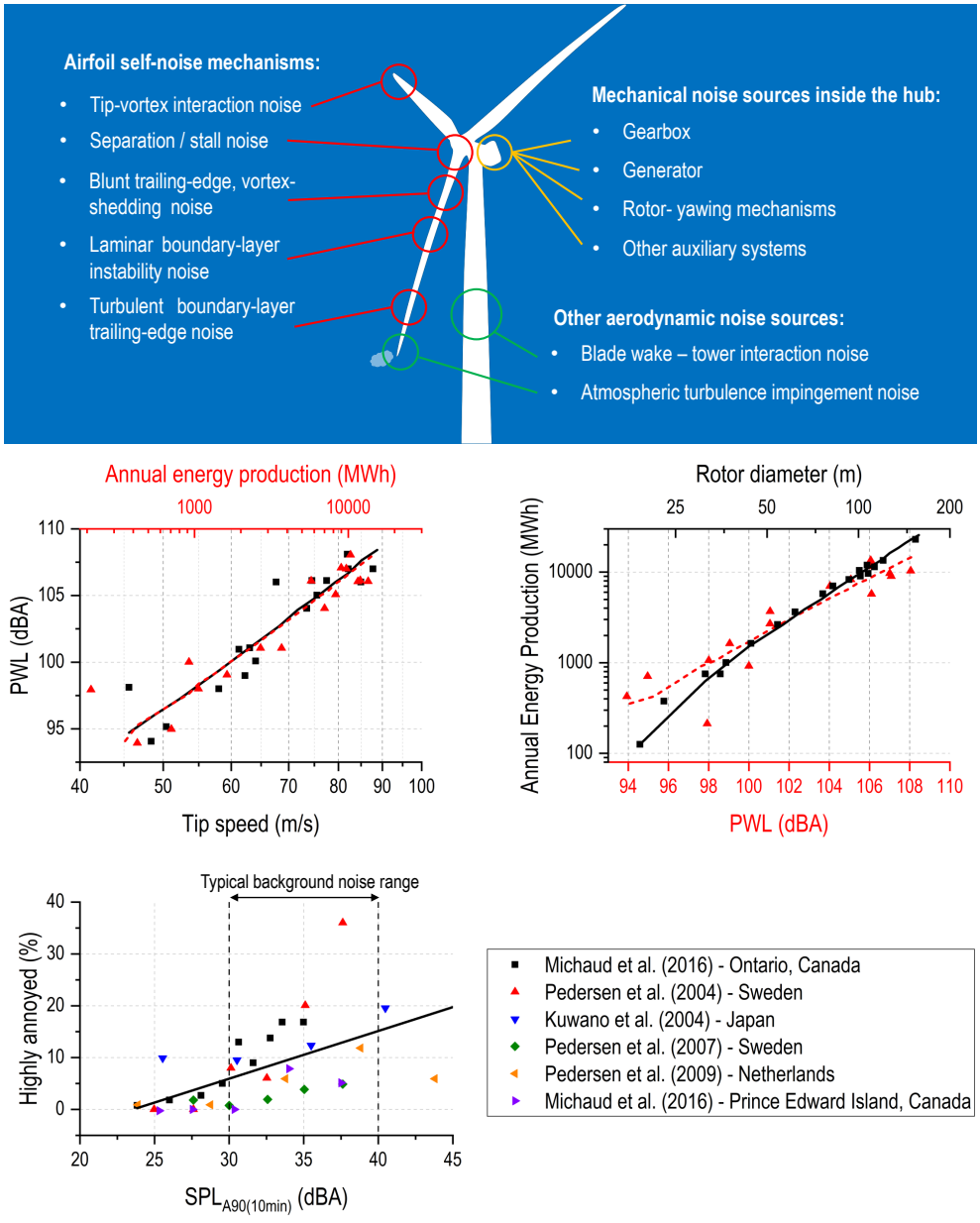

Figure 1.6: (Top) Various noise sources on a modern horizontal-axis wind turbine. (Middle) The correlation between sound power level (PWL) with rotor tip speed, rotor diameter, and the energy output of various types of Siemens wind turbines [36]. (Bottom) The correlation between the percentage of highly-annoyed people surveyed and the sound pressure level (SPL) of wind turbine noise that exceeds background noise level 90 % of the time within a 10-minute period. Data points were reproduced from Davy *et al.* [37].

that can provoke stronger annoyance compared to other noise pollution sources, such as road traffic. One possible cause is the periodic modulation of the TBL-TE noise amplitude and frequency due to the blade rotational motion, which generates the "swishing" sound phenomenon [36, 43]. Due to the detrimental effects of wind-turbine noise, in addition to visual pollution, some countries have imposed laws that prevent wind turbines from being built near housing areas. For instance, the "10-H"[3] rule in Germany [44] implies that a wind turbine can only be built at a minimum distance of 10 times of its height from the nearest residential building.

Modern wind turbines generally operate more silently than their predecessors thanks to optimised rotor designs and control systems, as depicted in figure 1.6. Nevertheless, the positive correlation between rotor diameter and noise emission level is still evident, which highlights the importance of new innovations in noise mitigation strategies as wind turbines continue to increase in size and number. Following equation 1.2, the noise intensity of TBL-TE noise depends on the incident flow velocity, or in other words, the turbine rotational speed (see figure 1.6). Thus, when the wind-turbine noise emission is above the allowed range, it is possible to limit the rotational speed as a means of noise reduction (i.e., curtailment). Curtailment also serves as a countermeasure against unfavourable situations, such as to prevent rotor overspeed under strong winds. However, curtailment would reduce the turbine's productivity under normal circumstances, and therefore, it is not an ideal noise mitigation solution. As a matter of fact, Oerlemans and Fuglsang [36] suggested that a sound power level reduction of 1 dBA potentially lead to 20 % additional energy production when a wind turbine is able to operate under the noise limit. Therefore, quieter wind turbines are necessary not only to promote public acceptance, but also to maximise their power output potential.

1.2. NOISE GENERATION BY TURBULENCE

Due to the negative implications of turbulence-induced noise in various engineering applications, extensive studies have been performed to better understand the underlying physical principles. Turbulence can be characterised by the presence of stochastic velocity and pressure fluctuations in a flow field [45]. In order to relate turbulence to the noise that it generates, Lighthill [15] introduced the concept of aeroacoustics analogy, where the Navier-Stokes equations that govern the motion of fluids were reorganised into an inhomogeneous wave equation that describes sound propagation. All terms that do not belong to the wave operator are interpreted as the flow quantities that are responsible for generating sound. Lighthill's analogy provides the theoretical foundation for understanding noise generation from the turbulence produced in the shear layer of a jet. Lighthill predicted that the jet-noise intensity varies with U^3M^5 (U and M are the mean flow velocity and Mach number respectively), and thus, turbulence by itself is not a very efficient noise radiator at low Mach number. Obviously, this is not always the case with aircraft engines whose exhaust velocity can approach transonic conditions in turbofans for civil aviation and fully supersonic conditions in military turbojets, although these are more common during the take-off and cruise phases rather than the approach one.

Lighthill's analogy was later expanded by Curle [46] who considered a situation where

[3] H is the total height of individual turbine

an arbitrary solid boundary exists in proximity of turbulence. Curle found an additional noise source term that was associated with the unsteady forces on the solid body induced by the flow fluctuations in the turbulence. The sound intensity corresponding to this source term scales with U^3M^3. Therefore, this implies that the interaction between turbulence and a solid body radiates noise at a higher efficiency compared to the turbulence itself at low Mach numbers. A more detailed description of the acoustic analogy will be provided in chapter 2, but it is possible to conclude that turbulence has a relevant role in generating flow-induced sound.

In the previous sections, two examples of turbulence-induced noise mechanisms have been discussed. These are the fan wake-OGV interaction noise in a turbofan and the turbulent boundary-layer trailing-edge (TBL-TE) noise on a wind-turbine blade. Simplified representations of these cases are shown in figure 1.7. The upper figure shows a cylinder leaving a trail of turbulent wake that impinges the downstream airfoil. The blockage induced by the airfoil leading edge deforms the eddies inside the turbulent wake. This process converts a small amount of the turbulent kinetic energy into sound waves, and its efficiency depends on multiple factors, such as the sharpness of the leading edge and the distance of the eddies from the airfoil surface [47–49]. In the figure, sound waves are visibly radiated away from nearby the airfoil leading edge, and therefore, TIN is often referred to as leading-edge noise in literature. The lower half of figure 1.7 shows the development of turbulent boundary layers on an airfoil. As the turbulent boundary layer flows past the trailing edge, the aerodynamic pressure fluctuations are scattered into sound waves [50–52]. This scattering phenomenon is the consequence of the pressure field adjustment in the turbulent boundary layer during the transition between the airfoil surface and the wake [53].

Although the physical mechanisms of TIN and TBL-TE noise appear different, it can be argued that both are caused by turbulence encountering boundary discontinuities in the flow-field [51, 52] (e.g., from a solid surface to a free fluid in TBL-TE noise case and the opposite in TIN). Therefore, it is reasonable to consider a noise mitigation approach by replacing the solid edge with a different material that realises an intermediate condition, such as permeable/porous material [54]. Prior to this discussion, however, the following subsection examines recent noise reduction approaches that have been considered in the industry.

1.3. NOISE MITIGATION STRATEGIES

1.3.1. CURRENT INDUSTRIAL APPROACHES

The reduction of turbofan fan-stage noise has been traditionally achieved by optimising the aerodynamic performance of the fan and OGV blades to lower the fan tip speed, the fan pressure ratio, and the jet exhaust velocity [55]. These changes have been realised by increasing the turbofan bypass ratio, but the noise reduction gains are expected to become smaller over time, as other noise generation mechanisms are becoming more dominant, such as the interaction between the fan wake and the OGV. In modern turbofans, acoustic treatments are employed to alter the sound propagation characteristics. For instance, acoustic liners are installed at the turbofan inlet and bypass duct to absorb sound waves [56] using the Helmholtz resonance principle. Following

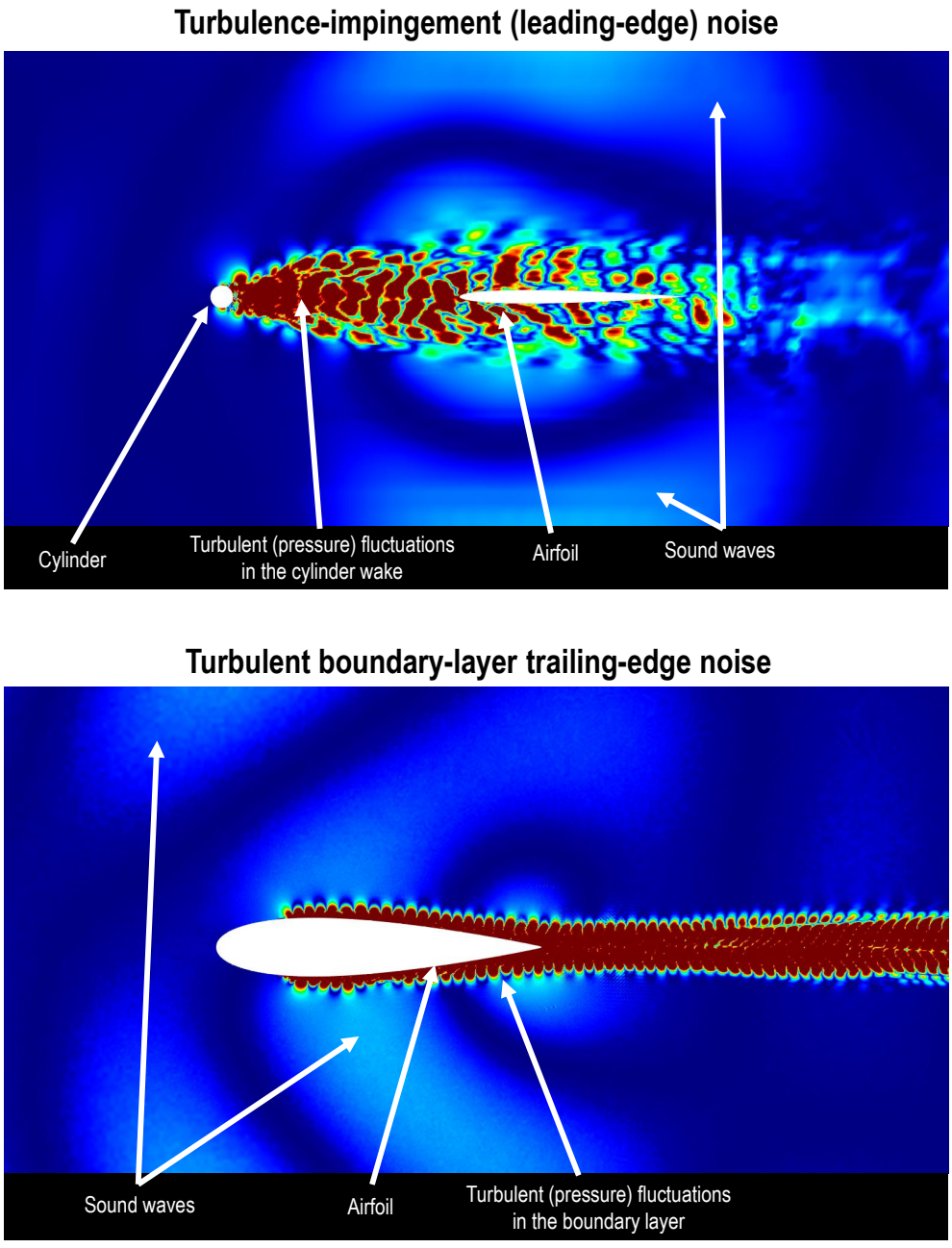

Figure 1.7: A visualisation of pressure fluctuations contours for two cases: turbulence-impingement noise (top) and turbulent boundary-layer trailing-edge noise (bottom). The flow is coming from the left side of the figure. The colour in the contour varies from dark blue to dark red representing the pressure fluctuations intensity in ascending order.

their widespread adoption, novel liner designs are still being actively investigated [57, 58]. Scarfed inlet has also been considered to deflect noise away from being radiated towards the ground [59], although it induces asymmetric inflow distortion that also has an effect on fan tonal noise emission.

Some unconventional aircraft designs can also realise a noise shielding effect. For instance, the turbofans of the VFW-Fokker 614 aircraft are mounted above the wings instead of underneath, which helps mitigating the noise radiation towards the ground. Future blended-wing-body aircraft designs are also likely to benefit from a similar design approach [60]. Some noise mitigation techniques aim at suppressing the noise sources directly. Leaned and swept vanes have been considered for mitigating the fan wake-OGV interaction noise [61]. Serrated nozzle, also referred to as the "chevron" modification has been found to reduce the turbulence intensity in the mixing layers at the turbofan outlet, which leads to a weaker jet noise emission [62, 63]. In fact, the chevron nozzle has now become one of the most iconic feature of the latest airliners, such as the Boeing 787-Dreamliner (see figure 1.8).

Noise sources in wind turbines can be broadly classified into mechanical and aerodynamic ones as depicted in figure 1.6. The former consists mainly of the noise contribution from the gearbox, transmission system, and generator. All of these are confined within the hub and the nacelle of the turbine [67], and thus, noise transmission can be prevented with sufficient insulation [68]. Consequently, the aerodynamic noise produced by the wind-turbine blades is usually the dominant one, including the TBL-TE noise mechanism [67]. Since insulating the noise generated by the wind turbine blade is practically impossible, it is necessary to treat the noise sources directly. TBL-TE noise characteristics are closely linked to the boundary layer properties [20], and consequently, the blade profile can be optimised to modify the boundary layer characteristics that are less favourable for noise generation [69, 70], such as by minimising the displacement thickness near the trailing edge [39]. More recently, trailing edge modifications, such as serrations (see figure 1.8), have also been deployed in many wind turbines [71]. The serrations essentially modify the planform of the trailing edge to suppress the noise scattering efficiency [72]. They are usually manufactured as trailing-edge addons, implying that serrations can be retrofitted onto older turbines, potentially extending their operational lifespan despite the constraints of newer noise regulations.

1.3.2. NOISE REDUCTION WITH POROUS MATERIALS

Flow-permeable materials, including porous materials, have been found in multiple studies to show promising aerodynamic noise suppression [54, 73–78]. Porous materials or porous media can be defined as a group of materials containing voids or pores [79]. The open pores are usually occupied by another medium of different phase, such as liquid or gas. The skeletal (solid) portion of the material is referred to as the matrix. Depending on the arrangement of the matrix and pores, porous materials can be classified into different types, such as rigid foams, porous crystals, and perforated materials. A few examples of these are shown in figure 1.9. Due to their shapes, porous materials possess several unique properties beyond those of their constituents, such as reduced density and increased specific surface area. Certain artificial porous media can also produce properties that otherwise can not be found in nature, and for this reason,

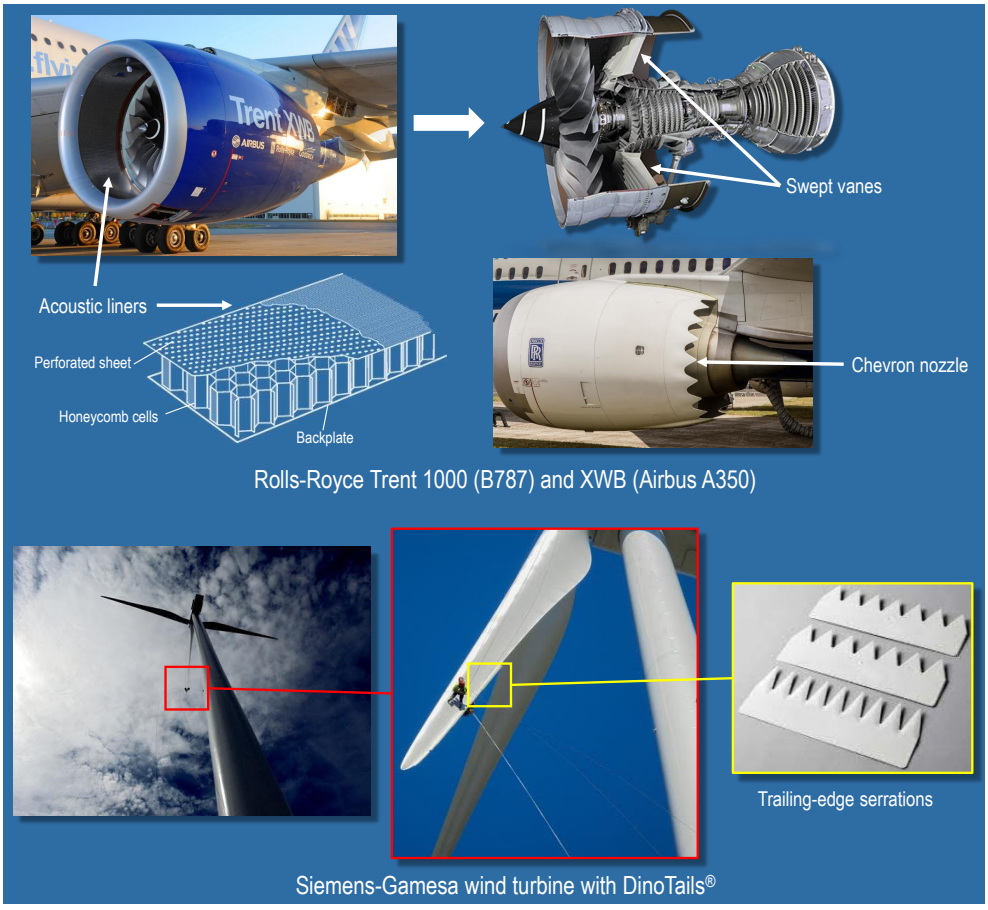

Figure 1.8: (Left) The applications of noise mitigation technologies on Rolls-Royce Trent 1000/XWB turbofan [64, 65]. (Right) A Siemens-Gamesa wind turbine that is equipped with trailing-edge serrations in Tohkoja, Finland [66].

they are also referred to as meta-materials[4]. Due to their unique properties, porous materials have been utilised in a wide range of applications, from sound absorber to heat exchanger.

Porous materials can be characterised based on various aspects [80], some of which are presented in figure 1.10. For instance, the geometry of a porous material can be described using the pore size or unit-cell dimension. There are up to 6 different parameters that can be used to characterise the transport properties of porous materials[74]. Among these, however, porosity, tortuosity, permeability, and form coefficient have been identified to be the most relevant ones in regard to aerodynamic noise mitigation [81, 82]. In certain applications, such as liners, the acoustic properties of porous materials, such as impedance, are also relevant. The characterisation of the

[4]Meta-material comes from the Greek word *meta* and *materia*, and it translates to "beyond (natural) material".

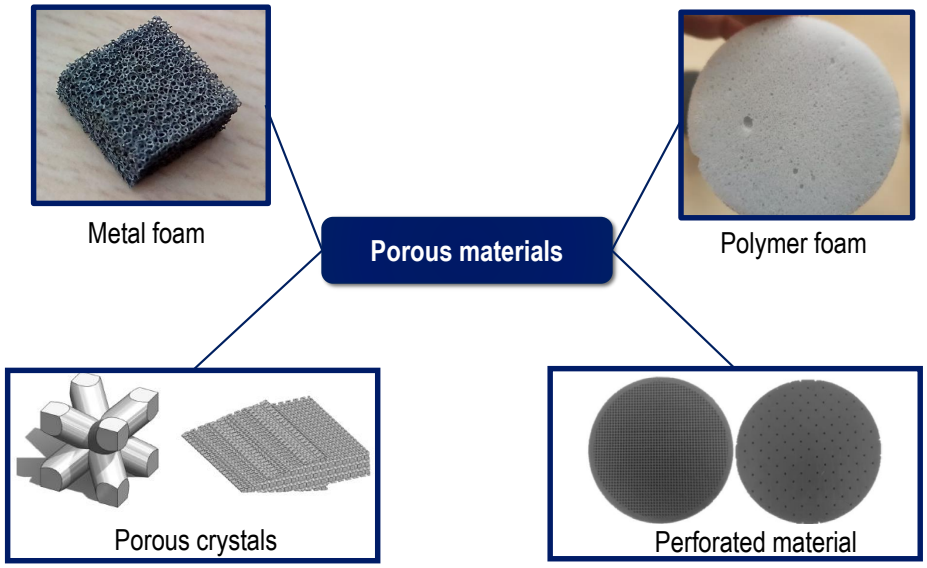

Figure 1.9: Several examples of porous materials with different topologies.

porous material will be discussed further in chapter 2.

Early ideas behind permeable material applications for noise reduction might have been inspired through biomimetics[5]. In 1934, Graham [83] associated the silent flight ability of owls to the permeable structures on their wings. More recently, similar observations were carried out by Lilley [84]. One of the earliest practical usage of permeable treatments has been demonstrated by Hayden [85] for mitigating jet-wing interaction noise, where a 10 dB noise reduction was achieved using a porous trailing-edge. Later, Lee [73] performed a numerical study about the application of a porous leading edge to mitigate blade-vortex interaction (BVI) noise on a helicopter rotor. The porous leading edge suppressed the pressure fluctuations at the blade surface, which was linked to noise attenuation. Porous edge concept was also studied by Revell *et al.* [86] to treat noise sources along the side-edge of a model flap of Lockheed L-1011 aircraft. Beneath the flap, a substantial reduction in sound pressure level was observed in the entire frequency range of interest. However, above the flap, there was a noticeable noise increase in the mid to high frequency range (2 to 10 kHz). Tinetti *et al.* [87] performed a numerical investigation on the application of porous edge treatment for OGVs of a turbofan to mitigate the fan wake-OGV interaction noise. The porosity of the edge treatment was varied between 10 % to 22 % depending on the chordwise position. In this study, the porous treatment achieved a relatively small noise reduction of around 2 dB, which was attributed to the low porosity value.

More recent investigations were also aimed at revealing the relationship between porous material properties and the noise reduction level [54, 74–78]. In general, the

[5] Engineering solutions derived from observations of nature.

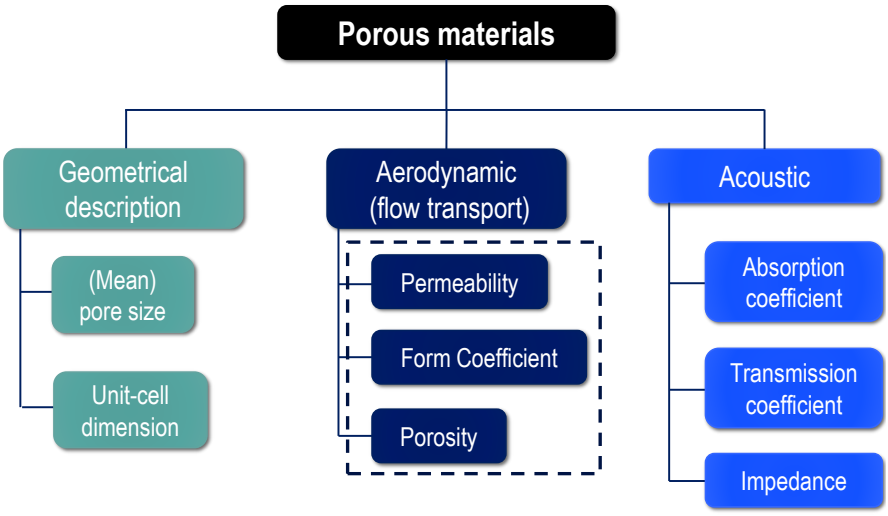

Figure 1.10: Porous material characteristics based on various aspects. The segment in dashed box contains the parameters that are commonly considered in aeroacoustics investigations.

applications of porous materials with higher permeability were found to achieve higher noise reduction. Despite this, the role of permeability in promoting noise attenuation has not been completely explored in the literature yet, although several hypotheses have been proposed. Herr *et al.* [54] suggested that a pressure release process between the opposite sides of a permeable edge is responsible for noise attenuation. A more recent study by Rubio Carpio *et al.* [88] also arrived at a similar conclusion. Aside from the noise mitigation mechanisms, there are also design aspects of a porous edge treatment that deserve a closer examination, including the variation of permeable chordwise extent and spanwise planform shape (e.g., the integration of serration-like shape). A better understanding on these aspects could provide hints towards optimisation. Previously, Carpio *et al.* [89] investigated the effects of varying the permeable extent of a porous trailing edge, where it was found that a longer permeable extent generally corresponds to a higher noise reduction level. However, no conclusive link between the observed trend and the noise mitigation mechanisms had been found.

Experimental flow measurements surrounding and inside a porous medium are often challenging to perform, as the installation of probes and transducers could alter the porous material properties [90]. Computational simulations can be considered as viable alternatives, although they are also not without issues. A simulation that replicates the porous medium geometry may become prohibitively expensive if there were a large discrepancy in geometrical scales between the porous medium and the main body. To circumvent this issue, the porous material can be replaced by an equivalent region where the effects on the permeating fluid are modelled, for instance, using the Darcy's law [91]. Using this method, the porous medium region imposes a resistance on the permeating flow field that is determined by the material resistivity, which is usually obtained

empirically. Porous material resistivity is often assumed to be constant irrespective of the sample thickness, but it is not always true for thin samples [92]. This behaviour should also be properly replicated in the simulation to produce an accurate aerodynamic and noise prediction, especially when a slender porous edge is involved.

Beyond the literature gaps that are mentioned earlier, this dissertation also aims to study the noise reduction capability of the different permeable treatments in proof-of-concepts that closely resemble their industrial counterparts. With these investigations, one would be able to observe not only the advantages of the permeable treatments, but also potential caveats that otherwise could not have been foreseen in simpler (laboratory) setups.

1.4. DISSERTATION OBJECTIVES AND ORGANISATION

Following the discussions in the previous subsection, the objectives of the present investigations can be summarised into the following:

1. **To examine the role of permeability of porous trailing edge and leading edge applications, especially its influences on the surrounding flow-field and the noise source characteristics.**
2. **To identify permeable edge design parameters that influence noise attenuation level, such as the chordwise permeable extent of a porous edge.**
3. **To discover an alternative porous medium modelling approach to circumvent the need to impose thickness-dependent resistivity values.**
4. **To assess the permeable treatments in proof-of-concepts, in order to evaluate their strengths and limitations in industrial applications.**

In line with the aforementioned objectives, this dissertation is organised into chapters as follows:

- **Chapter** 2 begins with a discussion on the computational approaches in aeroacoustics investigations, as well as an overview of the lattice-Boltzmann method (LBM), which has been employed throughout this dissertation. The second half of this chapter focuses on the numerical modelling of porous medium, including the implementation of the Darcy's law into a LBM solver. This is followed by the description of the multi-layer modelling approach that simplifies the definition of porous material resistivity for a thin geometry.
- **Chapter** 3 discusses about the application of porous trailing edge on a NACA 0018 airfoil. The porous trailing edge is modelled after a Ni-Cr-Al metal foam. The usage of the multi-layer modelling approach is also validated in this chapter. Afterward, the role of permeability for TBL-TE noise reduction is elaborated. The chapter also features an investigation on a fully-resolved porous trailing edge based on a porous crystal geometry. This is intended to verify the link between a physical porosity with the noise reduction mechanisms previously observed using the porous medium model. The chapter also examines the Reynolds number and angle-of-attack effects on the noise reduction of the metal-foam trailing edge.

- **Chapter** 4 addresses the application of porous leading edge concepts for a rod-airfoil configuration, which is a well-known benchmark configuration that mimics the fan wake-OGV interaction mechanism. In addition to the classical NACA 0012 airfoil, a NACA 5406 profile is also considered due to its slender and cambered features that are typical of turbomachinery blades. Both the aerodynamics and acoustics implications of the porous treatments are compared with those of leading-edge serrations, which represent the state-of-the-art solution. The chapter is concluded with an optimisation attempt using a poro-serrated leading edge concept.

- **Chapter** 5 initially discusses about the rod-linear cascade (RLC) model. It has been designed as an extension to the rod-airfoil configuration by including a linear cascade that better resembles a turbomachinery environment compared to a setup with an isolated airfoil. The first half of the chapter focuses on the acoustic and aerodynamic characterisation of the RLC model. Afterward, the latter half of the chapter looks into the application of a poro-serrated treatment at the outlet-guide vanes of a full-scale aircraft model.

- **Chapter** 6 concludes this dissertation by highlighting the key findings from the previous chapters. This is followed by several recommendations that encourage new ideas and plans for future investigations.

AERODYNAMIC NOISE REDUCTION WITH POROUS MATERIALS

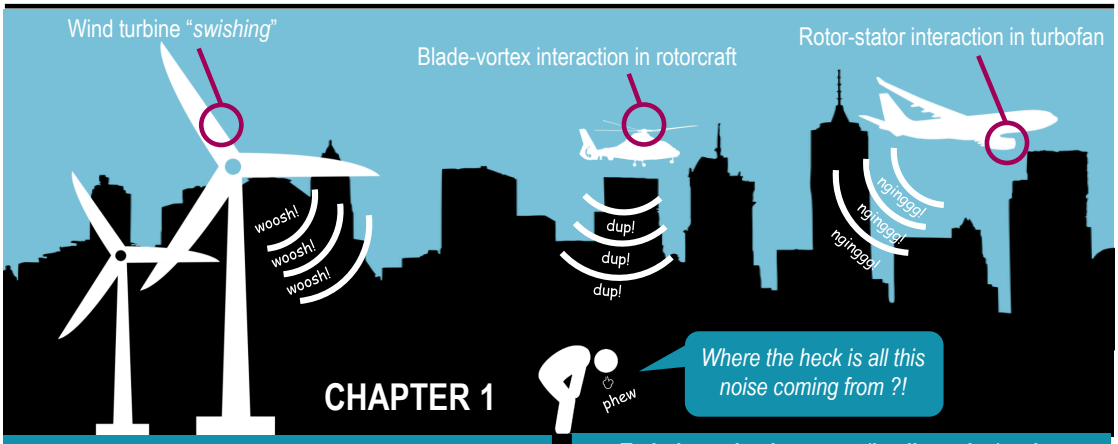

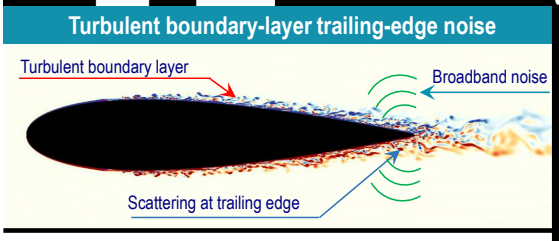

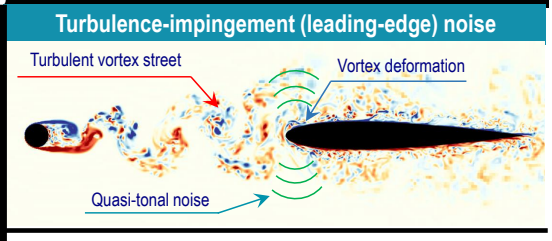

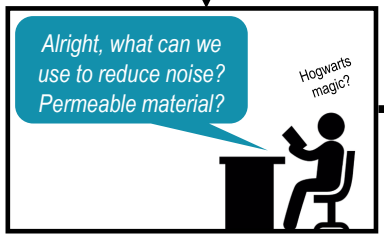

CHAPTER 2

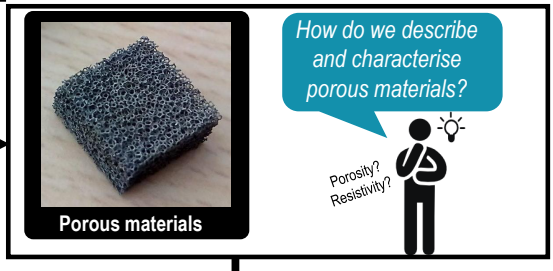

CHAPTER 3

CHAPTER 4

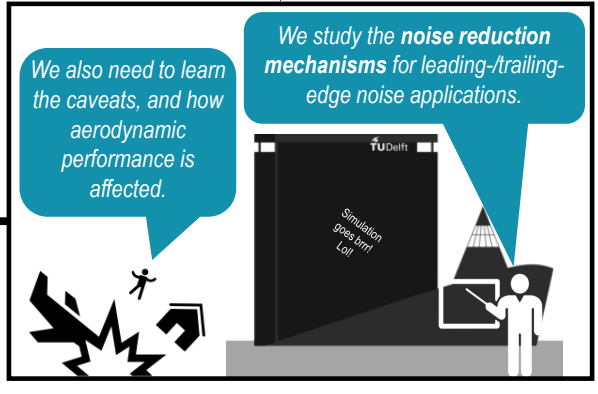

CHAPTER 5

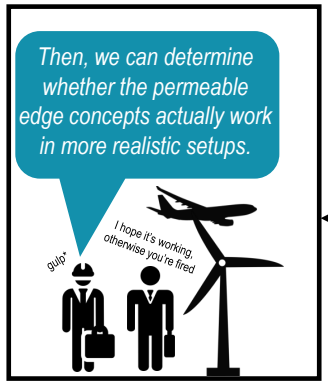

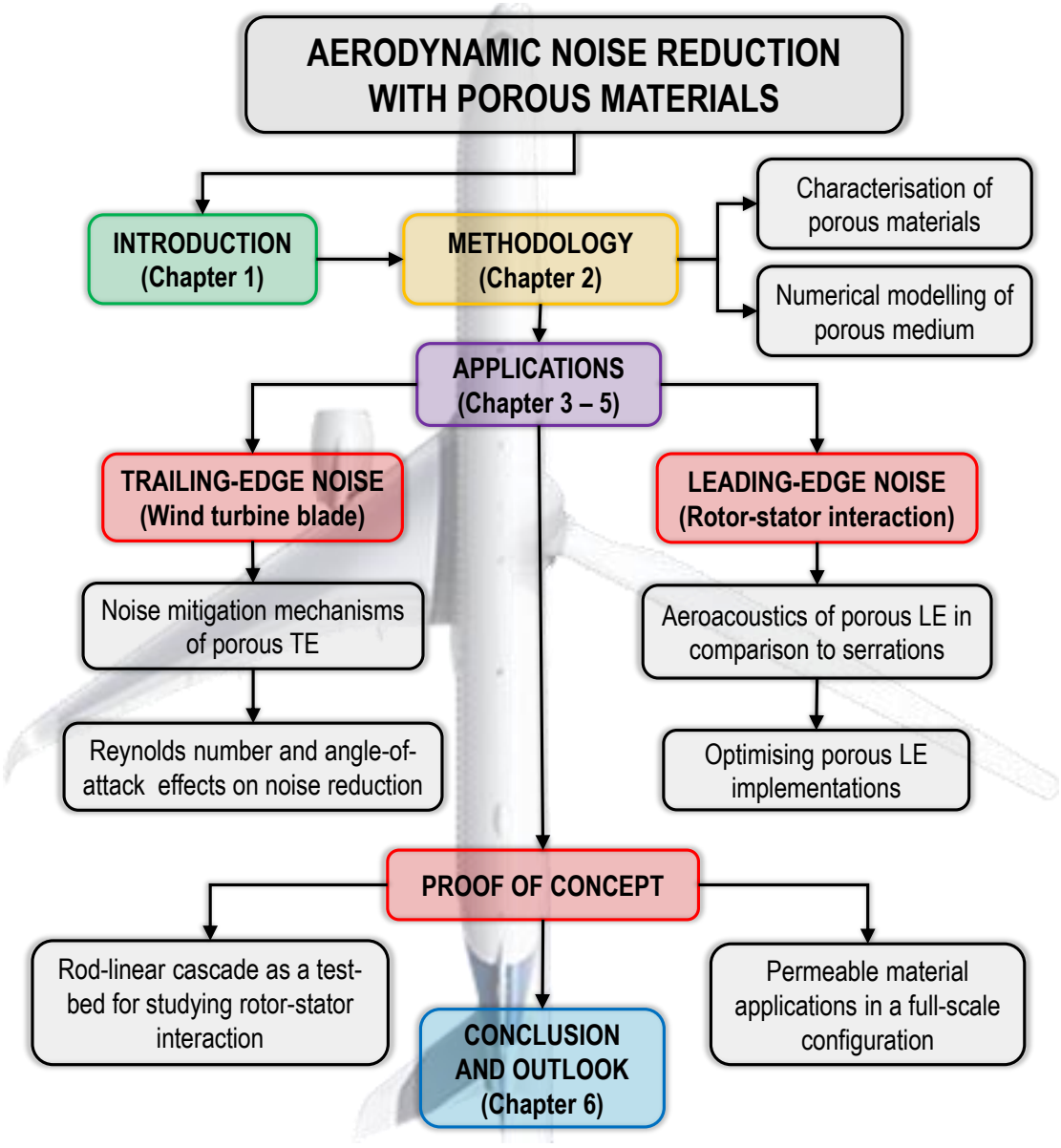
AERODYNAMIC NOISE REDUCTION WITH POROUS MATERIALS
INTRODUCTION (Chapter 1)
METHODOLOGY (Chapter 2)
Characterisation of porous materials
Numerical modelling of porous medium
APPLICATIONS (Chapter 3 – 5)
TRAILING-EDGE NOISE (Wind turbine blade)
LEADING-EDGE NOISE (Rotor-stator interaction)
Noise mitigation mechanisms of porous TE
Reynolds number and angle-of-attack effects on noise reduction
Aeroacoustics of porous LE in comparison to serrations
Optimising porous LE implementations
PROOF OF CONCEPT
Rod-linear cascade as a test-bed for studying rotor-stator interaction
CONCLUSION AND OUTLOOK (Chapter 6)
Permeable material applications in a full-scale configuration

1

REFERENCES

[1] B. Wehrmann, *Limits to growth: Resistance against wind power in germany,* (2020).

[2] EASA, *European aviation environmental report,* .

[3] L. L. Beranek, *The noisy dawn of the jet age,* Sound and vibration **41**, 94 (2007).

[4] H. H. Hubbard, *Aeroacoustics of flight vehicles: Theory and practice. volume 1. noise sources*, Tech. Rep. (NASA Langley Research Center, Hampton, VA, 1991).

[5] *De havilland comet 3 and 4: An extensively developed variant of the earlier comet 1 and 2, the world's first pressurised jet airliner.* .

[6] S. S. Airlines, *Sas se-210 caravelle in the air. 1960s.* .

[7] D. Green, *Aviation photo 1484982: Hawker siddeley hs-121 trident 1e - air ceylon,* (1978).

[8] A. Cros, *28.10.72 1er vol d'airbus,* (2018).

[9] K. Fielding, *Although it's the original a320-100 prototype, it had been fitted with -200 winglets.* (2014).

[10] D. Aiello, *9v-skd: Airbus a380-841: Singapore airlines: Damien aiello,* (2013).

[11] A. Cros, *Low altitude pass of the first model of the a350 at the airbus site in toulouse,* (2013).

[12] A. Malewar, (2020).

[13] EASA, *Easa jet aeroplanes noise database (issue 30 of 21/06/2018),* (2018).

[14] A. Kempton, *Acoustic liners for modern aero-engines,* in *15th CEAS-ASC Workshop and 1st Scientific Workshop of X-Noise EV* (2011).

[15] M. J. Lighthill, *On sound generated aerodynamically i. general theory,* Proceedings of the Royal Society of London. Series A. Mathematical and Physical Sciences **211**, 564 (1952).

[16] M. J. Lighthill, *On sound generated aerodynamically ii. turbulence as a source of sound,* Proceedings of the Royal Society of London. Series A. Mathematical and Physical Sciences **222**, 1 (1954).

[17] R. Grant, *Flight: the complete history of aviation* (Dorling Kindersley Ltd, 2017).

[18] N. Dickson, *Icao noise standards,* (2013).

[19] L. Gutin, *On the sound field of a rotating propeller* (National Advisory Committee for Aeronautics, 1948).

[20] T. F. Brooks, D. S. Pope, and M. A. Marcolini, *Airfoil self-noise and prediction,* NASA Reference Publication, NASA-RP-1218 (1989).

[21] U. W. Ganz, P. D. Joppa, T. J. Patten, and D. F. Scharpf, *Boeing 18-inch fan rig broadband noise test,* NASA CR-208704 (1998).

[22] O. Zaporozhets, V. Tokarev, and K. Attenborough, *Aircraft Noise: Assessment, prediction and control* (CRC Press, 2011).

[23] D. Casalino, A. Hazir, and A. Mann, *Turbofan broadband noise prediction using the lattice boltzmann method,* AIAA Journal **56**, 609 (2018).

[24] D. Wood, *6 charts that will make you optimistic about america's clean energy future,* (2016).

[25] P. Spodniak, K. Ollikka, and S. Honkapuro, *The relevance of wholesale electricity market places: the nordic case,* (2019).

[26] IRENA, *Renewable capacity statistics 2021,* (2021).

[27] E. Dupont, R. Koppelaar, and H. Jeanmart, *Global available wind energy with physical and energy return on investment constraints,* Applied Energy **209**, 322 (2018).

[28] S. Teske, J. Muth, S. Sawyer, T. Pregger, S. Simon, T. Naegler, M. O'sullivan, S. Schmid, J. Pagenkopf, B. Frieske, *et al.*, *Energy [r] evolution-a sustainable world energy outlook* (Greenpeace International, EREC and GWEC, 2012).

[29] S. Sawyer, S. Teske, L. Fried, and S. Shukla, *Global wind energy outlook| 2014,* (2014).

[30] WindEurope, *Wind energy is the cheapest source of electricity generation,* (2019).

[31] A. Betz, *Behavior of vortex systems,* NACA Technical Memorandum (1933).

[32] M. G. Molina and P. E. Mercado, *Modelling and control design of pitch-controlled variable speed wind turbines,* in *Wind turbines* (In Tech, 2011).

[33] L. Bauer and S. Matysik, *Windturbines database,* (2021).

[34] A. L. Rogers, J. F. Manwell, and S. Wright, *Wind turbine acoustic noise,* Renewable Energy Research Laboratory, Amherst: University of Massachusetts (2006).

[35] H. Møller and C. S. Pedersen, *Low-frequency noise from large wind turbines,* The Journal of the Acoustical Society of America **129**, 3727 (2011).

[36] S. Oerlemans and P. Fuglsang, *Low-noise wind turbine design,* in *EWEA Workshop on Sound, Dec* (2012) pp. 9–10.

[37] J. L. Davy, K. Burgemeister, and D. Hillman, *Wind turbine sound limits: Current status and recommendations based on mitigating noise annoyance,* Applied Acoustics **140**, 288 (2018).

[38] S. Oerlemans, M. Fisher, T. Maeder, and K. Kögler, *Reduction of wind turbine noise using optimized airfoils and trailing-edge serrations,* AIAA journal **47**, 1470 (2009).

[39] J. F. Williams and L. Hall, *Aerodynamic sound generation by turbulent flow in the vicinity of a scattering half plane,* Journal of fluid mechanics **40**, 657 (1970).

[40] T. Colonius and S. K. Lele, *Computational aeroacoustics: progress on nonlinear problems of sound generation,* Progress in Aerospace sciences **40**, 345 (2004).

[41] E. Pedersen, *Health aspects associated with wind turbine noise—results from three field studies,* Noise control engineering journal **59**, 47 (2011).

[42] F. D., *Not in my backyard! how annoying is wind turbine noise?* (2020).

[43] C. J. Doolan, D. J. Moreau, and L. A. Brooks, *Wind turbine noise mechanisms and some concepts for its control.* Acoustics Australia **40** (2012).

[44] M. Eichhorn, F. Masurowski, R. Becker, and D. Thrän, *Wind energy expansion scenarios–a spatial sustainability assessment,* Energy **180**, 367 (2019).

[45] G. Batchelor, *Pressure fluctuations in isotropic turbulence,* in *Mathematical Proceedings of the Cambridge Philosophical Society*, Vol. 47 (Cambridge University Press, 1951) pp. 359–374.

[46] N. Curle, *The influence of solid boundaries upon aerodynamic sound,* Proceedings of the Royal Society of London. Series A. Mathematical and Physical Sciences **231**, 505 (1955).

[47] W. J. Devenport, J. K. Staubs, and S. A. Glegg, *Sound radiation from real airfoils in turbulence,* Journal of Sound and Vibration **329**, 3470 (2010).

[48] M. Roger, C. Schram, and L. De Santana, *Reduction of airfoil turbulence-impingement noise by means of leading-edge serrations and/or porous material,* in *19th AIAA/CEAS aeroacoustics conference* (2013) p. 2108.

[49] J. R. Gill, X. Zhang, and P. Joseph, *Effects of real airfoil geometry on leading edge gust interaction noise,* in *19th AIAA/CEAS Aeroacoustics Conference* (2013) p. 2203.

[50] K. Chandiramani, *Diffraction of evanescent waves, with applications to aerodynamically scattered sound and radiation from unbaffled plates,* The Journal of the Acoustical Society of America **55**, 19 (1974).

[51] D. M. Chase, *Noise radiated from an edge in turbulent flow,* AIAA journal **13**, 1041 (1975).

[52] R. K. Amiet, *Noise due to turbulent flow past a trailing edge,* Journal of sound and vibration **47**, 387 (1976).

[53] T. F. Brooks and T. Hodgson, *Trailing edge noise prediction from measured surface pressures,* Journal of sound and vibration **78**, 69 (1981).

[54] M. Herr, K.-S. Rossignol, J. Delfs, N. Lippitz, and M. Mößner, *Specification of porous materials for low-noise trailing-edge applications,* in *20th AIAA/CEAS aeroacoustics conference* (2014) p. 3041.

[55] D. L. Huff *et al.*, *Noise reduction technologies for turbofan engines,* National Aeronautics and Space Administration (2007).

[56] G. W. Bielak, J. W. Premo, and A. S. Hersh, *Advanced turbofan duct liner concepts* (National Aeronautics and Space Administration, Langley Research Center, 1999).

[57] D. L. Sutliff, M. G. Jones, and D. M. Nark, *Acoustic directivity and insertion loss measurements of advanced liners installed the inlet of the dgen aeropropulsion research turbofan,* (2019).

[58] S. Palleja-Cabre, B. J. Tester, J. Astley, and G. Bampanis, *Aeroacoustic assessment of the performance of over-tip liners in reducing noise of an aerofoil over a flat surface,* in *AIAA AVIATION 2020 FORUM* (2020) p. 2608.

[59] D. Casalino, F. Diozzi, R. Sannino, and A. Paonessa, *Aircraft noise reduction technologies: a bibliographic review,* Aerospace Science and Technology **12**, 1 (2008).

[60] R. H. Liebeck, *Design of the blended wing body subsonic transport,* Journal of aircraft **41**, 10 (2004).

[61] R. Woodward, C. Hughes, R. Jeracki, and C. Miller, *Fan noise source diagnostic test–far-field acoustic results,* in *8th AIAA/CEAS Aeroacoustics Conference & Exhibit* (2002) p. 2427.

[62] G. Page, J. McGuirk, M. Hossain, N. Hughes, and M. Trumper, *A computational and experimental investigation of serrated coaxial nozzles,* in *8th AIAA/CEAS Aeroacoustics Conference & Exhibit* (2002) p. 2554.

[63] B. Callender, E. Gutmark, and S. Martens, *Far-field acoustic investigation into chevron nozzle mechanisms and trends,* AIAA journal **43**, 87 (2005).

[64] H. Gousse, *The a350 xwb's trent engine rolls out for initial flight tests,* (2017).

[65] M. Maatouk, *Credit suisse upgrades rolls-royce as trent 1000 issues on the mend,* (2019).

[66] R. Gąciarz, *Inspection and maintenance of wind turbines / trailing edge serrations repair, tower sealing, painting.* (2016).

[67] S. Oerlemans, *Wind turbine noise: primary noise sources,* (2011).

[68] O. Jianu, M. A. Rosen, and G. Naterer, *Noise pollution prevention in wind turbines: status and recent advances,* Sustainability **4**, 1104 (2012).

[69] S. Lee, S. Lee, J. Ryi, and J.-S. Choi, *Design optimization of wind turbine blades for reduction of airfoil self-noise,* Journal of Mechanical Science and Technology **27**, 413 (2013).

[70] H. Kaviani and A. Nejat, *Aeroacoustic and aerodynamic optimization of a mw class hawt using mopso algorithm,* Energy **140**, 1198 (2017).

[71] S. Oerlemans, *Reduction of wind turbine noise using blade trailing edge devices,* in *22nd AIAA/CEAS aeroacoustics conference* (2016) p. 3018.

[72] L. Jones and R. Sandberg, *Acoustic and hydrodynamic analysis of the flow around an aerofoil with trailing-edge serrations,* Journal of Fluid Mechanics **706**, 295 (2012).

[73] S. Lee, *Reduction of blade-vortex interaction noise through porous leading edge,* AIAA journal **32**, 480 (1994).

[74] E. Sarradj and T. Geyer, *Noise generation by porous airfoils,* in *13th AIAA/CEAS Aeroacoustics Conference (28th AIAA Aeroacoustics Conference)* (2007) p. 3719.

[75] T. Geyer, E. Sarradj, and C. Fritzsche, *Porous airfoils: noise reduction and boundary layer effects,* International journal of aeroacoustics **9**, 787 (2010).

[76] J. Delfs, B. Faßmann, N. Lippitz, M. Lummer, M. Mößner, L. Müller, K. Rurkowska, and S. Uphoff, *Sfb 880: Aeroacoustic research for low noise take-off and landing,* CEAS Aeronautical Journal **5**, 403 (2014).

[77] T. F. Geyer and E. Sarradj, *Trailing edge noise of partially porous airfoils,* in *20th AIAA/CEAS Aeroacoustics Conference* (2014) p. 3039.

[78] T. F. Geyer, A. Lucius, M. Schrödter, M. Schneider, and E. Sarradj, *Reduction of turbulence interaction noise through airfoils with perforated leading edges,* Acta Acustica united with Acustica **105**, 109 (2019).

[79] B.-L. Su, C. Sanchez, and X.-Y. Yang, *Hierarchically structured porous materials: from nanoscience to catalysis, separation, optics, energy, and life science* (John Wiley & Sons, 2012).

[80] D. B. Ingham and I. Pop, *Transport phenomena in porous media* (Elsevier, 1998).

[81] H. Liu, M. Azarpeyvand, J. Wei, and Z. Qu, *Tandem cylinder aerodynamic sound control using porous coating,* Journal of Sound and Vibration **334**, 190 (2015).

[82] A. Rubio Carpio, R. Merino Martinez, F. Avallone, D. Ragni, M. Snellen, and S. van der Zwaag, *Broadband trailing-edge noise reduction using permeable metal foams,* in *INTER-NOISE and NOISE-CON Congress and Conference Proceedings*, Vol. 255 (Institute of Noise Control Engineering, 2017) pp. 2755–2765.

[83] R. Graham, *The silent flight of owls,* The Aeronautical Journal **38**, 837 (1934).

[84] G. Lilley, *A study of the silent flight of the owl,* in *4th AIAA/CEAS aeroacoustics conference* (1998) p. 2340.

[85] R. E. Hayden, *Fundamental aspects of noise reduction from powered-lift devices,* SAE Transactions , 1287 (1973).

[86] J. Revell, J. Revell, H. Kuntz, F. Balena, C. Horne, B. Storms, R. Dougherty, H. Kuntz, F. Balena, C. Horne, *et al.*, *Trailing-edge flap noise reduction by porous acoustic treatment,* in *3rd AIAA/CEAS aeroacoustics conference* (1997) p. 1646.

[87] A. Tinetti, J. Kelly, R. Thomas, and S. Bauer, *Reduction of wake-stator interaction noise using passive porosity,* in *40th AIAA aerospace sciences meeting & exhibit* (2002) p. 1036.

[88] A. Rubio Carpio, F. Avallone, D. Ragni, M. Snellen, and S. van der Zwaag, *Mechanisms of broadband noise generation on metal foam edges,* Physics of Fluids **31**, 105110 (2019).

[89] A. R. Carpio, F. Avallone, D. Ragni, M. Snellen, and S. van der Zwaag, *Quantitative criteria to design optimal permeable trailing edges for noise abatement,* Journal of Sound and Vibration **485**, 115596 (2020).

[90] S. A. S. Ali, M. Azarpeyvand, and C. R. I. da Silva, *Trailing-edge flow and noise control using porous treatments,* Journal of Fluid Mechanics **850**, 83 (2018).

[91] S. P. Neuman, *Theoretical derivation of darcy's law,* Acta Mechanica **25**, 153 (1977).

[92] E. Baril, A. Mostafid, L.-P. Lefebvre, and M. Medraj, *Experimental demonstration of entrance/exit effects on the permeability measurements of porous materials,* Advanced Engineering Materials **10**, 889 (2008).

2

SIMULATION METHODOLOGY

The method of science is tried and true.
It is not perfect, it's just the best we have.

Carl Sagan

Research means that you don't know, but are willing to find out.

Charles F. Kettering

This chapter addresses the numerical methods employed in this dissertation. An overview of the theoretical framework behind the lattice-Boltzmann method will be provided, followed by the implementation of a porous medium model based on the Darcy's law. A procedure to empirically characterise a porous material using a one-dimensional-flow test rig is also discussed.

Parts of this chapter have been published in Teruna *et al.* [1]

2.1. COMPUTATIONAL FLUID DYNAMICS

PRIOR to the late 20th century, fluid dynamics have been mostly investigated using experimental and analytical approaches. However, thanks to the dramatic increase in computer processing power over the past few decades, computational fluid dynamics (CFD) have become a prominent third approach to study various flow phenomena [2]. There have been different CFD methods in development since the early 1970s. They can be categorised based on their frame of references in describing fluid quantities, such as Lagrangian and Eulerian methods. Under the Lagrangian perspective, the motion of individual fluid parcel (e.g., gas particle) is continuously tracked in space and time. This approach serves as the basis of smooth particle hydrodynamics (SPH) method, for instance. On the other hand, the Eulerian approach focuses on observing the changes in a certain region that is fixed in space. One of the most popular CFD method in this category is the finite-volume method (FVM) implementation of the Navier-Stokes (N-S) equations, where the fluid is assumed as a continuum. This implies that the (macroscopic) flow properties, such as momentum, pressure, and temperature, are continuous in space. Nevertheless, these macroscopic properties are the manifestation of the physical interactions of fluid particles at the molecular (microscopic) level. Hence, the mesoscopic theory, which is employed by the lattice-Boltzmann methods (LBM), presents an opportunity to reconcile such multi-scale problems. The usage of LBM for CFD is relatively recent compared to traditional N-S based methods, but the former has been demonstrated to be highly suited for aeroacoustic investigations [3–6] for multiple reasons that will be outlined later in this chapter. A commercial LBM solver, PowerFLOW from Dassault Systemes, has been employed throughout this dissertation. The theoretical foundations of the solver will be discussed in the following, although interested readers should consult Succi [7] for more details.

2.1.1. BOLTZMANN'S KINETIC THEORY

The LBM is derived from the Boltzmann's kinetic theory, which describes a fluid as a collection of particles that continuously evolve towards a thermodynamically equilibrium state. Macroscopic properties of the fluid, such as momentum, pressure, and temperature, are the resultant of microscopic particle motions and momentum exchanges. Nevertheless, instead of continuously tracking the state of each particle, Boltzmann's kinetic theory adopts a statistical treatment of the problem, which can be justified in many aerodynamic problems where the fluid can be considered as a continuum[1]. The instantaneous state of the fluid is defined using a probability density function $F(\boldsymbol{x}, t, \boldsymbol{V})$, which refers to the likelihood of finding a particle at a spatial coordinate $\boldsymbol{x}$ and time instance t, while having a velocity $\boldsymbol{V}$. The Boltzmann transport equation (BTE), after neglecting the body forces (e.g., gravity), is mathematically expressed as in equation 2.1.

$$\frac{\partial F}{\partial t} + \boldsymbol{V} \cdot \nabla F = \kappa \tag{2.1}$$

[1] At standard atmospheric condition, 1 mm^3 of air contains approximately 26.9 quadrillion (i.e., 10^{15}) molecules.

The left hand side of the equation describes the advection of fluid particles. The right hand side contains the collision operator κ, which causes the particle velocity distribution to change due to momentum exchanges between particles. It will be shown that the collision operator governs the evolution of the fluid particles towards a thermodynamic equilibrium. Therefore, various flow mechanisms, such as turbulence and the resistance encountered by flows inside a porous medium, can be introduced into the solution via the modification of the collision operator.

In Boltzmann's classical formulation, the collision operator assumes the fluid as "a dilute gas of point-like, structure-less molecules interacting via a short-range two-body potential" [7]. This implies that particles interact with each other only through elastic collisions, where energy is conserved both before and after the collision. LBM solvers often employ a simplified collision operator that approximates the integral formulation of κ given by the aforementioned definition. One of the most popular is the Bhatnagar-Gross-Krook (BGK) model [8], although several improvements have also been proposed [9]. More details on the collision operator will be given in a later subsection.

2.1.2. THE LATTICE-BOLTZMANN METHOD

Using the LBM approach, the BTE is discretized onto a cartesian grid (i.e., lattice) where fluid particles are confined within the nodes, and the velocity vector of the fluid particles are limited to a predetermined number of directions. The mathematical expression for the discrete lattice-Boltzmann equation is given as:

$$F_{\mathrm{q}}(\boldsymbol{x}+\boldsymbol{V}_{\mathrm{q}}\Delta t, t+\Delta t) - F_{\mathrm{q}}(\boldsymbol{x}, t) = \kappa_{\mathrm{q}}(\boldsymbol{x}, t) \tag{2.2}$$

where F_{q} is the particle distribution function in q^{th} direction of the lattice, and $\boldsymbol{V}_{\mathrm{q}}$ is the discrete particle velocity vector, and $q = 0, 1, \ldots, \mathrm{Q}$ is the number of the discrete velocity vectors. The left hand side of the discrete lattice-Boltzmann equation (2.2) is an expression for a time-explicit advection with the increment of $\Delta\boldsymbol{x} = \boldsymbol{V}_{\mathrm{q}}\Delta t$ (spatial) and Δt (temporal). On the right hand side is a collision operator κ_{q}.

Macroscopic flow quantities, such as density ρ, velocity $\boldsymbol{u}$, and total energy E, can be recovered by computing the following moments of the distribution function F_{q}.

$$\rho(\boldsymbol{x}, t) = \sum_{\mathrm{q}} F_{\mathrm{q}}(\boldsymbol{x}, t) \tag{2.3}$$

$$\rho\boldsymbol{u}(\boldsymbol{x}, t) = \sum_{\mathrm{q}} \boldsymbol{V}_{\mathrm{q}} F_{\mathrm{q}}(\boldsymbol{x}, t) \tag{2.4}$$

$$\rho E(\boldsymbol{x}, t) = \sum_{\mathrm{q}} \frac{1}{2}\boldsymbol{V}_{\mathrm{q}}^2 F_{\mathrm{q}}(\boldsymbol{x}, t) \tag{2.5}$$

As such, the macroscopic flow quantities can be considered as a weighted-average of the microscopic ones. The total energy E consists of the internal energy E_o and the kinetic energy as in equation 2.6.

$$E(\boldsymbol{x}, t) = E_o(\boldsymbol{x}, t) + \frac{1}{2}|\boldsymbol{u}(\boldsymbol{x}, t)|^2 \tag{2.6}$$

The internal energy of a gas represents the total of the kinetic energy of the gas particles corresponding to their entropy and temperature states. The internal energy should be distinguished from the macroscopic kinetic energy, which is linked to the flow velocity $\boldsymbol{u}$.

$$\rho E_o(\boldsymbol{x},t) = \sum_{\mathrm{q}} \frac{\left|\boldsymbol{V}_{\mathrm{q}} - \boldsymbol{u}\right|^2}{2} F_{\mathrm{q}}(\boldsymbol{x},t) \tag{2.7}$$

Consequently, the gas temperature can be computed using the internal energy,

$$T(\boldsymbol{x},t) = \frac{E_o(\boldsymbol{x},t)}{c_v} \tag{2.8}$$

with the specific heat capacity at constant volume $c_v = \mathrm{RD}/2$ for monoatomic gas, where R is the specific gas constant, and D is the number of spatial dimensions. Using the ideal gas law, the static pressure can be calculated.

$$p(\boldsymbol{x},t) = \rho(\boldsymbol{x},t)\mathrm{R}T(\boldsymbol{x},t) \tag{2.9}$$

It is also possible to show that the macroscopic conservation laws, including the Navier-Stokes equations, can be recovered from the BTE by computing the zeroth, first, and the trace of the second order moments of equation (2.2). However, the procedure leads to a closure problem [10], for which a solution has been proposed by Hilbert [11], Chapman and Cowling [12]. The solution is known as the Chapman-Enskog (C-E) expansion, in which the distribution function is expanded in term of Knudsen number Kn (i.e., a ratio between the mean free path of the particle and the characteristic length scale in the flow).

$$F = F^{(0)} + \mathrm{Kn}F^{(1)} + \mathrm{Kn}^2F^{(2)} + \cdots = \sum_{m=1}^{\infty} \mathrm{Kn}^m F^{(m)} \tag{2.10}$$

The index m in equation 2.10 is the expansion order. It has been shown [13] that the N-S equations can be retrieved from the Boltzmann equation using the first-order truncation of the C-E expansion. This procedure is usually valid for small Knudsen number ($\mathrm{Kn} < 10^{-2}$) where the fluid can be assumed as a continuum, as in the N-S equations.

2.1.3. THE LBM PROCEDURE AND DOMAIN DISCRETISATION

A LBM simulation generally involves these four steps: initialisation, advection, collision, and the adjustments due to the boundary conditions. An illustration of this process is provided in figure 2.1.

1. Initialisation
   The simulation domain is discretised and an initial state is imposed. For instance, a rest state (i.e., zero velocity) in the entire lattice can be applied. It is also quite common to use the solution from a previous simulation to prescribe the initial state. Such practice that is often referred to as "seeding".

2. Advection / streaming
   During this step, the particle distribution function in each lattice element is shifted towards its neighbours according to the discrete velocity directions, as implied in equation 2.11. While this process resembles the advection in typical N-S FVM solvers, the one in LBM does not involve any numerical (e.g., interpolation) scheme, and therefore it does not introduce any numerical dissipation[2]. Right after the advection phase, macroscopic flow quantities are computed at each node.

$$F_{\mathrm{q}}(\boldsymbol{x}+\boldsymbol{V}_{\mathrm{q}}\Delta t, t+\Delta t) = F_{\mathrm{q}}(\boldsymbol{x}, t) \tag{2.11}$$

3. Collision
   During the collision phase, macroscopic flow quantities are utilised for computing the local equilibrium distribution function, and in turn, the collision term in equation 2.2. Afterward, the local distribution functions are updated (denoted F^{*}_{q}) after incorporating the outcome of the collision process as in equation 2.12. The collision step takes place locally on each node, and thus, each nodal computation is independent from the others, which enables a very efficient parallelisation of the LBM computation processes.

$$F^{*}_{\mathrm{q}}(\boldsymbol{x}+\boldsymbol{V}_{\mathrm{q}}\Delta t, t+\Delta t) = F_{\mathrm{q}}(\boldsymbol{x}+\boldsymbol{V}_{\mathrm{q}}\Delta t, t+\Delta t) + \kappa_{\mathrm{q}} \tag{2.12}$$

4. Boundary condition
   Lattices adjacent to the boundary of the simulation domain would require a different treatment since some of the advected distribution functions may leave the domain while new ones may enter. The same concept also applies at the surface of a wall. The adjustment of the distribution function would be determined by the type of boundary condition (e.g., fluid inlet, no-slip wall, etc.), which will be detailed in a later part of this section.

The LBM scheme is carried out on a lattice made of cubic elements that are referred to as *voxels* (i.e., volume element) [14]. The simulation domain can be sub-divided into several regions with different voxel resolution levels (i.e., grid size), such that the resolution levels between adjacent regions vary by a factor of 2 [15]. The finest voxel dimension (highest resolution) is specified as a number of voxels along a pre-defined characteristic length (e.g., airfoil chord), with which a timestep is chosen such that the Courant number is equal to 1. The distribution function in each voxel is computed and updated at different time steps according to the voxel resolution level. This process takes place at every time step for the voxels with the highest resolution. Assuming that the highest voxel resolution level is M, the distribution function in coarser voxels with a resolution level of $M-N$ are updated every 2^{N} time steps. To ensure the conservation of

[2] Numerical dissipation in the scheme may still be introduced from the particle velocity discretisation and the collision operator

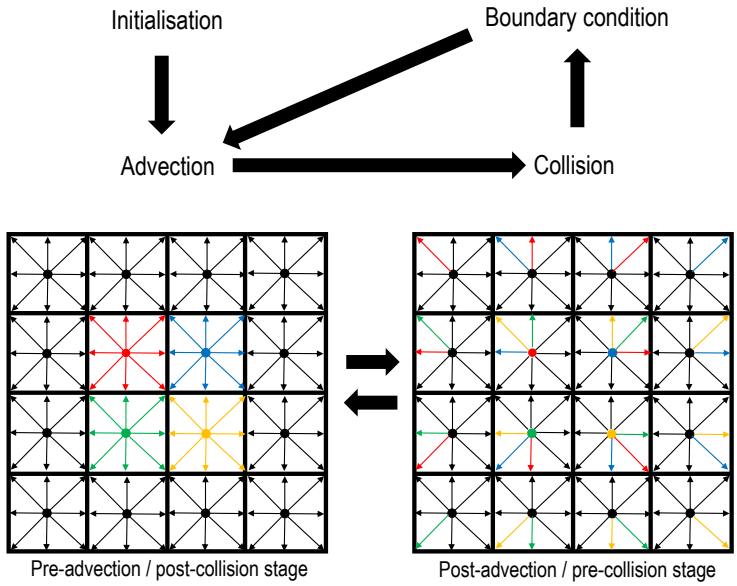

Figure 2.1: A schematic of LBM algorithm. Fluid particles in the lattice are represented as dots and the discrete particle velocity vectors as arrows. Coloured arrows have been used to indicate the advection of the velocity vectors from the 4 voxels at the center of the lattice.

mass, momentum, and energy, across regions with different resolution levels, a voxel-centered lattice scheme has been employed [15].

Solid walls are discretised using planar surfaces that are tangential to the surface curvature, and thus, a curved smooth surface is represented by a polygonal shape as shown in figure 2.2. These planar surfaces are referred to as the *surfels* (i.e., surface elements).

2.1.4. VELOCITY-SPACE DISCRETISATION AND THE COLLISION OPERATOR

It has been mentioned earlier in this section that one of the most commonly-used collision operator is the Bhatnagar-Gross-Krook (BGK) model [8], which is expressed as follows.

$$\kappa = -\frac{1}{\tau}\left[F_{\mathrm{q}}(\boldsymbol{x},t) - F_{\mathrm{q}}^{\mathrm{eq}}(\boldsymbol{x},t)\right] \tag{2.13}$$

The BGK model simplifies the discrete LB equation as it replaces the classical description of the collision operator by using a single relaxation time τ instead of a complicated integral function in the latter [7]. In essence, the BGK formulation states that the local distribution function F eventually returns to the equilbrium one F^{eq} within a time scale characterised by τ. While τ is generally a functional of F, the BGK model conveniently assumes that all scales of the relaxation processes happen at the same rate. In practice, this assumption is suitable for Newtonian flows (i.e., where shear stress is linearly proportional to shear rate through viscosity) where the deviation of the fluid

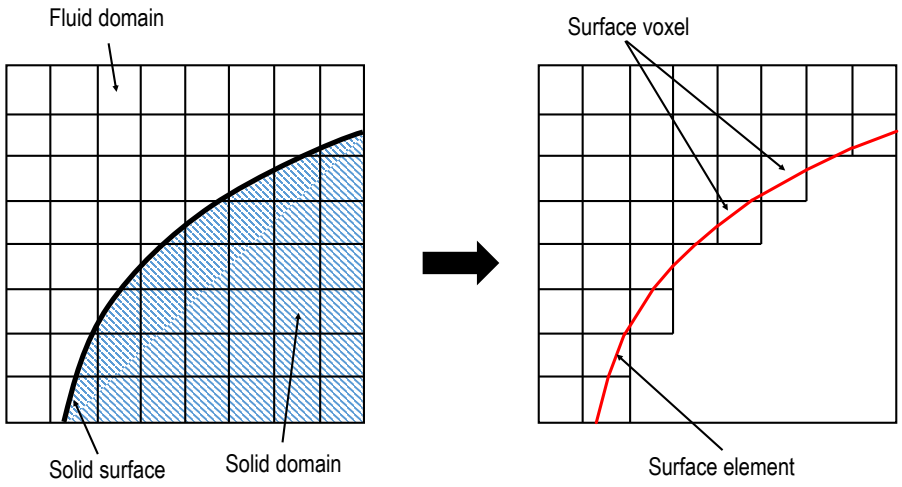

Figure 2.2: An illustration of the discretisation of the simulation domain. Note that although the surface voxels are drawn with a cubic shape, this is no longer accurate as the part of their volume inside the solid domain will be removed.

state from its equilibrium is small. It is worth mentioning that the equilibrium distribution function, $F_{\mathrm{q}}^{\mathrm{eq}}$, can take the form of the regular Maxwell-Boltzmann distribution as follows:

$$F_{\mathrm{q}}^{\mathrm{eq}} = \frac{\rho}{(2\pi \mathrm{R} T)^{\mathrm{D}/2}} e^{\left(-\frac{|\boldsymbol{v}_{\mathrm{q}}-\boldsymbol{u}|^2}{2\mathrm{R}T}\right)} \tag{2.14}$$

The Boltzmann equation is discretised not only in the spatial and temporal spaces, but also in the velocity space (V_{q}). To implement the latter, Gauss-Hermite quadrature has been shown to be an efficient method, which originated from the idea of expanding the distribution function in Hermite polynomial as proposed by Grad [16]. More recently, the completed formulation for the velocity discretisation procedure was presented by Shan *et al.* [17]. Grad argued that the Boltzmann-BGK equation can be projected onto Hermite orthogonal bases, such that equation 2.1 can be rewritten into equation 2.15,

$$\frac{\partial F_{\mathrm{q}}}{\partial t} + \boldsymbol{V}_{\mathrm{q}} \cdot \nabla F_{\mathrm{q}} = \frac{F_{\mathrm{q}}^{\mathrm{eq}} - F_{\mathrm{q}}}{\tau} \tag{2.15}$$

such that F_{q} is expressed in term of Hermite expansion for a set of discrete velocities $\boldsymbol{V}_{\mathrm{q}}$ ($\mathrm{q} = 0, 1, \ldots, \mathrm{Q}$). The selected number of discrete velocities Q depends on the truncation order of the Hermite expansion. Letting n denotes the order of truncation for F_{q}, then,

$$F_q = w_q \sum_{n=0}^{\infty} \frac{1}{n!} a^{(n)} \mathcal{H}^{(n)}(\boldsymbol{V}_q) \quad \text{, where}$$
$$a^{(n)} = \sum_{q=1}^{Q} F_q \mathcal{H}^{(n)}(\boldsymbol{V}_q) \tag{2.16}$$

is the Hermite expansion coefficient, w_q is a weight function, and $\mathcal{H}^{(n)}(V_q)$ is the n^{th} order Hermite polynomial. Unsurprisingly, the truncation order determines the accuracy of equation 2.16 in approximating the expression in equation 2.15. It has been reported that a fourth-order truncation (n = 4) is needed to recover the full N-S equations, satisfying both momentum and energy conservation laws. With n = 3, the conservation of energy is no longer satisfied, but the N-S equations can still be recovered for an isothermal condition without any error term. Once a second-order truncation is applied, additional error terms appear in the description of the viscous stress tensor with a M_∞^3 dependence, that is associated with the weakly compressible limit of the LBM approach [18].

Although the present study mainly involves low Mach number flows, a third-order expansion has been employed to approximate F_q as follows [13, 19].

$$F_q \approx \rho w_q \left[1 + \frac{\boldsymbol{V}_q \cdot \boldsymbol{u}}{\Theta} + \frac{(\boldsymbol{V}_q \cdot \boldsymbol{u})^2}{2\Theta^2} - \frac{\boldsymbol{u}^2}{2\Theta} + \frac{(\boldsymbol{V}_q \cdot \boldsymbol{u})^3}{6\Theta^3} - \frac{(\boldsymbol{V}_q \cdot \boldsymbol{u})\boldsymbol{u}^2}{2\Theta^2} \right] \tag{2.17}$$

The weighting functions w_q depend on the magnitude of $\boldsymbol{V}_q$ and the number of discrete velocity vectors, which have been chosen to fulfill mass and momentum conservation as well as the isotropy of the resulting moments. For the present study, the LBM solver utilises the aforementioned formulation in its low-Mach-number solver for a 3-dimensional lattice with 19 discrete velocity vectors, which is also referred to as the D3Q19 model (see figure 2.3). For this model, the non-dimensional lattice temperature is $\Theta = 1/3$, while $w_q = 1/3$ for the rest velocity (q = 0), 1/18 for the main axes, and 1/36 for the diagonals. In general, the weighting functions should fulfill the following conditions,

$$\sum_q w_q \underbrace{\boldsymbol{V}_q \dots \boldsymbol{V}_q}_{q} \begin{cases} \Theta^{q/2} \Delta^q, & q = 2, 4, \dots, 2q \\ 0, & q = 1, 3, \dots, 2q-1 \end{cases} \tag{2.18}$$

where Δ^q is the q^{th} order Kronecker delta function tensor.

It is worth mentioning that the relaxation time τ in the BGK model acts equivalently as a kinematic viscosity ν. For instance, for high Reynolds number flows, where viscous forces play a less relevant role, ν is expected to be small. Correspondingly, a small τ implies that the fluid particles return to their local equilibrium condition at a faster rate. For a lattice with a grid spacing of Δx and time-step Δt, it can be shown using a Chapman-Enskog expansion [18] that both ν and τ are related through equation 2.19.

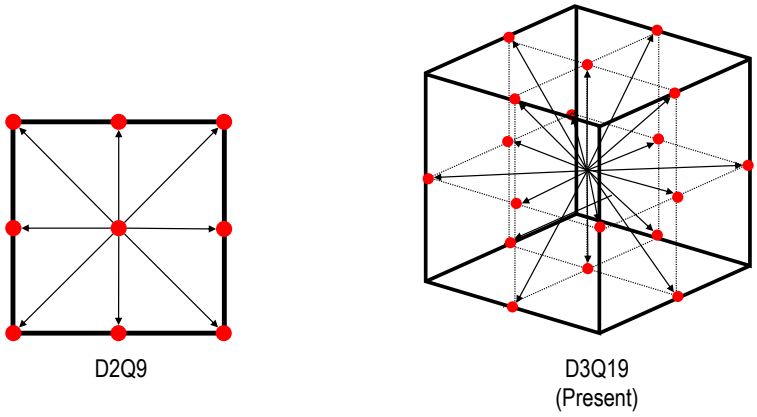

Figure 2.3: The illustration of two different LBM stencil examples: 2-dimension, 9-velocity vectors (D2Q9) and 3-dimension, 19-velocity vectors (D3Q19).

$$\nu = \frac{1}{3}\left(\frac{\Delta x}{\Delta t}\right)^2\left(\tau - \frac{\Delta t}{2}\right) \tag{2.19}$$

The BGK model, while often preferred for its simplicity, is not without limitations [20]. The usage of a single relaxation time implies that the BGK model cannot distinguish the relaxation rates between momentum exchanges through viscosity and energy exchanges through thermal conduction. Moreover, the BGK model assumes a unitary Prandtl number [9], which does not always match the empirical value for different types of fluid. Improvements were proposed to the BGK model to circumvent this issue [21], such as the multiple-relaxation-time (MRT) technique. The MRT model was proposed by d'Humières [22], in which the collision operator is expressed in term of the velocity moments of the particle distribution function instead of the function itself as in BGK model. As a consequence, the MRT model is more complex to implement than the BGK one. Furthermore, by imposing different relaxation rate in the same frame of reference can result in the violation of Galilean invariance[3]. On the other hand, the BGK model is always Galilean invariant. As an alternative, Chen *et al.* [9] proposed a two-relaxation-time (TRT) approach, where relaxation times are assigned separately for dynamic viscosity and thermal conductivity. It has also been demonstrated that Galilean invariance can be recovered by defining the collision operator in a relative reference frame, such that the discrete velocity vectors are expressed in relation to the flow (macroscopic) velocity.

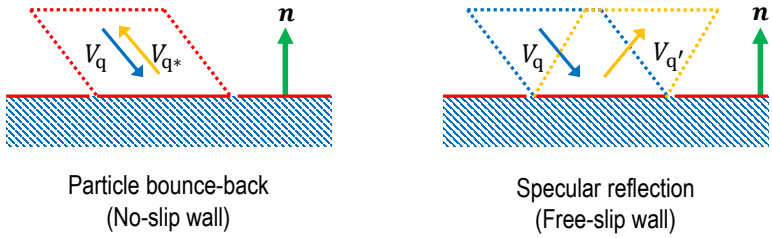

Figure 2.4: An illustration of the wall boundary conditions in LBM: the bounce-back process for no-slip wall, and specular-reflection for slip wall.

2.1.5. BOUNDARY CONDITIONS

Boundary conditions are necessary to define the distribution functions at the domain boundaries after the advection step. Several types of boundary conditions that are employed in the present study are listed in the following:

- Periodic boundary
  Periodic boundaries allow for approximating an infinite domain that contains geometry and flow features that are expected to repeat indefinitely. They are among the simplest boundary conditions to implement, such that the distribution functions from one side of the domain are advected directly to the opposite side.

- Inlet and outlet
  Inlet and outlet boundary conditions are modelled by applying the assumption that $F_q = F_q^{eq}$ at the boundary. This treatment allows for certain values of macroscopic quantities, such as density, pressure, and velocity, to be specified at the domain inlet and outlet.

- Wall boundary
  Wall boundary conditions are illustrated in figure 2.4 [14]. A *bounce-back* method is employed to realise a no-slip wall, such that particles impinging a wall are immediately reflected in the same direction they were coming from, while retaining the same velocities, i.e., $\boldsymbol{V}_{q*} = -\boldsymbol{V}_q$, where $\boldsymbol{V}_{q*}$ is the particle velocity after the bounce-back process. On the other hand, a free-slip wall is modelled using a *specular reflection* process, such that the wall deflects incoming particles while preserving their tangential velocity components. This process is expressed as $\boldsymbol{V}_{q'} \cdot \boldsymbol{n} = -\boldsymbol{V}_q \cdot \boldsymbol{n}$ for the wall-normal velocity component, and $\boldsymbol{V}_{q'} - (\boldsymbol{V}_{q'} \cdot \boldsymbol{n})\boldsymbol{n} = \boldsymbol{V}_q - (\boldsymbol{V}_q \cdot \boldsymbol{n})\boldsymbol{n}$ for the wall-parallel velocity component, in which $\boldsymbol{n}$ is a local unitary wall-normal vector.

[3] Galilean invariance implies that the laws of motion are identical in all inertial frames of reference. Thus, all inertial frames share the same universal time.

2.1.6. VLES TURBULENCE MODEL

PowerFLOW employs a Very Large Eddy Simulation (VLES) model, which can be classified as a hybrid turbulence-modelling approach (e.g., hybrid RANS/LES and Detached Eddy Simulation - DES), but it is fundamentally different from its Navier-Stokes-based counterparts. One of the most common approaches to turbulence modelling in CFD is the eddy viscosity model that has been derived from the Boussinesq hypothesis [23]. The hypothesis states that the turbulent shear stress is linearly proportional to the mean rate of strain via the eddy viscosity, which receives its name based on observations that turbulent eddies seemingly enhance the apparent viscosity of the flow-field. A few years after Boussinesq presented his hypothesis, Lord Kelvin [24] suggested that the eddy transport phenomena are analogous to Maxwell's kinetic theory of gas. This analogy was further expanded by Chen *et al.* [25] who drew a parallel between turbulent and thermal fluctuations. Thus, turbulent dynamics can be described using a Boltzmann equation with a distribution function F_{turb} as in equation 2.21.

$$\frac{\partial F_{\text{turb}}}{\partial t} + \boldsymbol{V} \cdot \frac{\partial F_{\text{turb}}}{\partial \boldsymbol{x}} = \boldsymbol{\kappa}_{\text{turb}} \tag{2.20}$$

$$\boldsymbol{\kappa}_{\text{turb}} = -\frac{1}{\tau_{\text{turb}}} \left(F_{\text{turb}} - F_{\text{turb}}^{\text{eq}} \right) \tag{2.21}$$

Note that $\boldsymbol{V}$ is no longer a particle velocity, but rather the velocity of a "turbulence" fluid parcel. Moreover, the collision term still follows the same expression as the BGK model [8] but with a turbulence relaxation time τ_{turb}. Chen *et al.* [25] argued that the equilibrium distribution $F_{\text{turb}}^{\text{eq}}$ can take the form of the usual Maxwell-Boltzmann distribution centered around a mean velocity $\boldsymbol{U}$ and a half-width of $\frac{2}{3}k$ (k is the turbulent kinetic energy). Subsequently, the density, mean velocity, and turbulent kinetic energy are defined using the following moments.

$$\rho = \int F_{\text{turb}} \, \mathrm{d}\boldsymbol{V} \tag{2.22}$$

$$\boldsymbol{U} = \langle \boldsymbol{V} \rangle = \int \frac{1}{\rho} F_{\text{turb}} \boldsymbol{V} \, \mathrm{d}\boldsymbol{V} \tag{2.23}$$

$$k = \frac{1}{2} \left\langle (\boldsymbol{u}')^2 \right\rangle = \frac{1}{2} \left\langle (\boldsymbol{V} - \boldsymbol{U})^2 \right\rangle \tag{2.24}$$

In equation 2.24, the operator $\langle A \rangle$ is $\int \frac{1}{\rho} F_{\text{turb}} A \, \mathrm{d}\boldsymbol{V}$. Subsequently, the Reynolds stress σ is expressed as,

$$\sigma_{ij} = -\left\langle u_i' u_j' \right\rangle = -\left\langle (\boldsymbol{V} - \boldsymbol{U})_i (\boldsymbol{V} - \boldsymbol{U})_j \right\rangle \tag{2.25}$$

Previously, it has been shown that the distribution function F_{turb} can be expanded in term of the Knudsen number Kn. Here, Knudsen number is interpreted as a ratio between the characteristic time scale of a turbulent eddy and that of the mean flow-field ($\text{Kn} \sim \tau_{\text{turb}} / t_{\text{mean}}$). When the Knudsen number is small, C-E expansion can be applied [12, 25], similar to equation 2.10:

$$F_{\text{turb}} = F^{(0)}_{\text{turb}} + \text{Kn}\, F^{(1)}_{\text{turb}} + \text{Kn}^2\, F^{(2)}_{\text{turb}} + \dots \tag{2.26}$$

where $F^{(0)}_{\text{turb}} \equiv F^{\text{eq}}_{\text{turb}}$. With this result, the following expressions for the Reynolds stress tensor can be obtained:

$$\sigma^{(\text{n})}_{ij} = -\int \frac{1}{\rho} F^{(\text{n})}_{\text{turb}} (\boldsymbol{V} - \boldsymbol{U})_i (\boldsymbol{V} - \boldsymbol{U})_j \, \text{d}\boldsymbol{V} \tag{2.27}$$

and the Reynolds stress tensor at various orders of n is given as:

$$\begin{aligned}
\sigma^{(0)}_{ij} &= -\frac{2}{3} k \delta_{ij} \\
\sigma^{(1)}_{ij} &= -2\nu_{\text{turb}} S_{ij} \;\;,\;\; \nu_{\text{turb}} = \frac{2}{3} k \tau_{\text{turb}} \\
\sigma^{(2)}_{ij} &= -2\nu_{\text{turb}} \frac{\text{D}}{\text{D}t} \left[\tau_{\text{turb}} S_{ij}\right] - 6\frac{\nu^2_{\text{turb}}}{k} \left[S_{ik}S_{kj} - \frac{1}{3}\delta_{ij} S_{kl} S_{kl}\right] \\
&\quad + 3\frac{\nu^2_{\text{turb}}}{k} \left[S_{ik}\Omega_{kj} + S_{jk}\Omega_{ki}\right]
\end{aligned} \tag{2.28}$$

where $\frac{\text{D}}{\text{D}t}$ is a material derivative operator, $S_{ij} = \frac{1}{2}\left(\frac{\partial U_i}{\partial x_j} + \frac{\partial U_j}{\partial x_i}\right)$, and $\Omega_{ij} = \frac{1}{2}\left(\frac{\partial U_i}{\partial x_j} - \frac{\partial U_j}{\partial x_i}\right)$. The last expression in equation 2.28 reveals two important properties. The first one is the material derivative of the strain rate tensor in the first term, which indicates that the local instantaneous Reynolds stress is linked to the changes in the strain rate with respect to an earlier time and location, depending on τ_{turb} (i.e., a memory effect). The second one is the higher-order terms, which are associated with the non-linearity in the Reynolds stresses. Mathematically, the terms also resemble the expression for the turbulence closure in non-linear turbulence models [26]. This is shown by reorganising equation 2.28 into:

$$\begin{aligned}
\sigma_{ij} =& \nu_{\text{turb}} \left[\frac{\partial u'_i}{\partial x_j} + \frac{\partial u'_j}{\partial x_i}\right] - \nu_{\text{turb}} \frac{\text{D}}{\text{D}t} \left[\nu_{\text{turb}} \left(\frac{\partial u'_i}{\partial x_j} + \frac{\partial u'_j}{\partial x_i}\right)\right] \\
&- \frac{k^3}{\epsilon^2} \left[C_1 \frac{\partial u'_i}{\partial x_k}\frac{\partial u'_j}{\partial x_k} + C_2 \left(\frac{\partial u'_i}{\partial x_k}\frac{\partial u'_k}{\partial x_j} + \frac{\partial u'_j}{\partial x_k}\frac{\partial u'_k}{\partial x_i}\right) + C_3 \frac{\partial u'_k}{\partial x_i}\frac{\partial u'_k}{\partial x_j}\right]
\end{aligned} \tag{2.29}$$

In order for the equation to match the $k-\epsilon$ model (ϵ is a rate of dissipation), $\tau_{\text{turb}} = \frac{3}{2} C_\mu \frac{k}{\epsilon}$ has been chosen with $C_\mu \approx 0.09$. With this, the coefficients in equation 2.29 are determined to be $C_1 = 0.024$, $C_2 = 0.012$, and $C_3 = 0$, which are reasonably close to those found by Rubinstein and Barton [26] ($C_1 = 0.034$, $C_2 = 0.104$, $C_2 = -0.014$). It is also shown here that the implementation of an eddy viscosity model will depend on choosing the appropriate τ_{turb}. Ideally, τ_{turb} should represent the combined contributions of turbulent eddies at all frequencies (i.e., the harmonic mean of all characteristic turbulent time scales[4]).

[4] such as k/ϵ, which is the dissipation time scale for a large eddy in an isotropic turbulence.

As mentioned previously, the formulation of $k-\epsilon$ renormalisation group (RNG) [27] has been employed in the present LBM-VLES implementation, which takes into account the diffusion contributed by all scales of turbulence, unlike in the classical $k-\epsilon$ model. The RNG model is given in the following:

$$\rho\frac{\mathrm{D}k}{\mathrm{D}t}=\frac{\partial}{\partial x_j}\left[\left(\frac{\rho\nu_o}{\varsigma_{k_o}}+\frac{\rho\nu_T}{\varsigma_{k_T}}\right)\frac{\partial k}{\partial x_j}\right]+\sigma_{ij}S_{ij}-\rho\epsilon \tag{2.30}$$

$$\rho\frac{\mathrm{D}\epsilon}{\mathrm{D}t}=\frac{\partial}{\partial x_j}\left[\left(\frac{\rho\nu_o}{\varsigma_{\epsilon_o}}+\frac{\rho\nu_T}{\varsigma_{\epsilon_T}}\right)\frac{\partial \epsilon}{\partial x_j}\right]+C_{\epsilon 1}\frac{\epsilon}{k}\sigma_{ij}S_{ij}-\left[C_{\epsilon 2}+C_\mu\frac{\eta^3(1-\eta/\eta_o)}{1+\beta\eta^3}\right]\rho\frac{\epsilon^2}{k} \tag{2.31}$$

where σ_{ij} and S_{ij} are the Reynolds stress and strain rate tensors respectively, and C_μ, C_ϵ, ς, η_o, and β are constants derived from the RNG procedure. η is a constant based on the local strain parameter ($k|S_{ij}/\epsilon|$), the local vorticity parameter ($k|\Omega_{ij}/\epsilon|$), and local helicity parameters. The output from the $k-\epsilon$ RNG model is then used to locally replace the original relaxation time τ with τ_{turb} as follows,

$$\tau_{\mathrm{turb}}=\tau+\frac{C_\mu k^2/\epsilon}{(1+\eta^2)^{0.5}} \tag{2.32}$$

Hence, the usage of the $k-\epsilon$ RNG model under the VLES model is very different from that in RANS. In the latter, the Reynolds stress tensor is computed directly using the turbulence model in order to solve a closure problem. In VLES, the output from the turbulence model only modifies the relaxation properties of the Boltzmann equation, and consequently, the local eddy viscosity; the Reynolds stress tensor is computed as part of the LBM solution. This implementation enables the development of large turbulent eddies in the simulation domain and allows for capturing the non-linearity of Reynolds stresses [25, 28].

In the LBM-VLES approach, a wall function is applied on the first voxel adjacent to a no-slip wall. This treatment is useful to avoid the need to employ high grid density near the wall to resolve the inner part of the boundary layer (e.g., viscous sublayer). The wall function is based on the generalized law-of-the-wall model [29], extended to consider the effects of pressure gradient and surface roughness. The wall function is expressed as follows,

$$U^+=\frac{1}{\mathsf{K}}\ln\left(\frac{y^+}{\mathsf{A}}\right)+\mathsf{B}, \tag{2.33}$$

where

$$\mathsf{A}=1+g\left(\frac{dp}{d\boldsymbol{s}}\right),\quad \mathsf{B}=5.0,\quad \mathsf{K}=0.41,\quad y^+=\frac{u_\tau y}{\nu} \tag{2.34a-d}$$

and A is a function of the pressure gradient $\frac{dp}{d\boldsymbol{s}}$.

2.2. COMPUTATIONAL AEROACOUSTICS

Computational aeroacoustics (CAA) refer to numerical methods for predicting the generation and propagation of aerodynamically-generated sound. In the following, a brief overview of different CAA methods will be presented, although these are not exhaustive, and more details can be found in references [30, 31].

2.2.1. DIRECT NOISE COMPUTATIONS

A direct noise computation (DNC) refers to a numerical technique, where acoustic information (e.g., acoustic pressure time history) are obtained directly from within the simulation domain as part of the numerical solution. While this approach appears to be intuitive and straightforward, DNC is usually computationally expensive to perform[5] for multiple reasons [30, 32].

Sound waves are generated over a wide range of frequencies, where the corresponding wavelengths can vary from the order of 10^1 m to 10^{-3} m within the human hearing range. As a consequence, the spatial resolution in the simulation domain must be sufficiently high to accurately resolve the acoustic waveform (e.g., more than 6 grid points per wavelength [32]), especially in the high-frequency range. Additionally, the simulation needs a sufficiently long acquisition time, in respect to the period of the sound wave, to obtain an accurate spectral information, especially in the low frequency range. Considering that many aeroacoustic problems are mainly interested with noise levels in the acoustic far-field (i.e., where the distance of the observer from the source region is several times the sound wavelength), a DNC would require an extensive simulation domain that encloses the observer location, while also being discretised with a relatively high spatial resolution. All of these requirements combined could incur an immense computational cost.

DNC also necessitates a numerical scheme with low dispersion and dissipation characteristics to prevent acoustic information from being artificially distorted or dampened while they propagate towards the far-field. Therefore, a DNC-capable solver would generally require high-order numerical schemes (e.g., those with order of accuracy equal to 3 or higher)[6]. The LBM scheme has been shown to be capable to perform DNC [4], but the more affordable hybrid CAA methods are often preferable [31].

2.2.2. AEROACOUSTIC ANALOGIES AND HYBRID CAA METHODS

Unlike DNC, a hybrid CAA method separates the noise computation process into two steps:

1. The computations of noise sources, including turbulence and other non-linearities in the flow-field, are performed using CFD, such as LBM-VLES or LES. This procedure is carried out for a relatively small domain that encompasses the source region where sound is generated.

2. Beyond the source region, the noise propagation problem is solved using techniques based on the linear acoustic theory [34].

[5] It is arguable that DNC for CAA is analogous to DNS for CFD simulations.

[6] A numerical method is of order n if the solution error ϵ is proportional to the grid size to the power of n, i.e., $\epsilon \propto (\Delta x)^n$ [33].

There are various hybrid CAA methods [35], such as the linearised Euler equations (LEE) [36], acoustic perturbation equations (APE) [37], and acoustic analogies, among others. The acoustic analogy was first derived by Lighthill [38] using the continuity and momentum conservation equations with the absence of mass injection and external forces.

$$\begin{aligned} \frac{\partial \rho}{\partial t} + \frac{\partial (\rho u_i)}{\partial x_i} &= 0 \\ \frac{\partial (\rho u_i)}{\partial t} + \frac{\partial (\rho u_i u_j)}{\partial x_i} &= -\frac{\partial p}{\partial x_i} + \frac{\partial \varsigma_{ij}}{\partial x_i} \end{aligned} \tag{2.35}$$

where ς_{ij} is the stress tensor. By taking the time derivative of continuity equation and subtracting it with the divergence of the momentum equation, the Lighthill's equation is obtained.

$$\frac{\partial}{\partial t}\left[\frac{\partial \rho}{\partial t} + \frac{\partial (\rho u_i)}{\partial x_i}\right] - \frac{\partial}{\partial x_i}\left[\frac{\partial (\rho u_i)}{\partial t} + \frac{\partial (\rho u_i u_j)}{\partial x_i} + \frac{\partial p}{\partial x_i} - \frac{\partial \varsigma_{ij}}{\partial x_i}\right] = 0 \tag{2.36}$$

$$\frac{\partial^2 \rho}{\partial t^2} - c_0^2 \frac{\partial^2 \rho}{\partial x_i^2} = \frac{\partial^2 \mathrm{T}_{ij}}{\partial x_i \partial x_j} \tag{2.37}$$

The constant c_0 can be shown to be equal to the speed of sound ($c_0 = a_\infty = \sqrt{\partial p / \partial \rho\big|_s} = \sqrt{\gamma \mathrm{R} T_\infty}$) following the assumption of sound propagation as an isentropic process in a region with a homogeneous temperature distribution. It is also possible to write equation 2.37 in term of pressure perturbations by applying the Reynolds decomposition $\rho' = \rho - \rho_\infty$ and using the isentropic relation $\rho' = p'/a_\infty^2$.

$$\begin{aligned} \frac{1}{a_\infty^2}\frac{\partial^2 p'}{\partial t^2} - \frac{\partial^2 p'}{\partial x_i^2} &= \frac{\partial^2 \mathrm{T}_{ij}}{\partial x_i \partial x_j} \\ \mathrm{T}_{ij} &= \rho u_i u_j - \zeta_{ij} + (p' - a_\infty^2 \rho')\delta_{ij} \end{aligned} \tag{2.38}$$

The Lighthill stress tensor T_{ij} contains three different contributions: the Reynolds stress ($\rho u_i u_j$), the viscous stress (ζ_{ij}), and an entropy term ($p' - a_\infty^2 \rho'$). Note that δ_{ij} is a Kronecker delta. At high Reynolds numbers, which is often the case in aerospace applications, the viscous stress term is expected to be relatively small compared to the inertial term (i.e., Reynolds stress). The entropy term would also be negligible with the absence of large density inhomogeneities in the flow-field. The presence of the second-order spatial derivative next to the Lightill's stress tensor implies that it can be described as a distribution of quadrupole sources. It is also worth mentioning that Lighthill's equation is mathematically exact, but it cannot be solved analytically as there are 11 unknowns (3 in u_i, 6 in $u_i u_j$, p', and ρ',) while there is only one equation. Despite

this, assuming that T_{ij} is known and the source region exists in an unbounded domain, then the free-field Green's function [7] can be used to solve equation 2.38.

$$p'(\boldsymbol{x}_o, t) = \frac{1}{4\pi} \iiint_{\mathbb{V}} \frac{\partial^2 T_{ij}\left(\boldsymbol{x}_s, t - \frac{|\boldsymbol{x}_s - \boldsymbol{x}_o|}{a_\infty}\right)}{\partial x_i x_j} \frac{1}{|\boldsymbol{x}_s - \boldsymbol{x}_o|} \mathrm{d}\mathbb{V} \tag{2.39}$$

where $\boldsymbol{x}_s$ and $\boldsymbol{x}_o$ are the source and observer locations respectively. $\mathbb{V}$ is a control volume where the quadrupole sources are contained. Note that the acoustic pressure at an observer time t is solved based on the information at an earlier time when the sound was emitted by the source (i.e., source time) [34]. This time difference is equal to that taken by a sound wave to travel from the source to the observer. This is referred to as the *retarded time* principle. A different formulation based on an advanced time interpretation has also been proposed by Casalino [39], which will be discussed in a later part of this section. Despite of the physical insight provided by the Lighthill's analogy, there are several limitations that prevent it from being applied in practice. Equation 2.39 requires the Lighthill's stress to be known at every point within the sound source region (i.e., the volume $\mathbb{V}$), and storing information in a 3-dimensional space would require a relatively large amount of memory.

Lighthill's idea was expanded further by Curle [40] by incorporating an arbitrary solid boundary in proximity of turbulence. This formulation is often referred to as the Curle's analogy, and once the non-isentropic effects are neglected, it reads as follows.

$$\rho'(\boldsymbol{x}_o, t) = \frac{1}{4\pi a_\infty^2} \left[\frac{\partial^2}{\partial x_i x_j} \iiint_{\mathbb{V}} \frac{\rho u_i u_j}{|\boldsymbol{x}_s - \boldsymbol{x}_o|^2} \mathrm{d}\mathbb{V} - \frac{\partial}{\partial x_i} \iint_{\mathbb{S}} \frac{p' \cdot \boldsymbol{n}}{|\boldsymbol{x}_s - \boldsymbol{x}_o|^2} \mathrm{d}\mathbb{S} \right] \tag{2.40}$$

The volume-integral term in equation 2.40 is the same as in Lighthill's analogy, which represents the noise contribution from the Reynolds shear stresses in turbulence. The second term contains a surface integral of the pressure fluctuations p' on the solid body. Correspondingly, this additional noise contribution comes from a distribution of dipole sources at the body surface. Curle also performed a dimensional analysis to compare the acoustic efficiency of each source term, and the sound intensity for the surface integral (dipole) term had been found to scale with $U_\infty^3 M_\infty^3$, and $U_\infty^3 M_\infty^5$ for the volume integral (quadrupole) one. Hence, for low Mach number flows, the interaction between turbulence and a solid body is a more efficient noise generation mechanism compared to the turbulence itself. Curle's analogy was further developed by Ffowcs-Williams and Hawkings [41] to include a moving boundary, which remains as a staple in many recent aeroacoustics studies.

2.2.3. FFOCWS-WILLIAMS & HAWKINGS ANALOGY AND THE ADVANCED TIME FORMULATION

As illustrated in figure 2.5, suppose that there exists a source region that is defined by a control surface $\mathbb{S}(\boldsymbol{x}, t) = 0$ whose surface points are moving with a velocity $\boldsymbol{u}_\mathbb{S}$. The local

[7] A function that realises an impulse response for an inhomogeneous linear differential operator is referred to as the Green's function.

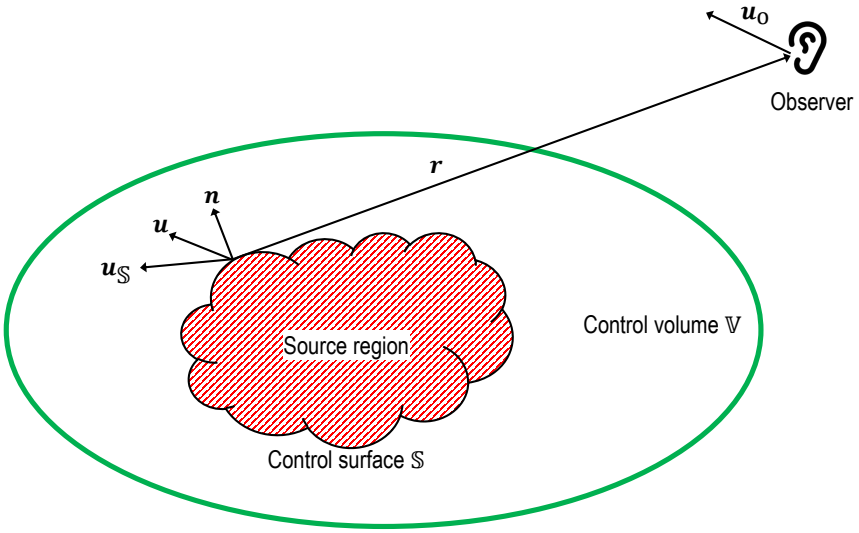

Figure 2.5: A schematic of the notations used in the formulation of the Ffocws-Williams & Hawkings (FW-H) analogy. The source region $\mathbb{V}$ is enclosed by a control surface $\mathbb{S}$. Vectors $\boldsymbol{u}$ and $\boldsymbol{v}$ refer to the flow velocity and the velocity of the control surface respectively. $\boldsymbol{u_o}$ is the velocity of the observer.

normal at the control surface is defined as $\boldsymbol{n}$. The source region is contained within a control volume $\mathbb{V}$. The FW-H analogy can be derived using generalised derivatives [42], such that a portion of the flow-field inside the control surface ($\mathbb{S} < 0$) can be replaced by a quiescent fluid and a collection of sources distributed on this surface. The continuity and momentum equations are written as follows:

$$\frac{\partial}{\partial t}\left[(\rho-\rho_\infty)\mathsf{H}(\mathbb{S})\right]+\frac{\partial}{\partial x_i}\left[\rho u_i \mathsf{H}(\mathbb{S})\right]=\mathsf{Q}\delta(\mathbb{S}) \tag{2.41}$$

$$\frac{\partial}{\partial t}\left[(\rho u_i)\mathsf{H}(\mathbb{S})\right]+\frac{\partial}{\partial x_i}\left[(\rho u_i u_j+\mathrm{P}_{ij})\mathsf{H}(\mathbb{S})\right]=\mathsf{L}_i\delta(\mathbb{S}) \tag{2.42}$$

where the source terms Q and L are defined in the following.

$$\mathsf{Q}=\rho_\infty \mathrm{U}_i n_i, \qquad \mathrm{U}_i=\left(1-\frac{\rho}{\rho_\infty}\right)u_{\mathbb{S},i}+\frac{\rho u_i}{\rho_\infty} \tag{2.43}$$

$$\mathsf{L}_i=\mathrm{P}_{ij}n_j+\rho u_i(u_n-u_{\mathbb{S},n}), \qquad \mathrm{P}_{ij}=(p-p_\infty)\delta_{ij}-\zeta_{ij} \tag{2.44}$$

Note that $\mathsf{H}(\mathbb{S})$ is a Heaviside function.

$$\begin{aligned}\mathsf{H}(\mathbb{S})&=0 \quad \text{if} \quad \mathbb{S}<0\\ \mathsf{H}(\mathbb{S})&=1 \quad \text{if} \quad \mathbb{S}\geq 0\end{aligned} \tag{2.45}$$

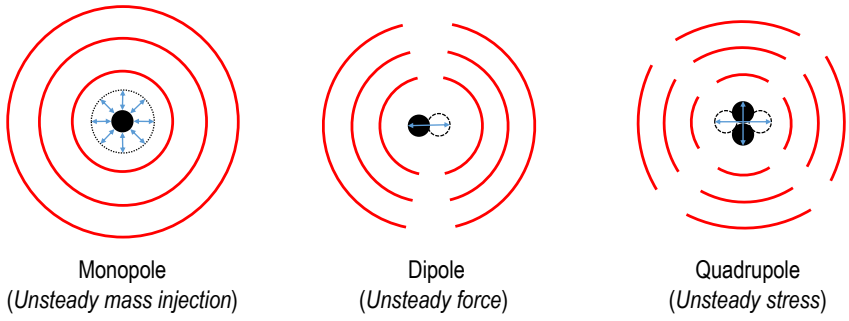

Figure 2.6: An illustration of different types of elementary acoustic sources in linear acoustic theory. The directivity for each source can be inferred from the wave propagation pattern.

Combining equations 2.41 and 2.42 leads to the classical FW-H equation.

$$\Box^2 \left\{\rho' a_\infty^2 \mathsf{H}(\mathbb{S})\right\} = \frac{\partial^2}{\partial x_i x_j}\left\{\mathsf{T}_{ij}\mathsf{H}(\mathbb{S})\right\} - \frac{\partial}{\partial x_i}\left\{\mathsf{L}_i \delta(\mathbb{S})\right\} + \frac{\partial}{\partial t}\left\{\mathsf{Q}_i \delta(\mathbb{S})\right\} \tag{2.46}$$

$\Box^2 = \frac{1}{a_\infty^2}\frac{\partial^2}{\partial t^2} - \frac{\partial^2}{\partial x_i^2}$ is the d'Alembert operator. $(\rho - \rho_\infty)a_\infty^2$ is equivalent to p' when density perturbations are small, which is generally the case at a sufficiently far distance from the source region (e.g., aerodynamic far-field). Similar to the expression in Lighthill's analogy, the left hand side of equation 2.46 describes the acoustic wave propagation, and the noise sources are collected at the right hand side. The first term contains the Lighthill stress tensor contribution within the control volume. The second term is related to the unsteady forces exerted by the control surface onto the surrounding fluid, otherwise referred to as the loading source term. The last one is the thickness source term, which accounts for the fluid displacement by the control surface. The Lighthill stress tensor is equivalent to a quadrupole source, while the loading source term corresponds to a dipole, and the thickness source term to a monopole.

An illustration of these sources is provided in figure 2.6. A monopole can be realised using a pulsating mass that continuously displaces the surrounding fluid, resulting in a omnidirectional wave propagation pattern. The same mechanism applies, for instance, to pneumatic sirens. A dipole is represented by two monopoles with opposite phases that are placed very close to each other (with respect to the acoustic wavelength). Such arrangement causes the surrounding fluid to slosh back and forth along the axis connecting the two monopoles. Consequently, the noise intensity along this axis is the highest, but it is the lowest perpendicular to the axis due to the waves emitted by each monopole cancelling each other out. Unsteady forces on aerodynamic bodies, such as the fluctuating lift due to the generation of Kármán vortex street in a cylinder wake, can be modelled as dipole sources. Placing two dipoles in phase opposition next to each other would yield a quadrupole. The Reynolds stresses in the turbulence produced by a high-speed jet can be considered as quadrupole-type sources.

The solution to the FW-H equation in the acoustic far-field can also be obtained by employing the free-space Green's function. The integral expression for the FW-H solution

is written as follows.

$$
\begin{aligned}
4\pi p' = & \frac{\partial^2}{\partial x_i x_j} \int_{\mathbb{S}>0} \left[\frac{\mathrm{T}_{ij}}{\boldsymbol{r}\,(1-M_{\boldsymbol{r}})} \right]_{t'} \mathrm{d}\mathbb{V} \\
& - \frac{\partial}{\partial x_i} \int_{\mathbb{S}=0} \left[\frac{\mathrm{L}_i}{\boldsymbol{r}\,(1-M_{\boldsymbol{r}})} \right]_{t'} \mathrm{d}\mathbb{S} \\
& + \frac{\partial}{\partial t} \int_{\mathbb{S}=0} \left[\frac{\mathrm{Q}}{\boldsymbol{r}\,(1-M_{\boldsymbol{r}})} \right]_{t'} \mathrm{d}\mathbb{S}
\end{aligned}
\tag{2.47}
$$

The subscript t' implies that each source term is evaluated at a retarded time $t' = t - \left(\left|\boldsymbol{x}_s(t) - \boldsymbol{x}_o(t')\right| / a_\infty\right)$. $M_{\boldsymbol{r}} = M_{\mathbb{S},i}\, r_i$ is the projected source Mach number vector in the direction of the observer. The denominator in each source term is a Doppler shift factor that is associated with the relative motion between the source and the observer.

Compared to Lighthill's formulation, the FW-H equation has two surface-integral terms. To recap, the acoustic intensity in the far-field for the quadrupole term scales with $U_\infty^3 M_\infty^5$ [38], the dipole term with $U_\infty^3 M_\infty^3$ [40], and the monopole one with $U_\infty^3 M_\infty$. Hence at low Mach number, it is usually practical to neglect the quadrupole sources as they are less efficient at radiating noise compared to the other two. Furthermore, if $\mathbb{S}$ only contains solid, rigid, and non-vibrating surfaces (i.e., $u_i n_i = u_{\mathbb{S},i} n_i = 0$), the monopole term would vanish. As a result, only the dipoles on the solid surface remain as the noise source. The resulting formulation is often referred to as *solid FW-H*. Due to its simplicity, the solid FW-H formulation has been widely used for aeroacoustics investigatons [43], although it remains unsuitable for cases where volumetric sources are important, such as in jet noise studies.

Di Francescantonio [44] proposed an alternative approach by extending the FW-H analogy with the usage of a permeable control surface, and thus, it is referred to as the *permeable FW-H* approach. The permeable surface is defined to enclose the source region, where flow non-linearities are present. In doing so, the quadrupole term in the FW-H equation vanishes since the Lighthill stress tensor is zero outside of the permeable surface (i.e., $\mathbb{S} > 0$) by definition. Instead, the contribution of quadrupoles inside $\mathbb{S}$ is taken into account by monopoles and dipoles that are distributed along the permeable surface. Hence, compared to the solid FW-H approach, the permeable one is more versatile without a significant difference in computational cost. In practice, however, the placement of the permeable surface in the simulation domain can become an issue [43].

In some situations, the permeable FW-H surface can cut across regions containing vortical perturbations, such as turbulence in the wake of an airfoil. Turbulent fluctuations passing through the permeable surface are essentially pseudo-sound sources that would corrupt the noise computation result. Spalart *et al.* [43] has summarised several workarounds for this issue. Firstly, the permeable surface is extended further downstream from the source region, where the simulation domain is intentionally discretised with coarser grid to introduce additional numerical dissipation for suppressing the contribution of the pseudo-sound sources. Another possible approach is the removal of a small segment of the permeable surface where it intersects with flow-field regions that contain turbulence, although it could affect the noise prediction accuracy. More recently, some authors employed a multi-end-caps approach

in jet noise investigations [45–47]. It entails the usage of several end-caps (i.e., downstream termination of the permeable surface) that are slightly separated from each other, and afterward, the noise computed using each end-cap is averaged. Fundamentally, this approach exploits the difference in convection velocities between the flow and sound. Unlike sound waves, turbulent fluctuations generally travel at the same velocity as the free stream, which is much slower than the speed of sound for low Mach number flows. Thus, each end-cap would perceive the pseudo-sound contribution with a larger phase variation compared to that of a sound wave, resulting in a cancellation effect of the former during the averaging procedure. The usage of multi-end-caps approach in the present study will be elaborated further in chapter 5 In order to improve the practicality of the FW-H solution for numerical implementation, Farassat [42] derived the formulation 1A. It involves converting the spatial derivatives in both quadrupole and dipole terms into time derivatives. Subsequently, the time derivatives are moved inside the integral by rewriting the derivatives with respect to the retarded time (i.e., from t to t') [48, 49]. Lastly, the integral formulation is extended to account for a moving observer with a constant velocity $u_o = M_o a_\infty$ as previously shown in figure 2.5. At the time of writing, Farrasat's formulation 1A is arguably the most frequently available method in CFD solvers.

It has been mentioned earlier that the retarded time approach can become inconvenient for numerical simulations. To circumvent this, Casalino [39] proposed a modification to the FW-H formulation, where the sound contributions from each location in the source region are computed at the emission time (or source time). Correspondingly, the time at which these sound waves arrive at the observer is referred to as the *advanced time*. At each instance of the emission time, the sound contributions from the source region are summed together to build the time history at the observer location. The retarded time formulation has been given previously as follows.

$$t' = t - \left(\frac{|\boldsymbol{x}_s(t) - \boldsymbol{x}_o(t')|}{a_\infty} \right) \tag{2.48}$$

If the observer time were shifted by $\mathcal{T}$, equation 2.48 becomes the following.

$$t^* = t + \mathcal{T} - \left(\frac{|\boldsymbol{x}_s(t+\mathcal{T}) - \boldsymbol{x}_o(t^*)|}{a_\infty} \right) \tag{2.49}$$

It can be shown that when $t^* \equiv t$,

$$\mathcal{T} = \frac{|\boldsymbol{x}_s(t+\mathcal{T}) - \boldsymbol{x}_o(t)|}{a_\infty} \tag{2.50}$$

Thus, $t+\mathcal{T}$ is interpreted as the time when the sound wave emitted at a source location $\boldsymbol{x}_s$ arrives at the observer location $\boldsymbol{x}_o$. $t_{\text{adv}} = t + \mathcal{T}$. is later referred to as the advanced time. Casalino [39] showed that equation 2.50 can be solved as,

$$\begin{aligned}\mathscr{T} &= \frac{r_i M_{o,i} \pm \sqrt{\left(r_i M_{o,i}\right) + |\boldsymbol{r}|^2 \left(1 - M_o^2\right)}}{a_\infty \left(1 - M_o^2\right)} \\ &= \frac{|\boldsymbol{r}|}{a_\infty} \left[\frac{M_{o,r} \pm \sqrt{M_{o,r}^2 - M_o^2 + 1}}{1 - M_o^2} \right]\end{aligned} \tag{2.51}$$

where $M_{o,r} = r_i M_{o,i}$ is the projection of the observer Mach number vector towards the source direction. Due to causality, $\mathscr{T}$ needs to be positive for an acoustic wave to be perceived by the observer only after it has been emitted from the source, instead of the opposite. Hence, for an observer in subsonic motion ($M_o < 1$), the numerator in the bracket of equation 2.51 must satisfy the following condition.

$$M_{o,r} \pm \sqrt{M_{o,r}^2 + (1 - M_o^2)} < 0 \tag{2.52}$$

The second term at the left hand side of equation 2.52 would generally be larger than the first term when $M_o < 1$, and thus, the advanced time solution is given by,

$$t_{\text{adv}} = t + \frac{|\boldsymbol{r}(t)|}{a_\infty} \left[\frac{M_{o,r}(t) + \sqrt{M_{o,r}^2(t) + (1 - M_o^2)}}{1 - M_o^2} \right] \tag{2.53}$$

While the advanced time approach for the FW-H analogy allows for noise computation to be carried out simultaneously as for CFD solution, the Doppler shift factor may cause a mismatch between the discrete timestep at the source time domain and the observer's. To overcome this issue, a linear interpolation procedure can be used to ensure the correspondence between both time series [39].

2.3. NUMERICAL MODELLING OF POROUS MATERIALS

2.3.1. MACROSCOPIC BEHAVIOR AND DARCY'S LAW

In general, there are two approaches for simulating porous media: 1) replicating the internal geometry of the porous medium and resolving its influence on the internal flow-field, or 2) modelling the spatially-averaged effects of porosity on the flow-field inside the porous medium. Analogous to turbulence simulation, the former is equivalent to DNS and the latter to RANS. The first approach presents several challenges. Firstly, the geometrical details of the porous material are not always known and it might not be possible to retrieve them. Then, the discretisation of the porous material matrix could require a relatively high grid resolution, implying an immense computational cost. Thus, the usage of a porous medium model is usually more attractive, where the porous medium geometry is replaced with either a boundary condition [50] or an equivalent fluid region [51].

A flow permeating a porous medium would encounter resistance that results in a pressure drop ∇p proportional to the transpiration velocity $\boldsymbol{u}$. This relationship is given in equation (2.54) and it was first demonstrated in 1856 by Darcy [52] using sand-column experiments, and thus this equation is also referred to as the Darcy's force term [53].

$$\nabla p = -\rho \boldsymbol{R} \cdot \boldsymbol{u} \tag{2.54}$$

where $\boldsymbol{R}$ is the resistance tensor. $\boldsymbol{R}$ can be further expanded as shown in equation (2.55), where $\boldsymbol{R}_V$ is the viscous resistivity and $\boldsymbol{R}_I$ is the inertial resistivity. The latter becomes more important as the Reynolds number inside the porous medium increases. Viscous resistivity is caused by the viscous effect as the permeating flow grazes the porous medium matrix, analogous to a flow inside a narrow channel. On the other hand, inertial resistivity is related to the unsteady acceleration that the flow experiences as it meanders around the porous medium matrix.

$$\boldsymbol{R} = \boldsymbol{R}_V + \boldsymbol{R}_I \boldsymbol{u}, \tag{2.55}$$

$$\boldsymbol{R}_V = \frac{\mu}{\rho \boldsymbol{K}}, \quad \boldsymbol{R}_I = \boldsymbol{C}. \tag{2.56}$$

Substituting equation (2.55) into equation (2.54) results in an equation with both linear and non-linear velocity terms that is subsequently known as the Hazen-Dupuit-Darcy equation[8] [54]. $\boldsymbol{R}_V$ can be shown to be inversely proportional to the permeability $\boldsymbol{K}$ via the fluid's kinematic viscosity (μ/ρ), and $\boldsymbol{R}_I$ is equal to the form coefficient $\boldsymbol{C}$, as shown in equation (2.56). This implies that the permeating flow would encounter stronger resistance from the porous material as permeability becomes smaller.

2.3.2. POROUS MEDIA EXTENSION FOR LBM

The implementation of porous medium model in SIMULIA PowerFLOW 5.4b is discussed in the following. For more details, readers are advised to refer to Freed [55] and Sun et al. [51]. In PowerFLOW, a porous medium can be modelled using an equivalent fluid region in which additional volume forces are applied as governed by the Darcy's law [55, 56]. Consequently, the model computes the spatially-averaged resistance encountered by the permeating flow due to its interaction with the internal structures of the porous medium. A similar approach has been employed for a N-S solver by Bernicke *et al.* [57], Ananthan *et al.* [58]. Following the Boltzmann's kinetic theory, an external force can be introduced by modifying the local flow velocity during the collision step [59]. Recalling the collision step in equation 2.12, it can be rewritten as follows,

$$\kappa_q = F_q + \frac{1}{\tau}\left[\tilde{F}_q^{eq} - F_q\right] \tag{2.57}$$

[8] In some literature, it is also referred to as the Brinkman-Forchheimer-Darcy equation.

where $\tilde{F}_q^{eq}$ is the equilibrium distribution function during the pre-collision (post-advection) step. Afterward, the pre-collision flow velocity $\tilde{\boldsymbol{u}}$ in $\tilde{F}_q^{eq}$ is replaced by the post-collision one $\boldsymbol{u}'$, and equation 2.57 is rewritten as in 2.58.

$$\kappa_q = F_q + \frac{1}{\tau}\left[F_q'^{eq} - F_q\right] \tag{2.58}$$

The difference between the pre- and post-collision velocities are directly linked to an external force (**F**) that is defined in equation 2.59.

$$\mathbf{F} = \rho\frac{1}{\tau}\left(\boldsymbol{u}' - \tilde{\boldsymbol{u}}\right) \tag{2.59}$$

The Darcy's force term is introduced into equation 2.59, which yields

$$\rho\frac{1}{\tau}\left(\boldsymbol{u}' - \tilde{\boldsymbol{u}}\right) = -\rho\boldsymbol{R}\cdot\bar{\boldsymbol{u}} \tag{2.60}$$

where $\bar{\boldsymbol{u}}$ is a "centered-mean" velocity that is defined using the following expression.

$$\bar{\boldsymbol{u}} = \tilde{\boldsymbol{u}} + \frac{\mathbf{F}}{2\rho} = \left(1 - \frac{1}{2\tau}\right)\tilde{\boldsymbol{u}} + \frac{1}{2\tau}\boldsymbol{u}' \tag{2.61}$$

Thus, solving equation 2.60 for $\boldsymbol{u}'$ yields

$$\boldsymbol{u}' = \left[\mathbf{I} + \frac{1}{2}\boldsymbol{R}\right]^{-1}\left[\mathbf{I} - \left(\tau - \frac{1}{2}\right)\boldsymbol{R}\cdot\tilde{\boldsymbol{u}}\right] = \mathbf{G}\cdot\tilde{\boldsymbol{u}} \tag{2.62}$$

where **G** is referred to as the "velocity adjustment tensor" that depends on resistance tensor and relaxation time, and **I** is an identity matrix. For a diagonal resistance tensor the expression in 2.62 can be simplified as

$$\begin{aligned} u'_\alpha &= G_\alpha\,\tilde{u}_\alpha \\ G_\alpha &= \frac{1 - \left(\tau - \frac{1}{2}\right)R_\alpha}{1 + \frac{R_\alpha}{2}} \end{aligned} \tag{2.63}$$

where α denotes the axis with respect to the incoming flow direction.

In summary, the present formulation incorporates the effects of the Darcy's force term into the flow solution by introducing a modified velocity $\boldsymbol{u}'$ that is solved together with equation 2.62. It has been shown that the LB equations are equivalent to Navier-Stokes equations using the Chapman-Enskog expansion up to third-order truncation for perfect gas at low Mach number [13]. Hence, equation (2.54) can be substituted to equation (2.2), and the resulting equation is equivalent to the following Navier-Stokes form:

$$\frac{\partial \rho}{\partial t} + \nabla \cdot (\rho \boldsymbol{u}) = 0, \tag{2.64}$$

$$\frac{\partial \rho \boldsymbol{u}}{\partial t} + \nabla \cdot (\rho \boldsymbol{u}\boldsymbol{u}) = -\nabla p - \rho \boldsymbol{R} \cdot \boldsymbol{u}, \tag{2.65}$$

where the velocity $\boldsymbol{u}$ is equal to the centered-mean velocity $\bar{\boldsymbol{u}}$. Note that the viscous term in the Navier-Stokes equation has been replaced with the Darcy's force term. Outside of the porous media region, however, the Darcy's force term vanishes and it is replaced with the original viscous term.

There are two slightly different porous-media models in PowerFLOW, namely the "APM" (acoustics-porous-medium) and the "PM" (porous-medium). While both models describe porous media as an equivalent fluid region where the Darcy's force term is applied, the APM also includes a physical interface between the regular fluid region and the porous media region. At this interface, double-sided surfaces are employed similarly to a sliding mesh mechanism [60]. Additionally, the mass flow through the interface is governed by the mass-flux conservation as:

$$|\rho \boldsymbol{u} \cdot \boldsymbol{n}|_{\infty} = \phi |\rho \boldsymbol{u} \cdot \boldsymbol{n}|_{\mathrm{PM}}, \tag{2.66}$$

where ϕ is the material porosity, $\boldsymbol{n}$ is a unitary normal vector at the interface, while the subscripts ∞ and PM denote the regular fluid region and porous media region, respectively. The porosity is defined as,

$$\phi = 1 - \frac{\rho_{\mathrm{PM}}}{\rho_{\mathrm{S}}}, \tag{2.67}$$

where ρ_{PM} and ρ_{S} are the density of the porous medium sample and that of the solid constituent (matrix), respectively.

It has been reported by Sun *et al.* [51] that using empirical resistivity and porosity values is sufficient for resolving the aerodynamic and acoustic behaviours of rigid porous materials such as metal foam. However, PowerFLOW's PM and APM models neglect other porous material properties, such as surface roughness and structural deformation. The latter can be safely neglected if the porous material is reasonably rigid, such as the Ni-Cr-Al metal foam [61, 62] that will be used in the subsequent chapters. Nevertheless, the surface roughness effect has been reported to cause noise increase in many instances [63, 64]. Hence, it is expected that the far-field noise of a porous surface in the simulation to deviate from experimental trends where surface roughness effects are relevant.

2.3.3. CHARACTERISATION OF POROUS MATERIALS

Porosity values are often available directly from the manufacturers, but they can also be computed by measuring the density of a porous material sample and that of its matrix (see equation 2.67). This can be done using a laboratory scale or spectroscopy equipment [61]. For certain types of porous material, such as porous crystal, porosity can be directly computed from the arrangement of its internal geometry.

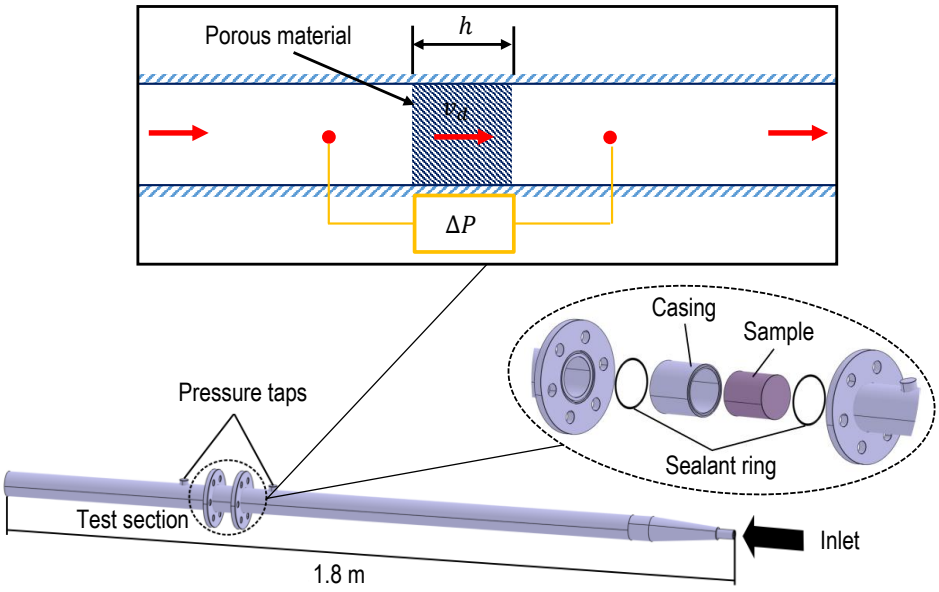

Figure 2.7: Porous material characterisation test rig at the Delft University of Technology. A simplified sketch is shown at the top.

In order to obtain the resistivity values, a dedicated test rig has been prepared as shown in figure 2.7. The test rig consists of two pieces of straight tubes, and a test section containing the porous material sample is placed in the middle. A valve next to the inlet controls the mass flow rate inside the tube. The pressure difference across the sample is measured using the pressure taps that are located upstream and downstream of the test section. By altering the mass flow rate in the tube and the sample thickness, various pressure drop trends can be measured. Then, these trends are curve-fitted into the Hazen-Dupuit-Darcy equation in 2.68, to obtain the viscous R_V and inertial resistivity (R_I) values.

$$\frac{\Delta P}{\rho h} = R_V v_d + R_I v_d^2 \tag{2.68}$$

ΔP is the pressure difference across the porous medium, h is the sample thickness, and v_d is the Darcian velocity (a ratio between the mass flow rate in the tube and the cross-section area of the test section).

An example of the data obtained using the test rig is given in figure 2.8. The plot on the left shows the absolute pressure drop values whereas the right one shows the same quantity that has been normalised with the sample thickness. The figure clearly illustrates that for a given v_d, the pressure drop increases as the porous material becomes thicker, as expected. Nevertheless, when the pressure drop is normalised with the material thickness, the curves tend to collapse as the sample thickness increases. This indicates that both permeability (viscous resistivity) and form coefficient (inertial resistivity) would converge

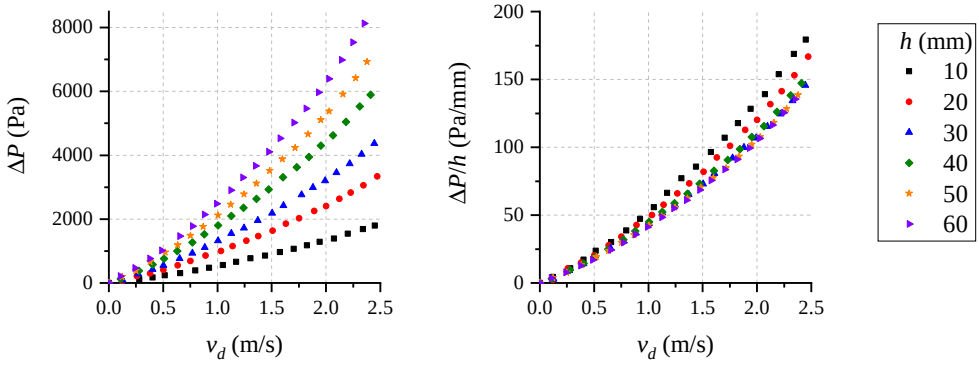

Figure 2.8: Pressure drop test result for a Ni-Cr-Al metal foam with the mean pore diameter of 0.45 mm. Data has been extracted from reference [61].

only at large material thicknesses.

A similar trend has been previously discussed in literature [65, 66]. Baril *et al.* [65] performed similar resistivity characterisations for metal foams, with the results shown in figure 2.9. They also observed that for any given Darcian velocity, the ratio $\Delta P/h$ becomes constant once the material thickness reached a certain value, which they referred to as the *critical thickness*. Based on this observation, they proposed that the porous material resistivity consisted of two components: 1) the bulk resistivity and 2) the resistivity due to the entrance effect. The latter is linked to the fact that the permeating flow does not become steady as soon as it enters the porous material, which implies that Darcy's definition of material resistivity is not fully applicable near the porous medium surface. This region is referred to as the *entrance length*, which has been empirically found to be roughly equal to the average pore size [67] for a metal foam. Hence, the entrance length can also be interpreted as a distance from the porous medium surface where the local flow-field still retains some influences (correlation) from the external region. The experimental data of Baril *et al.* [65] in figure 2.9 clearly show that the entrance effect becomes more relevant at small thicknesses. For a thin porous material, a majority of its thickness is comprised of the entrance length, and in such situation, the resistivity would diverge from the converged value for samples at larger thicknesses. Conversely, the entrance effect is less apparent for a thick porous material as the majority of its volume is dominated by the bulk effect, and thus the resistivity value remains constant even if the thickness is increased further.

2.3.4. MULTI-LAYER APPROACH TO POROUS MEDIUM MODELLING

From figure 2.9, it can be deduced that bulk resistivity does not vary with material thickness (i.e., the converged resistivity value), whereas the one associated with the entrance effect does, especially at small thicknesses. This has an inconvenient consequence for numerical simulations involving the application of porous medium model on aerodynamic bodies with slender parts, such as an airfoil leading and trailing edges. When the porous medium model replaces those edges, their tapering shapes

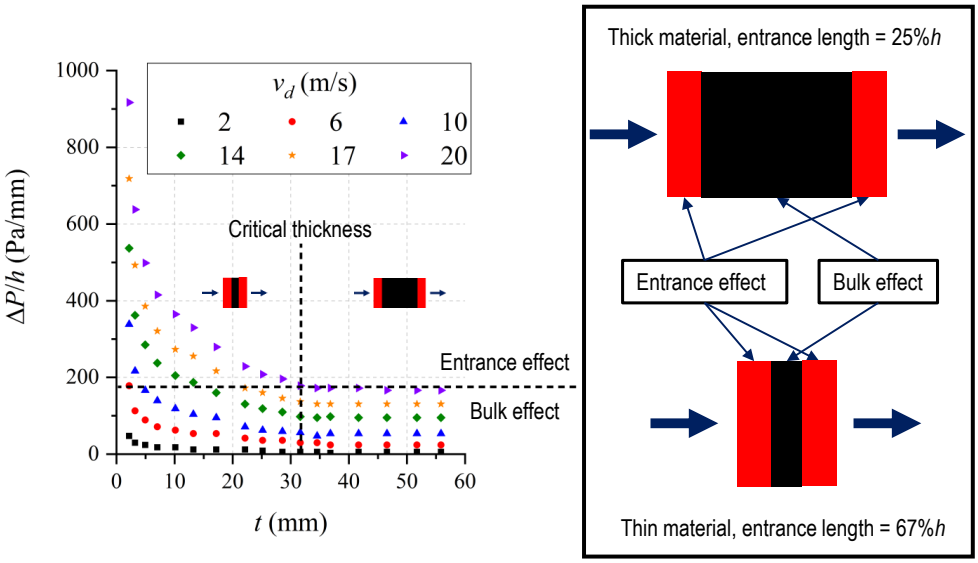

Figure 2.9: The entrance and bulk effects on the pressure drop data of a metal foam with the mean pore diameter of 0.6 mm. Data has been extracted from reference [65].

might require the resistivity values to be continuously adjusted along the chord, according to the local thickness. To circumvent such added complexity, a multi-layer porous medium modelling has been proposed. In essence, this approach aims to separate the region inside the porous medium that is dominated by the bulk effect from the one by the entrance effect, as previously illustrated in figure 2.9.

To verify the multi-layer approach, the porous material characterisation test rig is simulated using PowerFLOW. For this purpose, the properties of the previously mentioned Ni-Cr-Al metal foam will be applied. A sketch of the simulation domain is shown in figure 2.10. The cylindrical tubes and the test section have been combined into

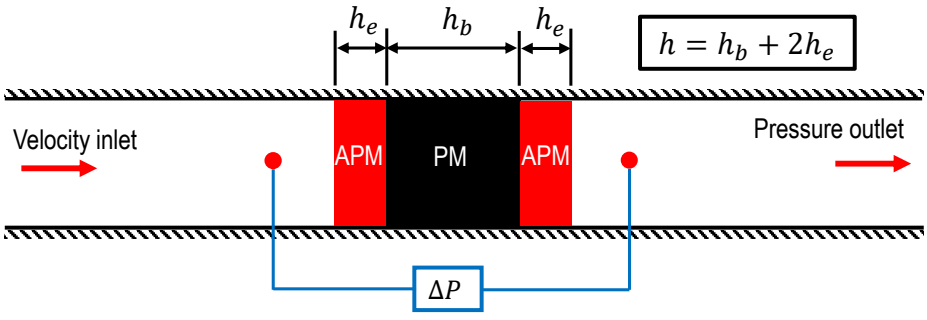

Figure 2.10: A sketch of the porous material permeability test rig in the numerical simulation.

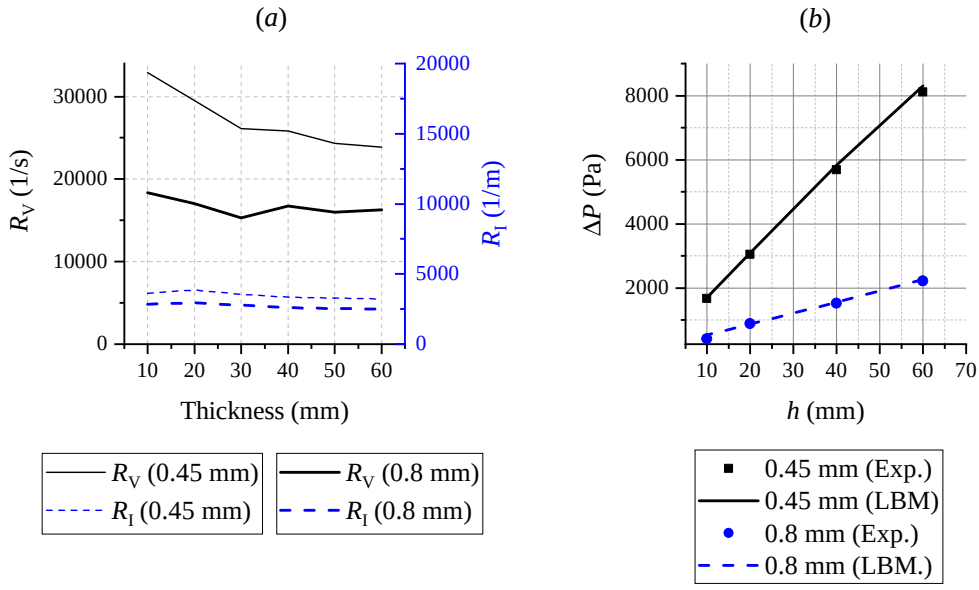

Figure 2.11: (*a*) Resistivity values for the Ni-Cr-Al metal-foam sample obtained from the experiment, and (*b*) the comparison of the pressure drop result between the experiment (Exp.) and simulation (LBM).

one continuous tube that is 1.5 m long with a constant diameter of 55 mm, which also serves as the simulation domain. At the tube inlet, a Darcian velocity of 2.5 m/s is specified, while at the tube outlet, an ambient pressure is applied. The porous material sample is put at the center of the tube, consisting of three separate layers. The outer layers, representing the entrance length, are modelled as acoustic porous-medium (APM) with the thickness of h_e. The inner volume, where bulk effect dominates, is a porous-medium (PM) region that has a thickness of h_b. Thus, the porous material thickness h is equal to $h_b + 2h_e$, where $h_e = 0.1h$ for this particular simulation. This ensures that entrance length of the porous material is embedded within the APM region. The resistivity of the PM region is specified using the value for $h = 60$ mm, which is the bulk resistivity. For the APM region, the resistivity is adjusted depending on its actual thickness (e.g., a 10-mm thick APM region is given the resistivity values corresponding to a 10-mm thick sample). Empirical values of viscous and inertial resistivity are reported in figure 2.11 (*a*) [61]. The simulation has been carried out for 10 flow passes based on the length of the simulation domain.

The pressure difference across the porous medium is measured between the locations of the pressure taps (i.e., 50 mm upstream/downstream of the center of the sample), and the values are reported in figure 2.11 (*b*). A good agreement between the simulation results and the experiment has been achieved for different sample thicknesses and mean pore sizes. Although it is not shown in the plot, a similar agreement can be obtained by modelling the metal-foam sample using a single APM region in which a resistivity that corresponds to its thickness is applied. Based on these results, the porous medium models in PowerFLOW and the multi-layer approach can be

considered reliable for simulating flow transport phenomena in a porous material. Nevertheless, it is worth mentioning that the present investigation only addresses the modelling of a metal-foam, which has isotropic and homogeneous resistivity.

REFERENCES

[1] C. Teruna, L. Rego, F. Avallone, D. Ragni, and D. Casalino, *Applications of the multilayer porous medium modeling approach for noise mitigation,* Journal of Aerospace Engineering **34**, 04021074 (2021).

[2] J. D. Anderson, G. Degrez, E. Dick, and R. Grundmann, *Computational fluid dynamics: an introduction* (Springer Science & Business Media, 2013).

[3] S. Chen and G. D. Doolen, *Lattice boltzmann method for fluid flows,* Annual review of fluid mechanics **30**, 329 (1998).

[4] S. Marié, D. Ricot, and P. Sagaut, *Comparison between lattice boltzmann method and navier–stokes high order schemes for computational aeroacoustics,* Journal of Computational Physics **228**, 1056 (2009).

[5] S. Weidong and L. Jun, *Review of lattice boltzmann method applied to computational aeroacoustics,* Archives of Acoustics **44**, 215 (2019).

[6] K. V. Sharma, R. Straka, and F. W. Tavares, *Current status of lattice boltzmann methods applied to aerodynamic, aeroacoustic, and thermal flows,* Progress in Aerospace Sciences **115**, 100616 (2020).

[7] S. Succi, *The Lattice Boltzmann Equation: for Fluid Dynamics and Beyond* (Oxford university press, 2001).

[8] P. L. Bhatnagar, E. P. Gross, and M. Krook, *A model for collision processes in gases. i. small amplitude processes in charged and neutral one-component systems,* Physical review **94**, 511 (1954).

[9] H. Chen, P. Gopalakrishnan, and R. Zhang, *Recovery of galilean invariance in thermal lattice boltzmann models for arbitrary prandtl number,* International Journal of Modern Physics C **25**, 1450046 (2014).

[10] A. Agrawal, H. M. Kushwaha, and R. S. Jadhav, *Burnett equations: derivation and analysis,* in *Microscale Flow and Heat Transfer* (Springer, 2020) pp. 125–188.

[11] D. Hilbert, *Begründung der kinetischen gastheorie,* Mathematische Annalen **72**, 562 (1912).

[12] S. Chapman and T. G. Cowling, *The mathematical theory of non-uniform gases: an account of the kinetic theory of viscosity, thermal conduction and diffusion in gases* (Cambridge university press, 1990).

[13] H. Chen, S. Chen, and W. H. Matthaeus, *Recovery of the navier-stokes equations using a lattice-gas boltzmann method,* Physical Review A **45**, R5339 (1992).

[14] H. Chen, C. Teixeira, and K. Molvig, *Realization of fluid boundary conditions via discrete boltzmann dynamics,* International Journal of Modern Physics C **9**, 1281 (1998).

[15] H. Chen, O. Filippova, J. Hoch, K. Molvig, R. Shock, C. Teixeira, and R. Zhang, *Grid refinement in lattice boltzmann methods based on volumetric formulation,* Physica A: Statistical Mechanics and its Applications **362**, 158 (2006).

[16] H. Grad, *Note on n-dimensional hermite polynomials,* Communications on Pure and Applied Mathematics **2**, 325 (1949).

[17] X. Shan, X.-F. Yuan, and H. Chen, *Kinetic theory representation of hydrodynamics: a way beyond the navier–stokes equation,* Journal of Fluid Mechanics **550**, 413 (2006).

[18] X. He and L.-S. Luo, *Lattice boltzmann model for the incompressible navier–stokes equation,* Journal of statistical Physics **88**, 927 (1997).

[19] H. Chen, I. Goldhirsch, and S. A. Orszag, *Discrete rotational symmetry, moment isotropy, and higher order lattice boltzmann models,* Journal of Scientific Computing **34**, 87 (2008).

[20] H. Xu and P. Sagaut, *Optimal low-dispersion low-dissipation lbm schemes for computational aeroacoustics,* Journal of Computational Physics **230**, 5353 (2011).

[21] L. Mieussens and H. Struchtrup, *Numerical comparison of bhatnagar–gross–krook models with proper prandtl number,* Physics of Fluids **16**, 2797 (2004).

[22] D. d'Humières, *Generalized lattice-boltzmann equations,* Rarefied gas dynamics (1992).

[23] J. Boussinesq, *Essai sur la théorie des eaux courantes* (Impr. nationale, 1877).

[24] W. Thomson, *Xlv. on the propagation of laminar motion through a turbulently moving inviscid liquid,* The London, Edinburgh, and Dublin Philosophical Magazine and Journal of Science **24**, 342 (1887).

[25] H. Chen, S. A. Orszag, I. Staroselsky, and S. Succi, *Expanded analogy between boltzmann kinetic theory of fluids and turbulence,* Journal of Fluid Mechanics **519**, 301 (2004).

[26] R. Rubinstein and J. M. Barton, *Nonlinear reynolds stress models and the renormalization group,* Physics of Fluids A: Fluid Dynamics **2**, 1472 (1990).

[27] V. Yakhot and S. A. Orszag, *Renormalization group analysis of turbulence. i. basic theory,* Journal of scientific computing **1**, 3 (1986).

[28] C. M. Teixeira, *Incorporating turbulence models into the lattice-boltzmann method,* International Journal of Modern Physics C **9**, 1159 (1998).

[29] B. E. Launder and D. B. Spalding, *The numerical computation of turbulent flows,* in *Numerical Prediction of Flow, Heat Transfer, Turbulence and Combustion* (Elsevier, 1983) pp. 96–116.

[30] C. K. Tam, *Computational aeroacoustics: An overview of computational challenges and applications,* International Journal of Computational Fluid Dynamics **18**, 547 (2004).

[31] S. K. Lele and J. W. Nichols, *A second golden age of aeroacoustics?* Philosophical Transactions of the Royal Society A: Mathematical, Physical and Engineering Sciences **372**, 20130321 (2014).

[32] C. K. Tam, *Computational aeroacoustics-issues and methods,* AIAA journal **33**, 1788 (1995).

[33] Z. J. Wang, K. Fidkowski, R. Abgrall, F. Bassi, D. Caraeni, A. Cary, H. Deconinck, R. Hartmann, K. Hillewaert, H. T. Huynh, *et al.*, *High-order cfd methods: current status and perspective,* International Journal for Numerical Methods in Fluids **72**, 811 (2013).

[34] S. Glegg and W. Devenport, *Aeroacoustics of low Mach number flows: fundamentals, analysis, and measurement* (Academic Press, 2017).

[35] A. S. Lyrintzis, *Surface integral methods in computational aeroacoustics—from the (cfd) near-field to the (acoustic) far-field,* International journal of aeroacoustics **2**, 95 (2003).

[36] C. Bailly and D. Juve, *Numerical solution of acoustic propagation problems using linearized euler equations,* AIAA journal **38**, 22 (2000).

[37] J. W. Delfs, M. Bauer, R. Ewert, H. A. Grogger, M. Lummer, and T. G. Lauke, *Numerical simulation of aerodynamic noise with dlr's aeroacoustic code piano,* (2008).

[38] M. J. Lighthill, *On sound generated aerodynamically i. general theory,* Proceedings of the Royal Society of London. Series A. Mathematical and Physical Sciences **211**, 564 (1952).

[39] D. Casalino, *An advanced time approach for acoustic analogy predictions,* Journal of Sound and Vibration **261**, 583 (2003).

[40] N. Curle, *The influence of solid boundaries upon aerodynamic sound,* Proceedings of the Royal Society of London. Series A. Mathematical and Physical Sciences **231**, 505 (1955).

[41] J. Ffowcs-Williams and D. L. Hawkings, *Sound generation by turbulence and surfaces in arbitrary motion,* Phil. Trans. R. Soc. Lond. A **264**, 321 (1969).

[42] F. Farassat, *Introduction to generalized functions with applications in aerodynamics and aeroacoustics,* Journal of Sound and Vibration **230**, 460 (2000).

[43] P. R. Spalart, K. V. Belyaev, M. L. Shur, M. Kh Strelets, and A. K. Travin, *On the differences in noise predictions based on solid and permeable surface ffowcs williams–hawkings integral solutions,* International Journal of Aeroacoustics **18**, 621 (2019).

[44] P. Di Francescantonio, *A new boundary integral formulation for the prediction of sound radiation,* Journal of Sound and Vibration **202**, 491 (1997).

[45] M. L. Shur, P. R. Spalart, and M. K. Strelets, *Noise prediction for increasingly complex jets. part i: Methods and tests,* International journal of aeroacoustics **4**, 213 (2005).

[46] S. Mendez, M. Shoeybi, S. Lele, and P. Moin, *On the use of the ffowcs williams-hawkings equation to predict far-field jet noise from large-eddy simulations,* International Journal of Aeroacoustics **12**, 1 (2013).

[47] M. R. Khorrami, P. A. Ravetta, D. P. Lockard, B. M. Duda, and R. Ferris, *Comparison of measured and simulated acoustic signatures for a full-scale aircraft with and without airframe noise abatement,* in *2018 AIAA/CEAS Aeroacoustics Conference* (2018) p. 2975.

[48] F. Farassat and G. P. Succi, *A review of propeller discrete frequency noise prediction technology with emphasis on two current methods for time domain calculations,* Journal of Sound and Vibration **71**, 399 (1980).

[49] K. S. Brentner, *An efficient and robust method for predicting helicopter high-speed impulsive noise,* Journal of Sound and Vibration **203**, 87 (1997).

[50] X. Li, X. Li, and C. Tam, *Construction and validation of a broadband time domain impedance boundary condition,* in *17th AIAA/CEAS Aeroacoustics Conference (32nd AIAA Aeroacoustics Conference)* (2011) p. 2870.

[51] C. Sun, F. Pérot, R. Zhang, P.-T. Lew, A. Mann, V. Gupta, D. M. Freed, I. Staroselsky, and H. Chen, *Lattice boltzmann formulation for flows with acoustic porous media,* Comptes Rendus Mécanique **343**, 533 (2015).

[52] H. Darcy, *Les fontaines publiques de la ville de Dijon: exposition et application...* (Victor Dalmont, 1856).

[53] D. Rochette and S. Clain, *Numerical simulation of darcy and forchheimer force distribution in a hbc fuse,* Transport in porous media **53**, 25 (2003).

[54] J. Bear, *Dynamics of fluids in porous media* (American Elsevier Pub. Co., 1972).

[55] D. M. Freed, *Lattice-boltzmann method for macroscopic porous media modeling,* International Journal of Modern Physics C **9**, 1491 (1998).

[56] S. P. Neuman, *Theoretical derivation of darcy's law,* Acta Mechanica **25**, 153 (1977).

[57] P. Bernicke, R. Akkermans, V. Bharadwaj, R. Ewert, J. Dierke, and L. Rossian, *Overset les of a solid and porous naca0012 trailing edge,* in *2018 AIAA/CEAS Aeroacoustics Conference* (2018) p. 3454.

[58] V. Ananthan, P. Bernicke, R. Akkermans, T. Hu, and P. Liu, *Effect of porous material on trailing edge sound sources of a lifting airfoil by zonal overset-les,* Journal of Sound and Vibration , 115386 (2020).

[59] M. A. Spaid and F. R. Phelan Jr, *Lattice boltzmann methods for modeling microscale flow in fibrous porous media,* Physics of fluids **9**, 2468 (1997).

[60] R. Zhang, C. Sun, Y. Li, R. Satti, R. Shock, J. Hoch, and H. Chen, *Lattice boltzmann approach for local reference frames,* Communications in Computational Physics **9**, 1193 (2011).

[61] A. Rubio Carpio, R. Merino Martinez, F. Avallone, D. Ragni, M. Snellen, and S. van der Zwaag, *Broadband trailing-edge noise reduction using permeable metal foams,* in *INTER-NOISE and NOISE-CON Congress and Conference Proceedings*, Vol. 255 (Institute of Noise Control Engineering, 2017) pp. 2755–2765.

[62] A. Rubio Carpio, R. M. Martínez, F. Avallone, D. Ragni, M. Snellen, and S. van der Zwaag, *Experimental characterization of the turbulent boundary layer over a porous trailing edge for noise abatement,* Journal of Sound and Vibration **443**, 537 (2019).

[63] T. F. Geyer and E. Sarradj, *Trailing edge noise of partially porous airfoils,* in *20th AIAA/CEAS Aeroacoustics Conference* (2014) p. 3039.

[64] A. Rubio Carpio, F. Avallone, and D. Ragni, *On the role of the flow permeability of metal foams on trailing edge noise reduction,* in *2018 AIAA/CEAS Aeroacoustics Conference* (2018) p. 2964.

[65] E. Baril, A. Mostafid, L.-P. Lefebvre, and M. Medraj, *Experimental demonstration of entrance/exit effects on the permeability measurements of porous materials,* Advanced Engineering Materials **10**, 889 (2008).

[66] N. Dukhan and C. Minjeur, *Minimum thickness for open-cell metal foam to behave as a porous medium,* in *40th Fluid Dynamics Conference and Exhibit* (2010) p. 4618.

[67] C. Naaktgeboren, P. Krueger, and J. Lage, *Limitations of darcy's law in light of inlet and exit pressure drops,* in *International Conference on Applications of Porous Media* (2004).

3

TRAILING-EDGE NOISE MITIGATION

Other sound than the owl's voice there was none, save the falling of a fountain into its stone basin; for, it was one of those dark nights that hold their breath by the hour together.

Charles Dickens

This chapter presents a numerical investigation on the applications of permeable trailing-edge (TE) inserts on a NACA 0018 airfoil to mitigate broadband noise emission. The inserts are made of two types of porous materials. The first one is a metal-foam that is modelled using the multi-layer porous medium approach. The second one is based on a porous cell whose geometrical details are fully resolved in the simulations. The resulting noise reduction is caused by a "communication" between turbulent boundary layers on both sides of the TE, which is subsequently referred to as the pressure-release process. This mechanism suppresses the noise source intensity near the tip of the porous insert, while also inducing out-of-phase relationship between sources that are distributed along the chord of the porous insert. The presence of the pressure release process has been linked to both the entrance length of the porous material and the TE geometry. The effects of angle-of-attack and Reynolds number are also examined. It is found that the porous inserts have a relatively minor impact on aerodynamic performance, and a mean cross-flow in the porous insert remains absent despite having the airfoil at a lifting condition. Present study also suggests that the permeability of the porous insert, rather than the surface roughness, has a stronger influence on the turbulent boundary layer characteristics.

Parts of this chapter have been published in Teruna *et al.* [1, 2, 3]

3.1. TURBULENT BOUNDARY-LAYER TRAILING-EDGE NOISE

AIRFOIL self noise arises from the interaction between an airfoil and the boundary layer developing on its surface. There are multiple self-noise generation mechanisms as summarised by Brooks *et al.* [4]:

1. *Turbulent boundary-layer trailing-edge (TBL-TE) noise*:
   TBL-TE noise is produced by the scattering of turbulent kinetic energy in the boundary layer as it flows past a sharp TE.

2. *Separation-stall noise*:
   At a large angle-of-attack, the flow on an airfoil can separate, creating a wake region with large-scale turbulence. The interaction between this wake and the TE results in the stall noise.

3. *Laminar-boundary-layer-vortex-shedding noise*:
   Narrowband/tonal noise can be generated by vortex shedding from a laminar boundary layer due to a feedback mechanism between the acoustic waves emitted at the trailing edge and the Tollmien-Schlichting instabilities in the boundary layer.

4. *Trailing-edge-bluntness noise*:
   A flow leaving a blunt trailing edge (e.g., when the incoming boundary layer thickness is comparable or smaller than the TE thickness) can lead to a quasi-periodic shedding of vortices, generating narrowband noise in the process.

5. *Tip-vortex formation noise*:
   Tip vortex is produced at the lateral edge of a wing/blade due to the pressure imbalance between its upper and lower sides. As a tip vortex forms, it may induce a local separation. Turbulence resulting from the separation produces noise when it interacts with the wing/blade tip or the TE.

TBL-TE noise mechanism has been found to define the floor noise level in both wind turbine blades [5] and aircraft high-lift devices [6, 7], since the other self-noise mechanisms can be mitigated or completely eliminated by using optimised airfoil or wing designs [8]. Thus, future noise reduction efforts would require addressing the TBL-TE noise mechanism directly. Before going into this subject, the theoretical framework describing the TBL-TE noise mechanism will be briefly discussed in the following subsection.

3.1.1. TBL-TE NOISE CHARACTERISTICS

As a turbulent boundary layer (TBL) flows past a surface, it induces an unsteady pressure field that is coupled to the turbulent velocity fluctuations. When the TBL encounters a discontinuity in the surface boundary condition, a portion of the turbulent kinetic energy is scattered into sound waves. This mechanism takes place near a geometrical discontinuity, such as at the airfoil trailing edge. Since turbulent fluctuations are stochastic while also existing over a large range of temporal and spatial scales, TBL-TE noise is broadband by nature. Nevertheless, the frequency of the peak noise intensity can

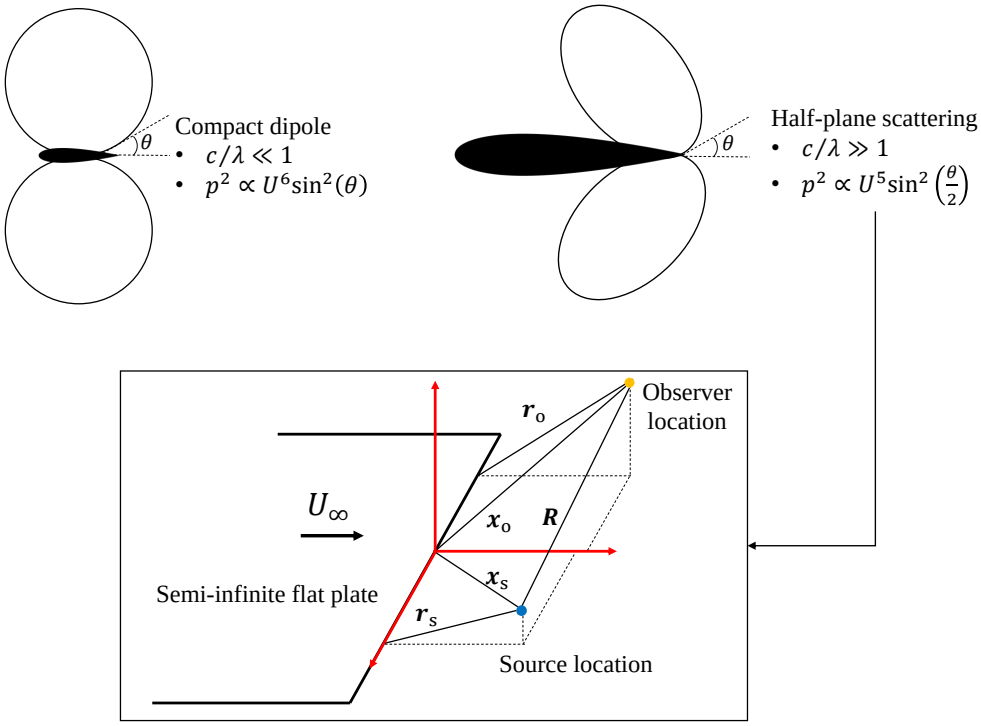

Figure 3.1: Airfoil self-noise characteristics for acoustically compact ($c/\lambda >> 1$) and non-compact cases ($c/\lambda << 1$); c is the airfoil chord. The half-plane scattering nomenclature is shown at the lower side of the figure [14].

be generally estimated based on a Strouhal number $f\delta^*/U_\infty = 0.06$ to 0.08, where δ^* is the displacement thickness [9].

The underlying physical mechanisms of TBL-TE noise have been studied extensively in the past few decades. One of the first investigations in this field was performed by Powell [10]. It was suggested that the TE noise intensity would scale with the freestream velocity, e.g., in between U_∞^4 and U_∞^5, and thus it is considered as a more efficient noise source (e.g., relative to the dipole [11] or quadrupole [12]) at low Mach numbers. Howe [13] wrote a comprehensive review of recent advancements in TBL-TE noise researches. The author suggested that the majority of the TBL-TE noise modelling approaches fall into 3 main categories: 1) those based on Lighthill's acoustic analogy [14], 2) the solutions obtained using linearised aeroacoustic equations [15, 16] and 3) *ad hoc* models that have been formulated using empirical data [17].

Williams and Hall [14] solved Lighthill's acoustic analogy for a scattering problem involving a semi-infinite flat plate. A schematic of this problem is shown in figure 3.1. The solution for the far-field acoustic pressure was obtained in the frequency-domain using a tailored Green's function for a half-plane that is suitable for a non-compact chord (i.e., $\lambda/c \ll 1$, where c is a characteristic length such as airfoil chord). The result implied that turbulent eddies (quadrupoles) that are located in proximity of the flat-plate edge

scatter noise more efficiently than those that are further away. The authors also predicted a scattering directivity resembling a cardioid shape towards the upstream direction. This is in contrast to the sound directivity for a compact body ($\lambda/c \gg 1$) that has a dipole-like shape. The maximum far-field noise intensity can be expressed as,

$$I \sim \rho_\infty U_\infty^3 M_\infty^2 \left(\frac{L}{|\boldsymbol{R}|}\right)^2 \tag{3.1}$$

where L is the correlation length of the turbulent eddies and $\boldsymbol{R}$ is the observer distance from the source. The Mach number exponent in equation 3.1 is smaller compared to M_∞^3 for an acoustically compact plane [11] and M_∞^5 when the plane is absent [12]. Thus, the edge scattering phenomenon can be considered to be a very efficient noise generation mechanism at low Mach number compared to that of free turbulence. The findings of Williams and Hall [14] have highlighted several possible noise mitigation approaches, such as by realising a smaller turbulence scale (reducing L) or by bringing the turbulent eddies further away from the wall [18] (increasing $\boldsymbol{r}_s$). As a matter of fact, halving L would immediately lead to a noise reduction of 3 dB (i.e., assuming that for a half-plane edge with a span b, there exists b/L uncorrelated eddies), while the doubling of $\boldsymbol{r}_s$ would achieve a noise reduction in between 3 dB to 9 dB depending on the quadrupole orientation.

As mentioned in chapter 2, the usage of a TE noise model based on Lighthill's acoustic analogy is impractical since the Lighthill's stress tensor in the source region has to be defined. Amiet [16] took a different approach using the diffraction theory. Consider a flow field containing both quadrupole (unsteady velocity gradients in the turbulent boundary layer) and dipole (surface pressure fluctuations) sources as shown in figure 3.2. Note that the origin of the coordinate system ($x_1 = x_2 = x_3 = 0$) is at the trailing edge midspan. Amiet reasoned that the scattered pressure field would be equivalent to a solution that cancels out the dipole distribution downstream of the flat plate. Initially, the surface pressure field is modelled as a harmonic wave with an amplitude p_0 and angular frequency ω, travelling at a convection speed U_c along the streamwise direction x_1.

$$p(x_1, \omega, U_c) = p_0 e^{j\omega(t - x_1/U_c) - jk_3 x_3} = p_0 e^{-j(k_1 x_1 - k_3 x_3) + j\omega t} \tag{3.2}$$

where k_1 and k_3 are the streamwise and spanwise wavenumbers respectively. Schwarzschild's technique has been employed to obtain the surface pressure jump description along the plate. The formulation in the high-frequency limit for a pressure wave parallel to the trailing edge is given as follows,

$$\begin{aligned} \Delta p(x_1, \omega, U_c) &= p_0 \overbrace{\left[(1+j)E^*\left(-\frac{x_1}{c/2}\left[(1+M_\infty)\mu_a + k_1\right]\right) - 1\right]}^{g(x_1,\omega,U_c)} e^{-jk_1 x_1} \\ \mu_a &= \frac{M_\infty \omega}{U_c(1 - M_\infty^2)} \end{aligned} \tag{3.3}$$

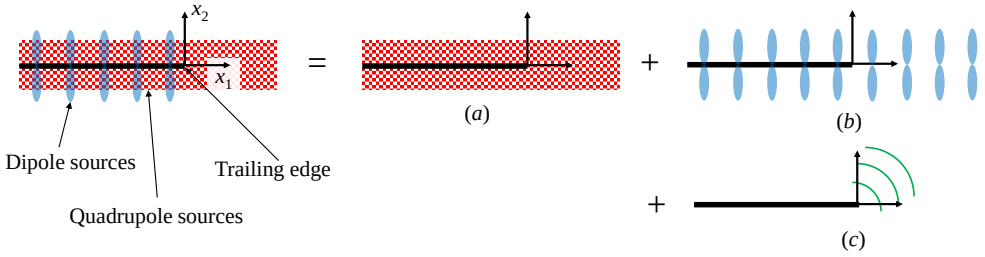

Figure 3.2: The distributions of dipole and quadrupole sources representing Amiet's solution to the TE noise problem. (*a*) and (*b*) show the quadrupole and dipole distributions that extend in both upstream and downstream directions, and (*c*) is the scattered acoustic pressure.

where $g(x_1, \omega, U_c)$ is Amiet's high-frequency airfoil response function, c is the flat-plate chord length, and $E^*(x)$ is a combination of Fresnel's integrals. Suppose that the condition $M_\infty k_1 b \gg 1$ (e.g., high-frequency limit where the surface pressure wave is compact relative to the flat-plate span b) is applicable and the observer is aligned with the trailing-edge midspan, the power spectral density of sound pressure p'^2 is expressed as,

$$\begin{aligned} p'^2(x_1, x_2, \omega) &= b\left(\frac{\omega c x_2}{4\pi a_\infty s^2}\right)^2 \int_0^\infty S_{pp}(\omega, x_3)\, \mathrm{d}x_3\, |\mathfrak{L}|^2 \\ s^2 &= \left(x_1^2 + (1 - M_\infty^2)^2 x_3^2\right) \\ \mathfrak{L} &= \frac{2}{c}\int_{-c}^{0} g(x_1, \omega, U_c) e^{-j\mu_a \zeta (M_\infty - x_1/s)\, \mathrm{d}\zeta} \end{aligned} \tag{3.4}$$

where $S_{pp}(\omega, x_3)$ is the spanwise cross-spectrum of surface pressure fluctuations. Note that equation 3.4 only contains the scattering contribution from one side of the flat plate. For an airfoil where turbulent boundary layers develop on both of its sides, the pressure jump in equation 3.3 will be doubled, and a factor of 4 needs to be added into equation 3.4. Assuming that the turbulence distribution in the boundary layer is statistically homogeneous, the integral of $S_{pp}(\omega, x_3)$ in the spanwise direction is equivalent to [19],

$$\int_0^\infty S_{pp}(\omega, x_3)\, \mathrm{d}x_3 = S_{pp}(\omega, 0)\, l_3(\omega) \tag{3.5}$$

where $l_3(\omega)$ is the spanwise length scale of the surface pressure fluctuations. Equation 3.4 is subsequently known as Amiet's TE noise model and it is still widely used for TBL-TE noise prediction. In essence, Amiet's model relates the statistics of surface pressure fluctuations near the TE to the far-field noise spectrum. Amiet's model was later extended to include the effect of leading-edge (LE) backscattering by Roger and Moreau [20], which becomes relevant when the distance between the LE and TE (i.e., the chord length) can no longer be considered non-compact relative to the acoustic wavelength.

TBL-TE noise mechanism has also been investigated experimentally, with some studies aimed at characterising the TE scattering phenomenon. Yu and Tam [17] were

among the first in this subject, where they studied a flat plate with sharp TE mounted at the outlet of a rectangular nozzle. Then, correlation analyses were performed between the data recorded by far-field microphones, flushed microphones at the flat plate surface, and a hotwire probe immersed in the boundary layer. The authors confirmed the far-field noise can be attributed to the interaction between large scale turbulence in the wall-jet shear layer and the TE. Additionally, the sound field at the upper side of the wall was found to be in exact phase opposition with respect to the lower one.

A few years later, Brooks and Hodgson [21] performed an experiment on a two-dimensional wing to analyse the scattered pressure field. For this purpose, they used miniature pressure transducers that could be installed in the vicinity of the airfoil TE. Their analyses confirmed several underlying assumptions in many analytical models. For instance, the turbulence in boundary layer was not significantly altered as it flowed past the TE, and turbulent fluctuations on either the suction or pressure sides of the airfoil were found to be statistically independent. The unsteady surface pressure field measured near the TE was found to contain both the perturbations convected by the turbulent eddy (i.e., incident pressure field) and the scattered pressure field from the TE, such that the difference in pressure fluctuations coming from both sides of the airfoil is equalised at the TE. Therefore, the scattering phenomenon provides the necessary adjustments to the pressure fields upstream and downstream of the TE without affecting the turbulent (vortical) structures in a substantial manner. The findings of Brooks and Hodgson [21] were in agreement with the evanescent wave theory of Chase [15] and Chandiramani [22], which later served as the basis for the TE noise model of Amiet [16].

3.1.2. TBL-TE NOISE MITIGATION APPROACHES

Considering that TBL-TE noise is relatively challenging to suppress [23], some scientists and engineers looked at the nature for inspirations. It has been widely known that owls are gifted with the ability to fly in silence compared to other birds. Graham [24], Lilley [25] and more recently Wagner *et al.* [26], looked into unique features of owls' wings that could be linked to the low-noise flight capability, which include: 1) fringe pattern along the TE, and 2) velvet-like canopy that covers the majority of the wing area. The fringed TE of the owl's wing was found by Lilley [25] to produce up to 7 dB of noise reduction when comparing certain owl species to other birds flying with similar speed.

Later, Jaworski and Peake [28] demonstrated that a poro-elastic flat plate could realise a weaker noise scattering process compared to a solid and rigid one, and they suggested that the permeable and elastic constructions of the owl's wings were indeed useful for enabling silent flight. More recently, Klän *et al.* [29] and Winzen *et al.* [30] attempted to reproduce the effects of velvety cover of owl's wings using artificial materials on an airfoil that resembles that of an owl's. The velvety cover was observed to prevent flow separation near the airfoil mid-chord, improving the aerodynamic performance. This would allow owls to fly slower and remain silent as they approach their preys. In the investigation of Clark *et al.* [31], the velvety canopy on the owl's wings has been identified to suppress the intensity of surface pressure fluctuations, which also helped reducing the noise level.

The features of owl's wings have inspired several passive TE noise mitigation strategies, such as serrations and permeable treatments (see figure 3.3). Serrations refer to the spanwise modification of the TE planform and they are often applied as a

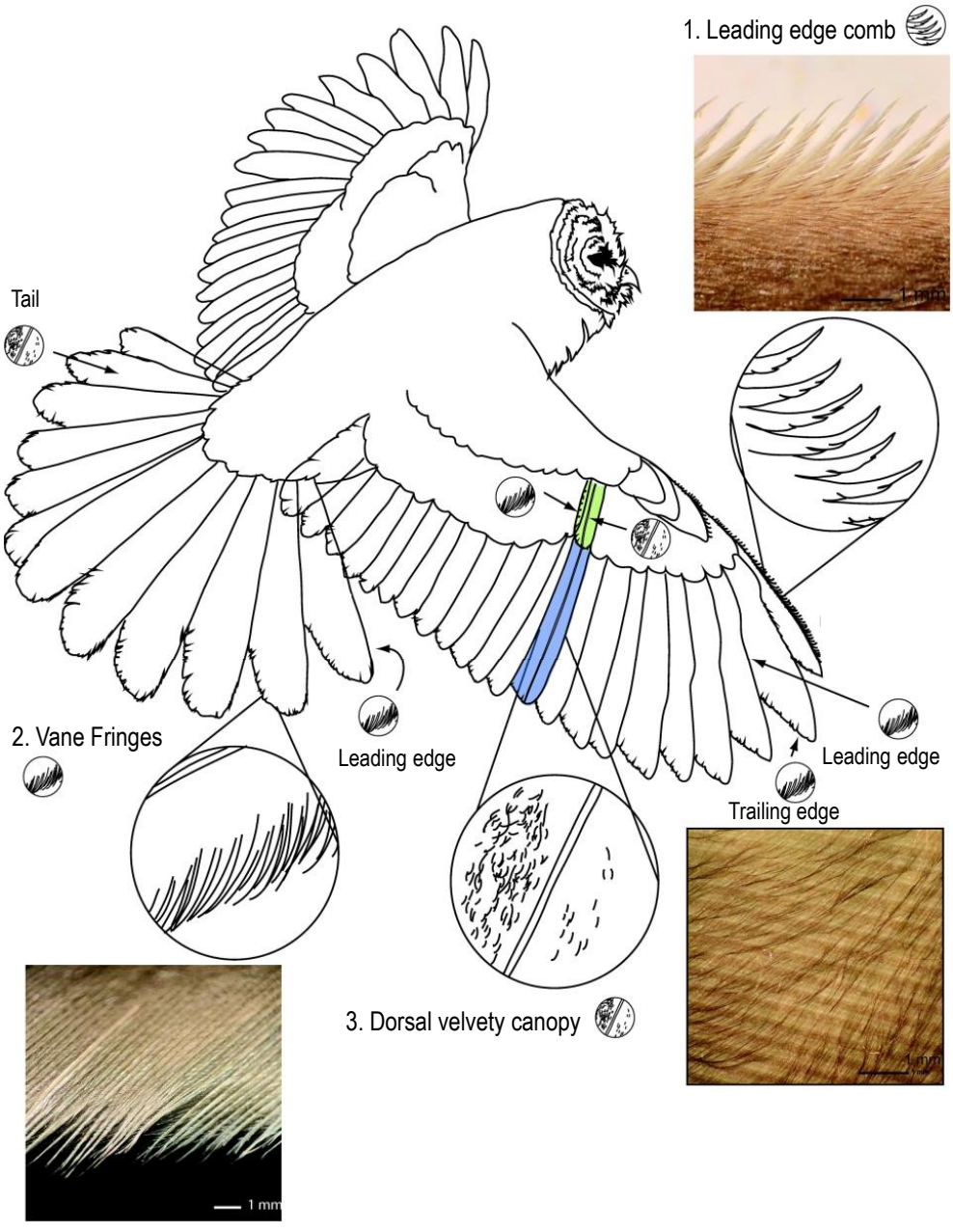

Figure 3.3: Typical features of owls' wings that are associated with the silent flight capability [24, 25]. This figure has been reproduced from Clark *et al.* [27].

downstream extension of the airfoil chord (i.e., as TE add-on) [23]. TE serrations can take different shapes, such as sawtooth [32] or iron-like [33]. In various studies, the applications of TE serrations have been found to produce substantial noise reduction, upwards of 5 dB [23, 33–37]. Differently, permeable treatments are usually employed as inserts that replace the aft section of the airfoils. Permeable (porous) inserts enable flow transpiration across their surfaces and internals, which can be considered as an intermediary condition between a fully-solid surface and free fluid. As such, a porous TE insert can be used to realise a smoother transition for the turbulent boundary layer as it leaves the airfoil, reducing the acoustic scattering efficiency in the process.

One of the earliest study about the permeable insert application was reported by Hayden [38] for a case of jet-flap interaction noise. By installing a porous flap edge, a noise reduction of up to 10 dB was observed for a relatively large frequency range. Subsequent investigations were aimed at identifying the role of different porous material parameters, such as permeability, porosity, and form coefficient [39], in affecting the noise reduction level. In general, porous materials with higher permeability were found to produce larger noise reduction [40–42]. However, a fully porous airfoil would be undesirable since it could incur a substantial aerodynamic penalty [43]. As suggested by Geyer and Sarradj [44], limiting the extent of the porosity treatment at the aft section of the airfoil can be considered as an acceptable trade-off between noise attenuation and aerodynamic degradation. Nevertheless, the relationship between the porous TE extent and the noise reduction level remains as an open question.

The problem of noise scattering by a permeable edge has also been examined analytically. Williams [45] determined that in the limit of low frequencies (i.e., the pore diameter is taken to be much smaller compared to the acoustic wavelengths), a perforated plate with high porosity would produce predominantly dipole-type sources whereas monopoles would become more relevant for the low-porosity case. Following this, he also predicted that the intensity of the scattered sound to be less if the plate porosity were increased. The concept of a porous edge as an extension to a flat plate was considered by Howe [46]. It was found that acoustic scattering takes place at multiple locations where the porosity value changes, e.g., at the location where the solid segment ends and the porous extension begins, as well as at the downstream end of the porous edge. The same phenomenon has been confirmed in more recent investigations [47–49]. Additionally, Howe suggested that implementing chordwise-varying porosity could further improve the noise attenuation level. Jaworski and Peake [28] employed the Wiener-Hopf technique to predict the acoustic scattering at a semi-infinite poro-elastic plate. They found that the power of the scattered pressure field scales with U_∞^6, which indicates a less efficient scattering compared to that of a solid edge (U_∞^5 [14]) at a low Mach number. Moreover, they predicted that the noise reduction of the porous plate was concentrated mainly in the low frequency region. This study was later extended by Cavalieri *et al.* [50] to include the effect of a finite chord length, in which the porous plate was found to alter the noise directivity into a dipole-like shape. This is different from the cardioid-like shape that is typical for a solid edge.

In addition to analytical studies, experiments have been carried out to better understand the noise mitigation mechanisms of porous inserts with finite thickness. Herr *et al.* [41] suggested that the interaction between pressure fluctuations at the

pressure and suction sides of the porous TE is responsible for promoting noise attenuation, which was referred to as the pressure release process. The authors arrived at this conclusion after observing that a porous insert, whose one side had been covered with tape, completely lost its noise reduction benefit. Rubio Carpio *et al.* [51] recreated a similar study, where a layer of adhesive was applied along the symmetry plane of a metal-foam insert in order to preserve the surface roughness effects. Whereas the fully-permeable insert produced up to 10 dB of noise attenuation in the low frequency range, the non-permeable metal-foam insert emitted similar noise level as the fully-solid one, in addition to a slight noise increase at high frequencies. The authors confirmed that the high-frequency excess noise from metal-foam inserts is associated with the surface roughness characteristic of the permeable material. More recently [49], they also observed that velocity fluctuations in the turbulent boundary layers on both sides of the porous TE remained correlated when the adhesive layer was absent, evidencing the role of the pressure release process in promoting noise reduction.

3.1.3. NUMERICAL INVESTIGATIONS OF POROUS TRAILING EDGE APPLICATIONS

The usage of numerical methods have allowed researchers to examine the aeroacoustics of porous media more closely. Delfs *et al.* [48] employed a hybrid-CAA method where the flow field is resolved using RANS combined with a synthetic turbulence generator, while the far-field noise is predicted using linearised Euler equations. They studied a NACA 0012 airfoil whose aft 11 % of the chord has been modified with streamwise slits. Two scenarios were considered: 1) an acoustic (i.e., non-vortical), dipole-like, source was added at the TE location, and 2) a single vortex was introduced upstream of the slitted TE. In the first scenario, the baseline TE diffracted the near-field perturbations induced by the dipole, resulting in a cardioid sound pattern towards the upstream direction. For the airfoil with slitted TE, the diffracted sound field could also pass through the slits. Since the sound waves at the upper and lower sides of the airfoil were in opposite phase, they partially annihilated each other in the near-field. As a result, the noise reduction level was more prominent in the upstream direction, and the sound radiation pattern became more similar to that of a dipole. In the second scenario, it was observed that a sound pulse was generated at the moment when the vortex went past the regular TE. When the slitted TE was installed, there were two pulses with smaller amplitudes, indicating a weaker noise intensity. The first pulse was generated at the upstream end of the slits, and the second one at the downstream end. Unlike in the first scenario, the noise reduction in the second one was relatively uniform in all observer directions. The authors also considered adding a splitter plate along the center of the slitted TE to prevent flow transpiration across the slits; this treatment lead to a smaller noise reduction level. The findings of this study are in line with the experiment of Rubio Carpio *et al.* [51] and Herr *et al.* [41] that have been discussed in the previous subsection.

While a numerical simulation could provide flow details inside and surrounding porous media, it could become very expensive for resolving micro-structures whose characteristic lengths are much smaller compared to the rest of the body [52]. Hence some studies employ a volume-averaging approach to model the overall effect of the interaction between a permeating flow and a porous medium [53]. This technique has

been widely used in recent years [54–57]. For instance, Ananthan *et al.* [58] investigated the noise mitigation of a porous TE on a DLR F16 airfoil. The porous insert was modelled as an equivalent fluid region, where a modified volume-averaged Navier-Stokes equations were solved. The flow resistance caused by the porous insert was taken into account using the Darcy's law [39]. The porous TE was observed to decrease both the spanwise coherence of surface pressure fluctuations and the convection velocity, which the authors linked to noise attenuation.

Beyond the aforementioned investigations, there are still several scientific gaps to be addressed. For instance, the role of permeability in promoting TBL-TE noise attenuation has not been fully elucidated. Herr *et al.* [41] and Rubio Carpio *et al.* [49] have suggested that a pressure release process across the porous TE insert plays a major role in promoting noise reduction, but the relationship between this mechanism and the porous material properties (e.g., permeability, porous insert geometry, etc.) was not elaborated further. Within this scope, a numerical study on the application of a porous TE insert has been carried out and presented in the subsequent sections.

The rest of this section will be arranged as follows: A description of the simulation setup is presented in 3.2, followed by the verification and validation of the simulation results in 3.3. Discussions on the simulation results are reported starting from 3.4. The chapter is concluded with a summary in 3.8.

3.2. SIMULATION SETUP

The present study employs a simulation setup that is based on the past experiments of Rubio Carpio *et al.* [51]. The simulation domain contains a NACA 0018 airfoil with a chord length $c = 200\,\text{mm}$. Several TE configurations have been considered as shown in figure 3.4. Aside from the solid (baseline) TE, there are porous inserts that replace the last 20 % of the airfoil chord. These inserts are made of two different types of porous materials. The first one is a metal (Ni-Cr-Al) foam manufactured by *Alantum* while the other is a porous cell that is based on a unit cell resembling the atomic arrangement of a diamond lattice. Their properties are reported in tables 3.1 and 3.2. Note that the permeability and form coefficient listed in table 3.1 are asymptotic values, i.e., they are valid for a sample whose thickness is above a critical value [59].

The metal foam has an internal topology that is geometrically stochastic, isotropic, and homogeneous. Mean pore diameter d_p and porosity ϕ have been provided by the manufacturer. Permeability K and form coefficient C are obtained using the pressure drop test [42] as previously discussed in section 2.3. As shown in figure 3.4 (*a*), the metal-foam insert is modelled as a combination of two equivalent fluid regions; the outer and inner volumes are specified as the APM and PM regions respectively. The APM layer follows the surface contour of the trailing edge with a constant thickness of 1 mm, except for the last $0.005c$ of the airfoil where the airfoil thickness is less than 1 mm. The PM region lies underneath the APM layer. As such, the entrance length of the metal-foam is fully contained within the APM region. For the blocked TE, a solid core whose thickness equals to 12 % of the local airfoil thickness has been applied along the symmetry plane of the airfoil (see the inset in figure 3.4). The solid core is intended to prevent any flow connection through the porous medium between both sides of the trailing edge [60].

Differently, the porous cell is constructed using a network of cylindrical struts whose

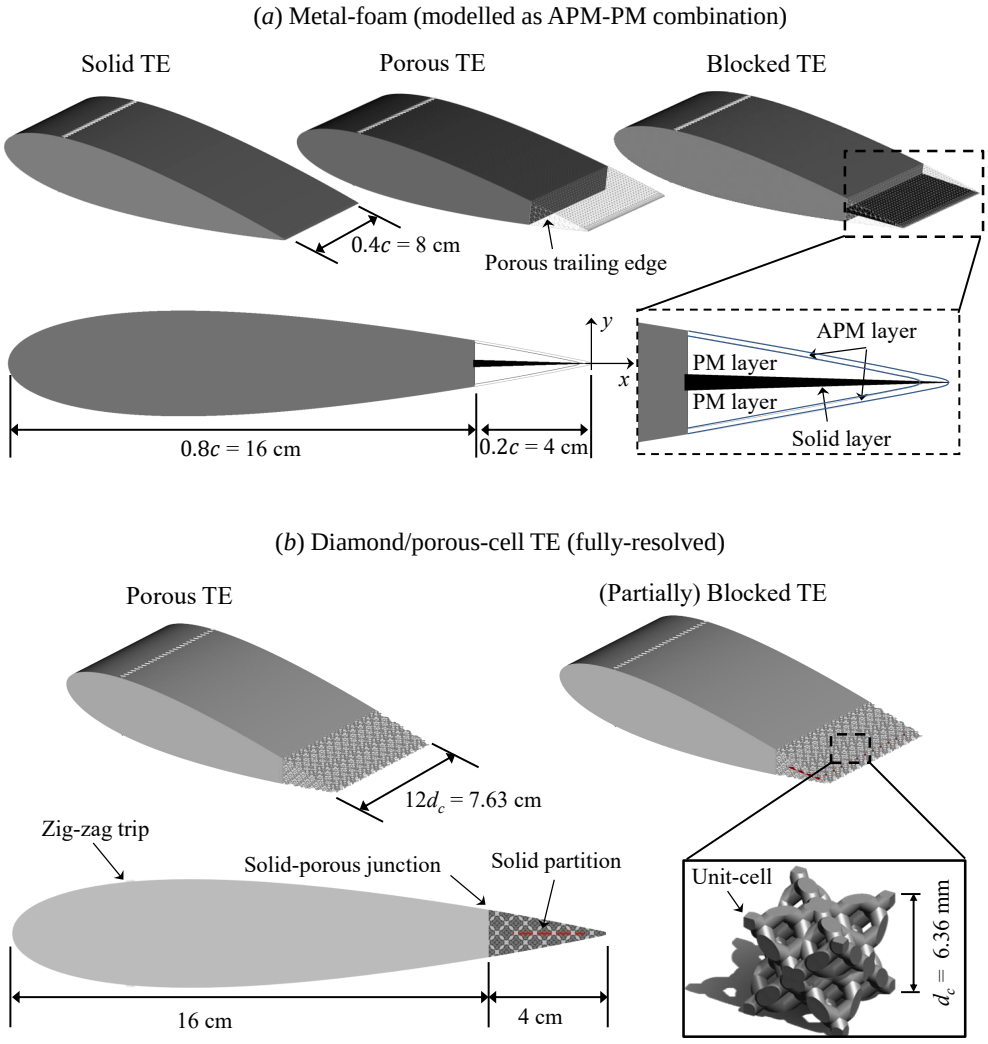

Figure 3.4: The NACA 0018 with three different trailing edge (TE) configurations. The side view of the blocked TE is shown at the bottom left, where an inset shows the internal arrangement of the trailing-edge region of the blocked TE.

Type	d_p (µm)	ϕ	K (m^2)	C (m^{-1})
Metal foam	800	0.917	2.7×10^{-9}	2613
Porous cell	1200	0.615	2.38×10^{-8}	2923

Table 3.1: The porous material properties as measured empirically [42, 61].

Type	Unit-cell size (D)	Mean strut thickness	Mean strut length
Metal foam	-	0.05	0.33
Porous cell	6.36	1.05	2.6

Table 3.2: The geometrical properties of the porous materials. Quantities are given in mm.

dimensions are reported in table 3.2. The unit-cell of the porous cell has a cubic outline with a dimension of $D = 6.36\,\text{mm}$, which is to be distinguished from the mean pore diameter $d_p = 1.2\,\text{mm}$. The surface outline of the porous insert follows the solid one. This implies that some unit-cells that are located near the surface are partially cut, and the resulting surface pore diameter varies between 0.45 mm and 5.3 mm. The geometrical details of the porous-cell insert will be resolved in the simulation for three reasons. Firstly, this simulation is intended for verifying that by using a physical porous body, TE noise reduction can be obtained. Moreover, it would be possible to investigate the influence of surface roughness on high-frequency excess noise [49] since the surface details of the porous insert are retained. Lastly, the porous-cell insert also allows for examining the flow field inside the porous medium without the uncertainty introduced by the porous medium model. Aside from the fully-permeable (regular) porous-cell insert, a partially-blocked variant has been designed with the solid partition spanning in between 20 % and 80 % of the porous TE extent (i.e., the last 16 % to 4 % of the airfoil chord). Hence it is to be distinguished from the fully-blocked metal-foam insert. The partially-blocked insert will be used for identifying the role of different segments of the porous insert in promoting noise reduction.

In the simulation, the airfoil span for the solid TE case equals to one-fifth of that in the experiment [49], i.e., $b = 0.4c = 8\,\text{cm}$. The porous and blocked TE inserts based on the metal foam have the same span. However, for those equipped with the porous-cell inserts, the airfoil span is slightly reduced to $76.32\,\text{mm} = 12D$ to ensure spanwise periodicity of the unit-cell. As a baseline setting, the airfoil is installed at zero incidence relative to a freestream with a velocity $U_\infty = 20\,\text{m/s}$, which corresponds to a chord-based Reynolds number of $Re_c = 2.7 \times 10^5$ and a freestream Mach number of $M_\infty = 0.06$. The airfoil with metal-foam insert is also studied under a higher freestream velocity of $U_\infty = 40\,\text{m/s}$ and a positive incidence of angle-of-attack (AoA) of 7.8°. These settings have been chosen to realise a high-lift condition without causing flow separation near the trailing-edge region. Nevertheless, unless explicitly mentioned, the baseline setting should be assumed. The complete list of airfoil configurations that will be presented in the upcoming sections is reported in table 3.3.

A sketch of the computational domain is shown in figure 3.5. The origin of the coordinate system is defined at the mid-span of the trailing edge with the x axis being aligned with the airfoil chord, and the z axis with the airfoil span. The y axis is

Table 3.3: A list of TE insert configurations and flow settings.

Type	Modelling approach	U_∞	Angle-of-attack (AoA)
Metal-foam	Modelled (APM-PM)	20 m/s	0°
Metal-foam	Modelled (APM-PM)	20 m/s, 40 m/s	7.8°
Porous cell	Fully resolved	20 m/s	0°

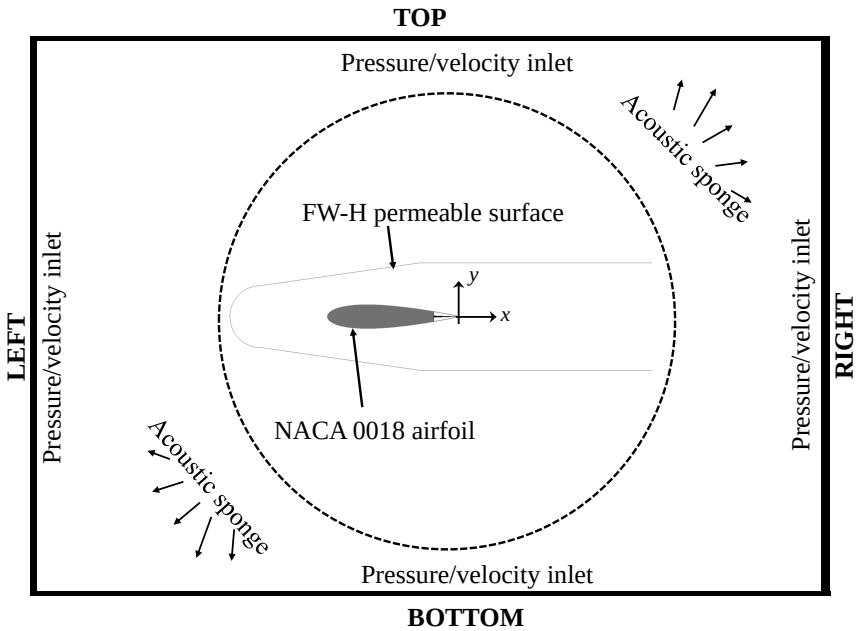

Figure 3.5: A sketch of the computational domain. Note that domain boundaries are not drawn to scale.

perpendicular to both x and z axes. The x, y, and z axes will also be referred to as streamwise, vertical, and spanwise directions respectively. Hence, the airfoil leading edge is located at $x/c = -1$, and the trailing edge at $x/c = 0$. Additionally for porous and blocked TE cases, the upstream onset of the permeable surface is referred to as the "solid-porous junction" ($x/c = -0.2$), while the downstream edge as the "TE tip" for brevity. Zig-zag strips [62] have been installed at $x/c = -0.8$ on both sides of the airfoil to force boundary-layer transition at the given Reynolds numbers. The zig-zag trip height is $t_{\text{trip}} = 0.003c = 0.6\,\text{mm}$, while the amplitude is $c_{\text{trip}} = 0.015c = 3\,\text{mm}$ and the wavelength is $\lambda_{\text{trip}} = 0.015c = 3\,\text{mm}$. The tripping elements are the same as those used in a similar study [33].

Since noise prediction will be obtained using the FW-H analogy, a control surface has been defined to enclose the airfoil at a distance where the voxel resolution is coarser by two levels than the finest one. The permeable surface is extended by $2c$ downstream of the TE with the downstream face removed to avoid unwanted perturbations from the turbulent airfoil wake (i.e., pseudo-noise associated to the suppression of the volume integral in the FW-H formulation) [63, 64].

The computational domain is a rectangular box that is $100c$ long in both x and y directions, while its length in the z direction equals b. To prevent acoustic field contamination due to reflection from the domain boundaries, an acoustic sponge region is applied starting from a radius of $36c$ from the origin. Periodic boundary conditions are applied at the lateral faces that are perpendicular to the z direction. The other boundaries are labelled "LEFT", "BOTTOM", "TOP", and "RIGHT" in the figure, where free-stream velocity and pressure are imposed for the first three and only free-stream pressure for the latter[1]. The simulation domain contains a total of 10 grid resolution regions with a refinement factor of 2. The grid in the finest refinement region has a dimension of $3.9 \times 10^{-4}c$, and this region completely envelopes the airfoil surface and the porous insert. For the metal-foam insert, this guarantees that there are approximately 10 grid points across the APM layer [65] in the y direction. Meanwhile for the porous cell, the diameter of each strut is approximately equal to 13 grid points. For the solid TE case, the finest grid dimension corresponds to the first wall-adjacent cell height of $y^+ = 3$ at $x/c = -0.01$. The discretization procedure produces a total of 218×10^6 voxels for the solid TE case. For the metal-foam and porous-cell inserts, the voxel count becomes 292×10^6 and 293×10^6 respectively. For each case, a simulation run is carried out for 20 flow passes, excluding the initial transient. The simulation cost for a simulation with the metal-foam TE (i.e., using porous medium models) is 27,000 CPU hours, whereas for the fully-resolved porous-cell insert, it amounts to 57,000 CPU hours.

3.3. VERIFICATION AND VALIDATION

3.3.1. GRID INDEPENDENCE STUDY

In this subsection, the sensitivity of the numerical solution to the grid resolution will be assessed. For brevity, the metal-foam insert is referred to as MF800 TE, and the porous cell one as DMND TE. Furthermore, only the results for zero angle-of-attack and for $U_\infty =$

[1] Despite the naming scheme, PowerFLOW allows some inlets to behave as fluid outlet depending on the solution.

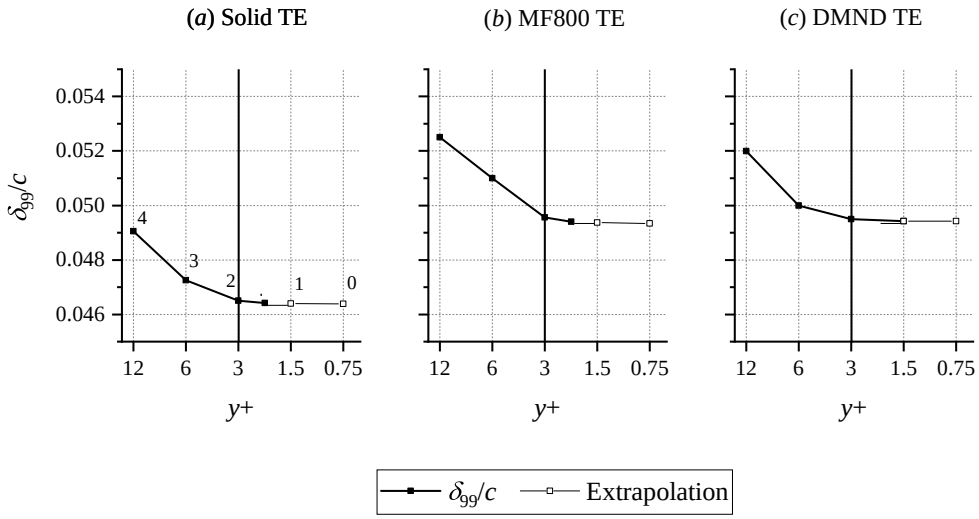

Figure 3.6: The comparison of boundary layer thickness at $x/c = -0.002$ for different grid resolutions. The Richardson extrapolation of the boundary layer thickness is plotted as empty square. The thick line at $y^+ = 3$ denotes the adopted grid resolution for the rest of the chapter. The corresponding resolution levels that are considered for the grid convergence index (GCI) studies are numbered next to the data point. MF800 - metal foam; DMND - porous cell.

20 m/s will be discussed here.

A grid independence study is performed using 4 resolution levels that correspond to y^+ values of the first wall-adjacent voxel height: coarse ($y^+ = 12$), medium ($y^+ = 6$), fine ($y^+ = 3$), and very-fine ($y^+ = 2.1$ for solid TE and MF800 TE, and $y^+ = 1.5$ for DMND TE). Note that these reference y^+ values are sampled at $x/c = -0.01$ for the solid TE case; y^+ values for both MF800 and DMND TE cases are slightly lower despite the same grid resolution is applied in both cases. At each resolution level, the grid refinement is applied uniformly across the simulation domain. For the very-fine setting, however, the DMND TE case is discretised using a higher grid resolution than the solid TE one in order to maintain spanwise periodicity of the porous-cell insert.

Figure 3.6 illustrates the convergence trend of the boundary layer thickness δ_{99} near the TE ($x/c = -0.002$). δ_{99} is defined as the distance from the wall where the mean wall-parallel velocity is 99 % of the boundary-layer edge velocity U_e. U_e is the mean velocity in the boundary layer where the integral of the spanwise vorticity along the wall-normal direction (i.e., $\int \omega_z \mathrm{d}y$) becomes asymptotic [66]. The figure also shows the Richardson extrapolation values as empty square markers up to $y^+ = 0.75$ using the refinement ratio $M = 2$ and the order of convergence $N = 3$. The convergence trend of the δ_{99} is evaluated using the Grid Convergence Index (GCI) [67]. The GCI allows for estimating the deviation, in percentage, of the numerical solution at a given grid resolution setting from that of an asymptotic solution. For the fine grid resolution ($y^+ = 3$), the solid TE has $\mathrm{GCI}_{\mathrm{medium,fine}} = 0.288\,\%$ and $\mathrm{GCI}_{\mathrm{fine,very\text{-}fine}} = 0.0385\,\%$; these are 0.519 % and 0.0687 % respectively for MF800 TE, and 0.183 % and 0.0258 % for the DMND TE. Moreover, the GCI ratio is also computed as in equation (3.6), after which GCI ratios

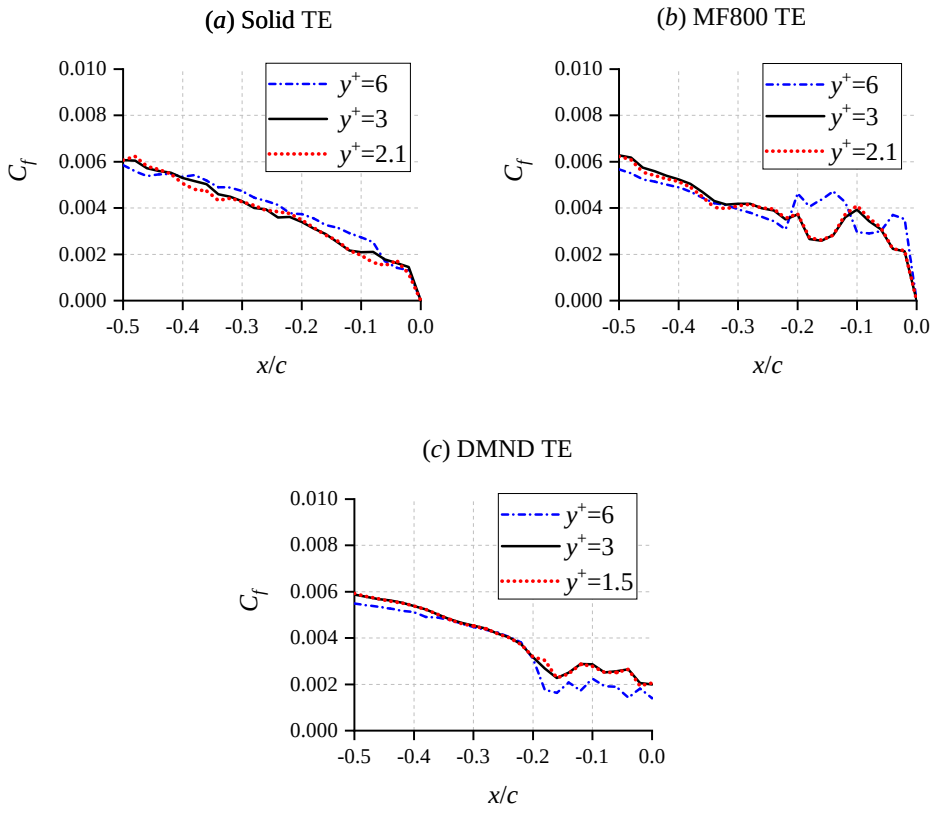

Figure 3.7: The comparison of mean wall-friction coefficient along the airfoil midspan ($-0.5 < x/c < 0$) for the different grid resolutions.

of 0.935, 0.944, and 0.875 are obtained for solid, MF800 TE, and DMND TE cases respectively. Since the GCI values next to the fine grid resolution are relatively small, and the corresponding GCI ratios are close to unity, it can be concluded that the numerical results obtained using the fine grid resolution is already within the asymptotic range of convergence [67].

$$\mathrm{GCI}_{\mathrm{ratio}}|_{\mathrm{fine,very\text{-}fine}} = \frac{\mathrm{GCI}_{\mathrm{fine,very\text{-}fine}}}{M^N \mathrm{GCI}_{\mathrm{medium,fine}}} \tag{3.6}$$

Aside from the boundary-layer thickness, the mean wall-friction coefficient ($C_f = \tau_w / q_\infty$ where τ_w is wall shear stress and $q_\infty = 0.5\rho_\infty U_\infty^2$ is the freestream dynamic pressure) is also used for evaluating grid convergence, since this quantity depends on the velocity gradient next to the wall. The C_f distributions for the aforementioned grid resolution levels are illustrated in figure 3.7. Note that the C_f distribution for the DMND TE case contains interpolated data points where open pores are located. For any given TE type, the C_f variations are larger between $y^+ = 6$ (medium) and $y^+ = 3$ (fine) results. This

	δ_{99} (mm)	δ^* (mm)	θ^* (mm)	H
LBM-VLES, Present, fine grid ($y^+ = 3$)	9.31	3.37	1.60	2.11
Experiment, Rubio Carpio *et al.* [51]	9.30	3.52	1.59	2.21
Experiment, León *et al.* [37]	9.40	2.10	1.30	1.62
XFOIL	–	2.30	1.20	1.92

Table 3.4: Comparison of boundary-layer properties on the solid TE ($x/c = -0.02$) against previous experimental and numerical studies.

is particularly noticeable on the permeable insert itself (i.e., $-0.2 < x/c < 0$). However, the C_f distributions for the fine and very-fine cases are almost identical when compared. Thus, it is possible to conclude that a voxel resolution corresponding to $y^+ = 3$ is sufficient, and subsequently, this resolution level is employed for the rest of this manuscript. In the following, the simulation results for each type of porous inserts will be validated in separate subsections.

3.3.2. VALIDATION - METAL-FOAM INSERT

Integral boundary layer parameters on the solid TE ($x/c = -0.02$) from the simulation are compared with those from the experiments [37, 51] in table 3.4. The parameters chosen include the boundary layer thickness δ_{99}, displacement thickness δ^*, momentum thickness θ^*, and the shape factor H. While the results of the current simulations are comparable to the experiments, there are small discrepancies which might have been attributed to the different tripping elements that are applied in the experiment (carborundum particles) and in the simulation (zig-zag trip). Similar agreement has also been found for the mean and turbulent velocity profiles as shown in figure 3.8. On a closer inspection, the mean velocity deficit caused by the permeability of the porous TE is slightly underpredicted. This is conjectured to be due to the neglected surface roughness since the discrepancy is more prominent near the porous wall. Nevertheless, the turbulent velocity fluctuation trends are still captured by the numerical results, suggesting that the zig-zag tripping elements, combined with the two-layer PM-APM approach, are capable to reproduce similar boundary layer characteristics as in the experiments.

Far-field noise prediction has been obtained by employing both the surface and permeable formulations of the FW-H analogy. Subsequently, Fourier analyses are performed using a periodogram method [68] with Hanning window and 50 % overlap. Then, the resulting spectra are converted into third octave bands. Far-field sound is computed at $x = 0, y = 7.4c, z = 0$, where the y coordinate corresponds to the distance of the microphone array from the trailing edge in the experiment [51]. The noise spectra is expressed in term of sound pressure level SPL = $10\log(p'^2(f)/p_{\text{ref}}^2)$, where $p'^2(f)$ is the power spectra of the acoustic pressure and p_{ref} is a reference pressure of 20 µPa. The raw spectra SPL_{raw} are scaled at a reference observer distance $D_o = 1$ m and a reference span $b = 1$ m. The scaling procedure is given in equation 3.7 [33, 69].

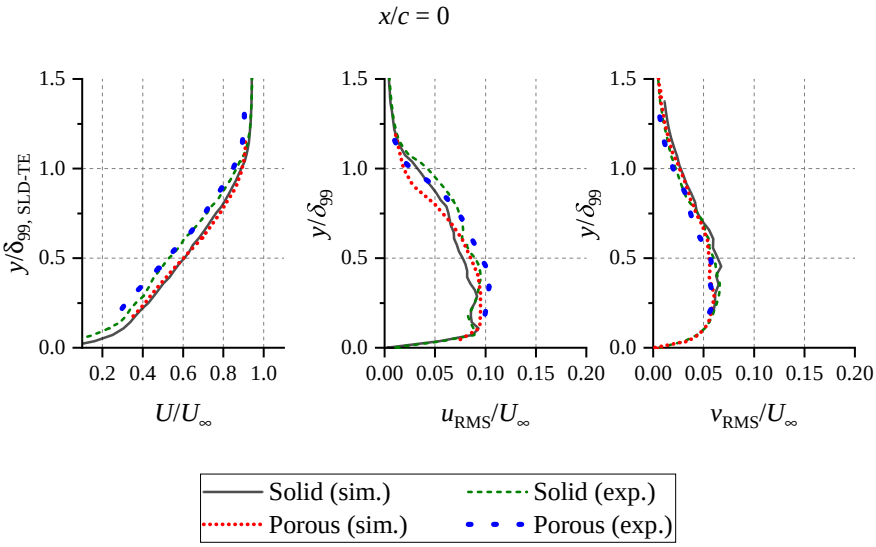

Figure 3.8: (Metal foam) Profiles of the time-averaged (U) and the root-mean-square of the wall-parallel (u_{RMS}) and of the wall-normal (v_{RMS}) velocity components at $x/c = 0$. Experimental data are extracted from Rubio Carpio *et al.* [51, 60].

$$\mathrm{SPL}_{\mathrm{scaled}} = \mathrm{SPL}_{\mathrm{raw}} + 20\log_{10}(D_o) - 10\log_{10}(b) \tag{3.7}$$

The scaled sound spectra ($\mathrm{SPL}_{\mathrm{scaled}}$) for each trailing-edge treatment are shown in figure 3.9. Note that the frequency axis has been made non-dimensional as Strouhal number based on the airfoil chord ($St_c = fc/U_\infty$). For the solid TE case (figure 3.9 (*a*)), both surface and permeable FW-H formulations produce similar spectra with a maximum difference of 1 dB at $St_c = 17.5$. The spectra are also in good agreement with experimental measurements, with discrepancies appearing only above $St_c = 22$. Spectra from different experimental datasets also show deviations in this frequency range, which might be due to the influence of the different tripping elements [71]. For the porous TE case, the surface and permeable FW-H results show a small difference (i.e., ≈ 2 dB) at frequencies above $St_c = 12$. This discrepancy can be attributed to the neglected contribution of monopole sources in the surface FW-H formulation (i.e., the unsteady flow injection and ejection at the porous medium surface [72]). This source term appears to be relevant in the high frequency range but not at low frequencies where most of the noise attenuation is obtained. Hence, the results of surface FW-H formulation can also be used for investigating the noise reduction mechanisms of the porous TE. Nonetheless, the sound spectra obtained from the simulation still underpredict that of the experiment, especially above $St_c = 15$. This is attributed to the surface roughness noise contribution that is not considered by the simulation. Good agreement with the reference data is obtained for the blocked TE case, in which the numerical result shows that the noise reduction at low frequencies is absent.

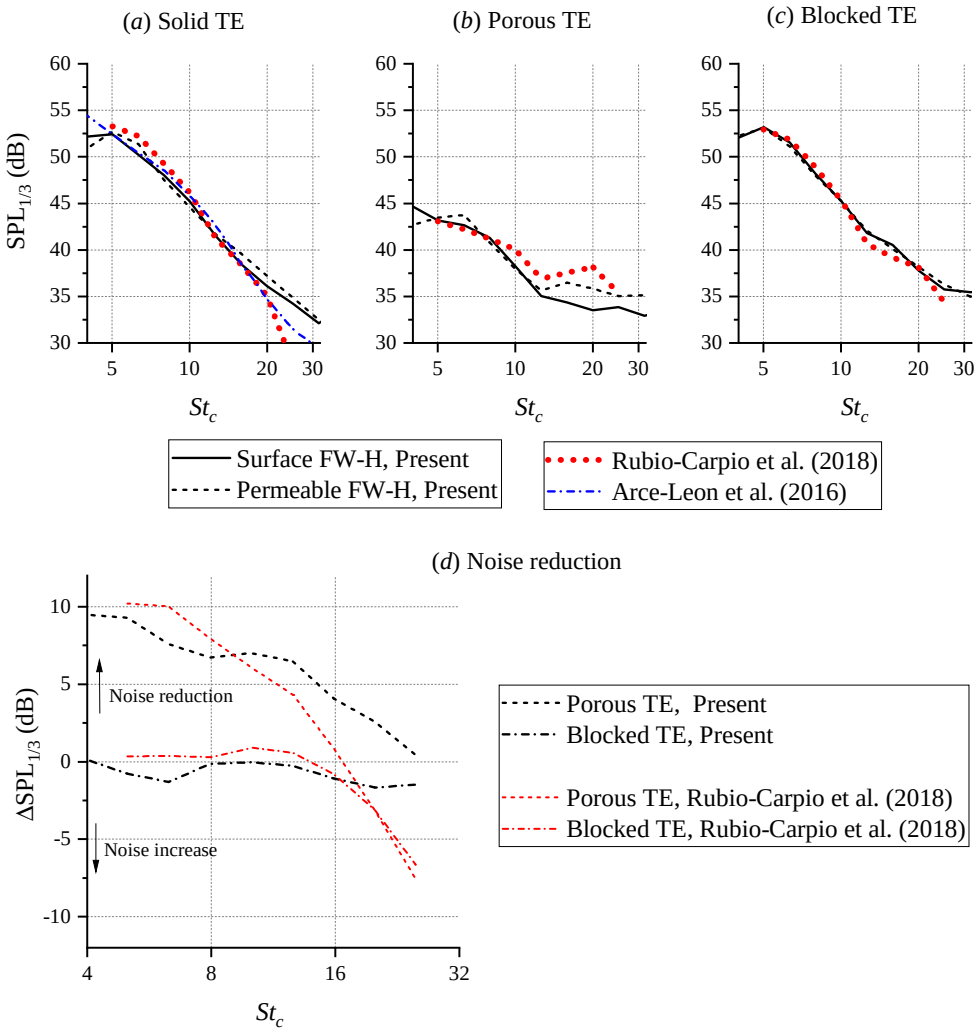

Figure 3.9: (Metal foam) Normalised one-third octave far-field sound spectra $SPL_{1/3}$ of the (*a*) solid, (*b*) porous, and (*c*) blocked trailing edge. The noise reduction spectra is shown in (*d*). Sound pressure is calculated directly above the TE ($x/c = 0$). Experimental data are extracted from León *et al.* [70] and Rubio Carpio *et al.* [51].

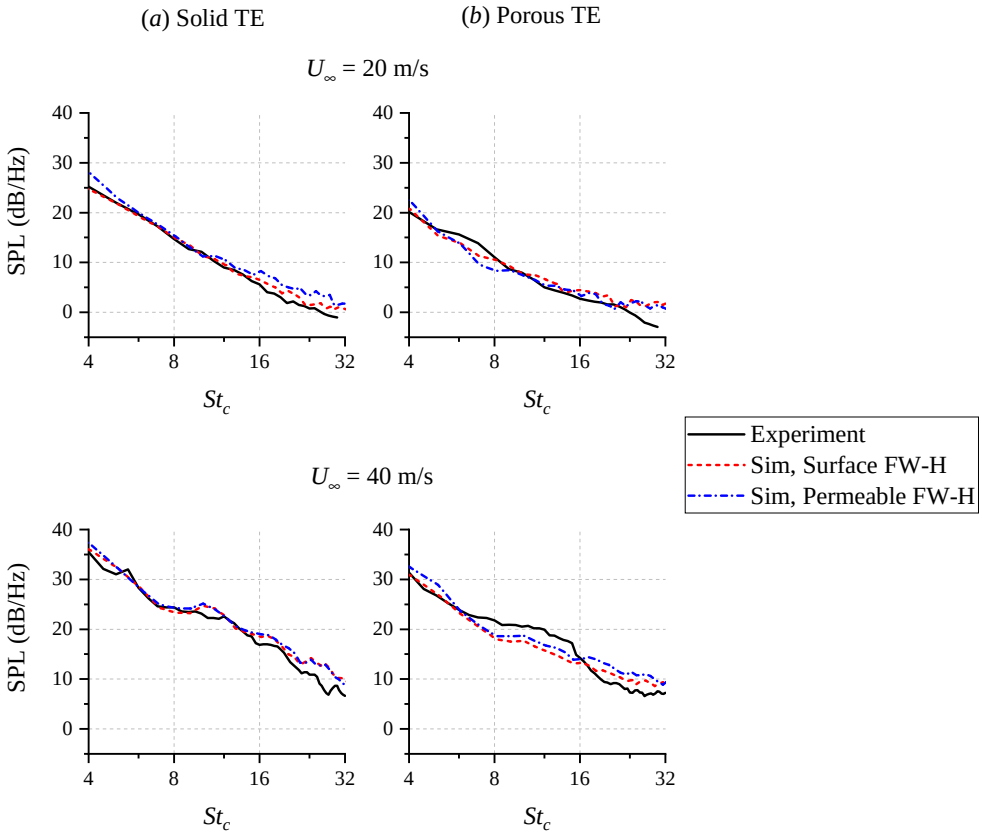

Figure 3.10: (Metal foam) Validation of far-field noise spectra from the simulation for a higher AoA (7.8°) and Reynolds number cases. Observer location is $x/c = -0.68$, $y/c = 4.95$.

The difference in the far-field noise produced by the porous trailing edges (i.e., porous and blocked TE) and the solid one is expressed as $\Delta\text{OSPL} = \text{OSPL}_{\text{solid}} - \text{OSPL}_{\text{porous}}$ and plotted in figure 3.9 (*d*). The experimental results reported in Rubio Carpio *et al.* [51] are also provided for comparison. The figure evidences that the trends of the experiment have been captured by the simulation, although discrepancies are present in the high-frequency range. The porous TE still shows noise reduction up to $St_c = 30$, while the noise increase caused by the blocked TE remains smaller than 2 dB. This further corroborates that the high-frequency noise increase is associated to the surface roughness of the porous insert, which cannot be replicated using the equivalent fluid region approach. Nonetheless, present results confirm that an unobstructed permeability between the opposite sides of the porous insert is necessary to achieve noise attenuation Herr *et al.* [41] and Rubio Carpio *et al.* [49, 51].

Noise predictions for the cases with non-zero AoA and higher Reynolds number are shown in figure 3.10. The noise spectra are given in plots (*a*) for the solid TE and (*b*) for the porous one. The figure shows that both the surface and permeable FW-H results for

different TE types and velocities are almost identical throughout the frequency range of interest. The spectra for the solid TE case have been found to be in good agreement compared to the experimental one. At 20 m/s, however, the spectra from the simulation overpredict the experiment starting from $St_c = 16$, which might be attributed to the self noise from the zig-zag trip. The self-noise contribution of the tripping device is also apparent in the spectra for the porous TE case. The agreement between the experiment and the simulation results for the porous TE is slightly poorer, particularly in the low to mid frequency range. This discrepancy might be attributed to artefacts that could arise at the porous TE tip where the local porous material thickness is too small to be adequately represented by the APM layer. Nevertheless, the simulation results still manage to capture the overall trends from the experiment.

3.3.3. VALIDATION - POROUS-CELL INSERT

In figure 3.11, the mean streamwise velocity profiles are plotted at three different locations in (*a*), while the velocity fluctuations profiles near the TE are shown in (*b*). It is worth mentioning that the boundary layer profiles from the experiment have been obtained using particle-image-velocimetry (PIV), and as a consequence, near-wall measurements are limited due to the presence of light reflections from the airfoil surface [60]. Nevertheless, the figure shows good agreement between the numerical results and the experimental ones. A more detailed comparison between the flow field on both the solid and porous TE will be provided in a later subsection.

The power spectral density of far-field acoustic pressure is provided in figure 3.12. The observer for this figure is located directly above the TE ($x/c = 0, y/c = 5$). Since the airfoil span in the simulation is smaller than in the experiment, the raw noise spectra from the simulation has been scaled accordingly to allow for comparison; the procedure is the same as given in equation 3.7. Figure 3.12 (*a*) compares the spectra calculated using the surface and permeable FW-H approaches, where both produce results that are in good agreement with each other. This implies that the noise sources on the airfoil are predominantly of dipole type, and thus quadrupole noise sources, such as those in the turbulent airfoil wake, do not have a substantial contribution towards noise generation, which is typically the case for low Mach number flows.

The validation of the far-field acoustic spectra for both TE types is provided in figure 3.12. Plot (*b*) shows that the noise prediction from the simulation generally agrees well against the experimental measurements, except for the solid TE case at $St_c > 16$. It has been deduced from the metal-foam TE cases that the overestimated high-frequency range for the solid TE is caused by the zig-zag trip. Such discrepancy is less apparent in the porous TE case, because the noise from the rough porous surface has become comparable to the self noise of the zig-zag trip. The noise reduction spectra are plotted in (*c*), where positive values correspond to noise attenuation, and the negative ones to noise increase. The noise reduction at low frequencies reaches up to 11 dB near $St_c = 6$, with an average of 10 dB in between the range of $4 < St_c < 8$. In the mid frequency range, the noise reduction gradually decreases from $St_c = 8$ and it eventually vanishes at around $St_c = 16$. At higher frequencies, a noise increase by around 2 dB can be observed. Thus, the spectra can be subdivided into three regions: 1) where large noise attenuation exists ($4 < St_c < 8$), 2) a transition region where the noise attenuation level gradually decreases ($8 < St_c < 16$), and

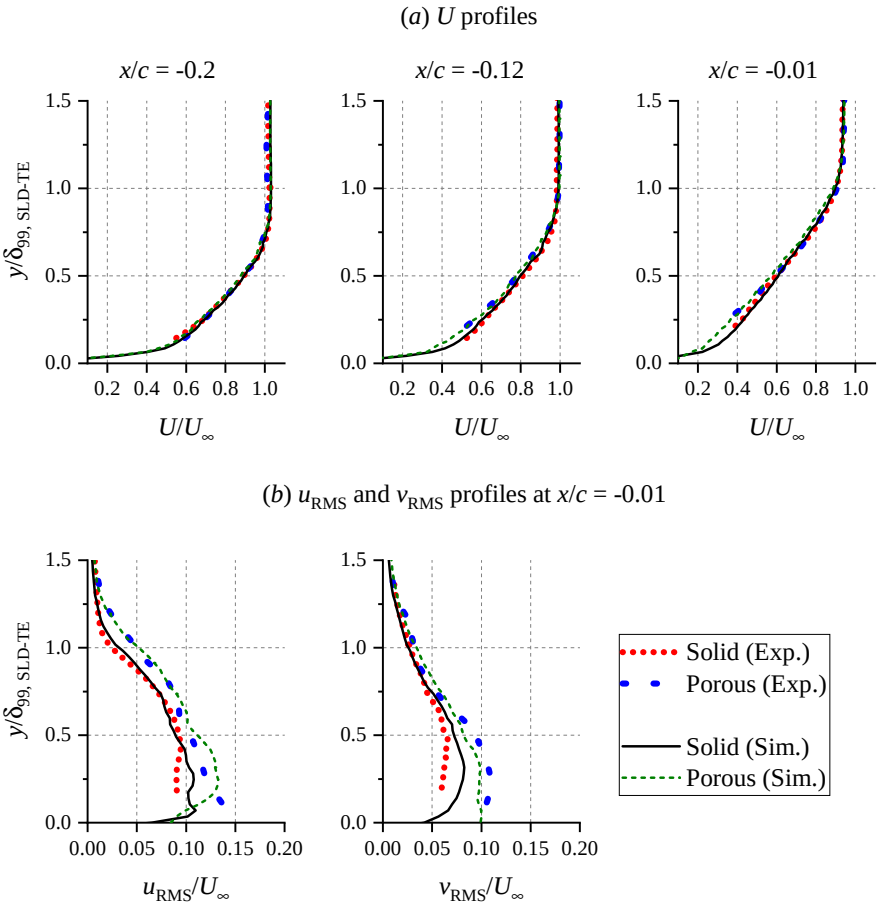

Figure 3.11: (Porous cell) Comparisons of flow statistics in the turbulent boundary layer. All data points have been extracted at the airfoil midspan. Mean wall-parallel velocity (U) profiles at several chordwise locations are shown in (*a*); profiles of root-mean-square (RMS) of velocity fluctuations in the wall-parallel (u_{RMS}) and wall-normal (v_{RMS}) directions are shown in (*b*). Note that "experiment" is abbreviated as (Exp.).

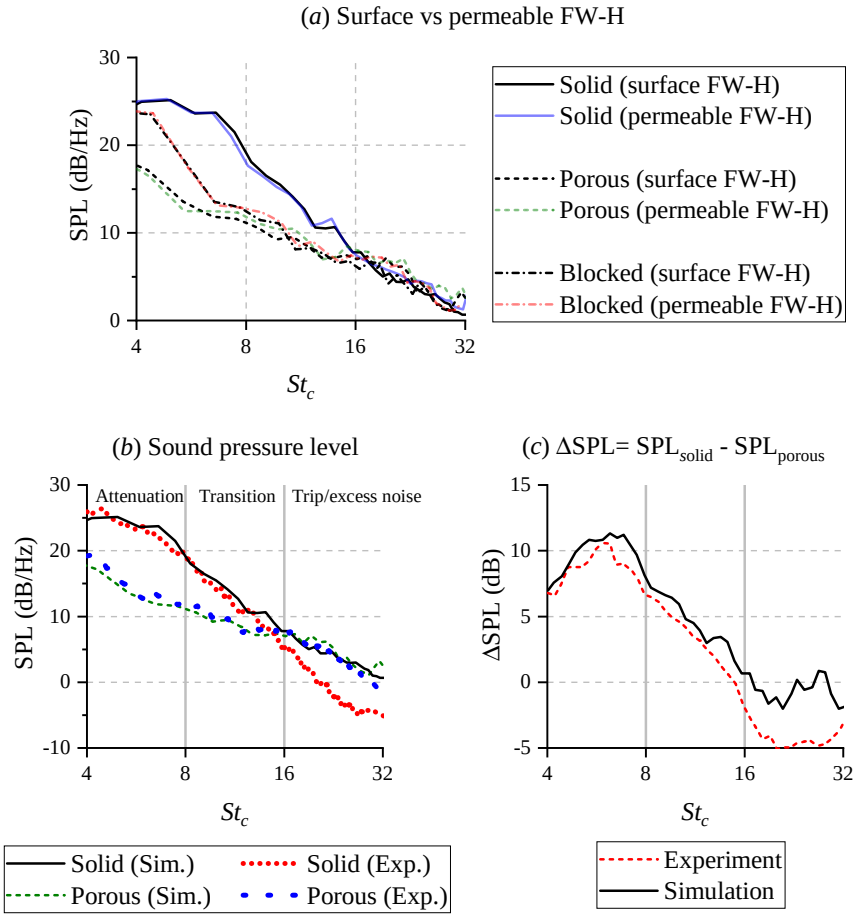

Figure 3.12: (Porous cell) Plot (*a*) shows the comparison between far-field noise spectra obtained using the FW-H analogy applied on the surface pressure fluctuations (surface FW-H), and that from the permeable surface (permeable FW-H) enclosing the airfoil. The far-field noise level and the noise reduction level are validated in plots (*b*) and (*c*). Observer location is at $x/c = 0$, $y/c = 5$.

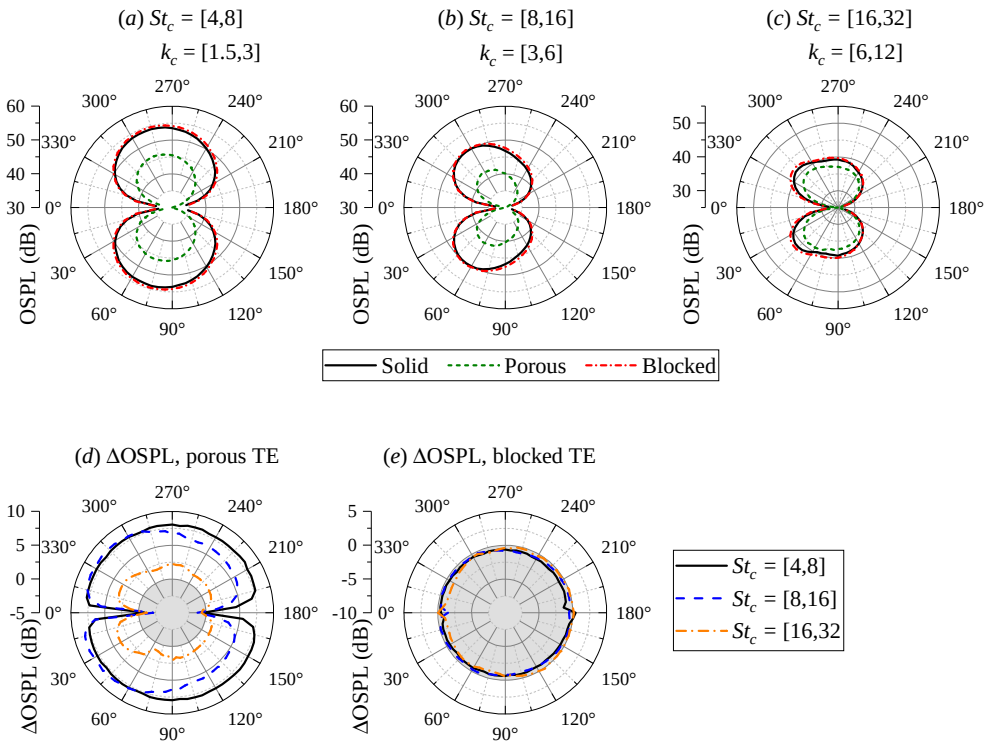

Figure 3.13: (Metal foam/modelled) Directivity of the far-field sound spectra for the different TE types, plotted in three different frequency ranges (*a*) $4 < St_c < 8$, (*b*) $8 < St_c < 16$, and (*c*) $16 < St_c < 32$. The airfoil leading edge is facing towards 0^o. The directivity of the noise reduction level is given in plots (*d*) and (*e*) with the area in grey delimiting the noise increase region. The airfoil leading edge is facing towards 0°.

3) where excess noise is present ($16 < St_c < 32$). This trend is in line with past analytical studies [28, 50], where the noise reduction of a perforated plate has been predicted to become smaller as frequency increases.

3.4. FAR-FIELD NOISE CHARACTERISTICS

3.4.1. EFFECTS OF POROUS INSERTS ON FAR-FIELD NOISE DIRECTIVITY

This subsection takes a closer look into how permeability influences the far-field noise directivity. Noise spectra have been computed at 72 locations that are equally spaced in a circular pattern on the x-y plane with a radius of $7.4c$ from the trailing-edge mid-span. The noise spectra are integrated as SPL in three frequency bands corresponding to the spectral features observed in the experiments [49, 51], i.e., at $4 < St_c < 8$ where the noise reduction is the highest, at $8 < St_c < 16$ which is a transitional region where the noise reduction becomes smaller, and at $16 < St_c < 32$ where noise reduction is no longer observed.

Considering that the metal-foam inserts have been modelled using the combined

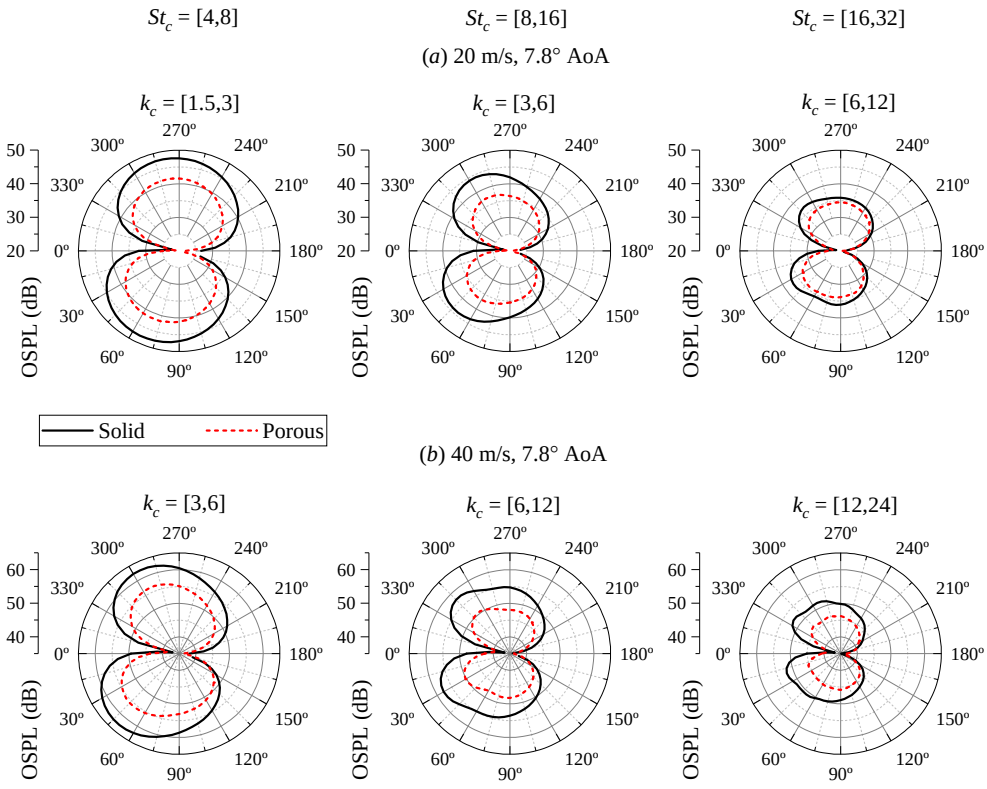

Figure 3.14: (Metal foam/modelled) The effect of angle-of-attack and Reynolds number on the noise directivity pattern for different Strouhal number ranges.

APM-PM approach while the porous-cell inserts are fully-resolved in the simulation domain, these descriptions have been added to the figure captions to help readers distinguishing the two different approaches.

Figure 3.13 presents the far-field directivity patterns for the metal-foam TE cases. The corresponding chord-based Helmholtz numbers ($k_c = 2\pi M_\infty St_c$) are also listed to indicate the acoustic-compactness of the airfoil at different frequency ranges. At the lowest frequency range, the directivity patterns for all three cases resemble that of a compact dipole. These dipole lobes are tilted towards the upstream direction in the mid frequency range (plot (*b*)) as the airfoil chord becomes less acoustically compact [23, 73]. In the highest frequency range (plot (*c*)), the directivity patterns become more similar to that of a cardioid as the main lobes are tilted further towards shallower angles. The noise reduction level of the porous TE is depicted in plot (*d*). At the lowest Strouhal range, the noise reduction level is relatively uniform in the direction of the main lobe, but it tends to be higher in the upstream direction at higher frequencies. A similar trend has been observed for a perforated plate by Cavalieri et al. [50] and for a permeable slitted TE by Delfs et al. [48]. Unlike the porous TE, the blocked TE, in plot (*e*), shows almost no difference relative to the solid TE. In other words, the blocked TE behaves almost

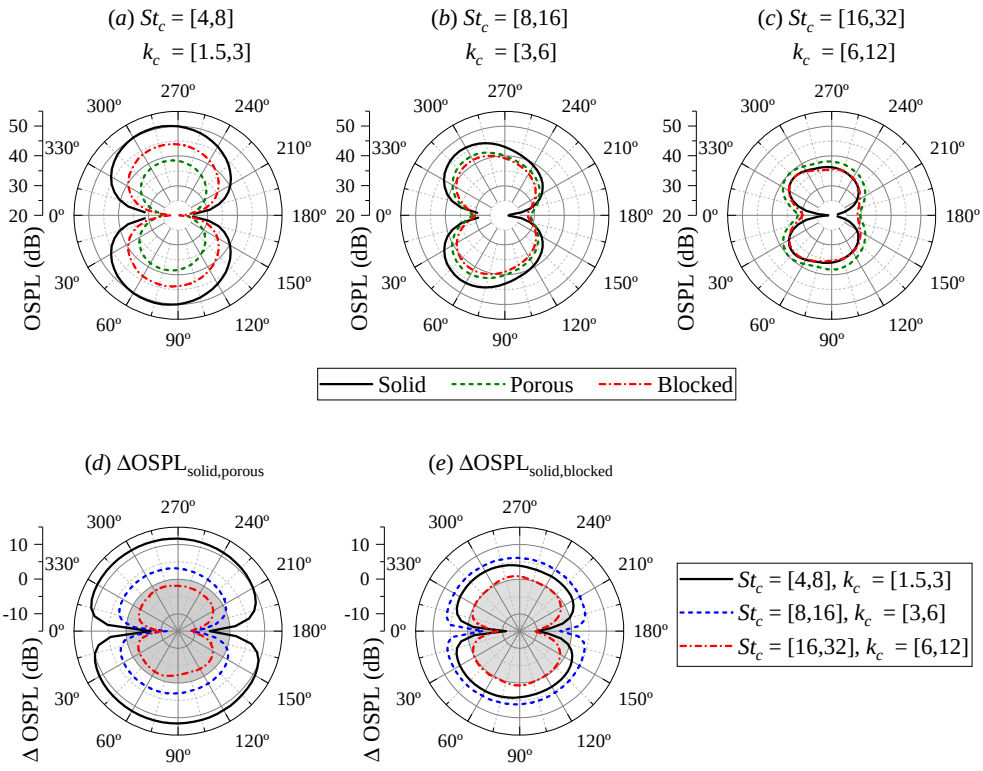

Figure 3.15: (Porous cell/full-resolved) Far-field noise directivity for solid and porous TE cases, plotted as the overall sound pressure level (OSPL) integrated over three different frequency ranges (*a*) $4 < St_c < 8$, (*b*) $8 < St_c < 16$, and (*c*) $16 < St_c < 32$. The OSPL difference relative to the solid TE is plotted in (*d*) and (*e*);

identically to its solid counterpart.

The effects of AoA and Reynolds number on the noise directivity for the metal-foam TE cases are shown in figure 3.14. Comparing the plots under (*a*) and (*b*), it appears that changing the AoA decreases the OSPL difference between the solid and porous TE. Furthermore, the orientation of the main lobes is slightly tilted when the AoA is increased, but the general shapes of the lobes remain unaltered with respect to the zero AoA case. For the Strouhal number range of $St_c = [4,8]$ in figure 3.14 (*a*), the solid TE at 20 m/s is still showing a dipole-like directivity given that the airfoil is acoustically compact ($k_c \sim 1$) in this frequency range. For the 40 m/s case, shown in figure 3.14 (*b*), the sound directivity slightly resembles a cardioid shape since the Strouhal number corresponds to a higher Helmholtz number at which the airfoil is no longer compact ($k_c > 1$). Nonetheless, increasing the Reynolds number does not appear to affect the tilt angle of the lobes.

It is possible to show that variations in the noise directivity are linked to the permeable extent of the porous insert using the porous-cell cases in figure 3.15. The porous TE achieves a noise reduction level of up to 11 dB along the main lobes. As

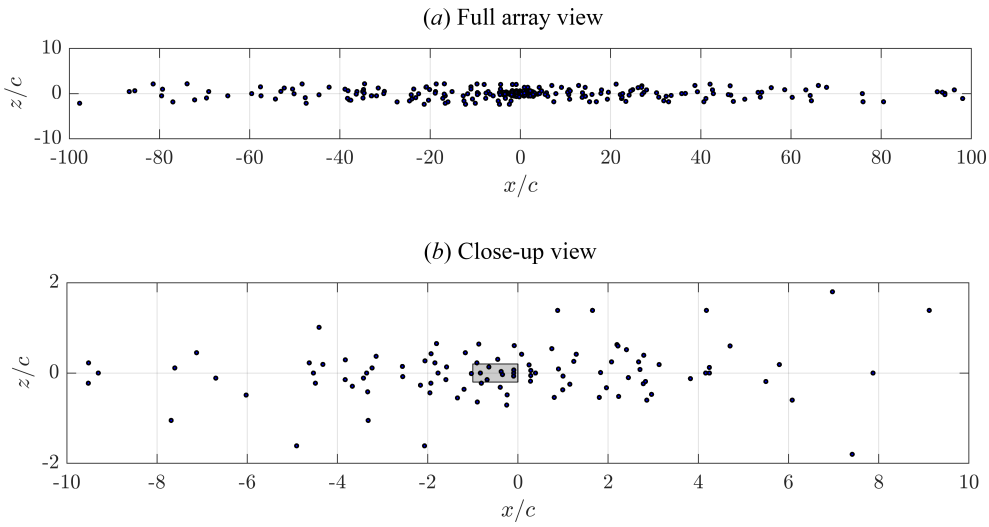

Figure 3.16: The distribution of 320 microphones in a modified Underbrink [74] configuration. The grey area represents the planform of the airfoil with the flow towards the positive x direction. The source maps are shown in figure 3.17.

previously implied in figure 3.12, the partially-blocked TE shows an overall smaller noise attenuation with an average of 4 dB. Non-compactness behavior can be found at higher Helmholtz number ranges. Nevertheless, both TE types exhibit comparable OSPL at $8 < St_c < 16$. In the highest Strouhal number range, which is shown in plot (c), the porous TE clearly shows the presence of excess noise, but the noise increase produced by the blocked TE is slightly lower except at shallow angles. The airfoils with porous and blocked TE exhibit a minor change in noise directivity pattern, indicated by the slightly higher noise reduction level towards the upstream direction as shown in figure 3.15 (d) and (e). As a result, the main directivity lobes of these modified airfoils resembles a more dipole-like shape, particularly at low to mid frequency ranges ($St_c = [4, 16]$). The porous inserts also produce excess noise at shallow angles (i.e., within ±30° with respect to the streamwise direction), which becomes more prominent at higher frequencies. It is possible to conjecture that the porous inserts, or at least a small extent of their surfaces, scatter noise with different directivity compared to the solid TE, which could contribute to noise reduction [47].

3.4.2. NOISE SOURCE LOCALISATION

A conventional beamforming algorithm[2] is employed to localise the dominant noise sources along the airfoil. The virtual microphone array that is used in this study is based on the Underbrink's spiral array configuration [74], as shown in figure 3.16. It is a modification of the 64-microphone array that has been used previously by Rubio Carpio *et al.* [51], whose Rayleigh limit is approximately equal to c at $St_c = 12.5$ in the chordwise

[2]Available in the tool *optydb_bf* that is developed by Dassault Systemes. It has been benchmarked against other beamforming codes, as shown by Lockard *et al.* [75].

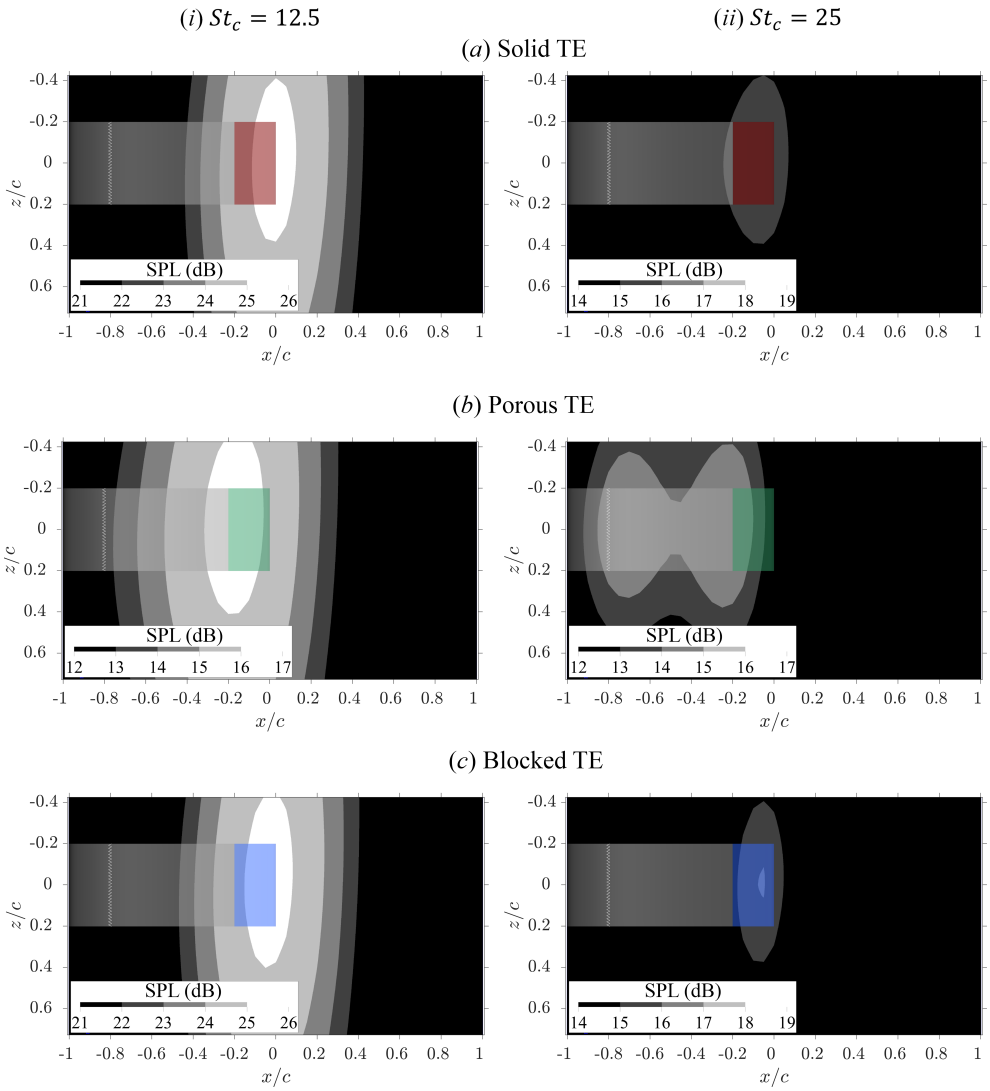

Figure 3.17: (Metal foam/modelled) Source maps for one-third octave band, centered at (*i*) 1250 Hz (St_c = 12.5) and (*ii*) 2500 Hz (St_c = 25) for the (*a*) solid , (*b*) porous, and (*c*) blocked TE cases. The trailing-edge region ($-0.2 < x/c < 0$) for each respective case is highlighted in different colours.

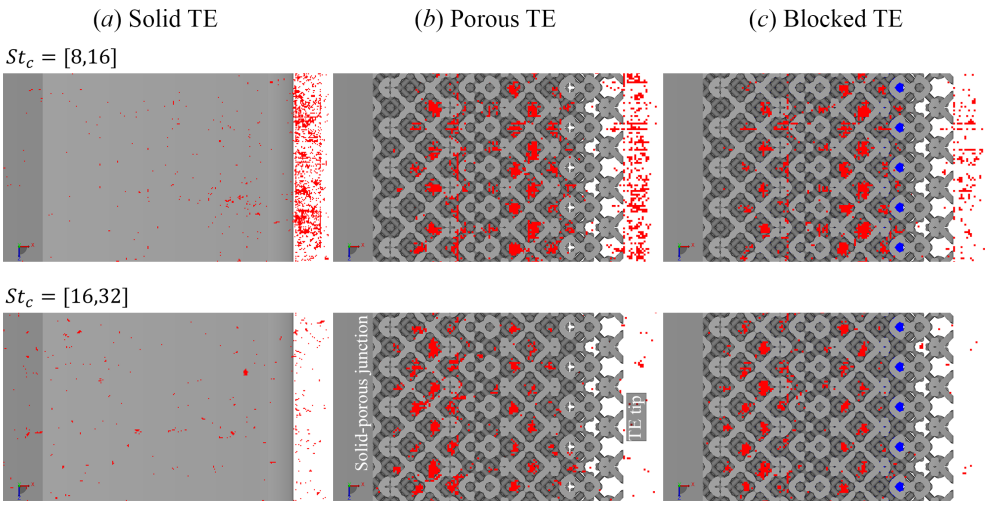

Figure 3.18: (Porous cell/full-resolved) Noise source localisation based on the vortex sound theory algorithm [77], FIND. The figure illustrates a top view of the airfoil. Clusters of noise sources are coloured in red, while the solid partition in the blocked TE is shown in blue. The last 20 % of the airfoil chord is coloured in light grey.

direction. In order to increase the spatial resolution (i.e., to decrease the Rayleight limit) with respect to the existing antenna, the present array is designed with a total of 320 microphones and increased dimensions. The antenna is built using 5 concentric arrays with 64 microphones each, where the innermost array is the same as that used by Rubio Carpio *et al.* [51] (see figure 3.16 (*b*)). The resulting array has an overall dimension of $200c \times 4c$ and the Rayleigh limit is approximately equal to $0.1c$ in the chordwise direction at $St_c = 12.5$. This allows distinguishing the noise sources at the solid-porous junction and the trailing edge for both porous and blocked TE cases provided that the sources at both locations have comparable intensities.

A beamforming technique has been employed for the metal-foam TE cases, and the resulting source maps are shown in figure 3.17. The source maps have been processed in one-third octave bands centered at (*i*) $St_c = 12.5$ and (*ii*) $St_c = 25$. At $St_c = 12.5$, the source of maximum noise generation for the solid TE is aligned with the TE ($x/c \simeq 0$); the same can be observed for the blocked TE. On the other hand, the location of the maximum noise intensity on the porous TE shifts upstream towards the solid-porous junction (i.e., $x/c = -0.2$). Although it has been reported [41, 47, 76] that the porous TE might still scatter noise from the TE tip in addition to the solid-porous junction, the source map of the porous TE implies that the acoustic scattering near the TE tip has been mitigated. At $St_c = 25$, the source map of the porous TE shows an additional source nearby the zig-zag trip in addition to the solid-porous junction. The sources nearby the tripping device do not appear prominently in other source maps due to their lower relative intensity.

By leveraging the vortex sound theory of Powell [77], PowerFLOW offers the *FIND* (Flow-Induced Noise Detection) tool to identify fluid regions where large vorticity gradient is present in the flow field. For completeness, Powell's acoustic analogy for low

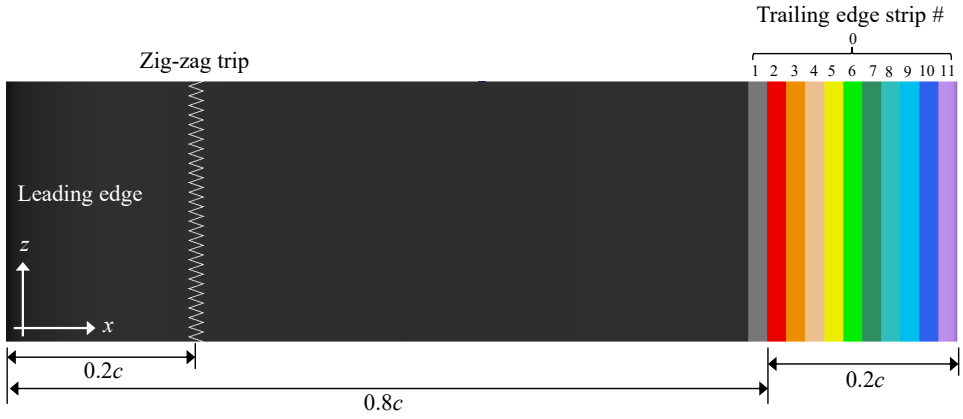

Figure 3.19: Top view of the airfoil planform, revealing the arrangement of the trailing edge strips for noise contribution analysis.

Mach number is given as follows [78],

$$p'(\boldsymbol{x}_o, t) = \frac{\rho_\infty}{4\pi} \int_{\mathbb{V}} \left[\frac{1}{|\boldsymbol{x}_s - \boldsymbol{x}_o|} \nabla \cdot (\boldsymbol{\Omega} \times \boldsymbol{u}) \right]_{t'} \mathrm{d}\mathbb{V} \tag{3.8}$$

where the divergence of the Lamb vector $\nabla \cdot (\boldsymbol{\Omega} \times \boldsymbol{u})$ serves as the equivalent noise source located within a control volume $\mathbb{V}$; $\boldsymbol{\Omega}$ is vorticity. The subscript t' implies that the right hand side of equation 3.8 is evaluated using the retarded time approach.

The FIND tool has been applied for the porous-cell TE case and the output is presented in figure 3.18. For the solid TE, the source map for $8 < St_c < 16$ shows that the noise sources are present mainly near the TE tip, which is expected. However, the source maps for the porous and partially-blocked TE are quite different. While noise sources are relatively absent on the surface of the solid TE, they can be found inside the open pores of both porous and blocked TE. A closer look also reveals that the sources are clustered near the downstream end of the open pores. This observation supports the conjecture that the high-frequency excess noise coming from the porous insert is related to the geometrical details at the surface of the porous medium, i.e., surface roughness noise [42, 44].

3.4.3. PARTIAL-SURFACE FW-H INTEGRATION ANALYSIS

The partial-surface FW-H integration [79] approach allows for quantifying the noise contribution from a smaller portion of the airfoil surface. This method has been considered to study the noise reduction mechanisms of permeable inserts by examining the noise contribution by different surface segments along the TE region. As illustrated in figure 3.19, the TE region is sub-divided into 11 strips, each with a chordwise length of $0.02c$. For the metal-foam and porous-cell inserts, the solid porous junction is located in between strip 1 and 2. For the blocked metal-foam TE, the solid partition extends from strip 2 to 11 ($-0.2 < x/c < 0$), whereas for the partially-blocked porous-cell TE, it extends from strip 4 to 9 ($-0.16 < x/c < -0.04$). Within the frequency range of interest, the

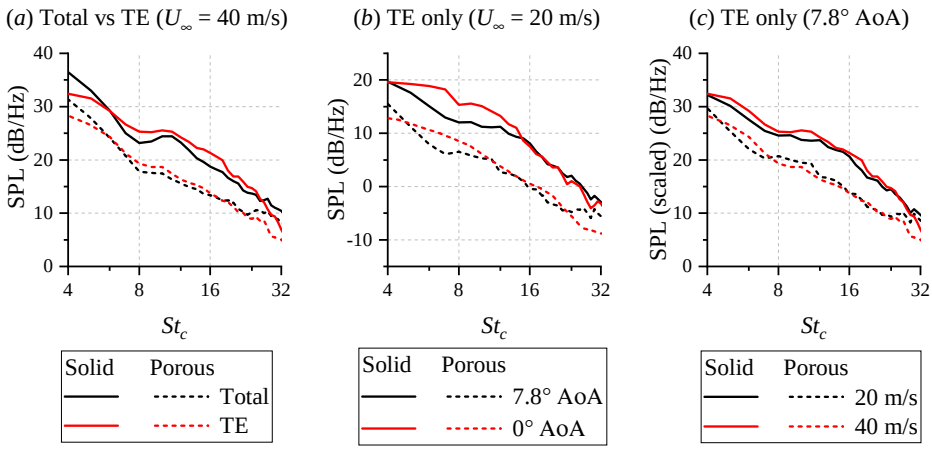

Figure 3.20: (Metal foam/modelled) Comparisons of sound pressure level based on the contribution of the TE region ($-0.22 < x/c < 0$). The effects of AoA and Reynolds number on the SPL are shown in (*a*) and (*b*) respectively. In (*a*), the SPL at 20 m/s has been scaled to 40 m/s following U_∞^5 for solid TE and $U_\infty^{5.7}$ for porous TE.

chordwise extent of each strip is smaller compared to the streamwise integral length scale of the surface pressure fluctuations such that each strip can be considered as an unique scattering surface. This procedure is carried out using the same observer location as that for far-field noise analysis in figure 3.9 and 3.12 ($x/c = 0, y/c = 5$).

For this analysis, $p'_m(t)$ defines the time history of acoustic pressure (fluctuations) contributed by a strip m, and $p'_0 = p'_1 + p'_2 + ... + p'_{11}$ is the total acoustic pressure produced by the 11 strips. Moreover, the cumulative acoustic pressure $p'_{\text{cumulative},m}$ is defined in a descending order (i.e., starting from strip 11 at $x/c = 0$), such that $p'_{\text{cumulative},m} = p'_{11} + ... + p'_m$. The power spectral density from these time series are subsequently computed, and integrated over several frequency bands.

Figure 3.20 (*a*) compares the noise spectra produced by the entire airfoil surface with that from the TE region ($-0.22 < x/c < 0$) for the metal-foam TE cases. It is clear that the latter dominates across the majority of the frequency range of interest, and thus, the TE region is indeed the location where the dominant noise sources are present. However, the TE contribution to the total SPL becomes smaller at both the lower and higher ends of the spectra. At low frequencies, the noise from the airfoil also includes the contribution of the LE back-scattering [20] which becomes relevant when the airfoil is acoustically compact. On the other hand, the discrepancy in the very high frequency range can be associated with the self-noise contribution of the zig-zag trip. While the plot shows only the 40 m/s cases, the spectra at 20 m/s exhibit similar behaviours although the effect of LE back-scattering can be found over a larger proportion of the low Strouhal number range given the lower Helmholtz number.

The spectra of the noise contribution from the TE region are shown in figure 3.20 (*b*) and (*c*). The effect of AoA on the TE noise is depicted in plot (*b*). For the solid TE, discrepancies are present in the spectra between $4 < St_c < 16$, which is due to the

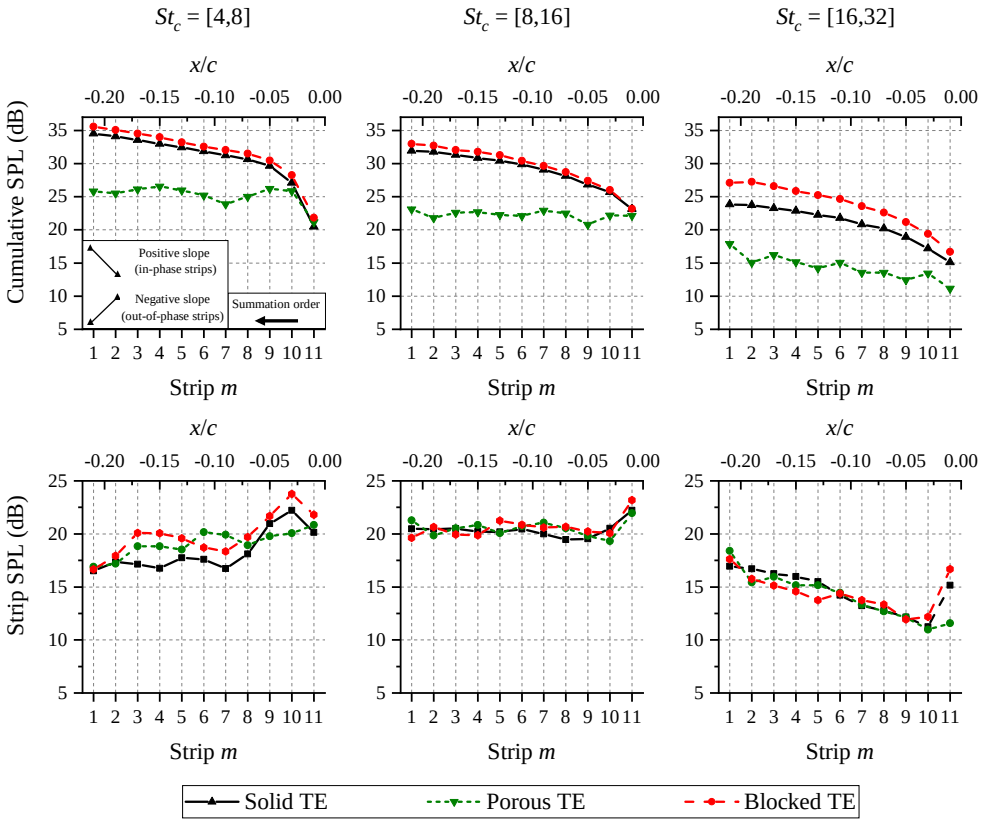

Figure 3.21: (Metal foam/modelled) The sound pressure level (SPL) produced by each strip and its cumulative, integrated over 3 different frequency bands. Note that the cumulative SPL is computed following a descending order (i.e., starting from strip 11).

frequency shift in the noise produced by the pressure (low frequency component) and suction sides (high frequency component) of the airfoil [4] . The same effect is also present in the porous TE case, which results in the convex shape of the spectra in between $6 < St_c < 12$. From this plot, it can be inferred that the porous TE becomes slightly less efficient when the AoA is increased. It is conjectured that this behavior is related to the increased turbulence scales at the airfoil suction side at higher AoA, considering that a sufficiently large ratio between the porous TE chordwise extent and the streamwise turbulence length scales in the boundary layer is necessary to mitigate noise effectively [80, 81]. In figure 3.20 (*c*), the spectra at 20 m/s have been scaled to 40 m/s following the acoustic intensity dependence [13, 14] on freestream velocity. To produce the best fit, a U_∞^5 scaling is applied for the solid TE, and $U_\infty^{5.7}$ for the porous TE; similar fit has been found experimentally [81]. The higher scaling exponent for the porous TE has also been observed in analytical studies [28], indicating that the porous TE has a lower scattering efficiency compared to the solid one at low Mach numbers.

The results of the strip analysis for the metal-foam cases at zero AoA are presented in

figure 3.21. The SPL contribution from individual strip is shown at the lower row, while the cumulative SPL values at the top. Note that the cumulative sum of the strip contribution starts from the TE tip (strip 11) as shown in the figure. A positive cumulative slope indicates in-phase relation between a strip and the previous ones, while a negative slope indicates the opposite.

At the lowest Strouhal range, the solid TE strips near the TE tip (i.e., strips 9 - 11) generate significantly higher SPL compared to the upstream ones. The same can be observed for blocked TE, but the individual SPL values are smaller for the porous TE. From strips 8 to 1, however, the SPL values on both the porous and blocked TE are on average higher than that on the solid TE. Correspondingly, the noise source intensity on the porous surface is stronger than on the solid one except at locations near the TE tip. The cumulative SPL plot also reveals an interesting phenomenon. For the solid and blocked TE, the slope of the cumulative SPL is relatively steep between strips 9 and 11, indicating that this is where noise is primarily scattered from. Further upstream the cumulative SPL slope decreases but remains positive. Thus, it can be inferred that the strips on solid and blocked TE are generally in-phase to each other, which is an expected behavior, especially at frequencies where the airfoil is acoustically compact [82]. Differently, the cumulative SPL trend for the porous TE shows a relatively flat slope between strips 10 and 1. Considering that the individual strip SPL of the porous TE is comparable to the others', it is possible to conclude that the strips on the porous TE are generally out-of-phase relative to each other. At the higher Strouhal range, the individual strip SPL values for all TE types become more similar to each other. However, the trend of the cumulative SPL values remains identical to that at lower frequencies.

From figure 3.21, porous TE is shown to possess at least two noise mitigation mechanisms. Firstly, the porous TE mitigates the intensity of scattering near the TE tip. Secondly, noise scattering on the porous TE takes place at multiple locations, which promotes destructive interference in the near field. Both mechanisms have been previously suggested by Delfs *et al.* [48], but they were not fully demonstrated.

The effects of AoA and Reynolds number on the cumulative SPL distribution on the metal-foam TE are presented in figure 3.22. Firstly, the effect of AoA is examined in plots (*a*). When airfoil AoA is increased to 7.8°, the cumulative SPL curves at low and mid frequency ranges ($4 < St_c < 16$) of the solid TE are shifted downward. The same shifts are present for the porous TE cases, but they are less prominent. As a result, the overall noise reduction of the porous TE becomes smaller for the higher AoA setting. Nonetheless, the cumulative SPL curves on the porous TE at the larger AoA tend to flatten further away from the TE tip, similar to the zero AoA case. This suggests that the noise reduction mechanisms of the porous TE remain the same regardless of the changes in the mean aerodynamic loading. Nevertheless, it is arguable that the scattering phenomena on the porous TE is less sensitive to the changes in AoA in comparison to the solid TE.

Figure 3.22 (*b*) shows the comparison of the cumulative SPL curves for the different Reynolds numbers. The cumulative SPL values for 20 m/s cases are scaled to 40 m/s following the proportionality $p'^2 \propto U_\infty^5$ for solid TE [14] and $p'^2 \propto U_\infty^{5.7}$ for porous TE [61, 81]. Despite the more noticeable differences in the shapes of the curves near the TE tip (strip 11), the cumulative SPL values at strip 1 (i.e., the noise emission from the entire TE region) are quite similar between both velocity settings. This finding suggests that the

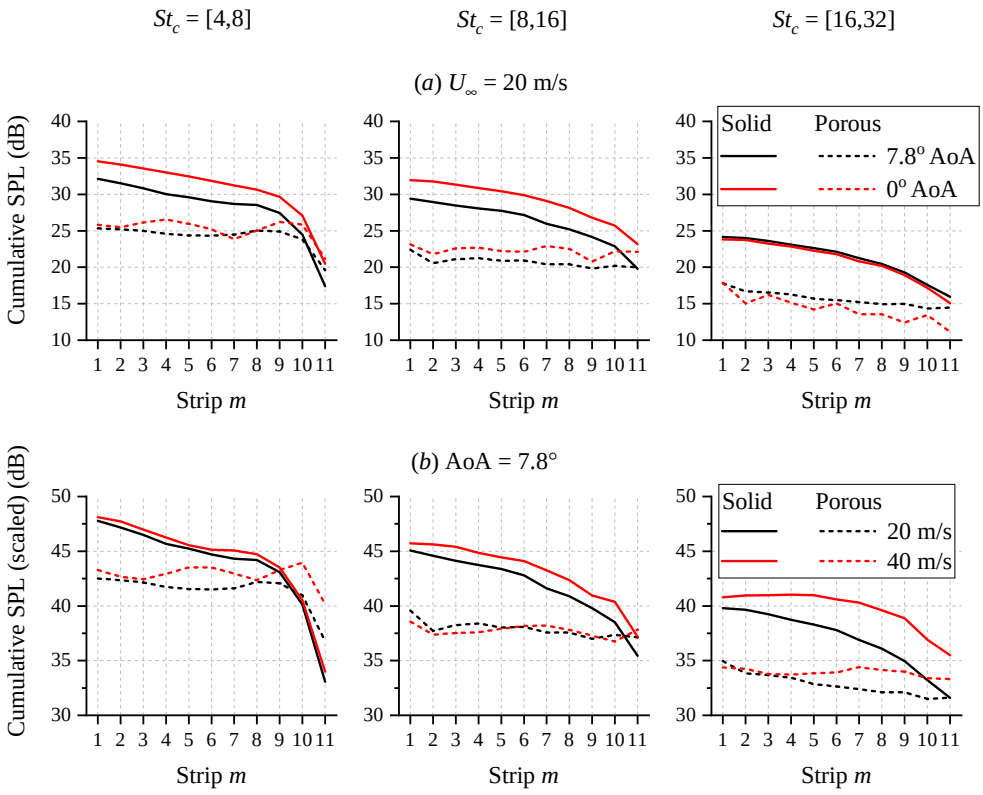

Figure 3.22: (Metal foam/modelled) The cumulative sum of noise contribution from different strips. The effect of AoA for the 20 m/s cases is shown in (*a*). In (*b*), the values at 20 m/s has been scaled to match that at 40 m/s following U_∞^5 for solid TE and $U_\infty^{5.7}$ for porous TE respectively.

porous TE enhances the local noise source intensity more significantly than the solid TE as the velocity increases.

In order to verify that the differences in the cumulative SPL curves between the solid and porous TE are indeed realised by a physical porosity, the same procedure is carried out for the fully-resolved porous cell cases. The results are provided in figure 3.23. In the Strouhal range $4 < St_c < 8$, it is evident that the strip SPL values of the porous TE near the TE tip (e.g., strip 10 and 11) are lower than those of the solid TE. Further upstream (strip 8 and below), the cumulative SPL curve of the porous TE also flattens in a similar fashion as the metal-foam one in figure 3.21. However, for the (partially-) blocked TE, the cumulative SPL curve climbs further before flattening at strip 7. This discrepancy can be attributed to the individual strip SPL of the blocked TE; those near the downstream edge of the solid partition (i.e., strips 8 and 9) generate higher SPL compared to their counterpart on the porous TE. Thus, the figure implies that the smaller low-frequency noise reduction of the blocked TE can be attributed to the additional noise scattered at the solid partition edge. The slopes of the cumulative SPL curves for both types of permeable TE increase again in between strip 1 and 2, implying that the scattering at the solid-porous junction also has

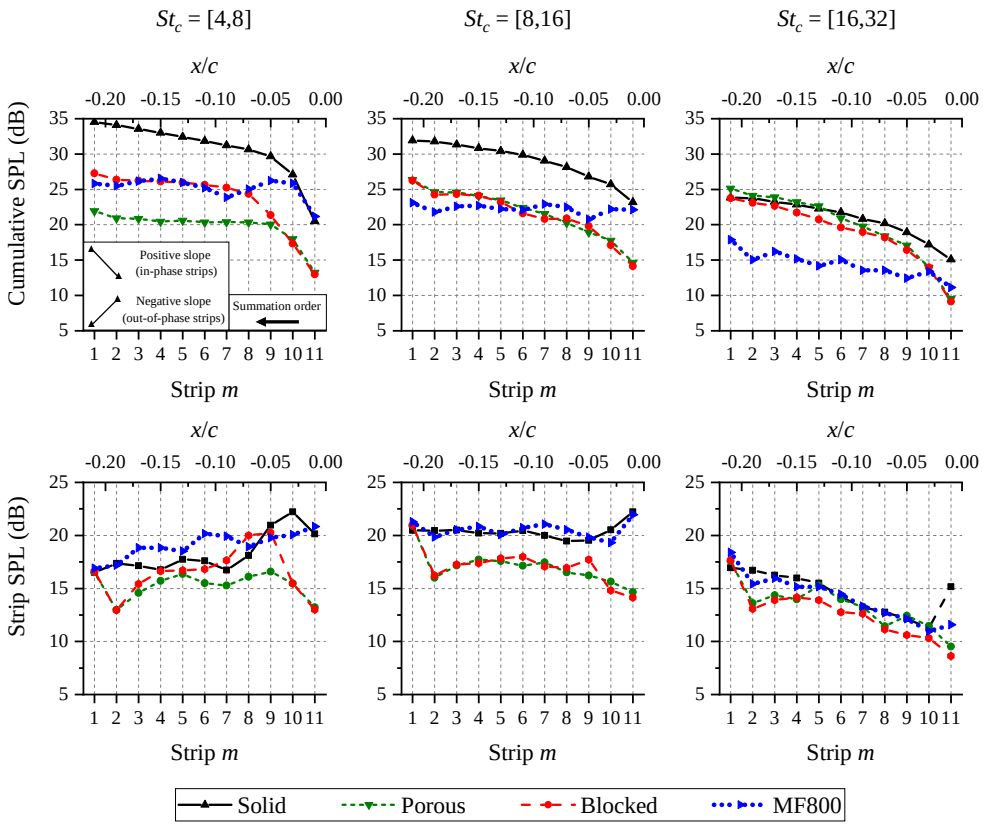

Figure 3.23: (Porous cell/fully-resolved) The sound pressure level (SPL) produced by each strip and its cumulative, integrated over 3 different frequency bands. The trends for the metal-foam TE are indicated as MF800.

a substantial contribution to far-field noise [42, 47, 48]. The difference in cumulative SPL between porous and blocked TE is relatively constant between strip 7 and 3. Hence, it is possible to deduce that the solid partition in the blocked TE has a smaller influence on the noise generation at strips near the solid-porous junction.

In the mid to high frequency ranges ($8 < St_c < 32$), noise generation at the solid-porous junction becomes more significant, given that the local SPL values at strip 1 of the porous and blocked TE are higher compared to those of the strips downstream. However, unlike at lower frequencies, both TE configurations exhibit similar trends, and consequently, noise attenuation level as depicted in figure 3.12. Thus, the influence of the solid partition on the acoustic scattering at the blocked TE appears to diminish as frequency increases. In this frequency range, the cumulative SPL values of both porous and blocked TE also exhibit uphill trends, similar to the solid TE. This indicates that the noise reduction mechanisms of the permeable TE become less effective at higher frequencies. Nonetheless, it is worth mentioning that the excess noise from surface roughness effects is also present for $St_c >$ 16. Nevertheless, this figure corroborates the two separate noise mitigation mechanisms

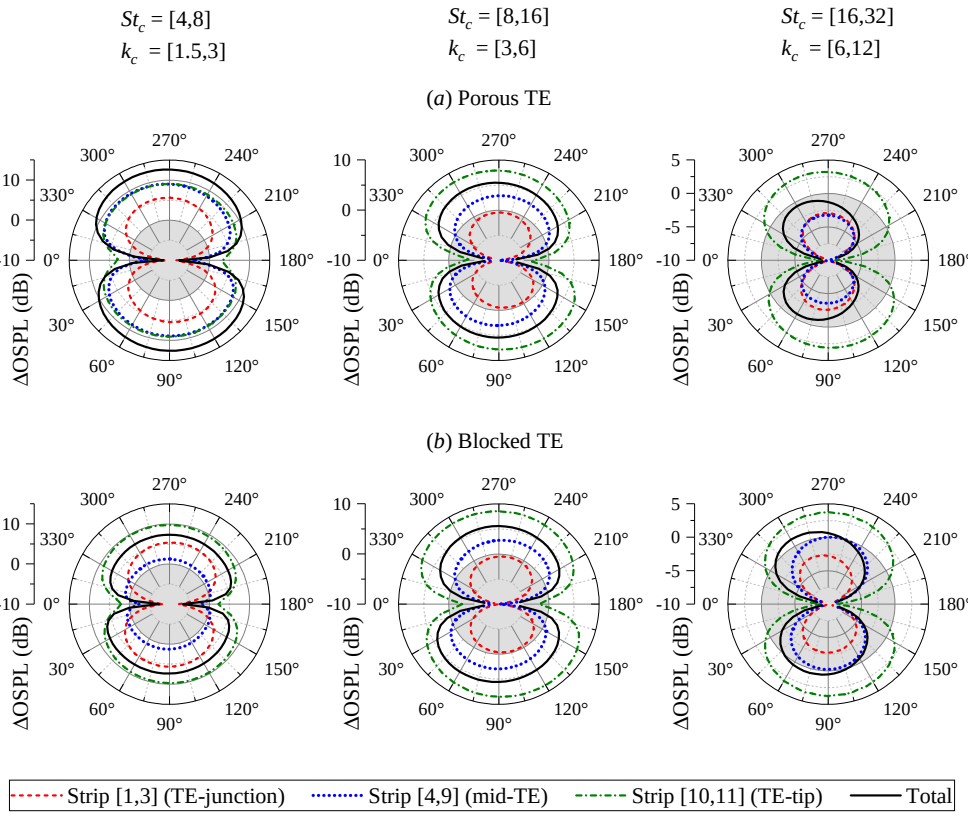

Figure 3.24: (Porous cell/fully-resolved) Noise directivity pattern, plotted as the difference between the SPL of permeable (porous and blocked TE) and solid TE cases, i.e., $\Delta\text{OSPL} = \text{OSPL}_{\text{solid}} - \text{OSPL}_{\text{permeable}}$, for groups of strips at different frequency bands. The grey circle at the center of the polar plot indicates regions of noise increase.

of the porous TE that have been mentioned earlier in this subsection.

Using the partial-surface FW-H integration approach, it is also possible to examine the far-field directivity of the noise emitted by different parts of the porous inserts. This is shown in figure 3.24. The strips are combined into 3 groups, namely: 1) TE-junction (strips 1 to 3), 2) mid-TE (strips 4 to 9), and 3) TE-tip (strips 10 to 11). The groups are based on the slope of the cumulative SPL plots in figure 3.23. The directivity of the sum of all strips, previously depicted in 3.15, is also added into the figure. The directivity plots are provided in term of $\Delta\text{OSPL} = \text{OSPL}_{\text{solid}} - \text{OSPL}_{\text{permeable}}$ to emphasise noise reduction/increase generated by specific parts of the permeable TE.

In the lowest frequency range, i.e., left-most polar plot under (*a*), noise reduction can be found for all strip groups, with the highest level (≈ 12 dB) found at the TE-tip group although it represents less than one-fifth of the TE planform area. For the blocked TE, the noise reduction levels at both TE-junction and TE-tip groups are similar to those of the porous TE. However, the former's mid-TE group shows significantly smaller values

compared to the latter's, which results in a lower total noise reduction level. In the frequency range $8 < St_c < 16$, the OSPL values for both porous and blocked TE are almost identical. The noise reduction at the TE-tip group remains the highest, although the maximum ΔOSPL is 2.5 dB lower than in the previous frequency range. Nevertheless, the decrease in ΔOSPL is more noticeable for mid-TE and TE-junction groups. This implies that the thicker segments of the porous insert (near the solid-porous junction) contribute less to noise attenuation compared to the thinner ones (near the TE tip). In the highest Strouhal number range, the mid-TE group of the porous TE generates substantial excess noise. However, the excess noise level is slightly lower for the blocked TE, suggesting that the presence of the solid partition also affects roughness-noise generation. The TE-junction also contributes to the high-frequency noise increase, particularly towards the downstream direction. This is in agreement with Kisil and Ayton [47], where the TE tip was found to scatter sound predominantly towards the upstream direction, similar to that of the solid TE. However, the noise radiation at the solid-porous junction tends to be towards the opposite direction, and this discrepancy becomes more prominent at higher frequencies. Unlike the others, the TE-tip groups for both types of permeable TE are still producing slight noise reduction.

3.5. FLOW FIELD CHARACTERISATION

The analyses in section 3.4 have confirmed that the permeability across the porous medium, which connects the flow fields on the suction and pressure sides of the airfoil, is essential for achieving noise reduction. Nevertheless, the porous inserts have been found in the previous sections to affect the boundary layer organisation, which is relevant to TE noise generation mechanisms. To obtain better insights into this aspect, the effects of different porous TE inserts, including the blocked variants, on the flow field are analysed in this section.

3.5.1. BOUNDARY-LAYER PROPERTIES

The integral boundary layer quantities and turbulence statistics for the airfoils with metal-foam inserts are presented in figure 3.25. Plot (a) compares the boundary layer thickness (δ_{99}), displacement thickness (δ^*), and momentum thickness (θ^*). Although, the no-slip condition is not applicable on a porous surface, boundary layer parameters for the porous and blocked TE cases are defined and evaluated in the same manner as the solid one. It is evident that the porous and blocked TE cause the boundary layer thickness to grow at a faster rate than on the solid TE, and thus, the permeable inserts are expected to produce higher drag. This finding is interesting considering that the metal-foam TE is modelled using the combined APM-PM layers and therefore, the surface roughness effect has been neglected. Figure 3.25 (b) presents the streamwise velocity fluctuations spectra S_{uu} in the turbulent boundary layer. The S_{uu} has been normalised with a reference velocity of 1 m/s. Compared to solid TE, the porous one has been found to enhance the velocity fluctuations mainly in the low frequency range ($St_c < 10$), but the higher frequencies are relatively unaffected.

The effects of the porous TE on the boundary layer profile are illustrated in figure 3.26, which shows the profiles of mean stream velocity U and root-mean-square of

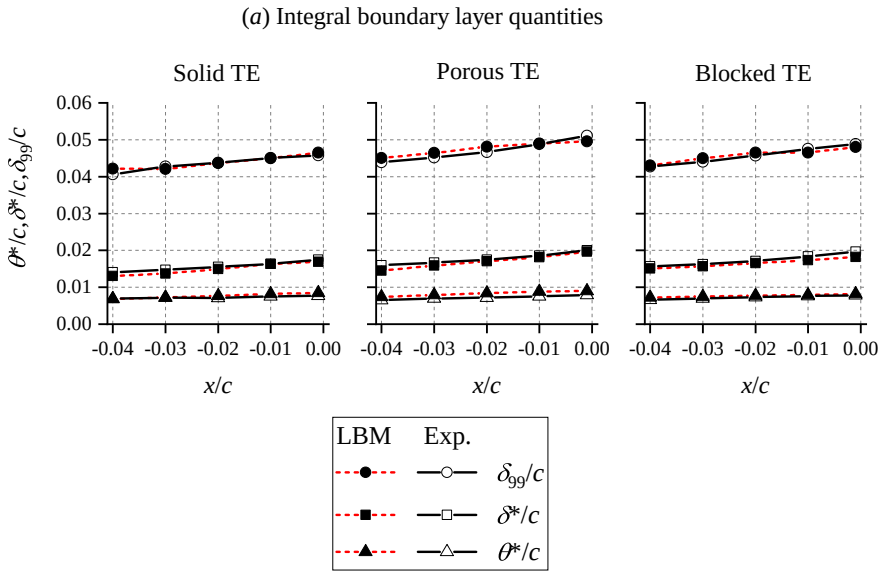

Figure 3.25: (Metal foam/modelled) (*a*) The integral boundary layer parameters along the last 4 % of the airfoil chord, and (*b*) the autospectra of streamwise velocity fluctuations S_{uu} near the TE. Experimental data are taken from Rubio Carpio *et al.* [51].

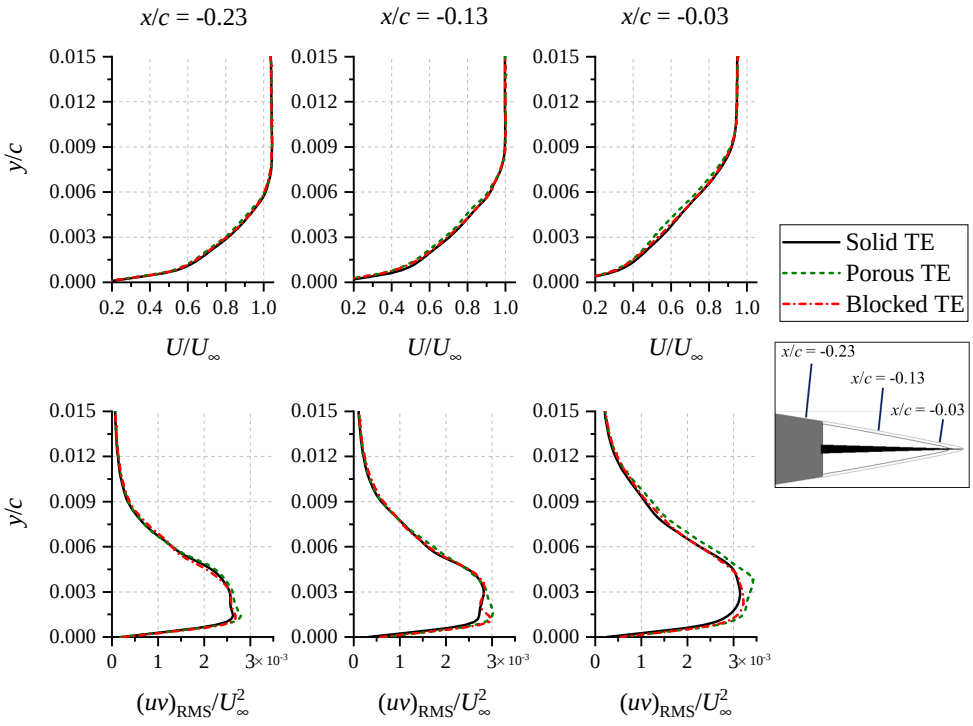

Figure 3.26: (Metal foam/modelled) Boundary layer profiles for the time-averaged streamwise velocity (U) and the root-mean-square of the Reynolds stress $(uv)_{\mathrm{RMS}}$ at different locations along the TE region. The sampling lines for the boundary layer profiles are shown in the inset depicting a segment of the blocked TE.

Reynolds stress $(uv)_{\mathrm{RMS}}$ at different locations along the TE region. Slightly upstream of the solid-porous junction ($x/c = -0.23$), the mean velocity profiles for all TE types can still be considered identical, although the porous TE has begun to exhibit slightly higher $(uv)_{\mathrm{RMS}}$ at the inner part of the boundary layer. The mean velocity deficit caused by the porous TE becomes more prominent downstream of the solid-porous junction, but the boundary layer profile on the blocked TE is still similar relative to that of solid TE. Both the porous and blocked TE exhibit enhanced Reynolds stress at the inner layer region, but the former affects a wider range of wall distance. At $x/c = -0.03$, near the TE tip, the mean velocity deficit of the porous TE increases further, but that of the blocked TE remains minor. The increase in $(uv)_{\mathrm{RMS}}$ for the porous TE is also found to affect the upper part of the boundary layer, unlike for the blocked TE where the $(uv)_{\mathrm{RMS}}$ level rises only at the inner region. Following this, one can conclude that the porous insert enhances the wall shear [83] due to surface permeability, which results in increased turbulence production. The porous-cell inserts also show similar trends in figure 3.11.

The boundary layer profiles for the metal-foam TE at a positive AoA are provided in figure 3.27; the zero AoA case at 20 m/s is included from figure 3.26 for completeness. The wall-distance (vertical axis) shows both positive and negative values corresponding to those for suction and pressure sides of the airfoil respectively. When the airfoil is at a

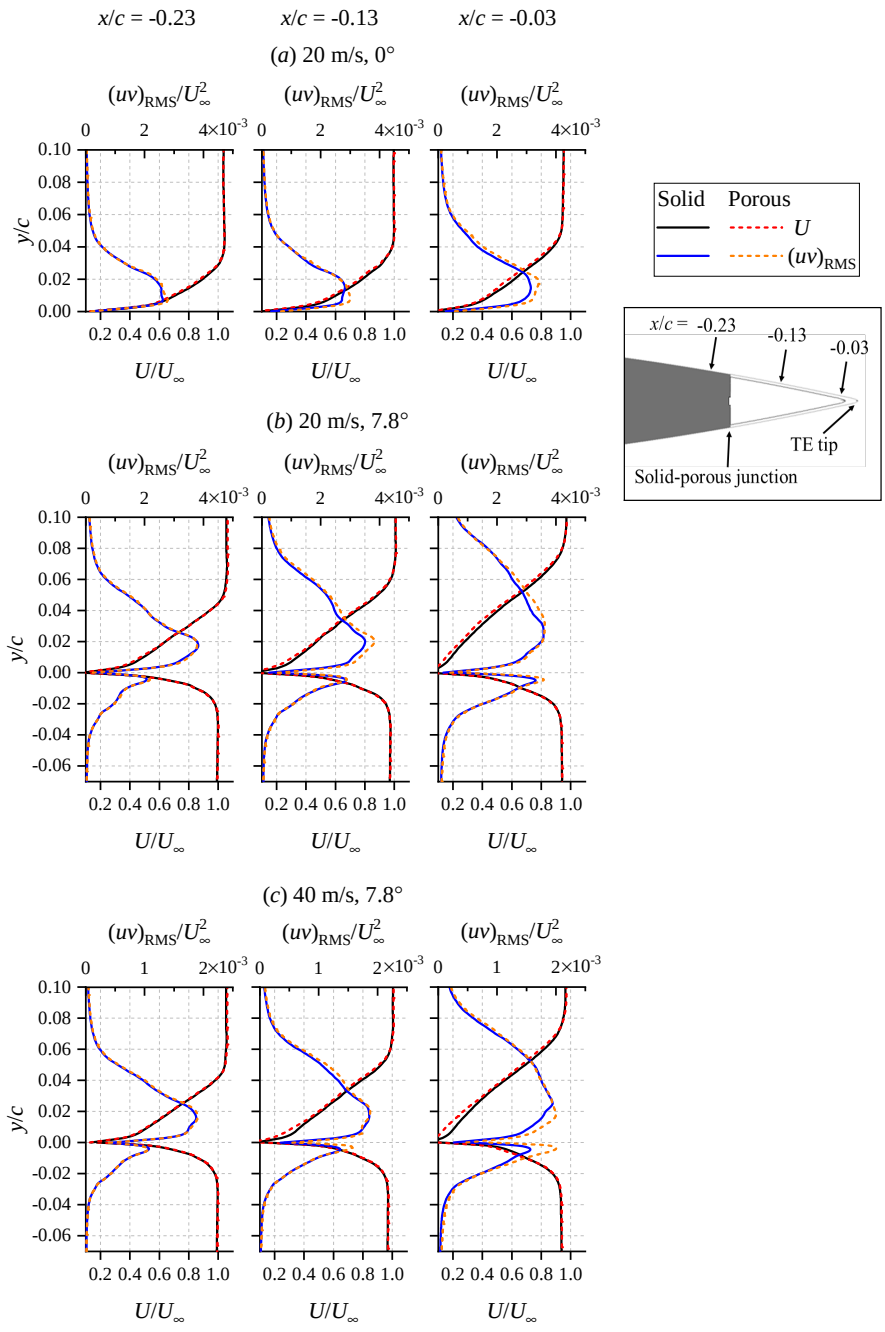

Figure 3.27: (Metal foam/modelled) Comparison of boundary layer profiles for solid and porous TE, depicting the mean wall-parallel velocity U and the root-mean-square of Reynolds stress $(uv)_{\mathrm{RMS}}$. The profiles are plotted along the local wall-normal direction. The inset below the legend illustrates the locations where the profiles are sampled.

lifting condition, the boundary layer grows at a faster rate along the suction side due to the stronger adverse pressure gradient, which also causes the mean velocity profile to inflect inward (i.e., flow deceleration) along the inner region of the boundary layer [84]. Similarly, the peak $(uv)_{\mathrm{RMS}}$ level is higher compared to that of the zero AoA condition. At the higher AoA, the velocity deficit caused by the porous TE becomes more noticeable along the suction side, especially at $x/c = -0.03$. Conversely, the velocity deficit at pressure side is quite small, although this is accompanied by a substantial increase in the peak $(uv)_{\mathrm{RMS}}$ value. A higher $(uv)_{\mathrm{RMS}}$ level can be linked to the generation of stronger surface pressure fluctuations [85, 86], and in turn, the presence of more intense noise sources on the porous TE, as discussed previously in figure 3.22. The plots corresponding to the 40 m/s cases also show similar phenomena, and in particular, the enhancement of the Reynolds stress by the porous medium surface near the TE tip becomes more prominent. It is also possible to deduce that the influence of the porous TE on turbulent fluctuations in the boundary layer depends on the proximity of the turbulent eddies to the porous medium surface.

The observations made throughout figures 3.26 and 3.27 also reflect the overall trends for the porous-cell inserts in figure 3.11, where the surface roughness effect is present. Hence, it is possible to conclude that the surface permeability plays a more dominant role than the surface roughness effect in altering the boundary-layer properties.

3.5.2. FLOW FIELD VISUALISATION INSIDE THE POROUS MEDIUM

The usage of numerical simulations allows for taking a glimpse at the flow field inside the porous medium, which will be discussed further in this subsection. Flow field information inside the metal-foam inserts are depicted using contours in figure 3.28. The figure shows that the contours of mean streamwise (x) velocity component U of both porous and blocked TE cases are dominated by regions with negative velocity. These are weak recirculation regions that resemble those observed in the porous flat-plate of Ali *et al.* [87]. Contours of the mean vertical (y) velocity component V confirm that there is no mean cross-flow between both sides of the airfoil due to symmetrical loading condition. However, the contours of root-mean-square (RMS) of velocity fluctuations show more noticeable differences between the porous and blocked TE. In both cases, nonetheless, the intensity of velocity fluctuations in the porous medium is relatively low (i.e., $\mathcal{O}(10^{-2})$ of U_∞), especially further away from the porous medium surface. This is related to the concept of entrance length that has been introduced in the previous chapter. Compared to the porous TE, the blocked TE shows a larger region near the TE tip where the u_{RMS} values are higher, although the u_{RMS} in both cases tend to increase in the downstream direction where the flow resistance is lower due to the smaller porous-medium thickness. The v_{RMS} of the blocked TE tends to zero towards the symmetry plane of the trailing edge due to the presence of the solid core. In contrast, the contour for the porous TE shows that the v_{RMS} gradually increases towards the downstream direction. It implies that the presence of aerodynamic interactions between the turbulent fluctuations at both sides of the airfoil, which is responsible for noise attenuation, is mainly concentrated near the TE tip. This further corroborates the findings in section 3.4.

When an airfoil with a porous TE is installed at a lifting condition, the pressure

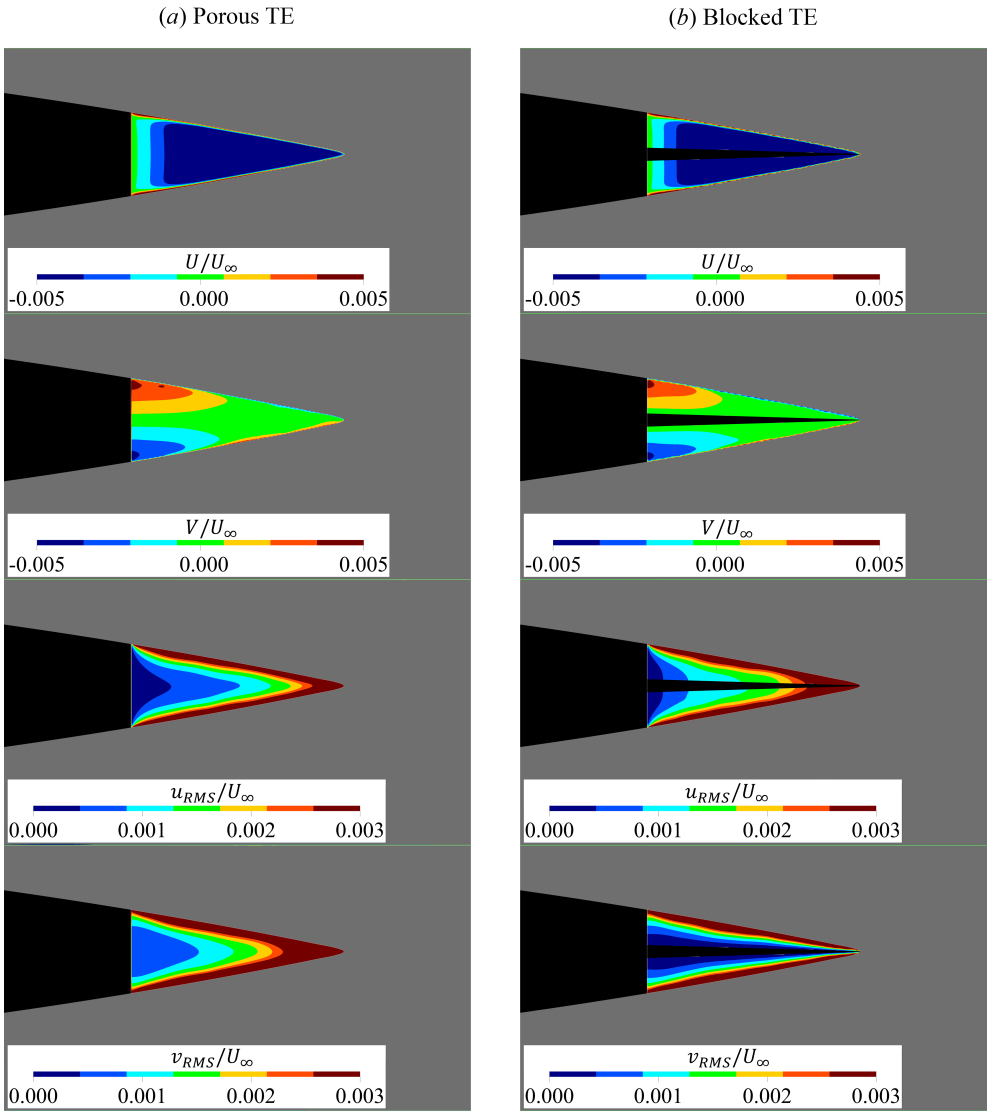

Figure 3.28: (Metal foam/modelled) Contours of velocity statistics in the porous-medium region of porous and blocked TE normalised with U_∞; the mean velocity components in x (U) and y directions (V) are in the first and second rows respectively, and the corresponding root-mean-square of velocity fluctuations (u_{RMS} and v_{RMS}) are in the third and fourth rows respectively. Regions outside of the porous medium are masked in grey.

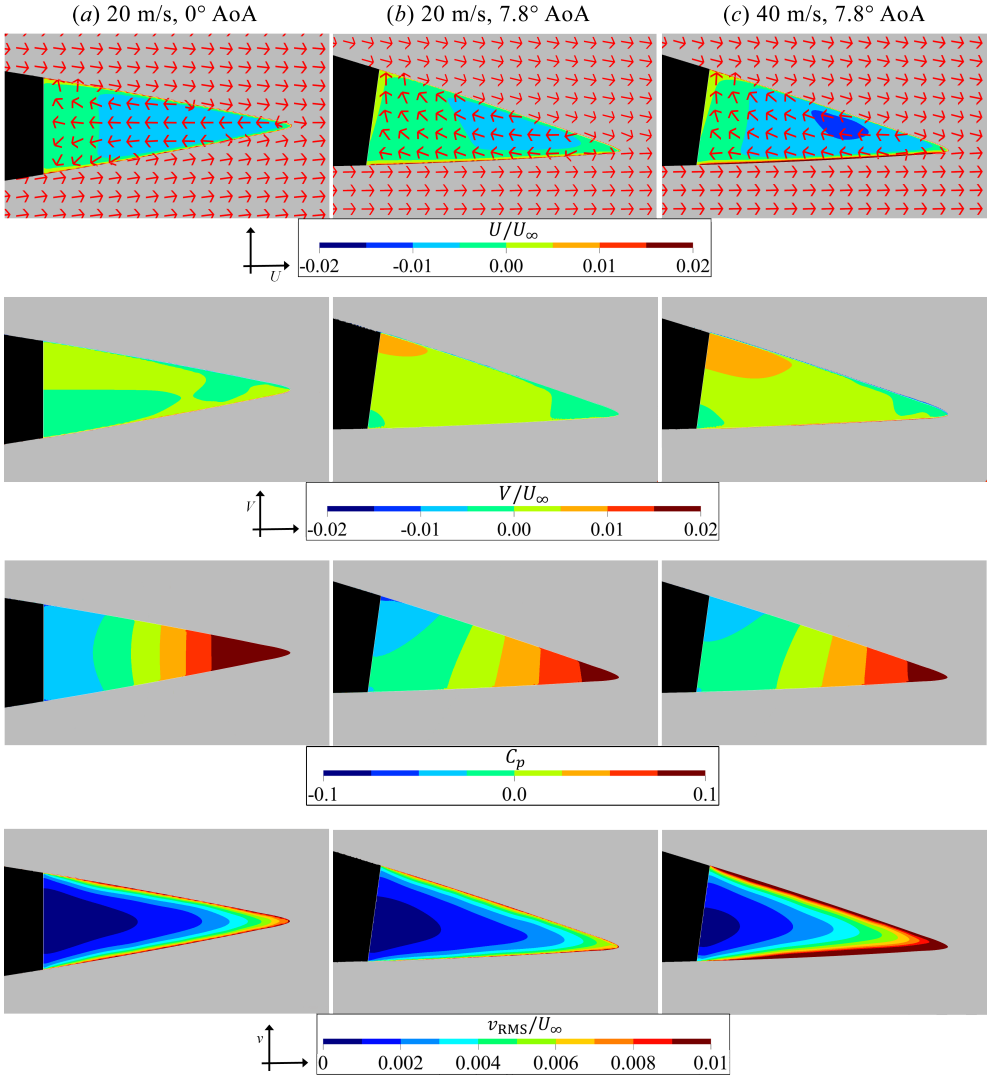

Figure 3.29: (Metal foam/modelled) The lateral view of the porous TE superimposed by contours of time-averaged streamwise and vertical velocity components (U and V respectively), time-averaged pressure coefficient C_p, and the root-mean-square of vertical velocity fluctuations (v_{RMS}) inside the porous medium region at 7.8° AoA. Mean velocity vectors are drawn as red arrows in the U contours. External fluid region is masked in grey color.

difference between the suction and pressure sides at the TE region may cause a mean cross-flow. This is verified further in figure 3.29. Note that the pressure coefficient has been defined as $C_p = (\langle p \rangle - p_\infty)/(0.5\rho_\infty U_\infty^2)$, where $\langle p \rangle$ is the time-averaged pressure.

The figure evidences that a mean cross-flow is negligible inside the porous medium given that the mean vertical velocity V is relatively small (i.e., $V \approx 0$). The same conclusion can be inferred from the velocity vectors in the mean streamwise velocity U contours. Furthermore, the C_p contours shows that the static pressure variation in the vertical direction is less prominent compared to that in the streamwise direction. It will be shown in section 3.7 that the surface pressure difference between the opposite sides of the NACA 0018 airfoil is quite small at the last 10 % of the chord. Since the C_p distribution is linked to the airfoil shape, it is still possible for a stronger mean cross-flow to be present in other airfoil types. The velocity vectors that are plotted in the U contours show that the flow field mainly enters the porous medium at the downstream half of the TE, recirculates, and later exits near the solid-porous junction. Such recirculation pattern has also been found previously for the zero AoA case, and it can be considered to be driven by the streamwise adverse pressure gradient that is shown in the C_p contours.

It would also be interesting to determine whether the trends for the metal-foam TE, which is modelled by an equivalent fluid region, would resemble those for the fully-resolved porous-cell insert. Note that both porous materials have different permeability values.

The flow field inside the porous-cell inserts are investigated using contours sampled at the airfoil midspan in figures 3.30 and 3.31. A comparison of the time-averaged contours between the solid, porous, and partially-blocked cases are shown in figure 3.30 (*a*). Both permeable TE configurations are found to promote faster boundary-layer growth, resulting in a wider wake compared to that of the solid TE. The velocity magnitude inside the porous medium is relatively small compared to that of the freestream (i.e., $|\boldsymbol{U}| < 0.1U_\infty$), which is also evidenced by the contours of streamwise and vertical velocity components in (*b*) and (*c*) respectively. Contours (*b*1) and (*b*2) depict the recirculation regions inside the porous medium, where U values tend to be negative. Streaklines in the contours clearly evidence the external flow entering the porous medium through the open pores at both sides of the porous insert. Some streaklines in the porous TE can be observed to flow past the chord line, but this not the case in the blocked TE due to the solid partition.

The contours of root-mean-square (RMS) of velocity and pressure fluctuations are provided in figure 3.31, where velocity quantities are normalised with the freestream velocity U_∞, and the pressure one with the freestream dynamic pressure q_∞. Comparing u_{RMS} and v_{RMS} contours between the three cases, it is clear that both types of porous-cell inserts cause stronger velocity fluctuations in the boundary layer, which also indicates an enhanced turbulence generation near the porous medium surface. Large velocity fluctuations can be found inside the porous medium, but they are limited to the first cells next to the surface. These regions roughly coincide with the predicted entrance length, which is delimited with red lines in the contours. Inside the porous TE, the intensity of velocity fluctuations along the chord line tends to increase in the downstream direction where the porous material thickness is smaller. However, it decreases to zero near the chord line of the blocked TE due to the solid partition, similar as in figure 3.28.

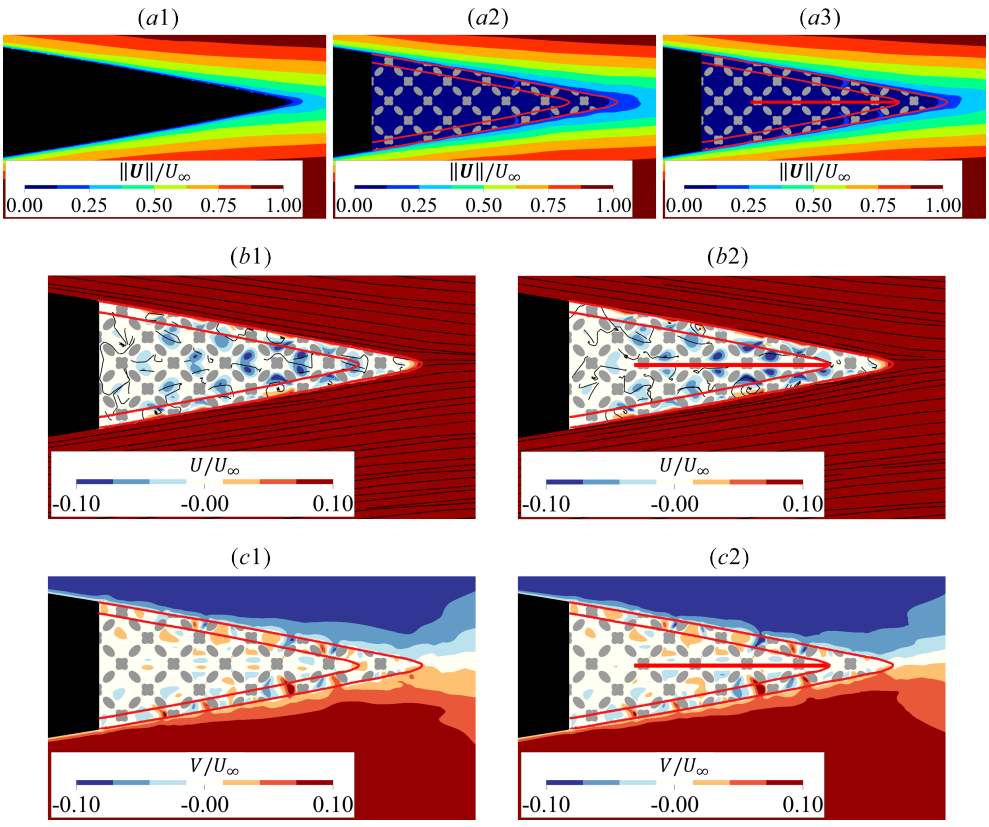

Figure 3.30: (Porous cell/fully-resolved) Comparison of contours of velocity magnitude $||\boldsymbol{U}||$ (*a*), and contours of mean velocity components in the streamwise U (*b*) and vertical V (*c*) directions for the porous and blocked TE cases. The estimated entrance length is outlined with red lines. Streaklines are also provided in contours (*b*1) and (*b*2).

In contours (*c*1-3), pressure fluctuations in the boundary layer are shown to be more intense for both porous and blocked TE cases compared to the solid one due to the enhanced turbulence intensity. Locally, higher p_{RMS} level at the porous medium surface tends to be concentrated at the downstream edge of the open pores. As described by Devenport *et al.* [88], these locations could be responsible for generating excess high-frequency noise as previously indicated by the FIND algorithm in figure 3.18. The flow field across the open pores also resembles that of cavity flow although resonance phenomenon appears to be absent from the acoustic results in figure 3.12. Compared to the porous TE, pressure fluctuations near the chord line of the blocked TE are more intense, which can be attributed to the higher velocity gradient [85] from the blockage introduced by the solid partition.

Based on the observations in figures 3.30 and 3.31, the solid partition of the blocked TE appears to have a relatively small influence on the flow field outside of the porous medium. However, it clearly alters pressure and velocity fluctuations inside the porous

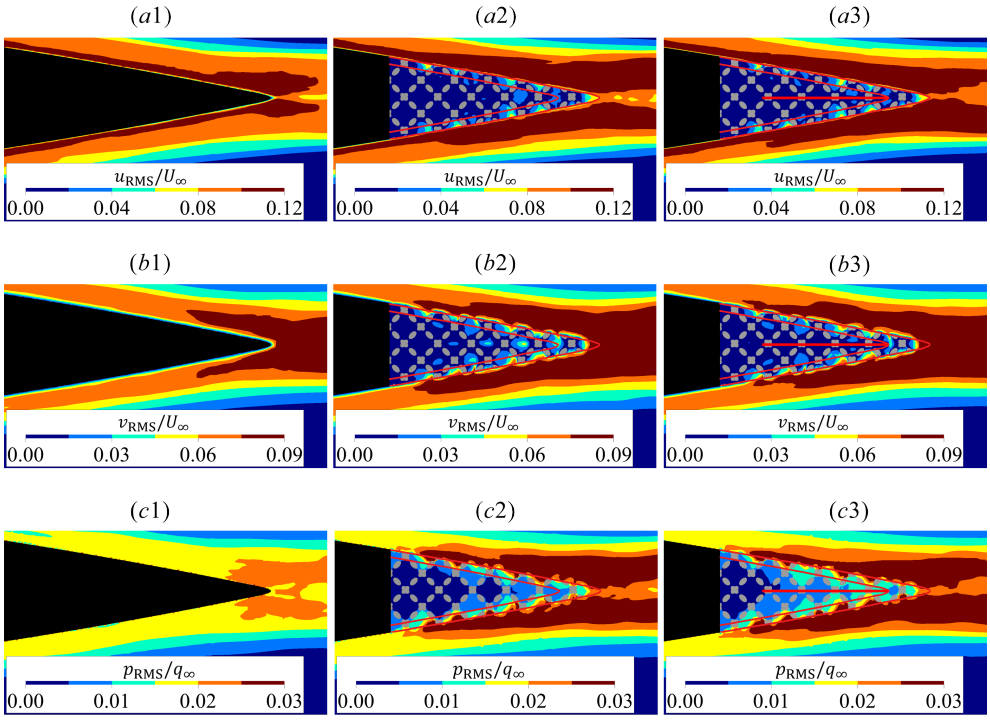

Figure 3.31: (Porous cell/fully-resolved) Contours of root-mean-square of velocity fluctuations in the streamwise u_{RMS} (*a*) and vertical directions v_{RMS} (*b*), and the contours of root-mean-square of pressure fluctuations p_{RMS} (*c*). The estimated entrance length is outlined with red lines. Solid TE is shown at the left column, porous TE at the middle, and blocked TE at the right one.

medium, particularly near the TE tip. This is unsurprising considering that as the local porous medium thickness becomes comparable to the entrance length, the flow field outside of the porous insert can start influencing that inside of it, and vice versa.

3.6. TURBULENT PRESSURE FLUCTUATIONS

3.6.1. SURFACE PRESSURE STATISTICS

In section 3.5, the usage of a permeable TE insert has been demonstrated to affect the inner region of the turbulent boundary layer [44, 60]. While the surface pressure field would be altered as a consequence, it is still unclear whether the changes could be directly associated with the noise reduction mechanism [16]. Therefore this subsection examines the surface pressure fluctuation statistics, such as autospectra (power spectral density) and spanwise coherence length. These parameters have been chosen as they are relevant in the analytical formulation of broadband TE noise for solid surfaces, such as the model of Amiet's [16, 92].

The analysis is first performed for the metal-foam TE cases, which is provided in figure 3.32. The power spectral density of surface pressure fluctuations Φ_{pp} are plotted at

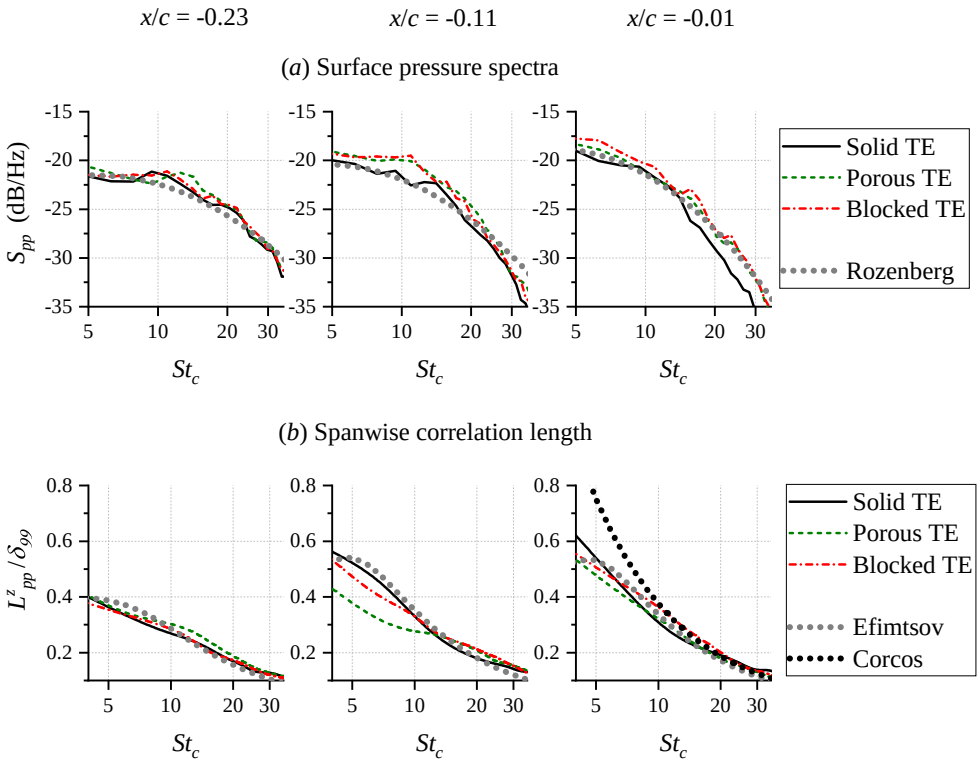

Figure 3.32: (Metal foam/modelled) The comparison of power spectral density of surface pressure fluctuations (S_{pp}) and spanwise coherence length (L^z_{pp}) between the three trailing edge treatments. The S_{pp} has been normalised with a reference pressure of 1 Pa, while L^z_{pp} with the δ_{99} for the solid TE. For comparison, the prediction of Rozenberg's model [89] is included in plot (*a*), and Corcos' [19] and Efimtsov's [90, 91] in (*b*).

$x/c = -0.23, -0.11,$ and -0.01, which correspond to a position upstream of the solid-porous junction for both porous and blocked TE cases, halfway between the solid-porous junction and the trailing edge, and near the trailing edge respectively. For both the porous and blocked TE, Φ_{pp} is computed at the external APM interface. Figure 3.32 (*a*) confirms that upstream of the solid-porous junction, pressure fluctuations in the boundary layer are hardly affected by the different TE types, which is in line with the experimental observation of Rubio Carpio *et al.* [60]. At $x/c = -0.11$, the Φ_{pp} for both the porous and blocked TE increase above that of the solid TE, with the largest difference being located in the low frequency range ($5 < St_c < 10$). The pressure fluctuations spectra of the solid TE are also compared with those predicted with the Rozenberg *et al.* [89] model using the boundary layer parameters on the solid TE as the input. A good agreement is found up to $St_c = 30$, while at higher frequencies, the slope of the simulation result is steeper than that of Rozenberg's. Near the TE tip, at $x/c = -0.01$, the Φ_{pp} difference between the solid TE and porous TE becomes smaller, particularly in the low frequency range.

Due to the unsteady flow transpiration at the porous medium surface, it is possible

that the spanwise coherence length in the turbulent boundary layer becomes smaller with respect to that on a solid TE. As a matter of fact, reducing the spanwise coherence of the surface pressure fluctuations would also contribute towards noise attenuation [16], and thus, the spanwise coherence length is also a relevant parameter to examine. The coherence length of the surface pressure fluctuations $l^z_{pp}(\omega)$ is defined as the integral of the coherence function in the spanwise direction as follows.

$$l^z_{pp}(\omega) = \lim_{L\to\infty} \int_0^L \sqrt{\gamma^2_{pp}(\omega, \Delta z)} \mathrm{d}\Delta z, \tag{3.9}$$

where γ^2_{pp} is the magnitude-squared coherence between surface pressure fluctuations at two points along the spanwise (z) direction and separated by Δz. γ^2 is defined as follows:

$$\gamma^2(\omega, \Delta z) = \frac{|C(\omega, z_1, z_2)|^2}{|C(\omega, z_1, z_1)||C(\omega, z_2, z_2)|}, \tag{3.10}$$

where $C(\omega, z_1, z_2)$ is the cross-power spectral density between the points at z_1 and z_2, which is defined as in equation 3.11.

$$C(\omega, z_1, z_2) = \int_{-\infty}^{\infty} \left[\int_{-\infty}^{\infty} p'_{z_1}(t) p'_{z_2}(t + \Delta t) \mathrm{d}\Delta t \right] \mathrm{e}^{j\omega t} \mathrm{d}t, \tag{3.11}$$

γ^2_{pp} is computed using a periodogram method with Hanning window and 50 % overlap, resulting in a frequency resolution of 100 Hz. However, due to the relatively short simulation time, additional procedures are employed to improve the convergence of the results. Firstly, the γ^2_{pp} value at each chordwise position is averaged along the airfoil span in between $-0.015 < z/c < 0.015$. Furthermore, a curve-fitting approach based on an exponential function is adopted to ensure that γ^2_{pp} is reduced to zero at large Δz. The exponential function is defined as follows [91, 93]:

$$\gamma(\omega, \Delta z)_{pp} = e^{-\frac{|\Delta z|}{l^z_{pp}(\omega)}}. \tag{3.12}$$

The coherence length l^z_{pp} plots at three different locations are shown in figure 3.32 (*b*). The quantity has been normalised with the boundary layer thickness at the trailing edge of the solid TE case (δ_{99}). Similarly to the surface pressure spectra trends in figure 3.32 (*a*), the coherence length distributions of the three types of TE insert have very similar trends at $x/c = -0.23$. Downstream of the solid-porous junction, at $x/c = -0.11$, the l^z_{pp} of the solid TE increases above the levels of both the porous and blocked TE, particularly in the low frequency range. Above $St_c = 12$, however, all three cases remain comparable to each other. This behaviour might be attributed to the enhanced turbulent mixing process near the porous-medium surface as reported by Koh *et al.* [55]. At $x/c = -0.01$, the l^z_{pp} plots for all three cases are also similar, although the coherence length for the solid TE is slightly higher at $St_c < 8$. The l^z_{pp} for the solid TE at the three stations are also compared with Corcos' [19] and Efimtsov's [90, 91] models using local flow-field information as input; the

Corcos constant is equal to 1/2.1 following Pröbsting *et al.* [94] and Amiet [16]. The trends from the simulations are generally in line with those of Efimtsov's. The curve of the solid TE at $x/c = -0.01$ is also in good agreement with Corcos' model for $St_c > 14$. Overall, the coherence length trends of the different trailing-edge treatments are of comparable magnitudes, particularly near the solid-porous interface and the TE tip.

These figures have shown that the porous trailing edge can affect the flow-field statistics at the TE region. Based on the observed trends, however, it can be deduced that a permeable TE insert would not attenuate noise if it were assumed to share similar aeroacoustics behaviours as a solid TE [16]. As a matter of fact, it has been shown previously in section 3.4 that the noise scattering descriptions of a permeable TE insert are quite different from its fully-solid counterpart. Thus, noise prediction methods for a solid TE might not always be readily applicable for the porous one [40, 60].

Similar analyses are performed for metal-foam inserts at different AoA and Reynolds number settings. The surface pressure fluctuations spectra S_{pp} are presented in figure 3.33 as contours that are plotted for several depth ratios y/d, where d equals to half of the local porous insert thickness. Thus, the porous medium surface corresponds to $y/d = 1$, whereas $y/d = 0$ is located along the chord line.

Figure 3.33 (*a*) shows the pressure fluctuations spectra for the zero AoA cases. On the solid TE, pressure fluctuations tend to become stronger towards the TE tip as the boundary layer grows due to the adverse pressure gradient on the airfoil [89]. The S_{pp} levels on the porous TE are similar to the solid one upstream of the solid-porous junction ($x/c < -0.2$), but it increases substantially further downstream, reflecting figure 3.32. This is related to the enhanced $(uv)_{\mathrm{RMS}}$ level as depicted in figure 3.27 (*a*). When a positive AoA is introduced as shown in figure 3.33 (*a*), the surface pressure fluctuations distribution on the porous TE is still closely resembling that of the solid TE, but a noticeable increase in S_{pp} level can be found along the pressure side. This is due to the dominant turbulent eddies, indicated by the peak $(uv)_{\mathrm{RMS}}$ in figure 3.27, on the suction side being convected further away from the porous surface as the boundary layer approaches the TE tip. On the other hand, the peak $(uv)_{\mathrm{RMS}}$ position on the pressure side does not vary substantially, despite the increasing Reynolds stress level following the boundary layer growth.

Overall, the surface pressure fluctuations levels on the porous TE are stronger than on the solid TE as the porous medium enhances the surface shear. This might be the reason behind the stronger local source intensity near the tip ($x/c = 0$) of the porous TE, particularly at low frequencies (see figure 3.22 for $4 < St_c < 8$). However, the pressure fluctuations level drops significantly inside the porous medium. Averaged along the upstream half of the porous TE extent ($-0.2 < x/c < -0.1$), the S_{pp} level along the chord line of the porous TE is 12 dB lower than that at the surface. This difference decreases to around 5 dB at the last 4 % of the airfoil chord where the local thickness is relatively small (e.g., approximately twice the pore diameter). Considering that the noise mitigation of a permeable TE insert is enabled by the unsteady pressure interaction across the porous material (i.e., pressure release process [41]), it is conjectured that the pressure release process would only take place at the segment of the porous insert near the TE tip. This hypothesis will be examined further in the upcoming subsection.

The spanwise coherence lengths (L^z_{pp}) corresponding to the different Reynolds

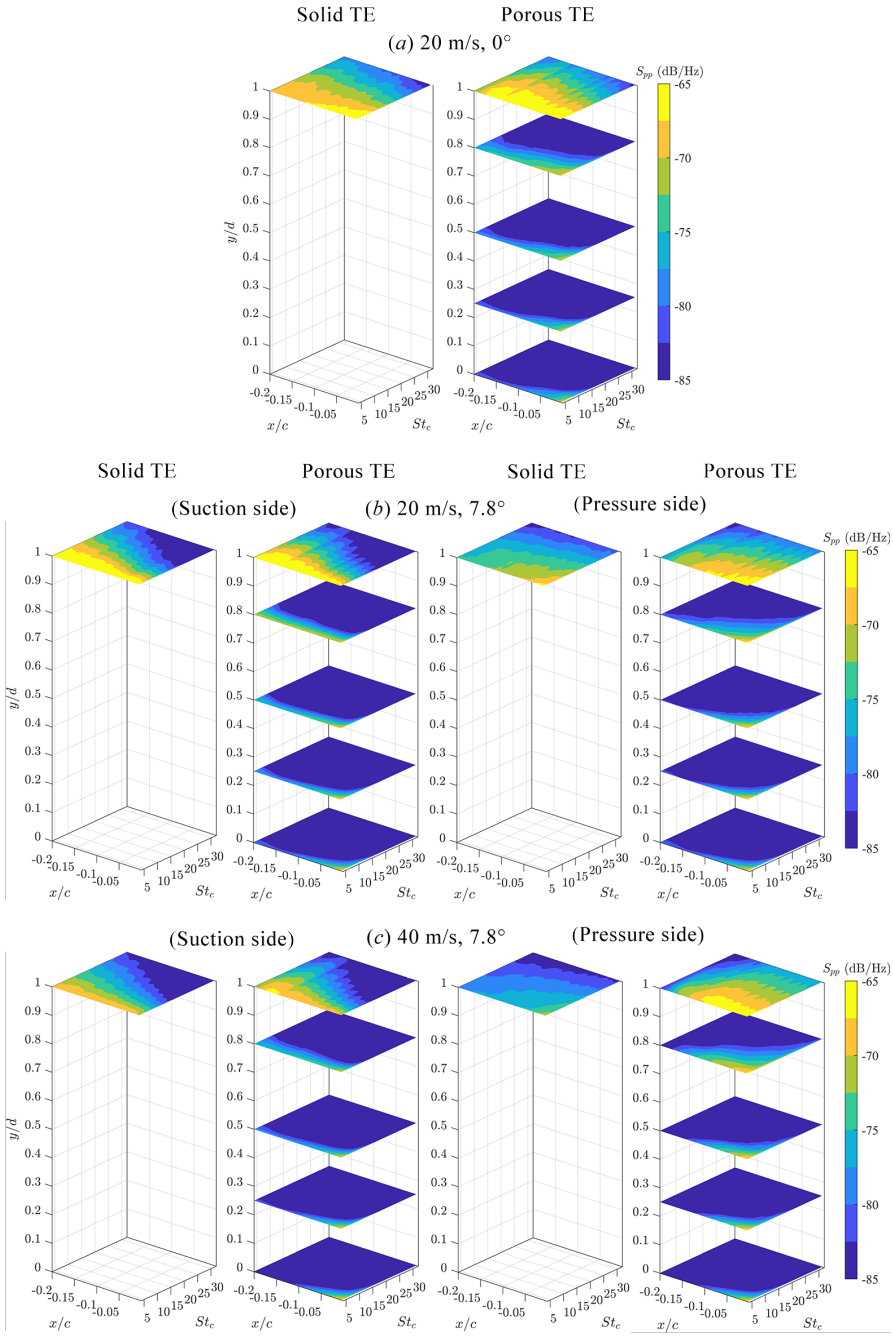

Figure 3.33: (Metal foam/modelled) Contours of spanwise-averaged pressure fluctuations spectra S_{pp} along the last 20 % of the airfoil chord. For porous TE, the contours are plotted for different depth ratio y/d; for pressure side plots, the y/d direction is reversed. S_{pp} has been normalized against freestream dynamic pressure q_∞^2.

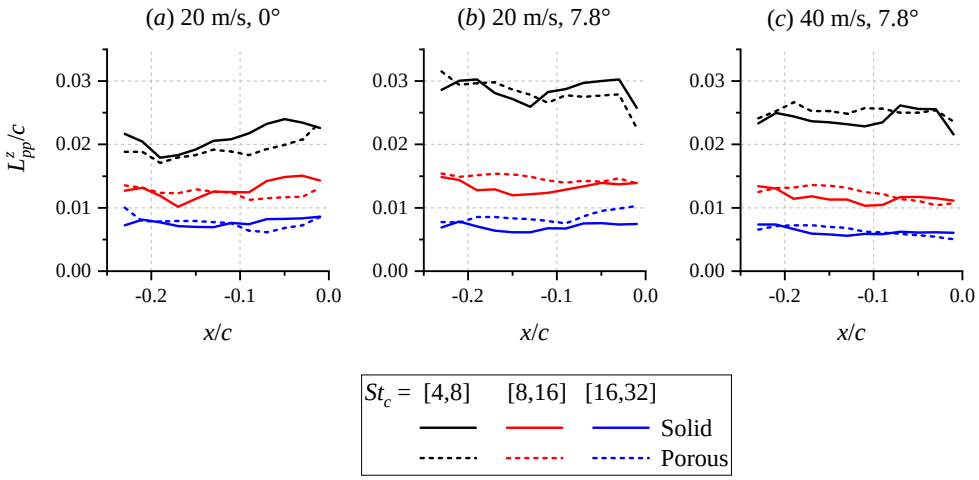

Figure 3.34: (Metal foam/modelled) Comparison of streamwise distribution of spanwise correlation length of surface pressure fluctuations L^z_{pp} between the solid and porous TE at different inflow conditions. For plots (*b*) and (*c*), the values at the suction side are presented.

numbers and AoA settings are given in figure 3.34. The L^z_{pp} values has been averaged in 3 frequency bands, and they are also computed at 2 additional reference spanwise locations that are $0.05c$ apart from the TE midspan to obtain the spanwise-averaged results. Plot (*a*) reveals that the correlation lengths tend to increase towards the TE tip as the boundary layer grows on the solid TE. Interestingly for the porous TE, the L^z_{pp} values become smaller than the solid TE ones near $x/c = -0.1$, but both TE types show similar correlation lengths near the TE tip. Increasing the AoA in plot (*b*), the L^z_{pp} values become larger, especially for the low frequency band ($St_c = [4,8]$). However, the difference between the solid and porous TE becomes less prominent at this inflow condition. Similar behaviors can be found for the higher Reynolds number case in plot (*c*). Thus, this finding further corroborates the argument that the spanwise correlation length does not play a major role in realising noise attenuation.

The analysis in figure 3.33 is also carried out for the fully-resolved porous-cell inserts, and the results are shown in figure 3.35. As expected, both types of permeable inserts generate higher S_{pp} level throughout the TE region, where an average difference of 4 dB with respect to that on the solid TE can be found in the low frequency range (i.e., $4 < St_c < 8$). Going deeper into the porous medium, the S_{pp} values drop substantially, especially near the solid-porous junction. This is expected since the resistance imposed on the unsteady pressure field is proportional to the distance from the porous medium surface [39]. For instance, S_{pp} level in the blocked TE decreases (along $-0.2 < x/c < 0$) by an average of 3 dB between $y/d = 1$ and $y/d = 0.8$. However, at the last 4 % of the airfoil chord ($x/c > -0.04$), the S_{pp} level remains comparable to that at the surface (< 2.5 dB difference). As shown in figure 3.36, the local TE thickness within this chordwise extent is less than half of the unit-cell dimension. Based on this, the entrance length of the porous-cell is estimated to be $1.5d_p$, at least for the present flow configuration. This

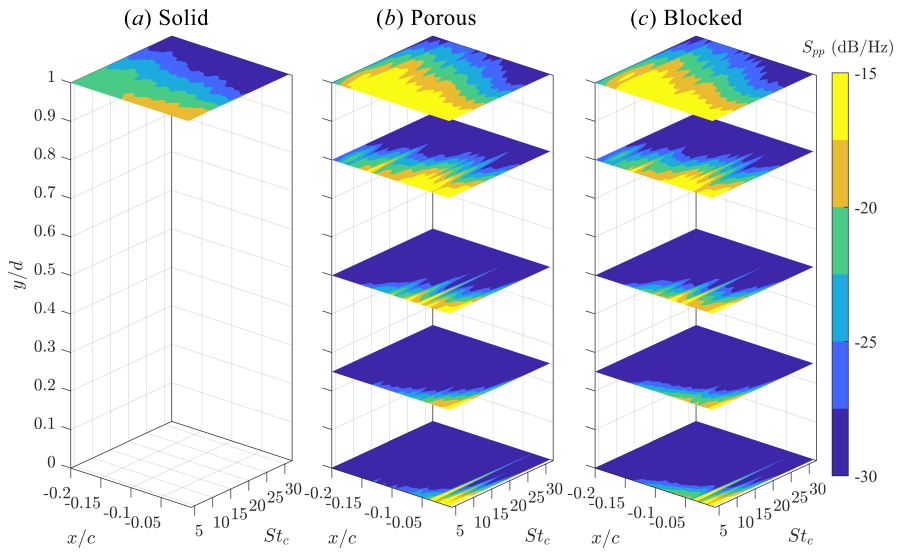

Figure 3.35: (Porous cell/fully-resolved) Contours of spanwise-averaged pressure fluctuations spectra S_{pp} along the last 20 % of the airfoil chord. For porous TE, the contours are drawn at different depth ratio y/d. S_{pp} is normalised with the reference pressure of 1 Pa.

estimate is larger than the 1-pore-diameter estimate that is typically applicable for metal foams [95, 96]. It is also worth mentioning that pressure fluctuations spectra in the blocked TE case are very similar to the porous TE ones, except along the solid partition ($y/d = 0$), where the pressure fluctuations level is slightly enhanced due to the solid partition blockage. Such behaviour further confirms that the solid partition does not significantly affect the external flow field as long as it is embedded beneath the entrance length.

3.6.2. CHARACTERISING PRESSURE RELEASE PROCESS

Following the evanescent wave formulation of Chase [15], the acoustic scattering at a TE is the consequence of a sudden boundary condition adjustment (e.g., from a solid surface to a free wake) encountered by the unsteady pressure field beneath a turbulent boundary layer. This mechanism becomes very efficient in proximity of a sharp edge. Hence, noise attenuation can be achieved by realising a more gradual transition of the surface boundary condition along the TE. This phenomenon has been referred to as the pressure release process in literature [41, 49], and it can be understood as the interaction between the unsteady pressure field on both sides of the porous insert.

In order to visualise the pressure release process, contours of the band-passed pressure fluctuations are plotted in figure 3.37. While this figure only shows the metal-foam TE cases (i.e., modelled using an equivalent fluid region), similar behaviours have been found for the fully-resolved porous-cell inserts. In (*b*), turbulent pressure fluctuations on both sides of the porous TE appear to be connected in the vertical direction, promoting a phase equalisation between the packets as they travel towards the

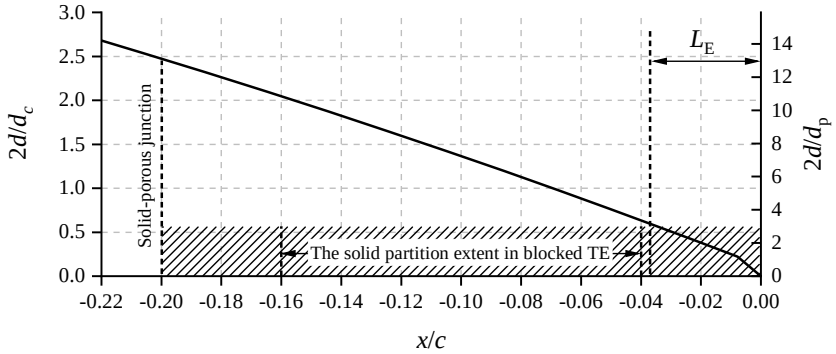

Figure 3.36: (Porous cell/fully-resolved)The chordwise distribution of TE thickness normalised by unit-cell dimension $2d/D$ and mean pore size $2d/d_p$. The estimated two-sided extent of the entrance length is shown as the shaded region. L_E is the chordwise extent of the porous insert where the local thickness is equal to the aforementioned entrance length extent.

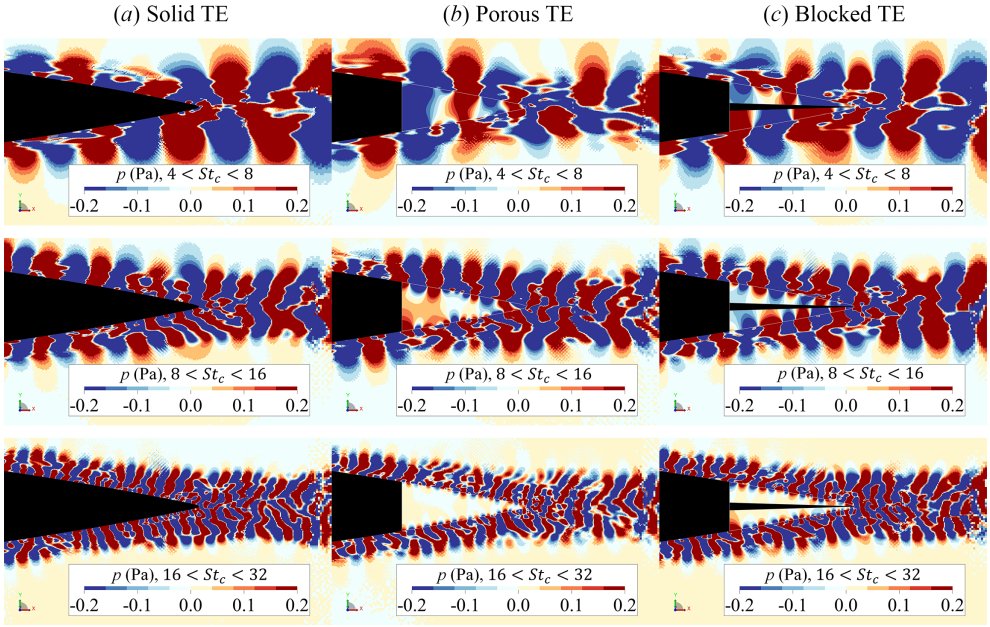

Figure 3.37: (Metal foam/modelled) Instantaneous contours of band-passed pressure fluctuations (p') at the mid-span of the three trailing edge treatments at different frequency bands, i.e., $4 < St_c < 8$ at the top row, $8 < St_c < 16$ at the middle, and $16 < St_c < 32$ at the bottom.

TE tip. However, this phenomenon becomes less prominent at higher frequencies as the weaker fluctuations are dampened more efficiently by the porous medium. Such behaviour might be associated with the smaller noise reduction level in the high-frequency range 3.9. The contours of the blocked TE show that the solid core completely prevents the interaction between pressure fluctuations along the two sides of the airfoil. Without the pressure release process, the blocked TE generates noise with similar intensity as the solid TE, since the acoustic scattering on the blocked TE also takes place primarily at the downstream edge of the solid partition.

For determining where the pressure release process can be found along the porous insert, coherence analyses of pressure and vertical velocity fluctuations on both sides of the porous TE are presented in figure 3.38. Note that the figure shows the results for the fully-resolved porous-cell inserts, and the chordwise extent of the solid partition in the blocked TE is shown in the contours as black and white horizontal lines . The magnitude squared coherence of the surface pressure fluctuations γ^2_{pp} is defined as follows,

$$\gamma^2_{pp}(f,x) = \frac{|C_{pp}(f,x,y_{ss},y_{ps})|^2}{|C_{pp}(f,x,y_{ss},y_{ss})||C_{pp}(f,x,y_{ps},y_{ps})|} \tag{3.13}$$

$$\begin{aligned} C_{pp}(f,x,y_{ss},y_{ps}) &= \int_0^T R(x,y_{ss},y_{ps},t)e^{-j2\pi ft}dt \\ &= |C_{pp}|\left[\cos\left(A_{pp}\right)+j\sin\left(A_{pp}\right)\right] \end{aligned} \tag{3.14}$$

where $C_{pp}(f,x,y_{ss},y_{ps})$ is the cross-power spectral density, at a given chordwise position x, of pressure fluctuations between the suction side y_{ss} and the pressure side y_{ps} of the airfoil. The cross-spectral phase angle is denoted as A_{pp}. γ^2_{pp} is computed using a periodogram method with Hanning window and 50 % overlap, resulting in a frequency resolution of $\Delta f = 100$ Hz (i.e., $\Delta St_c = 1$).

It is evident in figure 3.38 (*a*) that the porous TE allows pressure fluctuations on both sides of the airfoil to be correlated, although significant coherence levels are found only at the last 4 % of the chord; this is identical to the (partially) blocked TE case since the solid partition only extends in between $-0.16 < x/c < -0.04$, while for solid TE, the coherence level remains low in the entire region. Consistently, the A_{pp} contours show that the pressure fluctuations near the actual TE location ($x/c = 0$) are strongly in-phase for the porous and blocked TE cases. Recalling figure 3.36, this particular segment of the porous insert has a thickness that is comparable or smaller than the entrance length. Interestingly, the strip analysis in figure 3.23 previously showed that the cumulative SPL values at strips 10 and 11 ($-0.04 < x/c < 0$) of porous and blocked TE were substantially lower compared to the solid ones. This suggests that the attenuation of noise source intensity is strongly present at regions of the porous TE where the local thickness is small enough to be dominated by the entrance effect. The coherence and phase angle values for both types of porous insert are also almost identical in between $-0.2 < x/c < -0.08$, indicating that once the porous medium becomes sufficiently thick, the interaction between the pressure fluctuations across the porous medium vanishes. At such locations, e.g., near the solid-porous junction, the solid partition has a limited effect on the local

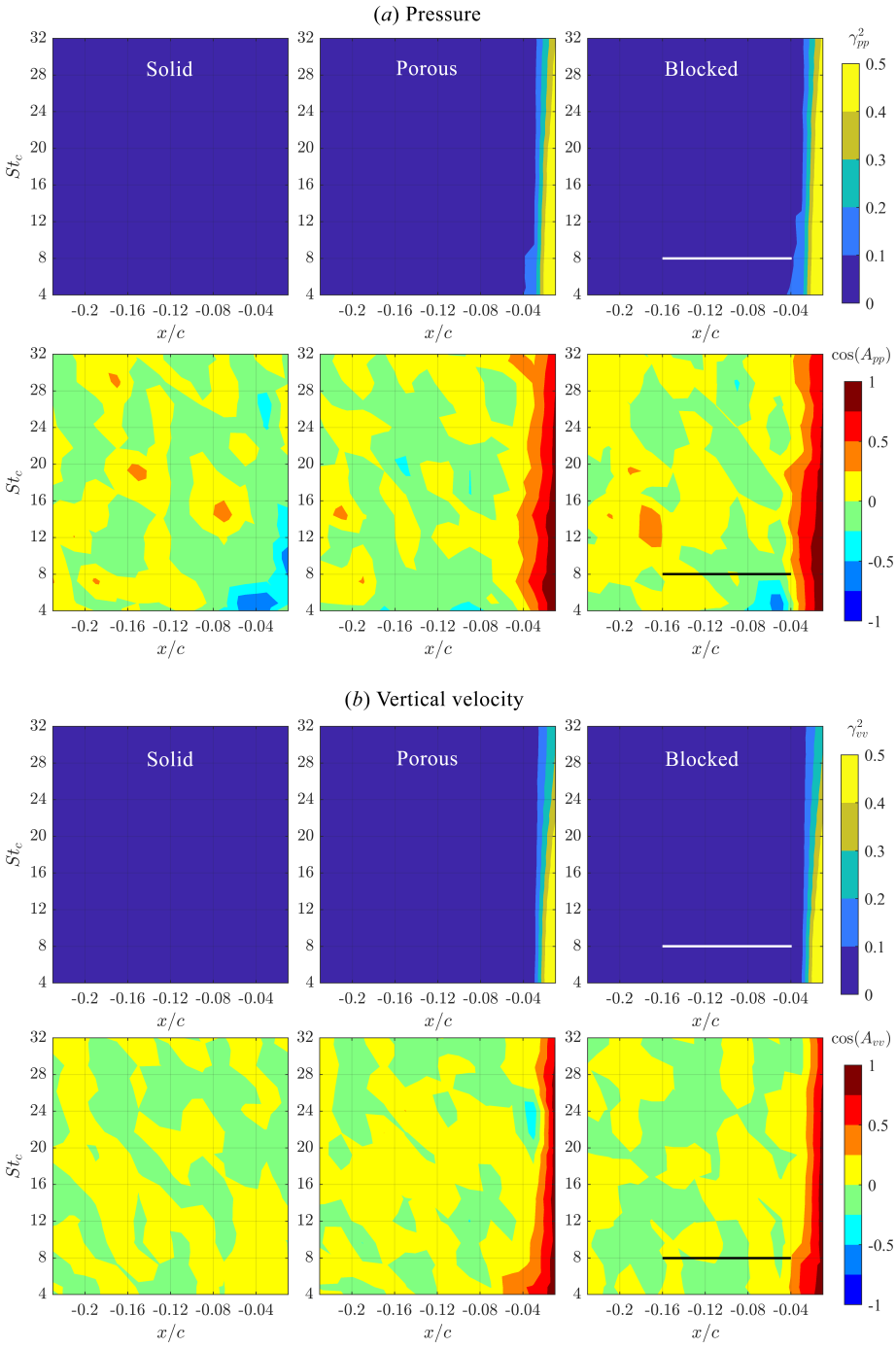

Figure 3.38: (Porous cell/fully-resolved) Contours of magnitude-squared-coherence of surface pressure fluctuations (γ^2_{pp}) and vertical velocity fluctuations (γ^2_{vv}), with the corresponding phase angle (A_{pp} and A_{vv}) between the suction and pressure sides of the airfoil.

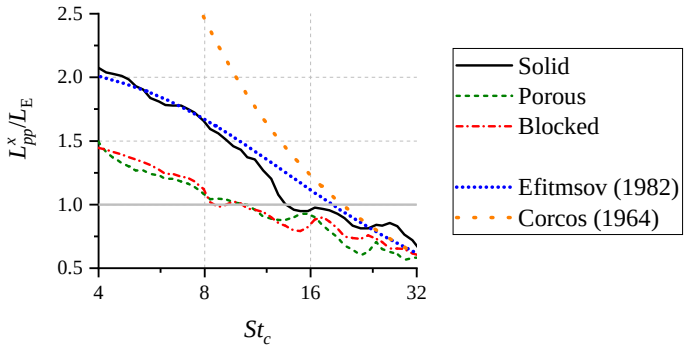

Figure 3.39: (Porous cell/fully-resolved) Streamwise correlation length of surface pressure fluctuations L^x_{pp} at $x/c = -0.05$. A comparison with Corcos [19] and Efimtsov [90] models are also provided.

noise source intensity, as demonstrated in figure 3.23. This analysis also corroborates the argument that the pressure release process is the most effective at locations where the porous medium is dominated by the entrance effect, i.e., where local thickness is approximately equal to twice the entrance length. The coherence analysis is also performed using the vertical velocity fluctuations with the results shown in figure 3.38 (*b*), and the trends are almost identical to those in (*a*).

Based on the acoustic spectra in figure 3.12, it appears that the permeable extent of the porous TE determines the frequency range where noise attenuation can be obtained. It has been suggested in literature [38, 46] that the porous TE extent should be comparable with respect to the characteristic aerodynamic length scale at the TE region in order to achieve noise attenuation. To ascertain this hypothesis for the porous-cell inserts, the streamwise correlation length of surface pressure fluctuations L^x_{pp} is computed as the following:

$$L^x_{pp}(f) = \lim_{\Delta x \to \infty} \int_0^{\Delta x} \sqrt{\gamma^2_{pp}(f, \Delta x)}\, \mathrm{d}x \tag{3.15}$$

where γ^2_{pp} is the magnitude-squared coherence of surface pressure fluctuations between a reference coordinate and a location further downstream along the streamwise (x) direction, separated by Δx. The formulation for γ^2_{pp} is similar to that in equation 3.10. The curve-fitting approach in equation 3.12 has also been applied [91, 93].

The streamwise correlation length values are plotted in figure 3.39, in which the reference location has been selected at $x/c = -0.05$. Comparisons are also made against Corcos [19] and Efimtsov [90] models, where the Corcos constant of 0.1 has been applied following Palumbo [91]. Note that the streamwise correlation length L^x_{pp} is normalised against the chordwise extent of the porous insert where its thickness is equal to the sum of the entrance length from both sides of the airfoil $L_E = 0.038c$ (see figure 3.36). Figure 3.39 evidences that a permeable surface decreases the streamwise correlation length with respect to the solid one, especially at low frequencies ($St_c < 12$). However, the L^x_{pp} values of both porous TE and blocked TE are quite similar throughout the entire frequency

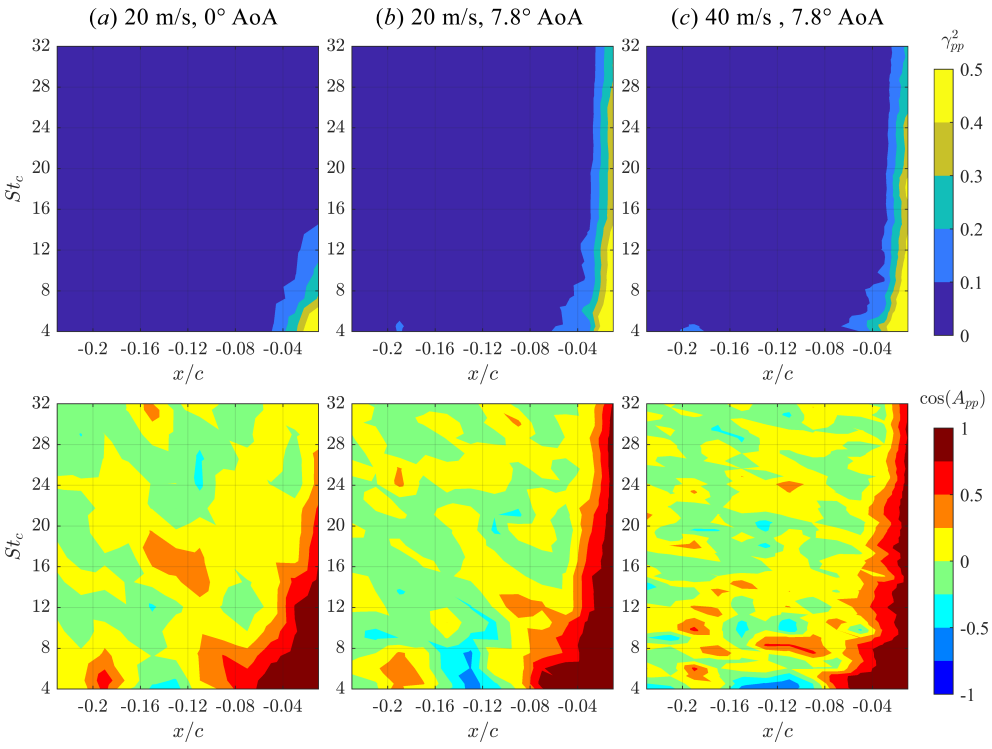

Figure 3.40: (Metal foam/modelled) The spatial distribution of magnitude-squared coherence of surface pressure fluctuations γ^2_{pp} at the airfoil surface and the corresponding phase angle A_{pp} between the suction and pressure sides.

range. The plot for the blocked TE shows that the correlation length becomes smaller than L_E at around $St_c = 8$, which is roughly the Strouhal number below which the blocked TE begins to lose its noise reduction capability in comparison to the porous TE (see figure 3.12). Simultaneously, the airfoil with blocked TE has the last 4 % of its chord being fully permeable, which is almost equal to L_E where the pressure release process is the most effective for noise mitigation. This observation supports the argument that the permeable TE extent needs to be sufficiently long compared to the characteristic length of aerodynamic fluctuations in the boundary layer to enable noise reduction. This also justifies the noise reduction level of both porous TE and blocked TE being rather similar at $St_c > 8$; the aerodynamic length scale at these frequencies is smaller compared to the fully-permeable extent of the blocked TE.

The coherence analysis of the surface pressure fluctuations is also carried out for the metal-foam TE cases at higher AoA and Reynolds number. As expected, figure 3.40 shows that the coherence level on the porous insert increases towards the TE tip regardless of the AoA and Reynolds number settings. This trend is also reflected in the $\cos(A_{pp})$ contours, where areas with higher coherence level also tend to have positive phase angle. It is interesting to observe that increasing the AoA leads to an enhanced coherence level

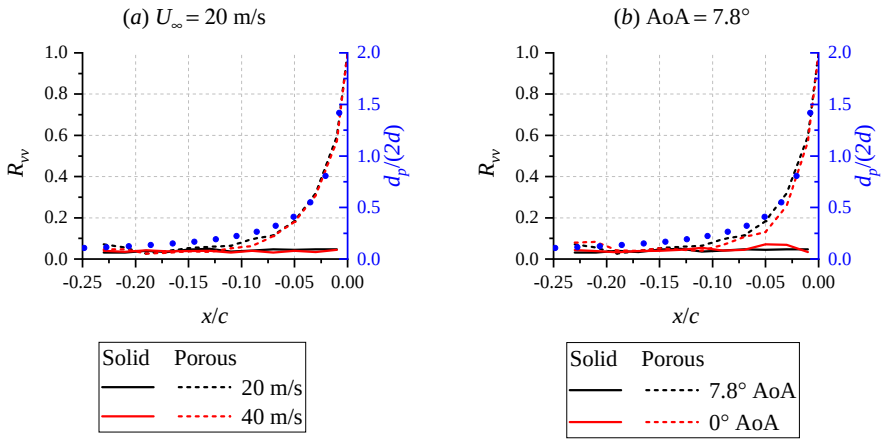

Figure 3.41: (Metal foam/modelled) The correlation coefficients of vertical velocity fluctuations (R_{vv}) between the suction and pressure sides of the porous TE. The secondary vertical axis (in blue) shows the ratio between the mean pore diameter of the metal-foam (d_p) and the local airfoil thickness ($2d$).

in the mid- and high-frequency ranges, which might be associated with the dominant eddies on the pressure side being brought closer to the porous medium surface. Furthermore, since the noise reduction level is generally lower for an airfoil with assymetric loading, it is conjectured that the pressure release process is the most optimal when the spectral features of the pressure field on both sides of the porous insert are identical.

Based on the results in figures 3.38 and 3.40, it is possible to conclude that the pressure release process leads to a gradual phase equalisation of the surface pressure fluctuations as they approach the TE tip. Following the analytical model of Chase [15], this mechanism would realise a milder acoustic scattering. Recalling the strip analysis in section 3.4, the pressure release process is responsible for modifying the phase relationship between noise sources that are distributed along the porous TE inserts. This leads to the phase interference effect observed in the cumulative SPL plots (see figures 3.21, 3.23, and 3.22). Such phenomenon is expected to be more effective for promoting noise attenuation in the low frequency range where the airfoil is acoustically compact (i.e., when the dipole sources at the airfoil surface are generally strongly in-phase [13]). Conversely, at frequencies where the airfoil is no longer compact, the dipole sources are distributed with a larger phase variation, and therefore, further phase modification would become less effective for noise reduction.

The pressure release process was examined in Rubio Carpio *et al.* [49] by performing a correlation analysis on the vertical velocity fluctuations. The same procedure has been carried out for the metal-foam TE cases and the results reported in figure 3.41. In addition to the correlation curve, the ratio between the pore diameter and the local airfoil thickness (d_c/h) is shown to determine a link between the pressure release process and the TE geometry. As expected, the pressure release process does not take place in the solid TE. Conversely, the porous TE shows a dramatic increase in correlation level as the local TE thickness approaches the mean pore diameter of the metal-foam. The

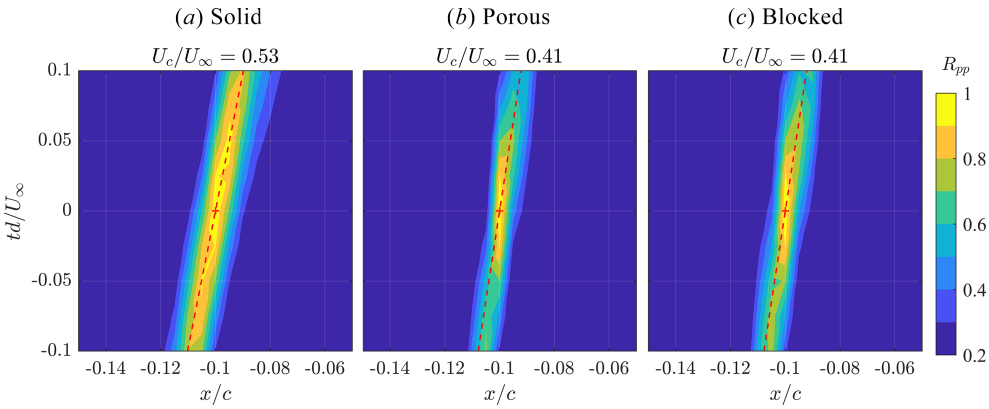

Figure 3.42: (Porous cell/fully-resolved) Contours of spatio-temporal correlation coefficient of surface pressure fluctuations R_{pp}. The reference location is at $x/c = -0.1$, marked by the red cross at the center of each contour. The gradient that corresponds to the convection velocity U_c is plotted as red dashed-line.

correlation curves appear to be slightly affected by the different Reynolds numbers and AoA settings, which suggests that the efficacy of the pressure release process depends mainly on the porous material properties and the TE geometry, at least within the present range of AoA and Reynolds numbers.

3.6.3. CONVECTION VELOCITY

The convective behaviour in the boundary layer might also affect the scattered noise intensity as reported by Ananthan *et al.* [58]. The unsteady pressure field beneath a turbulent boundary layer is generally dominated by the wavenumber component in the convective region f/U_c [32, 85], where U_c is the convection velocity. The convection velocity is evaluated by computing the space-time correlation of the surface pressure fluctuations R_{pp} as follows:

$$R_{pp}(\Delta x, \Delta t) = \frac{\langle p'(x,t)\, p' x + \Delta x, t + \Delta t)\rangle}{\sqrt{\langle p'^2(x,t)\rangle}\sqrt{\langle p'^2(x+\Delta x, t+\Delta t)\rangle}} \tag{3.16}$$

where $p'(x,t)$ is the time history of surface pressure fluctuations at a reference coordinate x and time t, whereas Δx and Δt are the spatial and temporal separations respectively. The contours of spatio-temporal correlation coefficient are provided in figure 3.42, in which the reference location is at $x/c = -0.1$. The convection velocity U_c can be obtained by sampling maximum R_{pp} values at different Δx and Δt, such that $U_c = \Delta x/\Delta t$. The U_c value is shown above each contour and it is represented as red dashed-line in the contour. The convection velocities of both porous and blocked TE are found to be the same, but they are lower compared to that of the solid TE. Similar findings have also been reported in literature [58, 60]. The figure also shows that the spatial correlation values decay at a faster rate on the permeable TE than on the solid one, corresponding to the smaller streamwise correlation length as shown in figure 3.39.

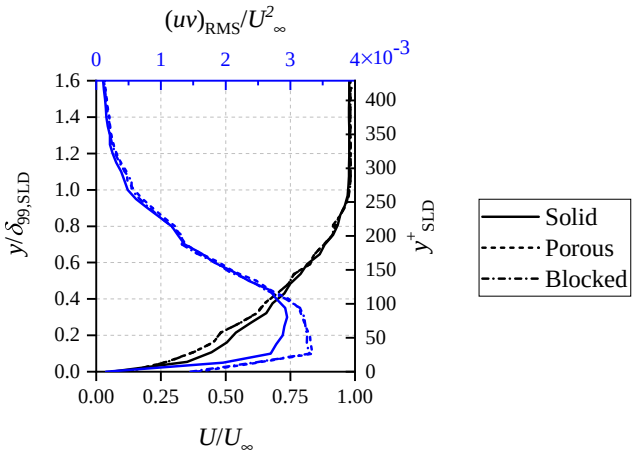

Figure 3.43: (Porous cell/fully-resolved) Boundary-layer profiles at $x/c = -0.1$. The plots show mean wall-parallel velocity component U (black lines) and the root-mean-square of Reynolds stress component in the wall-parallel and wall-normal directions $(uv)_{\text{RMS}}$ (blue lines). The wall-normal coordinates are also provided in term of y^+ based on the solid TE case.

The convection velocity can also be estimated by examining the mean wall-parallel velocity and Reynolds stress profiles of the solid and porous TE cases in figure 3.43. A noticeable mean velocity deficit in porous and blocked TE cases can be found relatively close to the surface ($y^+ < 150$), which corresponds to the higher shear stress that is evident in the $(uv)_{\text{RMS}}$ profile [83]. Since the shear stress in the boundary layer is associated with the generation of pressure fluctuations [85, 86], the convection velocity of the turbulent eddies is approximately equal to the local mean velocity where the $(uv)_{\text{RMS}}$ peak is found. For instance, This peak is located near $y/\delta_{99} = 0.3$ for the solid TE case where the $U/U_\infty = 0.56$. For the porous TE, the highest $(uv)_{\text{RMS}}$ value is at $y/\delta_{99} = 0.15$ where the $U/U_\infty = 0.43$. These convection velocity estimates are quite close to those obtained in figure 3.42. Similar result is obtained when applying this procedure for the blocked TE since the corresponding boundary layer profiles are very similar to those of porous TE. Figures 3.42 and 3.43 indicate that the dominant turbulent eddies are brought closer to the surface when a permeable insert is present. As a consequence, pressure fluctuations at the surface of both the porous and blocked TE are more intense in comparison to those in the case of solid TE, as previously discussed in figure 3.35.

3.7. AERODYNAMIC PERFORMANCE

The application of permeable TE insert is likely to adversely impact aerodynamic performance implied by the mean velocity deficit in the turbulent boundary layer (see figures 3.8 and 3.11). Porous materials have been reported to enhance surface friction [55, 83], and the same phenomenon can be found in figure 3.44. Upstream of the solid-porous junction, C_f values on both porous and blocked TE are almost identical to the solid TE ones, which indicates that the porous insert only affects the flow field locally [42]. Immediately downstream of the solid-porous junction, the wall friction decreases

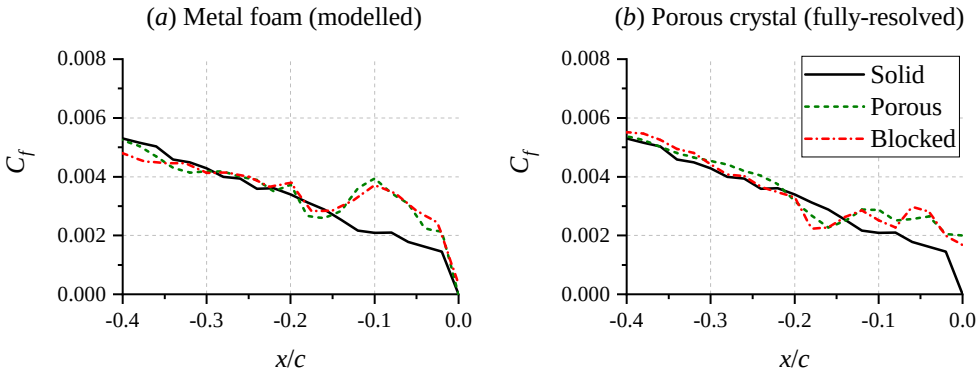

Figure 3.44: Streamwise distribution of mean wall-friction coefficient C_f for the different TE types at zero AoA and $U_\infty = 20\,\mathrm{m/s}$.

	Solid TE	Porous TE	Blocked TE
	Metal-foam (modelled)		
C_d	0.0240	0.0250	0.0244
ΔC_d relative to solid TE	-	+ 4%	+1.7%
	Porous cell (fully resolved)		
C_d	0.0240	0.0262	0.0259
ΔC_d relative to solid TE	-	+8.9%	+7.9%

Table 3.5: The comparison of time-averaged drag coefficient between airfoils with different TE types at zero AoA and $U_\infty = 20\,\mathrm{m/s}$.

slightly on the porous TE, which might be attributed to the ejection of low speed stream from within the porous medium (see the recirculation pattern in figure 3.28). Further downstream, however, the wall friction increases as the inner region of the boundary layer sinks into the porous medium.

In order to quantify the drag penalty induced by the permeable TE inserts, the time-average drag coefficient has been estimated using a wake survey method outlined in Faleiros *et al.* [97]:

$$C_d = 2\int_{-\infty}^{\infty}\left(1-\frac{U(y)}{U_\infty}\right)\left(\frac{U(y)}{U_\infty}\right)\mathrm{d}y \tag{3.17}$$

where $U(y)$ is the distribution of time-averaged streamwise velocity component along the vertical (y) direction (i.e., perpendicular to the freestream direction). $U(y)$ is sampled along $-2.5 < y/c < 2.5$ over a period of 10 flow passes. Spanwise-averaging has also been performed to improve statistical convergence of the results. In addition, the drag coefficient is evaluated based on $U(y)$ at different positions downstream of the airfoil (i.e., $x/c > 1$) to ensure that changing the wake survey position does not significantly affect the result.

The drag coefficient estimates are shown in table 3.5, where both the metal-foam and

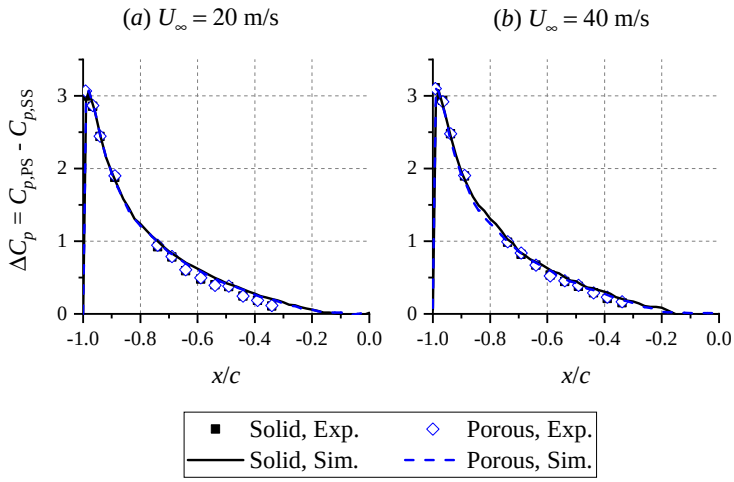

Figure 3.45: (Metal-foam/modelled) The mean surface pressure difference ΔC_p between the pressure and suction sides of the airfoil at 7.8° AoA. Plot (*a*) shows the distribution for $U_\infty = 20\,\mathrm{m/s}$, and (*b*) for $U_\infty = 40\,\mathrm{m/s}$.

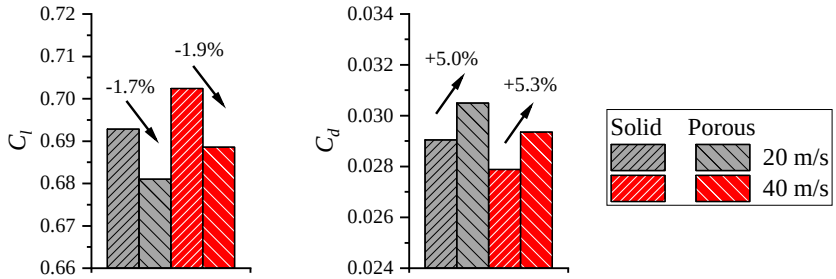

Figure 3.46: (Metal-foam/modelled) The comparison of lift and drag coefficients between the airfoils with solid and porous TE at 7.8° AoA. The percentage and the arrow above the bars indicate the difference between the coefficients for the porous TE relative to the solid TE.

porous-cell inserts show slightly increased C_d values with respect to that of the solid TE. Nevertheless, the blocked variants incur smaller drag penalty compared to the porous ones, which also highlights the impact of the solid partition on aerodynamic performance. It is also worth mentioning that the drag increase in the metal-foam TE cases is solely attributed to the permeability of the porous insert as the surface roughness effect has been neglected, and therefore, the actual drag increase might be higher than the predicted values in the table.

The metal-foam TE cases at 7.8° AoA allow for examining the impact of the porous insert on the aerodynamic performance at a lifting condition. Figure 3.45 presents the mean pressure difference between the suction and pressure sides of the airfoil. Data points from experiments have been added for comparison, although these are only available up to $x/c = -0.3$. From the experimental data [42], it has been found that the porous TE does not affect the pressure distribution at the upstream segment of the

airfoil, which is evident in the simulations as well. The slight discrepancy in the ΔC_p values downstream of $x/c = -0.8$ is likely to be related to the fact that the simulation employs different tripping device than in the experiment, but this has been previously shown to have minimal effect on acoustic scattering at the TE [71].

Subsequently, the airfoil lift coefficient C_l is computed by integrating the time-averaged surface pressure coefficient C_p that is shown in figure 3.45, along the airfoil surface, and the drag coefficient using equation 3.17. The results for the 7.8° AoA cases are reported in figure 3.46. It is evident that the porous TE lowers the overall aerodynamic efficiency of the airfoil. However, the effect is arguably minor given that the lift penalty is less than 2 % and the average drag increase is slightly above 5 %. Compared to the information in table 3.5, the lift and drag penalty appear to be exacerbated at higher AoA and Reynolds number settings. The amount of lift reduction is also likely to depend on the airfoil geometry. The NACA 0018 in the present study has relatively small ΔC_p values along the extent of the porous insert as shown in figure 3.45, which helps preventing a significant pressure leakage between the suction and pressure sides of the TE. It is also possible to conjecture that the lift degradation would become more severe for asymmetrical airfoils and those that possess relatively thin geometry at the TE region, such as the DU-96 airfoils that are widely used in wind-turbine aerodynamic studies.

3.8. SUMMARY

This chapter presents a numerical study to obtain better insights into the aeroacoustics of permeable TE inserts, which have been employed for mitigating TBL-TE noise. Within this scope, two types of porous inserts have been considered. One of them is based on a metal foam, which is modelled using the multi-layer porous-medium modelling approach. The other insert is made from porous cells whose geometrical details are fully resolved in the simulation. As a consequence, surface roughness effects are present only for the latter.

It has been established that acoustic scattering on a porous insert is less efficient than on a solid one, due to the combination of two phenomena. Firstly, the local source intensity near the tip of the porous insert is suppressed. Secondly, the porous insert promotes out-of-phase relationsip between sources that are distributed on the porous medium surface, even when the airfoil is acoustically compact. These phenomena are driven by the interaction between the pressure fluctuations on both sides of the TE across the porous insert, which is referred to as the pressure release process. Consequently, when an impermeable partition is introduced along the centre of the porous insert, the noise reduction level is adversely affected. Nevertheless, the pressure release process is strongly present at the downstream segment of the porous insert where the local thickness is smaller than twice the entrance length. This finding can become useful to determine the required chordwise extent of a porous TE to achieve optimal trade-off between noise reduction, aerodynamic performance, and high-frequency noise increase.

Present study suggests that the permeability of the porous insert, rather than the surface roughness, has a more relevant role in affecting the turbulent boundary layer properties. These include the enhancement of turbulent fluctuations intensity and the slight reduction in correlation lengths. It is also found that the surface pressure statistics on a porous TE would be associated with a more intense noise radiation relative to the solid TE according to the classical TE noise model, such as the one of Amiet [16].

However, this is not the case due to the fact that the porous inserts possess different scattering phenomena, which are not considered by analytical models for solid TE. Nevertheless, the impact of the porous inserts on aerodynamic performance remains relatively minor, at least for the current operating conditions and types of porous materials.

To sum up, this chapter has demonstrated that the porous TE has a promising noise reduction capability with potential applications in treating airframe (e.g., high-lift devices) and wind-turbine noise sources. Future investigations are still necessary to determine a better means to characterise the pressure release process, which can eventually be used to formulate a model for predicting the noise reduction level for a given TE shape, flow configuration, and porous material type.

REFERENCES

[1] C. Teruna, F. A. Manegar, F. Avallone, D. Casalino, D. Ragni, A. Rubio Carpio, and T. Carolus, *Numerical analysis of metal-foam application for trailing edge noise reduction,* in *25th AIAA/CEAS Aeroacoustics Conference* (2019) p. 2650.

[2] C. Teruna, F. Manegar, F. Avallone, D. Ragni, D. Casalino, and T. Carolus, *Noise reduction mechanisms of an open-cell metal-foam trailing edge,* Journal of Fluid Mechanics **898** (2020).

[3] C. Teruna, F. Avallone, D. Ragni, A. Rubio-Carpio, and D. Casalino, *Numerical analysis of a 3-d printed porous trailing edge for broadband noise reduction,* Journal of Fluid Mechanics **926** (2021), 10.1017/jfm.2021.704.

[4] T. F. Brooks, D. S. Pope, and M. A. Marcolini, *Airfoil self-noise and prediction,* NASA Reference Publication, NASA-RP-1218 (1989).

[5] S. Oerlemans and J. G. Schepers, *Prediction of wind turbine noise and validation against experiment,* International journal of aeroacoustics **8**, 555 (2009).

[6] M. Herr, *Design criteria for low-noise trailing-edges,* in *13th AIAA/CEAS Aeroacoustics Conference (28th AIAA Aeroacoustics Conference)* (2007) p. 3470.

[7] Y. Guo and R. H. Thomas, *On aircraft trailing edge noise,* in *25th AIAA/CEAS Aeroacoustics Conference* (2019) p. 2610.

[8] S. Oerlemans, *Reduction of wind turbine noise using blade trailing edge devices,* in *22nd AIAA/CEAS aeroacoustics conference* (2016) p. 3018.

[9] T. Colonius and S. K. Lele, *Computational aeroacoustics: progress on nonlinear problems of sound generation,* Progress in Aerospace sciences **40**, 345 (2004).

[10] A. Powell, *On the aerodynamic noise of a rigid flat plate moving at zero incidence,* The Journal of the Acoustical Society of America **31**, 1649 (1959).

[11] N. Curle, *The influence of solid boundaries upon aerodynamic sound,* Proceedings of the Royal Society of London. Series A. Mathematical and Physical Sciences **231**, 505 (1955).

[12] M. J. Lighthill, *On sound generated aerodynamically i. general theory,* Proceedings of the Royal Society of London. Series A. Mathematical and Physical Sciences **211**, 564 (1952).

[13] M. S. Howe, *A review of the theory of trailing edge noise,* Journal of sound and vibration **61**, 437 (1978).

[14] J. F. Williams and L. Hall, *Aerodynamic sound generation by turbulent flow in the vicinity of a scattering half plane,* Journal of fluid mechanics **40**, 657 (1970).

[15] D. M. Chase, *Noise radiated from an edge in turbulent flow,* AIAA journal **13**, 1041 (1975).

[16] R. K. Amiet, *Noise due to turbulent flow past a trailing edge,* Journal of sound and vibration **47**, 387 (1976).

[17] J. Yu and C. Tam, *Experimental investigation of the trailing edge noise mechanism,* AIAA Journal **16**, 1046 (1978).

[18] M. Szőke, D. Fiscaletti, and M. Azarpeyvand, *Uniform flow injection into a turbulent boundary layer for trailing edge noise reduction,* Physics of Fluids **32**, 085104 (2020).

[19] G. Corcos, *The structure of the turbulent pressure field in boundary-layer flows,* Journal of Fluid Mechanics **18**, 353 (1964).

[20] M. Roger and S. Moreau, *Back-scattering correction and further extensions of amiet's trailing-edge noise model. part 1: theory,* Journal of Sound and vibration **286**, 477 (2005).

[21] T. F. Brooks and T. Hodgson, *Trailing edge noise prediction from measured surface pressures,* Journal of sound and vibration **78**, 69 (1981).

[22] K. Chandiramani, *Diffraction of evanescent waves, with applications to aerodynamically scattered sound and radiation from unbaffled plates,* The Journal of the Acoustical Society of America **55**, 19 (1974).

[23] S. Oerlemans, M. Fisher, T. Maeder, and K. Kögler, *Reduction of wind turbine noise using optimized airfoils and trailing-edge serrations,* AIAA journal **47**, 1470 (2009).

[24] R. Graham, *The silent flight of owls,* The Aeronautical Journal **38**, 837 (1934).

[25] G. Lilley, *A study of the silent flight of the owl,* in *4th AIAA/CEAS aeroacoustics conference* (1998) p. 2340.

[26] H. Wagner, M. Weger, M. Klaas, and W. Schröder, *Features of owl wings that promote silent flight,* Interface focus **7**, 20160078 (2017).

[27] C. J. Clark, K. LePiane, and L. Liu, *Evolution and ecology of silent flight in owls and other flying vertebrates,* Integrative Organismal Biology **2**, obaa001 (2020).

[28] J. W. Jaworski and N. Peake, *Aerodynamic noise from a poroelastic edge with implications for the silent flight of owls,* Journal of Fluid Mechanics **723**, 456 (2013).

[29] S. Klän, S. Burgmann, T. Bachmann, M. Klaas, H. Wagner, and W. Schröder, *Surface structure and dimensional effects on the aerodynamics of an owl-based wing model,* European Journal of Mechanics-B/Fluids **33**, 58 (2012).

[30] A. Winzen, M. Klaas, and W. Schröder, *High-speed particle image velocimetry and force measurements of bio-inspired surfaces,* Journal of Aircraft **52**, 471 (2015).

[31] I. Clark, W. J. Devenport, J. Jaworski, C. Daly, N. Peake, and S. A. Glegg, *The noise generating and suppressing characteristics of bio-inspired rough surfaces,* in *20th AIAA/CEAS aeroacoustics conference* (2014) p. 2911.

[32] M. S. Howe, *Noise produced by a sawtooth trailing edge,* The Journal of the Acoustical society of America **90**, 482 (1991).

[33] F. Avallone, W. Van Der Velden, D. Ragni, and D. Casalino, *Noise reduction mechanisms of sawtooth and combed-sawtooth trailing-edge serrations,* Journal of Fluid Mechanics **848**, 560 (2018).

[34] M. Gruber, P. Joseph, and T. P. Chong, *Experimental investigation of airfoil self noise and turbulent wake reduction by the use of trailing edge serrations,* in *16th AIAA/CEAS aeroacoustics conference* (2010) p. 3803.

[35] L. Jones and R. Sandberg, *Acoustic and hydrodynamic analysis of the flow around an aerofoil with trailing-edge serrations,* Journal of Fluid Mechanics **706**, 295 (2012).

[36] T. P. Chong, A. Vathylakis, P. F. Joseph, and M. Gruber, *Self-noise produced by an airfoil with nonflat plate trailing-edge serrations,* AIAA journal **51**, 2665 (2013).

[37] C. A. León, R. Merino-Martínez, D. Ragni, F. Avallone, and M. Snellen, *Boundary layer characterization and acoustic measurements of flow-aligned trailing edge serrations,* Experiments in Fluids **57**, 182 (2016).

[38] R. E. Hayden, *Fundamental aspects of noise reduction from powered-lift devices,* SAE Transactions , 1287 (1973).

[39] D. B. Ingham and I. Pop, *Transport phenomena in porous media* (Elsevier, 1998).

[40] T. Geyer, E. Sarradj, and C. Fritzsche, *Porous airfoils: noise reduction and boundary layer effects,* International journal of aeroacoustics **9**, 787 (2010).

[41] M. Herr, K.-S. Rossignol, J. Delfs, N. Lippitz, and M. Mößner, *Specification of porous materials for low-noise trailing-edge applications,* in *20th AIAA/CEAS aeroacoustics conference* (2014) p. 3041.

[42] A. Rubio Carpio, R. Merino Martinez, F. Avallone, D. Ragni, M. Snellen, and S. van der Zwaag, *Broadband trailing-edge noise reduction using permeable metal foams,* in *INTER-NOISE and NOISE-CON Congress and Conference Proceedings*, Vol. 255 (Institute of Noise Control Engineering, 2017) pp. 2755–2765.

[43] E. Sarradj and T. Geyer, *Noise generation by porous airfoils,* in *13th AIAA/CEAS Aeroacoustics Conference (28th AIAA Aeroacoustics Conference)* (2007) p. 3719.

[44] T. F. Geyer and E. Sarradj, *Trailing edge noise of partially porous airfoils,* in *20th AIAA/CEAS Aeroacoustics Conference* (2014) p. 3039.

[45] J. E. F. Williams, *The acoustics of turbulence near sound-absorbent liners,* Journal of Fluid Mechanics **51**, 737 (1972).

[46] M. Howe, *On the added mass of a perforated shell, with application to the generation of aerodynamic sound by a perforated trailing edge,* Proceedings of the Royal Society of London. A. Mathematical and Physical Sciences **365**, 209 (1979).

[47] A. Kisil and L. J. Ayton, *Aerodynamic noise from rigid trailing edges with finite porous extensions,* Journal of Fluid Mechanics **836**, 117 (2018).

[48] J. Delfs, B. Faßmann, N. Lippitz, M. Lummer, M. Mößner, L. Müller, K. Rurkowska, and S. Uphoff, *Sfb 880: Aeroacoustic research for low noise take-off and landing,* CEAS Aeronautical Journal **5**, 403 (2014).

[49] A. Rubio Carpio, F. Avallone, D. Ragni, M. Snellen, and S. van der Zwaag, *Mechanisms of broadband noise generation on metal foam edges,* Physics of Fluids **31**, 105110 (2019).

[50] A. Cavalieri, W. Wolf, and J. Jaworski, *Numerical solution of acoustic scattering by finite perforated elastic plates,* Proceedings of the royal society A: mathematical, physical and engineering sciences **472**, 20150767 (2016).

[51] A. Rubio Carpio, F. Avallone, and D. Ragni, *On the role of the flow permeability of metal foams on trailing edge noise reduction,* in *2018 AIAA/CEAS Aeroacoustics Conference* (2018) p. 2964.

[52] D. M. Freed, *Lattice-boltzmann method for macroscopic porous media modeling,* International Journal of Modern Physics C **9**, 1491 (1998).

[53] M. Quintard and S. Whitaker, *Transport in ordered and disordered porous media ii: Generalized volume averaging,* Transport in porous media **14**, 179 (1994).

[54] Y. Bae and Y. J. Moon, *Effect of passive porous surface on the trailing-edge noise,* Physics of Fluids **23**, 126101 (2011).

[55] S. R. Koh, M. Meinke, and W. Schröder, *Numerical analysis of the impact of permeability on trailing-edge noise,* Journal of Sound and Vibration **421**, 348 (2018).

[56] L. Rossian, R. Ewert, and J. W. Delfs, *Prediction of airfoil trailing edge noise reduction by application of complex porous material,* in *New Results in Numerical and Experimental Fluid Mechanics XI* (Springer, 2018) pp. 647–657.

[57] P. Bernicke, R. Akkermans, V. Ananthan, R. Ewert, J. Dierke, and L. Rossian, *A zonal noise prediction method for trailing-edge noise with a porous model,* International Journal of Heat and Fluid Flow **80**, 108469 (2019).

[58] V. Ananthan, P. Bernicke, R. Akkermans, T. Hu, and P. Liu, *Effect of porous material on trailing edge sound sources of a lifting airfoil by zonal overset-les,* Journal of Sound and Vibration , 115386 (2020).

[59] N. Dukhan and C. Minjeur, *Minimum thickness for open-cell metal foam to behave as a porous medium,* in *40th Fluid Dynamics Conference and Exhibit* (2010) p. 4618.

[60] A. Rubio Carpio, R. M. Martínez, F. Avallone, D. Ragni, M. Snellen, and S. van der Zwaag, *Experimental characterization of the turbulent boundary layer over a porous trailing edge for noise abatement,* Journal of Sound and Vibration **443**, 537 (2019).

[61] C. Teruna, F. Avallone, D. Ragni, and D. Casalino, *On the noise reduction of a porous trailing edge applied to an airfoil at lifting condition,* Physics of Fluids **33**, 055132 (2021), https://aip.scitation.org/doi/pdf/10.1063/5.0047512 .

[62] G. Elsinga and J. Westerweel, *Tomographic-piv measurement of the flow around a zigzag boundary layer trip,* Experiments in fluids **52**, 865 (2012).

[63] J. Casper, D. Lockard, M. Khorrami, and C. Streett, *Investigation of volumetric sources in airframe noise simulations,* in *10th AIAA/CEAS Aeroacoustics Conference* (2004) p. 2805.

[64] D. Lockard and J. Casper, *Permeable surface corrections for ffowcs williams and hawkings integrals,* in *11th AIAA/CEAS Aeroacoustics Conference* (2005) p. 2995.

[65] C. Sun, F. Pérot, R. Zhang, P.-T. Lew, A. Mann, V. Gupta, D. M. Freed, I. Staroselsky, and H. Chen, *Lattice boltzmann formulation for flows with acoustic porous media,* Comptes Rendus Mécanique **343**, 533 (2015).

[66] P. R. Spalart and J. H. Watmuff, *Experimental and numerical study of a turbulent boundary layer with pressure gradients,* Journal of Fluid Mechanics **249**, 337 (1993).

[67] P. J. Roache, *Verification and validation in computational science and engineering*, Vol. 895 (Hermosa Albuquerque, NM, 1998).

[68] P. Welch, *The use of fast fourier transform for the estimation of power spectra: a method based on time averaging over short, modified periodograms,* IEEE Transactions on audio and electroacoustics **15**, 70 (1967).

[69] W. C. van der Velden, A. van Zuijlen, and D. Ragni, *Flow topology and noise emission around straight, serrated and slitted trailing edges using the lattice boltzmann methodology,* in *22nd AIAA/CEAS Aeroacoustics Conference* (2016) p. 3021.

[70] C. A. León, D. Ragni, S. Pröbsting, F. Scarano, and J. Madsen, *Flow topology and acoustic emissions of trailing edge serrations at incidence,* Experiments in Fluids **57**, 91 (2016).

[71] Q. Ye, F. Avallone, D. Ragni, M. Choudhari, and D. Casalino, *Effect of surface roughness geometry on boundary-layer transition and far-field noise,* AIAA Journal , 1 (2021).

[72] P. Nelson, *Noise generated by flow over perforated surfaces,* Journal of Sound and Vibration **83**, 11 (1982).

[73] M. Roger and S. Moreau, *Trailing edge noise measurements and prediction for subsonic loaded fan blades,* in *8th AIAA/CEAS aeroacoustics conference & exhibit* (2002) p. 2460.

[74] J. R. Underbrink, *Circularly symmetric, zero redundancy, planar array having broad frequency range applications,* (2001), uS Patent 6,205,224.

[75] D. P. Lockard, W. M. Humphreys, M. R. Khorrami, E. Fares, D. Casalino, and P. A. Ravetta, *Comparison of computational and experimental microphone array results for an 18% scale aircraft model,* International Journal of Aeroacoustics **16**, 358 (2017).

[76] P. Bernicke, R. Akkermans, V. Bharadwaj, R. Ewert, J. Dierke, and L. Rossian, *Overset les of a solid and porous naca0012 trailing edge,* in *2018 AIAA/CEAS Aeroacoustics Conference* (2018) p. 3454.

[77] A. Powell, *Theory of vortex sound,* The journal of the acoustical society of America **36**, 177 (1964).

[78] D. Violato, P. Moore, K. Bryon, and F. Scarano, *Application of powell's analogy for the prediction of vortex-pairing sound in a low-mach number jet based on time-resolved planar and tomographic piv,* in *16th AIAA/CEAS Aeroacoustics Conference* (2010) p. 3959.

[79] P. R. Spalart, K. V. Belyaev, M. L. Shur, M. Kh Strelets, and A. K. Travin, *On the differences in noise predictions based on solid and permeable surface ffowcs williams–hawkings integral solutions,* International Journal of Aeroacoustics **18**, 621 (2019).

[80] M. Howe, *The role of surface shear stress fluctuations in the generation of boundary layer noise,* Journal of Sound and Vibration **65**, 159 (1979).

[81] A. R. Carpio, F. Avallone, D. Ragni, M. Snellen, and S. van der Zwaag, *Quantitative criteria to design optimal permeable trailing edges for noise abatement,* Journal of Sound and Vibration **485**, 115596 (2020).

[82] M. S. Howe, *Trailing edge noise at low mach numbers,* Journal of Sound and Vibration **225**, 211 (1999).

[83] J. Jimenez, M. Uhlmann, A. Pinelli, and G. Kawahara, *Turbulent shear flow over active and passive porous surfaces,* Journal of Fluid Mechanics **442**, 89 (2001).

[84] J.-H. Lee and H. J. Sung, *Effects of an adverse pressure gradient on a turbulent boundary layer,* International Journal of Heat and Fluid Flow **29**, 568 (2008).

[85] W. K. Blake, *Turbulent boundary-layer wall-pressure fluctuations on smooth and rough walls,* Journal of Fluid Mechanics **44**, 637 (1970).

[86] N. Hu, N. Reiche, and R. Ewert, *Simulation of turbulent boundary layer wall pressure fluctuations via poisson equation and synthetic turbulence,* Journal of Fluid Mechanics **826**, 421 (2017).

[87] S. A. S. Ali, M. Azarpeyvand, and C. R. I. da Silva, *Trailing-edge flow and noise control using porous treatments,* Journal of Fluid Mechanics **850**, 83 (2018).

[88] W. Devenport, N. Alexander, S. Glegg, and M. Wang, *The sound of flow over rigid walls,* Annual Review of Fluid Mechanics **50**, 435 (2018).

[89] Y. Rozenberg, G. Robert, and S. Moreau, *Wall-pressure spectral model including the adverse pressure gradient effects,* AIAA journal **50**, 2168 (2012).

[90] B. Efimtsov, *Characteristics of the field of turbulent wall pressure-fluctuations at large reynolds-numbers,* Soviet Physics Acoustics-USSR **28**, 289 (1982).

[91] D. Palumbo, *Determining correlation and coherence lengths in turbulent boundary layer flight data,* Journal of Sound and Vibration **331**, 3721 (2012).

[92] M. Roger and S. Moreau, *Extensions and limitations of analytical airfoil broadband noise models,* International Journal of Aeroacoustics **9**, 273 (2010).

[93] W. Van der Velden, A. Van Zuijlen, A. De Jong, and H. Bijl, *On the estimation of spanwise pressure coherence of a turbulent boundary layer over a flat plate,* in *Proceedings-WCCM XI: 11th World Congress on Computational Mechanics; ECCM V: 5th European Conference on Computational Mechanics; ECFD VI: 6th European Conference on Computational Fluid Dynamics, Barcelona, Spain, 20-25 July 2014* (CIMNE, 2014).

[94] S. Pröbsting, M. Tuinstra, and F. Scarano, *Trailing edge noise estimation by tomographic particle image velocimetry,* Journal of Sound and Vibration **346**, 117 (2015).

[95] C. Naaktgeboren, P. Krueger, and J. Lage, *Limitations of darcy's law in light of inlet and exit pressure drops,* in *International Conference on Applications of Porous Media* (2004).

[96] M. Kaviany, *Principles of heat transfer in porous media* (Springer Science & Business Media, 2012).

[97] D. E. Faleiros, M. Tuinstra, and H. Hoeijmakers, *Drag, lift and effective angle of attack from analysis wake of an airfoil in open-jet wind tunnel,* in *54th AIAA Aerospace Sciences Meeting 2016: 4-8 January 2016, San Diego, California, USA* (American Institute of Aeronautics and Astronautics Inc.(AIAA), 2016).

4

LEADING-EDGE NOISE MITIGATION

For the first time I was flying by jet propulsion. No engine vibrations. No torque and no lashing sound of the propeller. Accompanied by a whistling sound, my jet shot through the air. Later when asked what it felt like, I said, "It felt as though angels were pushing".

Adolf Galland

This chapter investigates the applications of leading-edge (LE) treatments, such as porous LE and serrations, on a rod-airfoil configuration, which is a simplified setup to emulate the aeroacoustics of wake-body interaction in a turbofan fan stage. The porous LE is found to suppress the lift fluctuations intensity on the airfoil, but the resulting noise reduction is only noticeable in the high-frequency range. Differently, LE serrations possess the additional benefit from a spanwise decorrelation effect on the unsteady surface pressure field along the LE span, which has been associated with a substantial tonal noise reduction. The porous LE is also found to cause a more severe aerodynamic performance penalty, particularly at a lifting condition, due to a cross-flow through the porous medium driven by the pressure imbalance between the suction and pressure sides of the airfoil. A porous leading-edge with serration-like planform has been proposed, which is observed to improve the broadband noise reduction level beyond that of the regular serrations, while retaining a similar tonal noise reduction level.

Parts of this chapter have been published in Teruna *et al.* [1].

4.1. TURBULENCE-IMPINGEMENT NOISE

TURBULENCE-impingement noise (TIN) is produced as a body travels through a turbulent flow field. TIN can become more relevant than trailing-edge noise [2] for an inflow with medium turbulence intensity (e.g., > 3 %), which is often found in different industrial applications, such as the interaction between atmospheric turbulence with wind turbine blades [3], the rotor-stator interaction in a modern high-bypass turbofan [4], and BVI (blade-vortex interaction) noise in rotorcrafts. These examples are illustrated in figure 4.1.

As described by the acoustic analogy of Curle [5], inflow disturbances or gusts can induce unsteady loading on a nearby solid body (e.g., airfoil), which leads to noise generation. Amiet [6] proposed a method to relate the far-field noise to the spectral characteristics of an airfoil lift response induced by the inflow turbulence. He used the lift response function of Sears [7] that is suitable for a thin airfoil at a low Mach number. The power spectral density of sound pressure (S_{pp}) for an observer directly above the airfoil (e.g., at a distance of $\boldsymbol{r}_o$ from the LE) is expressed as in the following.

$$S_{pp}(\boldsymbol{r}_o,\omega) = \left(\frac{\omega\rho_\infty c}{2a_\infty|\boldsymbol{r}_o|}\right)^2 \frac{\pi U_\infty b}{2}|\mathrm{G}|^2\Phi_{vv}(K_x,0,L) \tag{4.1}$$

The airfoil lift response function is contained within G, while Φ_{vv} is the power spectral density of the turbulent velocity fluctuations in the normal direction relative to the airfoil planform, with a spanwise correlation length of L. The mathematical model was found to be in good agreement with experimental data for $M_\infty K_x b/2 > 1$, where K_x is the streamwise convective wavenumber and b is the airfoil span. This implies that Amiet's formulation is generally suitable for predicting the effect of high-frequency gusts. Paterson and Amiet [8] further developed the model into one that is based on surface-pressure fluctuations, which was subsequently validated using an experiment on a NACA 0012 airfoil that is place downstream of a turbulence grid. They also concluded that the dominant noise sources are located near the airfoil leading edge, and thus, TIN is sometimes referred to as leading-edge (LE) noise.

The numerical study of Marshall and Grant [9] provides a good overview of the turbulence behavior in proximity of an airfoil LE. The authors described two phenomena, namely vortex bending and vortex chopping. The latter could take place for a blade that is sufficiently thin compared to the vortex diameter, but otherwise, the vortex "bends" around the airfoil leading edge. Once a vortex chopping occurs, the two halves are convected along the opposite sides of the airfoil. However, one of them would expand in radius while the other would contract. Regardless, the unsteady distortion experienced by the vortical structures near the blade LE induces a scattering of a small part of their kinetic energy into sound.

The physical mechanism behind TIN receives a significant amount of attention due to its relevance in BVI phenomenon in rotorcrafts. Widnall and Wolf [10] developed a theoretical model to describe the unsteady lift distribution on a two-dimensional airfoil when impinged by a line vortex. Using the vortex model of Betz [11], they were able to predict the lift fluctuations induced by the vortex and to relate these to the far-field acoustic signal. The authors also suggested the application of swept rotor blades to

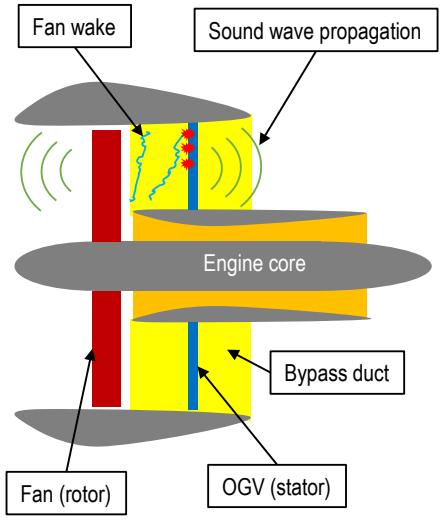

Rotor-stator interaction in a high-bypass turbofan (side view)

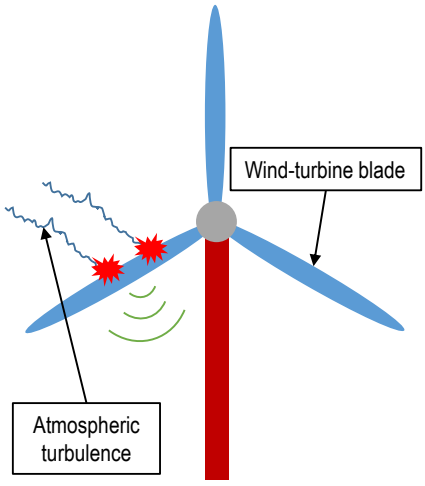

Atmospheric turbulence interaction with a wind-turbine blade (front view)

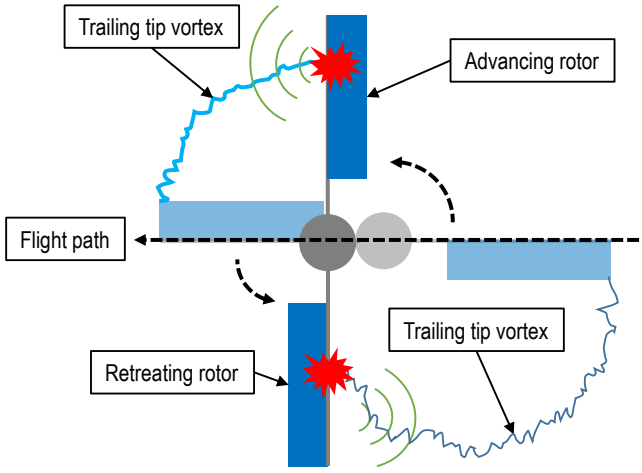

Blade-Vortex Interaction (BVI) on a two-blade rotor (top view)

Figure 4.1: Several examples of turbulence-impingement noise cases.

mitigate BVI noise by controlling the formation of tip vortices. Later, Booth Jr [12] performed experiments to elucidate the relationship between the steady loading on the blade, the distance of the vortical structures from the leading-edge (LE), and the noise level. In particular, they found out that the blade mean loading could affect the trajectory of the incoming vortex and the amount of distortion of the vortex core. As expected, vortices that directly strike the blade LE have a stronger contribution on noise radiation compared to those that flow around it. For more information on BVI, readers are advised to consult Lowson [13].

Multiple studies have been dedicated to better understand the influence of angle-of-attack (AoA) and airfoil shape on TIN. Moreau and Roger [2] performed an experimental study that resembled the environment surrounding a typical automotive cooling fan. They embedded a flat-plate (3 % thickness ratio), a controlled-diffusion (CD) airfoil (4 % thickness ratio), and a NACA 0012 in a turbulent flow field at a turbulence intensity of 5 %. The flat-plate and the CD airfoil produced similar level of noise that was still higher compared to that of NACA 0012. Nevertheless, the authors did not find the AoA effect to be significant, similar to the findings of Devenport *et al.* [14]. More recently, Gill *et al.* [15] also investigated the effect of airfoil geometry on TIN using high-order Linearised-Euler-Equation (LEE) in combination with the FW-H analogy. A wide range of airfoils with different thicknesses and LE radii were considered. It was found out that increasing the airfoil thickness would reduce the noise level at frequencies where $c/\lambda > 1$; λ is the acoustic wavelength. The noise reduction level was also found to be higher in the downstream direction. The authors concluded that the unsteady loading induced by the impinging vortices would be milder when the local velocity gradient at the LE is weak.

As mentioned earlier, TIN is generated inside a turbofan fan stage, where the turbulent fan-wake impinges the downstream outlet-guide vanes (OGV) [4, 16]. As a side note, the OGV functions to recover the circumferential component of the flow induced by the fan rotational motion, resulting in a more efficient thrust generation. The noise from fan wake-OGV interaction mechanism is expected to become more relevant as turbofan bypass ratio is increased in future designs. Due to weight and dimension limitations, the axial distance between the fan and the OGV might have to be reduced, and as a consequence, the fan wake is more coherent when impinging the OGV that results in stronger generation of tonal noise component. Additionally, the shorter nacelle also presents a challenge for the installation of acoustic wall-treatment (e.g., liners).

4.1.1. LEADING-EDGE NOISE MITIGATION APPROACHES

Due to the various negative implications of LE noise, several noise mitigation approaches have been investigated in literature. In the context of BVI noise on helicopters, Hardin and Lamkin [17] identified several important parameters, including the incoming vortex strength, mean blade loading, the spanwise interaction length of the vortex impingement process, and the distance between the incoming vortex sheet with the blade. Exploiting these parameters, the authors proposed several noise mitigation techniques, such as a higher-harmonic pitch control (HHC) system and a swept blade design. The HHC system entails exciting the swashplate[1] at harmonics based on the number of rotor blades. This method has been successfully demonstrated on many occasions [18], including in a full-

[1] A device that transmits flight control inputs for controlling the orientation of the rotor blades.

scale test [19]. More recently, active control methods were also considered, such as LE blowing [20]. LE blowing was found to generate a buffer zone around the LE, which helps deflecting the incoming vortex away from the LE.

Several noise mitigation approaches have also been proposed to address rotor-stator interaction noise in turbofans. Since the fan stage is enclosed in a duct, noise propagates as acoustic modes that conform to the duct geometry. Tyler and Sofrin [21] proposed a rather simple yet elegant design rule for selecting the number of rotor blades and stator vane that would cause some duct modes to be cut-off (non-propagating). Nevertheless, the Tyler-Sofrin rule assumes a perfectly radially symmetric mean flow, which is often not the case in practice. For instance, an inflow distortion at the fan inlet can give rise to additional modes that cannot be predicted by the Tyler-Sofrin rule.

Unsurprisingly, increasing the sweep angle of the stator vanes was found to be an effective noise mitigation solution [22], since the radial fluctuating component (i.e., spanwise component in the blade-relative coordinate system) of the impinging turbulence does not contribute towards noise scattering [23]. Later, this was confirmed in the experiment of NASA's Turbofan Source-Diagnoistics-Test (SDT) rig [24]. In this study, the authors also highlighted the relevance of broadband noise in a fan stage, as it was predicted that a complete removal of tonal noise component in the spectra would only cause a maximum reduction of 3 EPNdB (effective-perceived-noise in decibels). Additionally, the tonal noise component became less prominent when a smaller number of stator vanes was used.

Serrations, similar to those previously discussed in chapter 3 have also been considered for LE noise mitigation, in spite of the different operating principles. The applications of LE serrations might have been inspired by the wavy protuberance on the flippers of humpback whales, which was considered to promote higher maneuverability compared to other whale species [25, 26]. Graham [27] studied several unique features of owl wings that could be related to their silent flight capability, such as the comb-like structure at the wing LE. LE serrations have been demonstrated in experiments as promising noise mitigation techniques [28–31], with some studies attempted at understanding their physical principles.

Kim *et al.* [32] employed a high-order fully-compressible Euler solver to study the TIN on a serrated flat-plate. The serrations followed a sinusoidal shape, and referred to the protruding points as the "peaks", the recessed ones as the "roots", and the region in between as the "hills". They found out that overall sound pressure level (OSPL) decreased linearly as the serration amplitude was increased, which was attributed to the reduction in source intensity at the serration hill. Later, Gea Aguilera *et al.* [33] employed the same methodology to study the relationship between the serrations geometrical parameters and the inflow turbulence length scales. They concluded that the serration amplitude and wavelength were to be at least twice the streamwise and spanwise integral turbulence length scales to achieve the maximum decorrelation between noise sources along the serration span. Chaitanya *et al.* [34] performed experimental studies using a serrated flat plate and a NACA 65(12)10 airfoil to retrieve the optimum serration wavelength, which was approximately 4 times the spanwise integral length scale of the inflow turbulence, such that the source distribution along the serration span became fully incoherent. Turner and Kim [35] performed a numerical investigation on the

impingement of a single vortex onto a serrated flat-plate. They found out that the surface pressure fluctuations intensity at the serration root was comparable to that of the regular straight LE, whereas at the serration tip, it was significantly reduced. This phenomenon was caused by the partial cancellation between the upwash/downwash induced by the approaching vortex and those by a secondary horseshoe vortex system forming along the side of the serrations.

Aside from LE serrations, the usage of porosity for mitigating TIN has also been considered. Lee [36] performed a numerical study to demonstrate BVI noise reduction by applying a porous LE tip. The author employed a Navier-Stokes-based solver and the effects of porosity were taken into account by specifying a finite surface transpiration velocity determined from the Darcy's law. The resulting noise reduction was found to be in between 2 and 4 dB depending on the porosity of the LE treatment.

Sarradj and Geyer [37] experimentally examined fully-porous SD7003 airfoils made of various commercially-available foam-like materials, such as *Basotect*, *Panacell*, and *Reapor*. The airfoils were mounted at the outlet of a wind-tunnel contraction and as a consequence, they were interacting with turbulent mixing layer of the exhaust jet. The authors observed that more permeable material generally produces higher noise reduction level, although this was also accompanied with more significant aerodynamic penalty. Geyer *et al.* [38] extended their past study by limiting the porosity treatment only at first 5 % of the airfoil. The porous LE was designed based on perforations that are oblique relative to the direction of the incoming free stream. The result was a porous LE with criss-cross pattern when viewed laterally. Perforations with different hole diameters and inclination angles were investigated. Inflow turbulence was generated by mounting a grid at the outlet of the wind tunnel contraction, resulting in a turbulence length scale that was 2-4 times the perforation diameter. Large noise reduction of up to 8 dB was observed in the low to mid frequency range with a slight high-frequency excess noise.

Roger *et al.* [29] considered a different porous NACA 0012 airfoil concept by using a perforated rigid exoskeleton covered with wire mesh, which was put on top of a solid flat-plate core and filled the rest of the volume with steel wool. The modified airfoil produced up to 10 dB of noise reduction under the influence of grid-generated turbulence, which was considered very promising despite no optimisation had been done for this design. The authors suggested that the porous material absorbed the kinetic energy of the impinging eddies, which reduced the scattering intensity at the LE.

More recently, Chaitanya *et al.* [39] experimented on a perforated flat plate immersed in a grid-generated turbulent flow field in order to link the noise reduction level with the streamwise extent of the porous LE. They found out that the noise reduction spectra collapsed when a Strouhal-number scaling based on the chordwise extent of the porous LE was used. It was proposed that the pressure communication between the upper and lower side of the perforated plate forced the airfoil aerodynamic response to propagate at the flow velocity, instead of at acoustic one in the solid plate case. This phenomenon lowered the noise scattering efficiency of the porous plate compared to the solid one, leading to noise reduction.

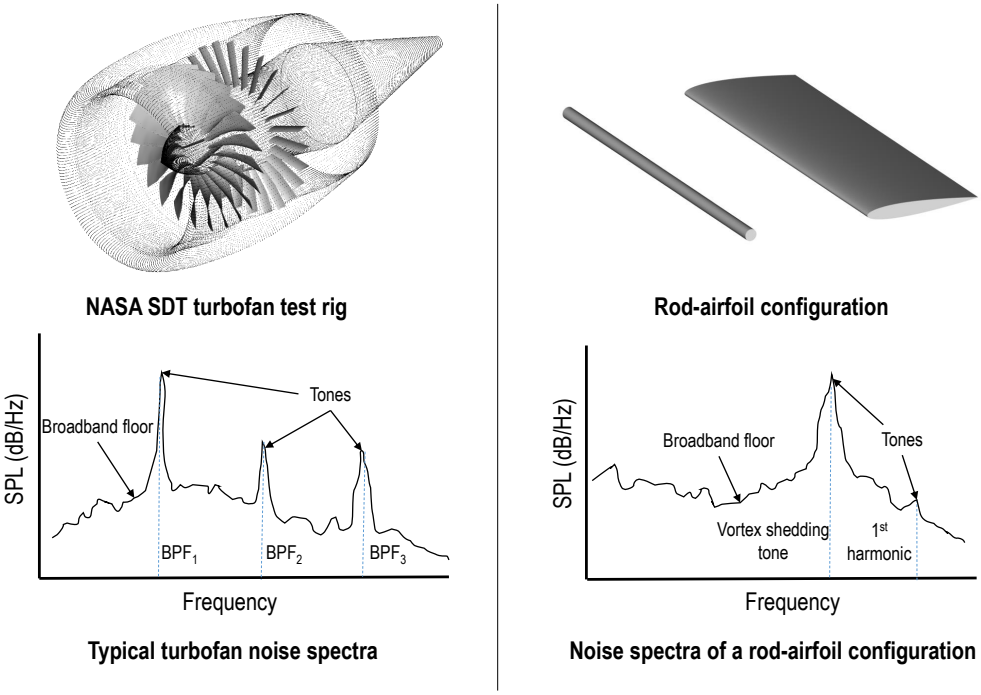

Figure 4.2: A comparison of typical noise spectra between a turbofan and a rod-airfoil configuration. BPF: blade-passage frequency.

4.1.2. ROD-AIRFOIL CONFIGURATION AS A TESTBED FOR TIN REDUCTION

The present study aims to evaluate the application of permeable material to mitigate turbulence-impingement noise mechanism, such as the rotor-stator interaction in a fan stage. Nevertheless, investigating a complete turbofan geometry is likely to be quite expensive, both experimentally and numerically, given its inherent complexity. A simplified setup that still retains the essential flow mechanisms would be more desirable as an alternative. For this purpose, Jacob *et al.* [40] proposed the rod-airfoil tandem configuration as shown in figure 4.2. At moderate Reynolds number, the rod periodically sheds turbulent vortices [41], which are impinging the downstream airfoil. Consequently, the airfoil is subjected to aerodynamic excitations with both narrowband (quasi-tonal) and broadband characteristics. This process resembles the periodic impingement of turbulent fan wake onto stator vanes inside a turbofan [42]. Jacob *et al.* [40] also reported that the TIN from the airfoil outranges that of an isolated rod, and a more noticeable spectral broadening at the vortex shedding frequency has been observed. The authors compared the experimental data with the corresponding LES and 3D-URANS data, and only the former was found to produce satisfactory agreement. Most of the recent benchmark studies using the rod-airfoil configuration has been summarised by Giret *et al.* [43] and Chen *et al.* [44].

The rod-airfoil configuration has often been modified for studying the aeroacoustics of different noise mitigation treatments. Agrawal and Sharma [45] and Chen *et al.* [44]

applied sinusoidal serrations at the airfoil LE. The serration wavelengths were $0.3c$ for the former and $0.1c$ for the latter, whereas the amplitudes were $0.06c$ and $0.12c$ respectively; c is the airfoil chord length. The noise reduction as observed by Agrawal and Sharma [45] was 3 dB when averaged across the frequency range of interest, although the noise reduction level was larger at higher frequencies. Similar trends were found by Chen *et al.* [44], but the frequency-averaged noise reduction level was slightly higher at 4.5 dB. This difference is likely to be related to the discrepancy in the serration amplitude between the two cases [33]. Chen *et al.* [44] also concluded that the LE serrations suppress the surface pressure fluctuations at the serration sides and tip, in addition to a decorrelation effect along the serration span.

The applications of permeable treatments for rod-airfoil configuration can also be found in literature, such as the one of Roger *et al.* [29] that has been mentioned in the previous subsection. A more recent study was performed by Zamponi *et al.* [46], although the setup used was different than the classical one [40]. Specifically, the rod diameter was twice as large, and a NACA 0024 airfoil has been used with a chord length that was 57 % longer. The authors considered a porous implementation that was almost identical to that in Roger *et al.* [29], i.e., a melamine-filled perforated exoskeleton that is fully-covered in metallic wire-mesh. To maintain the Reynolds number of the rod as in Jacob *et al.* [40], the flow speed in the experiment was reduced. The authors observed that the porous LE produced larger noise reduction level in the low frequency range, before monotonically decreasing towards the higher frequencies. On average, the noise reduction level was around 1.5 dB in the frequency range before the second harmonics. The authors concluded that the LE permeability has prolonged the evolution of the vortices as they impinged the LE, which led to a weaker noise radiation.

Porous LE and serrations are usually treated separately in literature, and thus, it is also interesting to evaluate both treatments in an identical setup in order to determine the similarities and differences in terms of TIN mitigation mechanisms. The findings would be useful for obtaining better noise mitigation techniques, which may include a combination of both, such as a poro-serrated LE. The present study also aims to look into the impact of the different noise mitigation techniques on aerodynamic performance, which has not been fully discussed in literature. However, the classical NACA 0012 airfoil lacks the feature of a typical turbomachinery blade, such as a pronounced camber and thin profile. For this purpose, a different airfoil profile will be used.

4.2. LE TREATMENTS FOR MITIGATING TIN IN A ROD-AIRFOIL CONFIGURATION

4.2.1. SIMULATION SETUP

In the present study, a simulation setup that replicates the rod-airfoil configuration of Jacob *et al.* [40] has been prepared, as shown in figure 4.3. In essence, the setup consists of a rod with the diameter $D = 10\,\text{mm}$ and an airfoil with a chord length $c = 100\,\text{mm} = 10D$. The airfoil LE is separated from the rod base (i.e., the most downstream point at the rod surface) by $10D$. The rod-airfoil configuration is positioned $15D$ downstream of an open-jet contraction that is $30D$ wide and $40D$ tall. The contraction width is identical to the span of both the rod and the airfoil and both

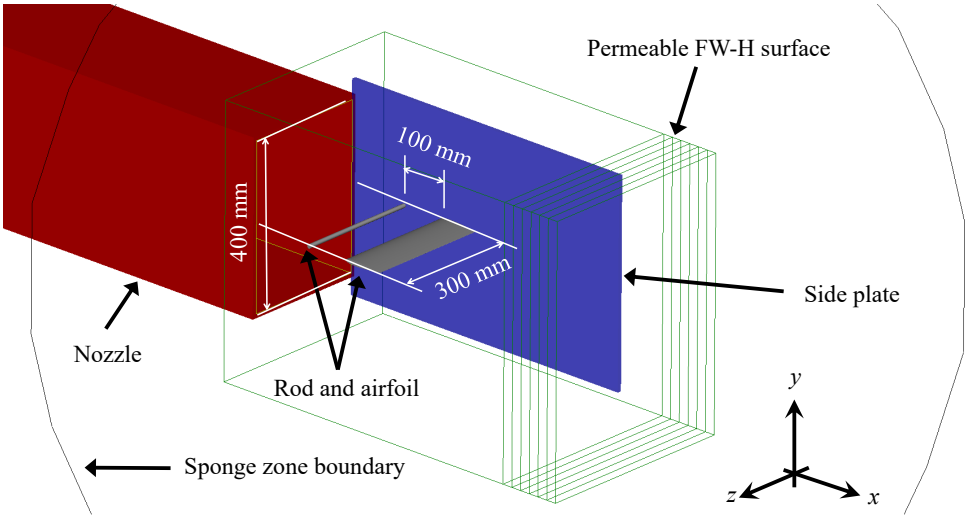

Figure 4.3: An isometric view of the rod-airfoil simulation setup. One of the side plate has been hidden from view. The outer black circular boundary delimits the sponge region.

components are mounted on side plates as they were in the original experiment. Since the present simulation takes into account the full span of the models, the far-field noise correction that is typical for narrow-span models [44, 45] to account for spanwise decorrelation of sources at the airfoil and rod surfaces (e.g., see Kato *et al.* [47], Seo and Moon [48]) is no longer necessary.

There are 3 airfoil profiles considered in this study as listed in figure 4.4; the NACA 0012, NACA 0006, and the cambered NACA 5406. Nevertheless, simulations with LE treatments will only be performed for the NACA 0012 and 5406 ones. For the sake of brevity, the NACA prefix will not be mentioned hereafter. The 0012 profile is used for validating the simulation setup while serving as a baseline when looking into the effects of the different LE treatments. The 5406 profile has been chosen as it has the geometrical features typically found in stator vanes, which include a relatively small thickness ratio and a pronounced camber. On the other hand, the 0006 profile is added to the list as it has similar LE radius as the 5406, and thus this symmetrical profile would be useful for verifying that the camber effect on TIN generation is minor [14, 49]. Both 0012 and 0006 airfoils are mounted at zero angle-of-attack (AoA), whereas the 5406 is given a 8° AoA to closely match the mean loading distribution on the stator vanes in the NASA SDT test rig [24, 42] at 90 % of the outer span at approach settings. Since the 5406 profile generates an asymmetrical loading, the trajectory of the rod wake is also affected, and thus, the airfoil is shifted upward by 4 mm ($0.4D$) for this specific configuration to ensure a direct impingement of the rod wake at the LE.

This investigation considers several types of LE treatments, including LE serrations, porous LE, or a combination of both. All of the different airfoil variants are shown in figure 4.4, and each treatment type is labeled with acronyms that are described in the figure caption. In the following, the specifications of each LE treatment will be provided.

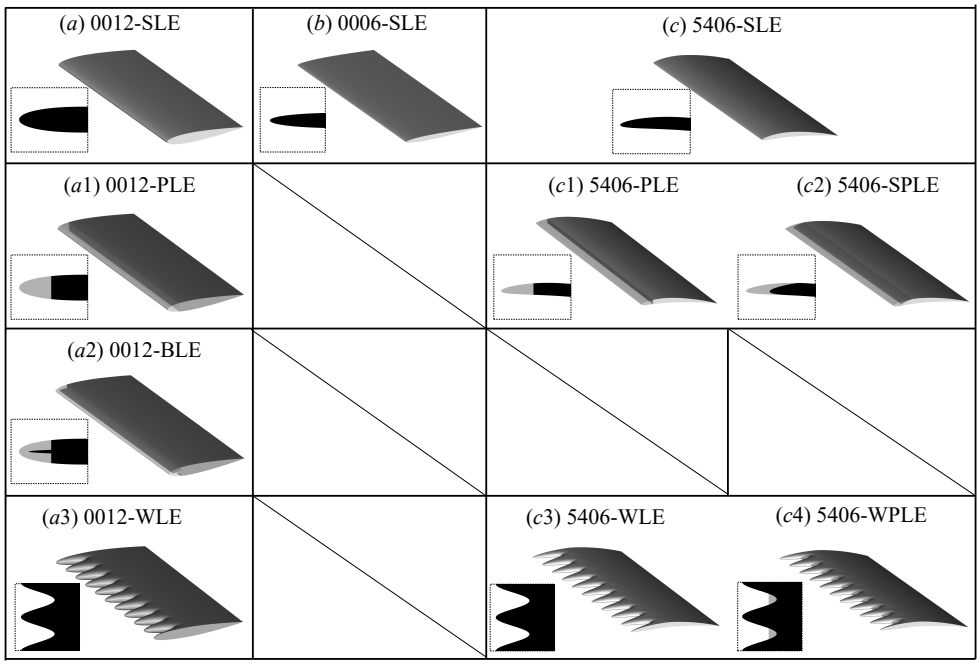

Figure 4.4: The types of airfoil and leading-edge treatments; SLE (straight-LE), PLE (porous-LE), SPLE (streamlined porous-LE), BLE (blocked porous-LE), WLE (serrated/wavy-LE), WPLE (serrations-porous-LE). The porous section of the airfoil is shown with lower opacity. Insets provide the zoomed-in lateral view at the LE. Note that for the insets of WLE/WPLE configurations, the top-down view is shown instead.

The sinusoidal LE serrations or wavy LE (WLE) can be characterised using the amplitude H (i.e., the chordwise distance between the serration tip and root) and wavelength (i.e., spanwise distance between adjacent serration tips) Λ; this is also shown in figure 4.5 (*a*). Currently, both parameters have been tuned to achieve optimal noise reduction based on the spanwise and streamwise integral length scales of the inflow turbulence (i.e., L^z_{ww} and L^x_{uu} respectively) [33, 34, 50] such that $\Lambda/L^z_{ww} \simeq 4$ and $H/L^x_{uu} > 2$. Consequently, both H and Λ are chosen to be $3D$ ($0.3c$), after following the estimation procedure for the value of L that will be discussed in subsection 4.2.2. Thus, the airfoil span equals to 10 serration wavelengths.

The LE serrations modify the chord length of the airfoil c_{WLE} with a periodic variation along the spanwise direction (z), following the procedure outlined in Chen *et al.* [44]. The chord length of the serrated airfoil c_{WLE} at any spanwise position z is defined as:

$$c_{\mathrm{WLE}}(z) = c + \frac{H}{2}\cos\left(\frac{2\pi z}{\Lambda}\right) \tag{4.2}$$

LE serrations are integrated into the rest of the airfoil by modifying the coordinates (x_{WLE}) upstream of a predetermined limit (x_{lim}); coordinates downstream of x_{lim} remain unchanged.

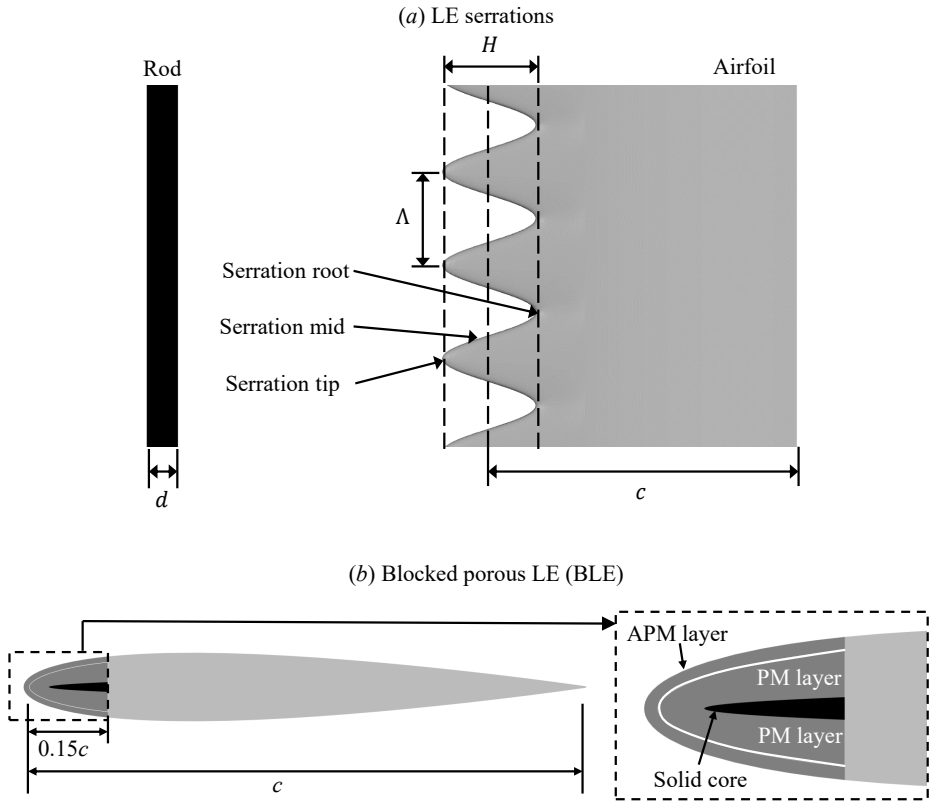

Figure 4.5: The nomenclature for the rod-serrated airfoil (WLE) configuration (*a*), and for the porous LE arrangement of the 0012-BLE configuration (*b*).

$$x_{\mathrm{WLE}} = \left(\frac{x_{\mathrm{SLE}}}{x_{\mathrm{lim}}}\right)[c_{\mathrm{WLE}}(z) - c + x_{\mathrm{lim}}] - (c_{\mathrm{WLE}}(z) - c) \tag{4.3}$$

For modelling the porous LE, an equivalent fluid region approach [51, 52] based on the Darcy's law has been employed, similar as in chapter 3. As shown in figure 4.5 (*b*), the multi-layer modelling approach is also present here. The outer layer of the porous LE is prescribed as Acoustic Porous Medium (APM), while the Porous Medium (PM) model is applied to the rest of the internal volume. The APM layer of the porous LE has a constant thickness of 1 mm, which encompasses the entrance length of the metal foam with a mean pore size of 0.8 mm. The details of the porous medium models have also been outlined previously in subsection 2.3, and the porous material properties are identical to those of the Ni-Cr-Al metal foam in table 3.2.

The porous treatment is applied at the first 15 % of the chord length, which is identical to the extent of airfoil chord that is modified by the LE serrations. Aside from the regular porous LE (PLE), there are other modified configurations. The 0012-BLE has a

solid core along the symmetry plane of the airfoil starting from $x/c = 0.05$ (i.e., 5 percent of the chord). This modification is intended to examine the effect of varying the fully-permeable extent of the porous LE. Differently, the 5406-SPLE has been designed to study the effect of streamlining the solid-porous junction. The porous treatment is also applied in the 5406-WPLE case where the porous medium covers the area surrounding the serration root (i.e., the inner 25 % of the serration amplitude). The WPLE configuration is considered to suppress the noise sources at the serration root, which might improve the noise reduction level compared to regular serrations.

A sketch depicting the lateral view of the simulation domain with the boundary conditions is shown in figure 4.6 (*a*). The simulation domain is enclosed inside a cube whose sides are 4 m ($400D$ or $40c$) long; note that the domain boundaries in the figure are not drawn to scale. The origin of the coordinate system is located at the midspan of the airfoil LE as illustrated in (*b*). A mass flow inlet is prescribed at the upstream face of the nozzle to obtain a mean velocity of 72 m/s at the nozzle outlet. Inlet condition with zero velocity are specified at the upper, lower, the far-left, and lateral faces of the simulation domain, whereas the far-right face is an outlet where the ambient pressure of 1 bar is specified. All solid surfaces are no-slip walls with the exception of the nozzle which is specified as a slip wall. An acoustic sponge region is prescribed outside a spherical boundary with a radius of $10c$ that encloses the near-field region. The simulation domain is subdivided into 13 grid refinement regions with the finest grid being applied next to the rod and the airfoil surfaces. At the finest grid configuration, there are 125 grid points assigned along the rod diameter, and thus the smallest grid dimension equals $8 \times 10^{-3} D$. This corresponds to the average y^+ of the first wall-adjacent cell of 25 on the rod and 15 on the airfoil. Among the different airfoil configurations, domain discretization results in a total of approximately 200×10^6 voxels on average for the finest voxel resolution. Airfoils with porous treatments would require a larger number of voxels due to the discretization of the porous medium region. More details of the grid configuration will be provided in the next subsection.

For obtaining far-field noise prediction, the FW-H analogy has been employed using the pressure and velocity fluctuations sampled at a permeable surface enclosing the near-field region. In order to mitigate the pseudo-sound contamination at the downstream face of the permeable surface, 6 planar surfaces have been added that are separated by $2D$ between each other. This stack of surfaces allow for averaging-out the pseudo-sound contribution (e.g., from the airfoil wake and the open-jet shear layer) while preserving the acoustic ones. The permeable FW-H surface records acoustic pressure at a rate of 29.5 kHz. The power spectral density of the acoustics pressure is obtained using Welch's method [53], in which a Hanning window with 50 % overlap has been applied to obtain a frequency resolution of 100 Hz. The simulation for each airfoil configuration has been carried out for 67 flow passes along the airfoil chord (i.e., total physical time of 0.108 s), excluding the initial transient of 10 flow passes. Therefore, the simulation time is equal to approximately 150 vortex shedding cycles. The required computational time varies slightly with different LE treatment, which will be reported in the next subsection.

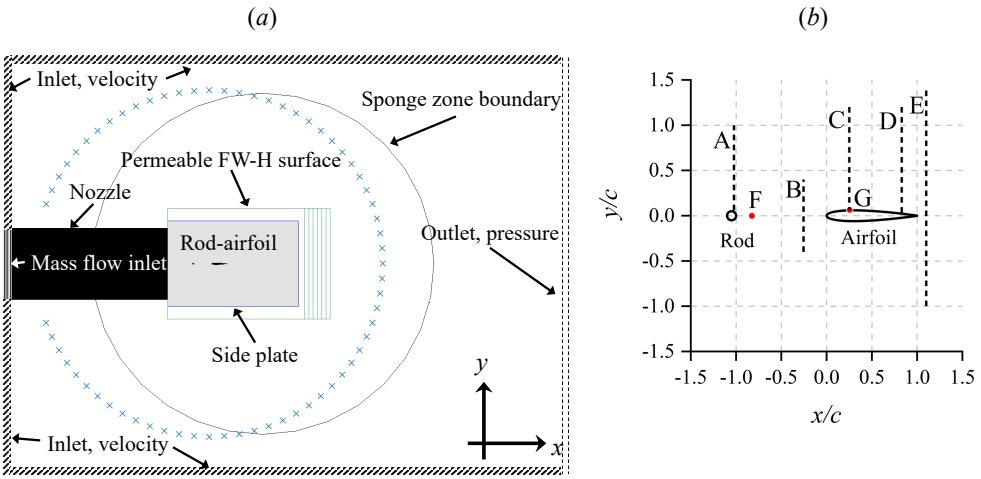

Figure 4.6: (*a*) Side view of the simulation domain for the rod-airfoil configuration; the outer boundaries are not drawn to scale. Blue crosses indicate microphone locations for far-field noise computation. A closer view on the baseline rod-NACA 0012 configuration (0012-SLE) is provided on the right (*b*). Vertical dashed lines indicate the locations where the velocity statistics are sampled and shown in figure 4.7.

.

4.2.2. VALIDATION AND GRID INDEPENDENCE ANALYSES

The validation for the baseline rod-airfoil configuration (0012-SLE) is reported in the following. Firstly, flow-field statistics are analysed in figure 4.7, where boundary layer profiles at several locations, as indicated in figure 4.6 (*b*), are shown at the top row. Present results are relatively in good agreement against previous numerical and experimental data. Small discrepancies are present, however, at locations C, D, and E, where the experimental data are skewed towards positive y/c with respect to the present ones. This is attributed to the vertical shift of the airfoil position in the experiment that is not considered in the simulation. Furthermore, it has been reported in [56] that the airfoil in the experiment has surface imperfections at the suction side, which may have caused a more noticeable velocity deficit and stronger turbulence level. The lower row in figure 4.7 shows the streamwise velocity fluctuation spectra at points F and G. Present results are generally in line with previous LES works of Chen et al. [44], Giret et al. [56], and Eltaweel et al. [57], where overprediction of turbulence fluctuations below the vortex shedding frequency (St_D = 0.195) can be observed, but the agreement of the present results compared to the experimental result remains satisfactory in the high frequency range. It is worth noting that the narrowband peak of the present simulation is slightly higher than the experimental one (i.e., St_D = 0.19). This discrepancy can be associated with the tendency of boundary layer separation at the rod being delayed in simulations [44, 58], which is often influenced by the turbulence model.

The validation of the surface pressure statistics on both the rod and airfoil is depicted in figure 4.8. The time-averaged surface pressure has been expressed as pressure coefficient $C_{p,\text{mean}}$, while the root-mean-square of surface pressure fluctuations p_{RMS} is

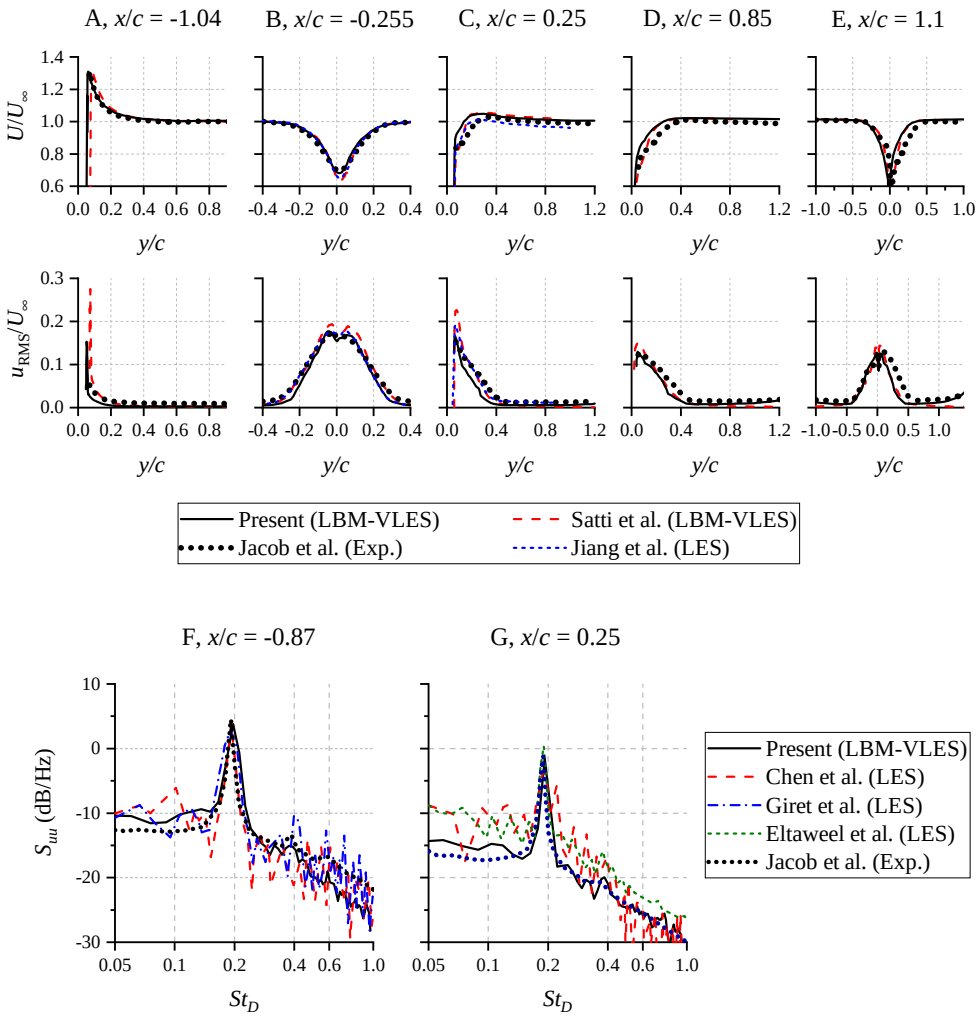

Figure 4.7: The upper row shows the profiles of mean (U) and root-mean-square (RMS) (u_{RMS}) of fluctuations of the streamwise velocity component at different locations along the rod-airfoil configuration. The lower row shows the power spectral density of streamwise velocity fluctuations S_{uu} at points (F) ($x/c = -0.87$, $y/c = 0.05$) and (G) ($x/c = 0.25$, $y/c = 0.08$), normalized with a reference velocity of 1 m/s. Current simulation results are compared against those from Jacob *et al.* [40] (experiment), Satti *et al.* [54] (LBM-VLES), Jiang *et al.* [55] (LES), Chen *et al.* [44] (LES), Giret *et al.* [56] (LES), and Eltaweel and Wang [57] (LES).

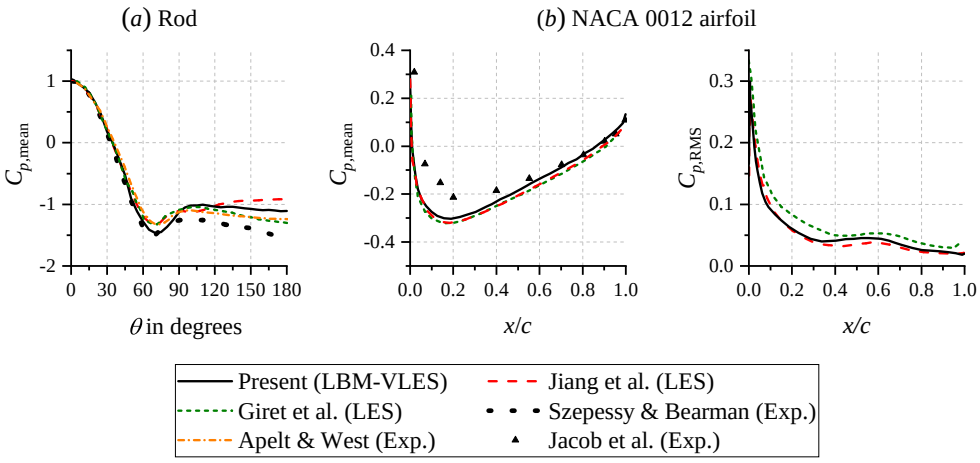

Figure 4.8: Validation of surface pressure statistics on the rod and the 0012-SLE airfoil. Time-averaged surface pressure is normalised as pressure coefficient $C_{p,\mathrm{mean}} = (p_{\mathrm{mean}} - p_\infty)/q_\infty$, where $q_\infty = 0.5\rho_\infty U_\infty^2$. In (*a*), the reference angle $\theta = 0$ faces towards the inflow direction. In (*b*), the root-mean-square of surface pressure fluctuations is expressed as $C_{p,\mathrm{RMS}} = p_{\mathrm{RMS}}/q_\infty$. Additional experimental data for the rod $C_{p,\mathrm{mean}}$ have been taken from Apelt *et al.* [59] and Szepessy and Bearman [60].

normalized with the freestream dynamic pressure $q_\infty = 0.5\rho_\infty U_\infty^2$. The $C_{p,\mathrm{mean}}$ of the rod in (*a*) is plotted in cylindrical coordinate with the zero-angle facing towards the inflow direction. The figure shows that the surface pressure distribution on the rod is in good agreement with the experimental ones, especially with that from Apelt *et al.* [59]. Meanwhile in (*b*), the $C_{p,\mathrm{mean}}$ plot on the airfoil shows a good collapse among all of the simulation results, but a noticeable discrepancy against the experiment of Jacob *et al.* [40] is present. As reported by Giret *et al.* [56], this behavior is attributed to the surface imperfection of the airfoil model in the experiment. The distribution of surface pressure fluctuations from the present simulation is also in line with that of Jiang *et al.* [55], although it slightly underpredicts the data of Giret *et al.* [56].

Measuring the turbulence length scales in the rod wake will be needed to produce optimal LE serrations design [34]. The integral scale of turbulence (i.e., the largest eddy in the flow-field [61]) is estimated as follows [33]:

$$L_{ij}^m(\boldsymbol{x}, l) = \int_0^\infty R_{ij}^m(\boldsymbol{x})\,\mathrm{d}l = \int_0^\infty \frac{\langle u_i(\boldsymbol{x} + \boldsymbol{l}\boldsymbol{e}_m)u_j(\boldsymbol{x})\rangle}{\langle u_i(\boldsymbol{x})u_j(\boldsymbol{x})\rangle}\,\mathrm{d}l \tag{4.4}$$

where R_{ij}^m is the correlation coefficient of turbulent velocity fluctuations u_i and u_j in the i^{th} and j^{th} directions respectively. $\boldsymbol{e}_m$ the unitary vector in the m^{th} direction, and $l = \boldsymbol{l}\cdot\boldsymbol{e}_m$ is the separation from the reference location. $\langle\cdot\rangle$ is the temporal-averaging operator.

Figure 4.9 shows the correlation coefficient distribution starting from the reference location $x/c = -0.25$, $y/c = z/c = 0$ (i.e., $2.5D$ upstream of the airfoil LE in the mid-section plane). The discrete integration of equation 4.4 has been performed with a separation of $0.1D$ along the streamwise (x), vertical (y), and spanwise (z) directions, for which the

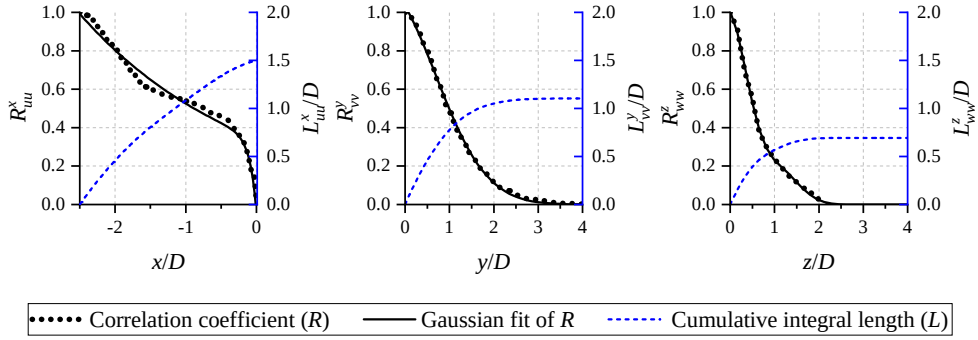

Figure 4.9: The distributions of correlation coefficients of turbulent velocity fluctuations along the streamwise (R^x_{uu}), vertical (R^y_{vv}), and spanwise (R^z_{ww}) directions for the NACA 0012-SLE case. The secondary axis (in blue) shows the cumulative integral length (L) based on the correlation coefficients. The reference location is at $x/c = -0.25$, $y/c = z/c = 0$.

Table 4.1: The integral length scales L^m_{ij} in the rod wake at $2.5D$ upstream of the airfoil LE.

Airfoil	L^x_{uu}/D	L^y_{vv}/D	L^z_{ww}/D
NACA 0012	1.50	1.10	0.73
NACA 5406	1.42	1.09	0.73

corresponding velocity components are denoted u, v, and w respectively. Such separation is significantly larger compared to the local grid size, and thus spatial aliasing would not affect the results. The integral lengths are summarised in table 4.1, in which the streamwise length scale is slightly reduced when the NACA 5406 is installed; the vertical and spanwise length scales are relatively unaffected. The information in table suggests that the serration amplitude and wavelength of $3D$ ($0.3c$) would satisfy the requirements of $H/L^x_{uu} \geq 2$ and $\Lambda/L^z_{ww} \simeq 4$ for obtaining optimal serration design for both airfoil profiles [33, 34].

Validation of the acoustic results for the present simulation is shown in figure 4.10. Far-field noise is computed using the FW-H analogy at several observer points along an arc in the $x-y$ plane with a radius of $185D$, centered at the airfoil LE. As shown by the blue crosses in figure 4.6 (a), the observer points are separated with 5-degree increment with zero-angle reference facing towards the downstream direction, such that $\theta = 90°$ corresponds to a location directly above the airfoil LE. The comparisons of the noise spectra at $\theta = 90°$ are given in figure 4.10 (a). Present result shows good prediction of both the spectral broadening and the amplitude of the fundamental tone in comparison with the experiment, although the high-frequency component has been underpredicted. Nevertheless, this behavior is also present in other numerical results [54, 56]. The far-field directivity pattern is examined in 4.10 (b), in which the present simulation is shown to be in agreement with experimental data. Discrepancies at shallow angles in the downstream direction between the present result and the LES of Giret *et al.* [56] can be attributed to the omission of the downstream face of the FW-H permeable surface in the latter, unlike the present one that completely encloses the rod-airfoil setup.

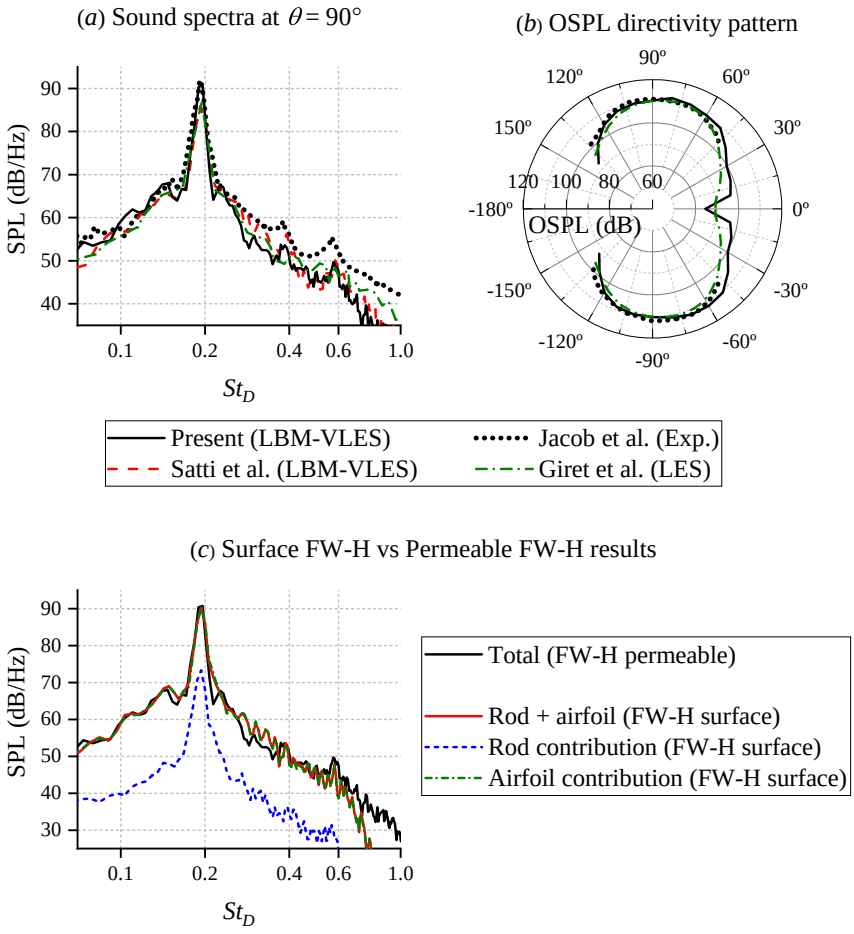

Figure 4.10: (*a*) Sound spectra in the far-field, computed at a location directly above the airfoil LE ($\theta = 90°$, i.e., $x/c = 0$ and $y/c = 18.5$) and (*b*) OSPL directivity pattern with zero degree reference towards the downstream direction. Plot (*c*) shows the far-field noise contribution of the rod, the airfoil, and both combined using the surface FW-H approach in comparison with that from the permeable FW-H approach.

Table 4.2: Comparison of domain statistics for the different grid resolution levels.

Type	Resolution (grid points/D)	Grid count (10^6)	CPU hours (10^3)
	5406-SLE		
Coarse	62.5	43.5	6.6
Medium	88.4	89.5	19.2
Fine	125	200.5	60.8
	5406-PLE		
Coarse	62.5	44.1	7.4
Medium	88.4	91.1	21.1
Fine	125	205.1	67.1
	5406-WLE		
Coarse	62.5	45.7	6.9
Medium	88.4	91.9	19.9
Fine	125	205.8	62.3

The quality of the permeable FW-H surface is examined further by comparing the resulting spectra to those obtained using the surface FW-H formulation. This is due to the fact that the noise sources in the rod-airfoil setup are expected to be predominantly of dipole type [5]. The usage of surface FW-H formulation also allows for examining the difference in the noise contribution between the rod and the airfoil. As shown in figure 4.10 (*c*), the spectra from the FW-H permeable formulation is very similar to the FW-H surface one (i.e., rod + airfoil), at least up to the second harmonic (St_D = 0.6). This suggests that the at higher frequencies, installation effects and the contribution of other source types, such as quadrupoles in the open jet shear layer, have become relevant. When the individual noise contributions of the rod and the airfoil are separated, it is evident that the TIN from the airfoil outranges the rod self-noise from the vortex shedding process. This confirms that the interaction between the rod wake and the airfoil LE is the dominant noise generation mechanism. Moreover, the figure implies that installation effects are relatively minor, as suggested by Jacob *et al.* [40].

A grid independence study is also performed to ensure that the selected grid resolution is sufficient to achieve converged solutions for the different cases. In the following, the grid independence analyses for the 5406-SLE, 5406-WLE, and 5406-PLE are provided. For each configuration, three different grid resolutions have been selected with a refinement ratio of $\sqrt{2}$, namely *coarse*, *medium*, and *fine*, as reported in table 4.2. Note that the grid count can differ from one case to the other, even for the same grid resolution setting. In general, the number of grid points is larger for PLE and WLE configurations due to the additional grid points needed to discretise the porous medium region and to resolve the more complex edge curvature of the LE serrations. Subsequently, the convergence trend of the simulation results will be evaluated based on the mean lift and drag coefficients ($C_{l,\text{mean}}$ and $C_{d,\text{mean}}$) of the airfoil, and the acoustic source power level (PWL).

Figure 4.11 (*a*) shows the variation of $C_{l,\text{mean}}$ and $C_{d,\text{mean}}$ with the number of grid points for each resolution setting. The number next to each data point corresponds to the grid resolution level, starting from level 3 (coarse) to 1 (fine), and level 0 is the Richardson extrapolation for a hypothetical "very-fine" case. Following the method

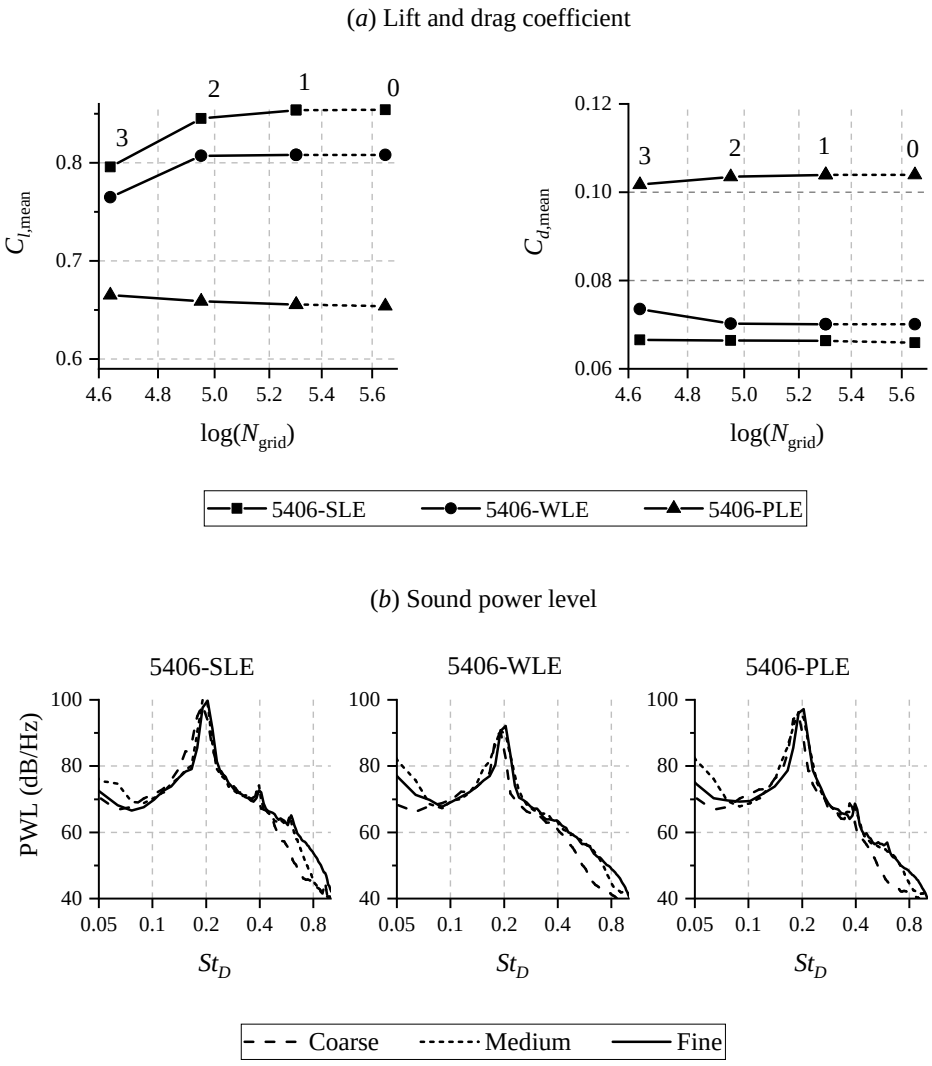

Figure 4.11: (*a*) The trend of the time-averaged lift $C_{l,\text{mean}}$ and drag $C_{d,\text{mean}}$ against the number of grid elements in the simulation domain (N_{grid}). The number next to each data point corresponds to the resolution level (3 - coarse, 2 - medium, 1 - fine), with level 0 being the Richardson extrapolation for the "very-fine" case. (*b*) The influence of the grid resolution on the sound power level (PWL) of different LE treatments on the 5406 airfoils.

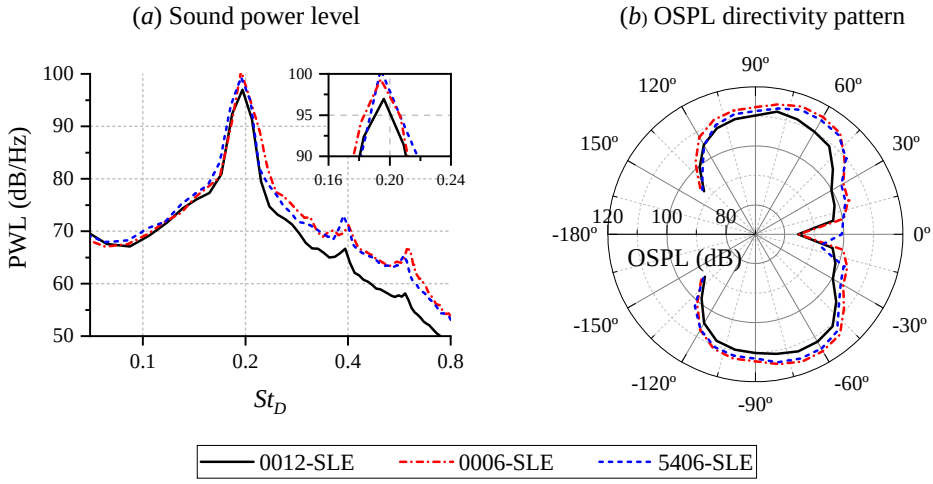

Figure 4.12: The comparison of the sound power level (PWL) (*a*) and the far-field directivity pattern (*b*) of the baseline airfoils.

proposed by Roache [62], the grid convergence index (GCI) is computed to help assessing grid convergence trend. For instance, $GCI_{1,2} = 0.0298\,\%$ and $GCI_{0,1} = 0.0009\,\%$ for $C_{l,\text{mean}}$ of the SLE case with the GCI ratio equals to $1.0099 \approx 1$. The small GCI value and the GCI ratio being close to unity indicate that the computational grids are within the asymptotic range of convergence. The GCI values and ratios for the other cases have been verified to exhibit similar trends. The influence of the grid resolution level on the source power level (PWL) of the rod-airfoil configuration is depicted in figure 4.11 (*b*). While the spectra in the mid Strouhal range ($0.1 < St_D < 0.4$) are relatively insensitive to the variation in the grid resolution, larger discrepancies are present at low and high frequencies. The former might be related to the installation effect (e.g., the scattering of the shear layer by the nozzle lip), while the latter can be associated with the cut-off frequency associated with the grid size at the permeable FW-H surface. Nevertheless, the figure clearly shows that a converging trend is present in the frequency range where LE noise is the most relevant (i.e., $0.08 < St_D < 0.8$).

4.2.3. ACOUSTIC EFFECTS OF THE LE TREATMENTS

The effect of airfoil geometry on TIN is examined in figure 4.12, where the source power level (PWL) and the far-field directivity pattern of the baseline 0012, 0006, and 5406 are compared between each other. In plot (*a*), the PWL spectra of 0006 and 5406 profiles show higher levels starting from the fundamental tone frequency (i.e., $St_D > 0.195$), which evidences the influence of airfoil thickness on the TIN intensity. This can be attributed to the stronger vortical distortion due to a higher velocity gradient near a LE with small radius [49]. The same effect can be found in plot (*b*), where the 0006 and 5406 profiles show an average of 2.5 dB higher OSPL compared to the 0012. On the other hand, the effect of camber and AoA is less pronounced given that the PWL spectra and the noise directivity pattern of the 0006 and 5406 profiles are almost identical to each other; this

is in line with findings of Devenport *et al.* [14]. Thus, this justifies the usage of the 5406 profile in the present investigation over the 0006 as the former also allows for studying the effects of the LE treatment on the lift generation of the airfoil.

Figure 4.13 provides the comparisons of the PWL for airfoils equipped with different LE treatments with the results for the 0012 profiles shown at the left column, and 5406 ones at the right. To better illustrate the PWL changes, the overall PWL (OAPWL) differences between the airfoils with LE treatments (LET) and the baseline (SLE) are shown at the lower row, categorised into tonal ($0.15 < St_D < 0.25$) and broadband components ($St_D > 0.25$). For the 0012 profile, the LE serrations (WLE) reduces the peak level at the fundamental tone frequency by around 9 dB as well as the high-frequency broadband noise by an average of 4.5 dB. On the other hand, the regular porous LE (PLE) does not produce any noticeable reduction for the tonal component, while the broadband component reduction is 2 dB on average. The blocked porous LE (BLE) exhibits the worse performance since it only eliminates the harmonic peaks at higher frequencies, leading to an average of 1 dB OAPWL reduction for the broadband category. In the case of 5406 profiles, the WLE configuration produces 7 dB and 4 dB noise reduction for the tonal and broadband components respectively, both of which are less compared to those for the 0012 profile. However, the porous treatments (PLE and SPLE) for the cambered airfoil perform better than in the 0012 profile, particularly for the broadband category (i.e., up to 3 dB for 5406 profile as opposed to 2 dB for 0012 one). The application of the porous cover at the serration root (WPLE) appears to be detrimental as the noise reduction levels of the tonal and broadband component are smaller than the WLE ones, which are 5 dB and 3.5 dB respectively.

The usage of LE treatments may alter the noise radiation pattern, and this is examined in figure 4.14. The OSPL in this plot is computed by integrating the SPL spectra in between $0.08 < St_D < 0.8$. In plot (*a*), the baseline (SLE) model produces a noise radiation pattern that resembles a compact dipole with slightly higher levels towards the downstream direction, which is caused by the refraction at the open-jet shear layer. Both the porous (PLE) and the blocked-porous (BLE) treatments do not appear to substantially modify the noise directivity. Nevertheless, the PLE treatment still generates an average noise reduction of 1.5 dB at angles above ±45°, although excess noise can be found at shallower angles. The LE serrations (WLE) clearly shows a large noise reduction level, and the presence of two main lobes, i.e. at ±115° and ±60°, which indicate a non-compact source behavior. In plot (*b*), the baseline (SLE) model still produces a dipole-like directivity, but the main axis is slightly tilted in the clockwise direction by almost 10°, which can be linked to the airfoil AoA. The 5406-PLE produces an asymmetrical noise directivity, such that the lower side of the arc shows lower noise level than the upper side, unlike its 0012 counterpart. This might be related to the mean loading effect, which may have caused stronger aerodynamic perturbations along the suction side of the LE. The porous LE with the streamlined solid-porous junction (SPLE) also shows similar behavior, but the average OSPL is around 1 dB lower than the PLE one. The LE serrations (WLE) possesses the largest noise reduction level while also exhibiting the presence of two main lobes. The same can be observed for the WPLE configuration except that the noise reduction level is smaller than the WLE one.

To study the sound source locations on each LE treatment, a conventional

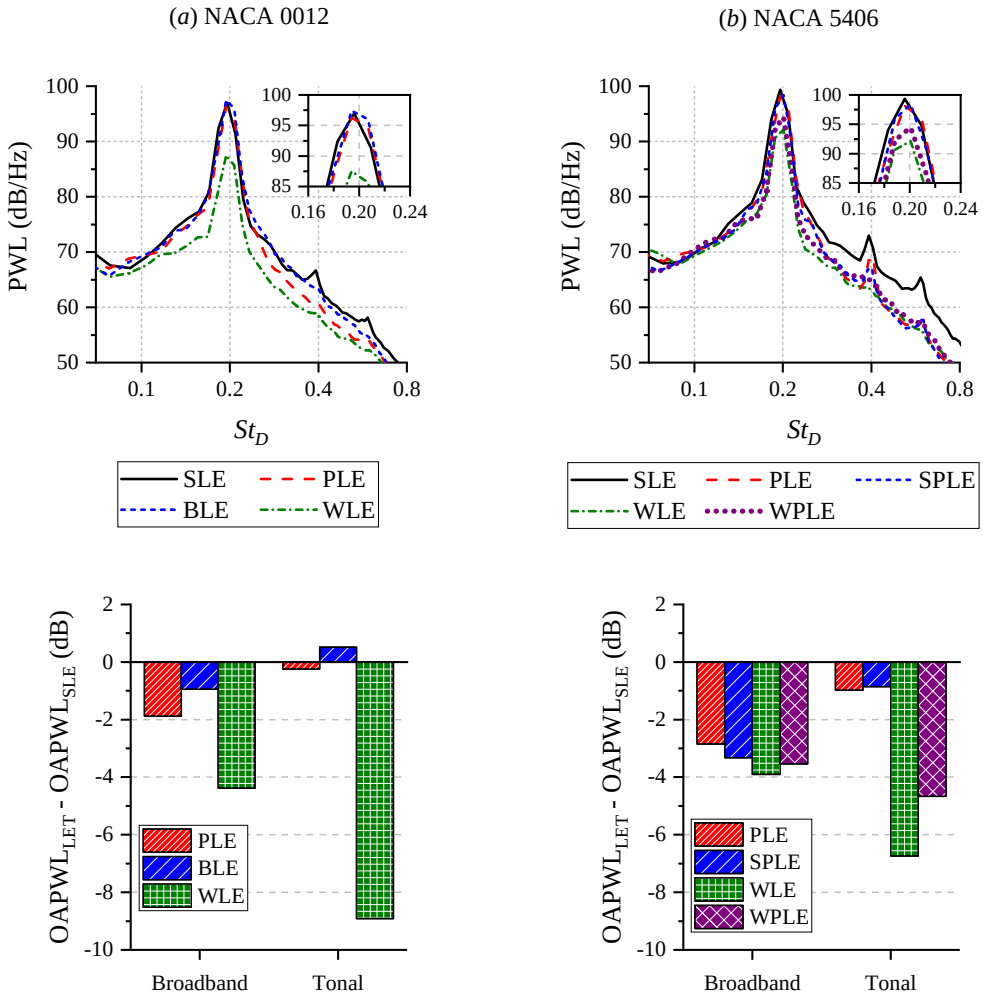

Figure 4.13: The upper row shows the comparison of the sound power level (PWL) for the different LE treatments. The lower one shows the OAPWL difference between the airfoils with LE treatments (LET) and the baseline (SLE) in tonal ($0.15 < St_D < 0.25$) and broadband noise components ($St_D > 0.25$).

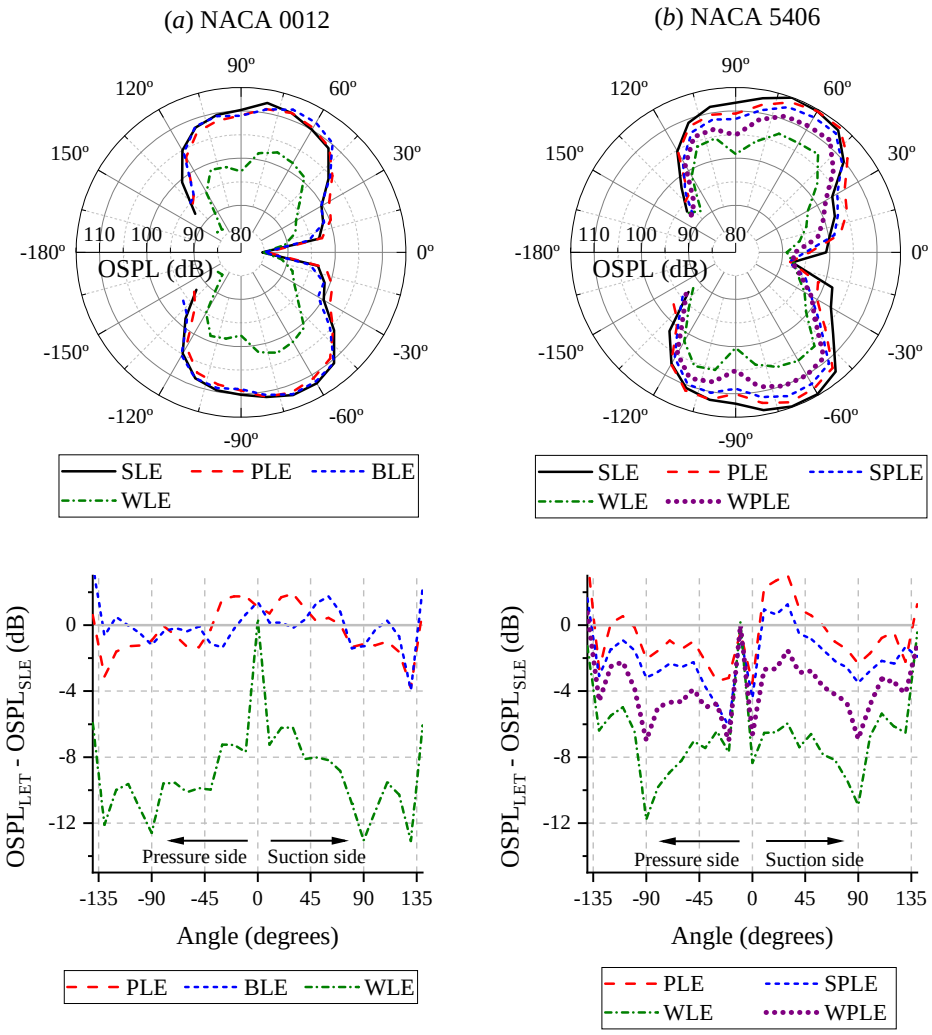

Figure 4.14: The comparison of the far-field noise directivity pattern for the different LE treatments is given at the upper row. The lower row shows the OSPL difference between the LET cases and the baseline.

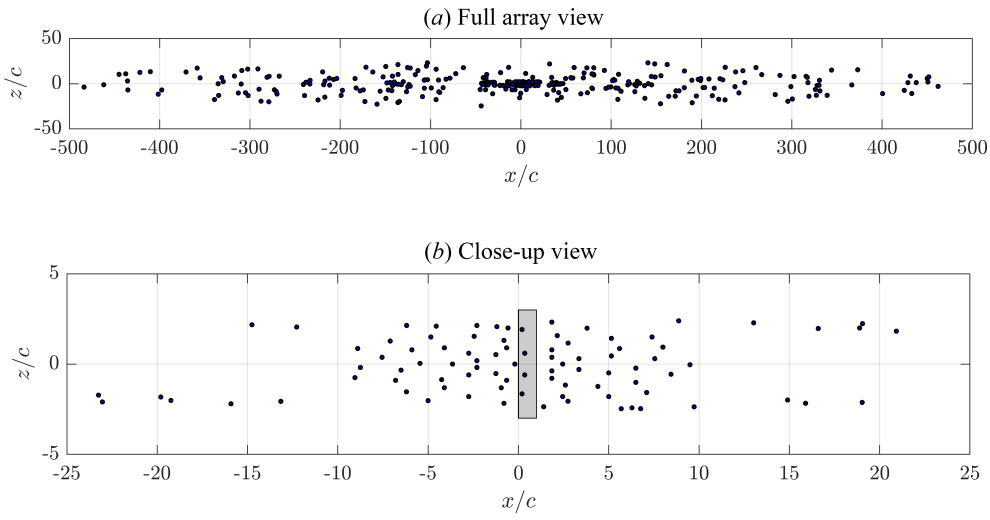

Figure 4.15: Microphone array used to obtain the acoustic source map. Overall dimension is 98 m × 24 m with the Rayleigh limit of 0.008 m (0.08c) at $St_D = 0.2$. The airfoil planform is shown as grey rectangle in (b).

beamforming algorithm has been used[2]. The arrangement of the beamforming antenna is illustrated in figure 4.15. The antenna is built by combining 5 concentric microphone arrays, resulting in a total of 365 microphones which are placed following an Underbrink's spiral configuration [63]. The center of the antenna is aligned with the midspan of the airfoil leading edge as depicted in figure 4.15 (b). The Rayleigh limit (i.e., spatial resolution) of the microphone array is estimated to be ≈ 0.008 m (0.08c) at $St_D = 0.2$. This allows detecting the shift in the dominant noise source location along the first 0.15c of the airfoil where LE treatments are applied. The sound spectra for each microphone is computed by applying the FW-H analogy with the permeable surface previously shown in figure 4.4.

The acoustic source maps for the one-third octave band at the fundamental tone are plotted in figure 4.16 (a)−(d) for 0012 series, and (e)−(i) for 5406 series. The maps confirm that the LE region is where noise is predominantly generated for all cases. The trends produced by the beamforming technique are in agreement with figure 4.13. The 0012-PLE is shown to have slightly smaller source intensity compared to its SLE counterpart, whereas the BLE one shows an increase. Furthermore, the 0012-WLE exhibits higher noise reduction of about 10 dB. For the 5406 series, both PLE and SPLE show around 1-2 dB noise reduction relative to the SLE one, while that for WLE and WPLE is 6 dB and 3 dB respectively.

The position of the dominant source for each LE treatment is also found to vary with frequency, which is plotted in figure 4.17. Within the frequency range of interest, the figure shows that the dominant source for the baseline (SLE) configuration of both 0012 and 5406 profiles is located around the LE ($x/c = 0$). For the 0012 airfoils, the dominant source location for the PLE case is at $x/c = 0.1$ at lower frequencies ($St_D < 0.2$) before

[2]The same tool has been used earlier in chapter 3.

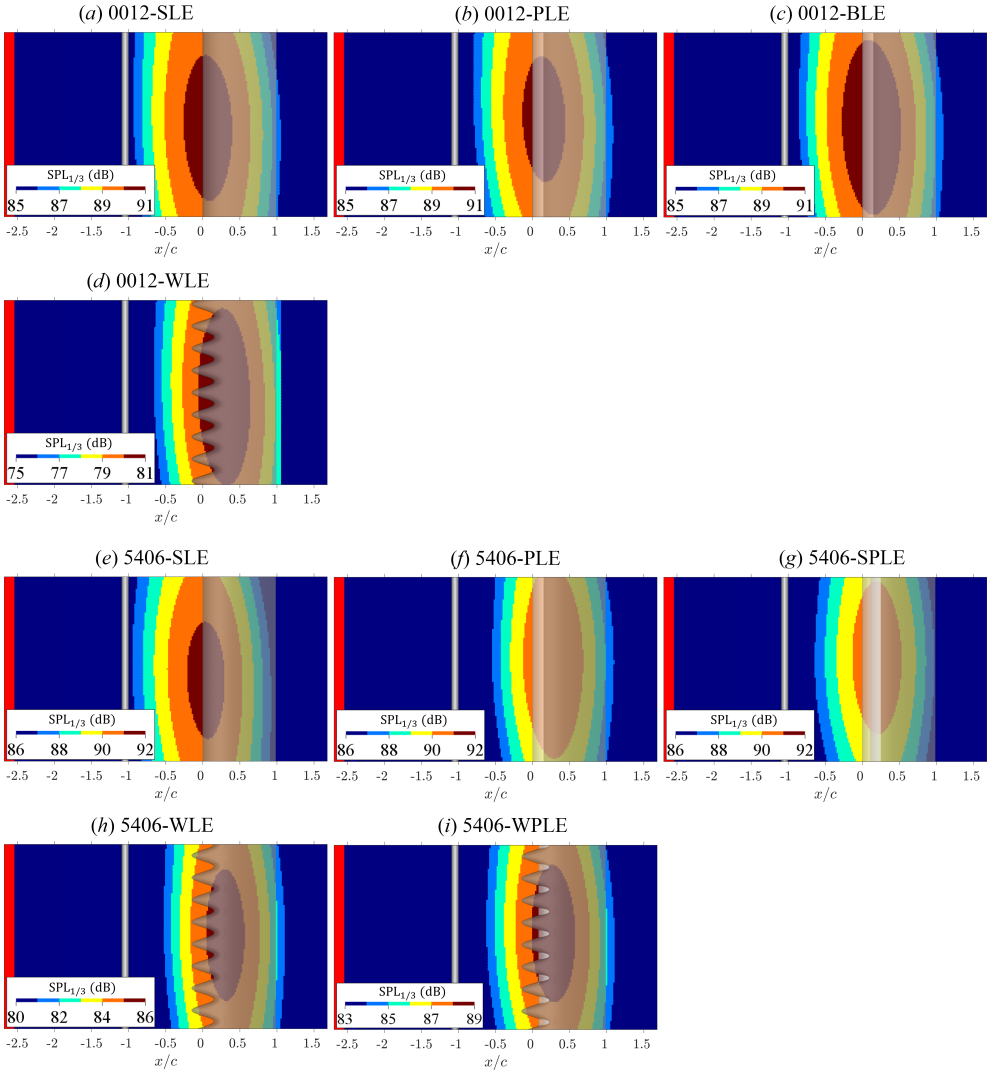

Figure 4.16: Acoustic source map of the different LE treatments for the one-third octave band at the fundamental tone ($St_D = 0.2$). The nozzle outlet is shown as the red area at the left of each plot. Porous medium region is coloured with brighter shade.

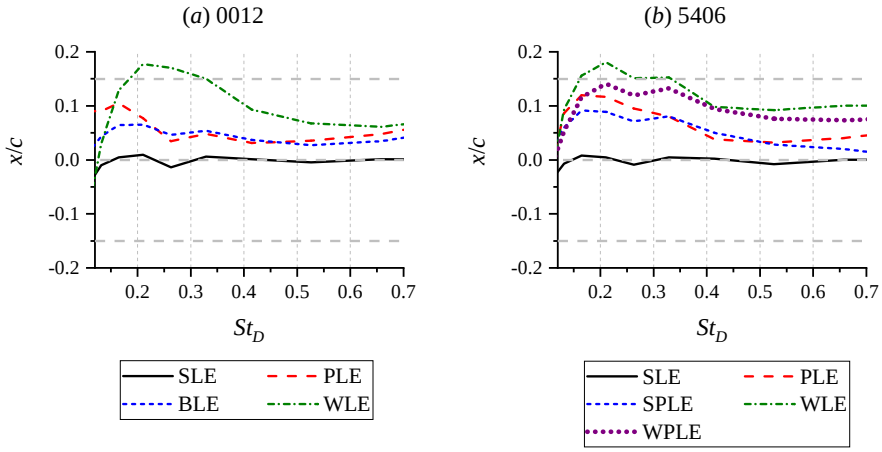

Figure 4.17: The x/c position of maximum SPL in the acoustic source map at different frequencies.

moving slightly upstream for $0.25 < St_D < 0.5$, and again in downstream direction at higher frequencies. The shift of the dominant source location is less prominent for the BLE configuration, where it remains at $x/c \approx 0.05$ (i.e., the edge of the solid core) throughout the entire frequency range. This evidences that the solid core of the BLE serves as the actual leading edge where acoustic waves are scattered from. The dominant source on the airfoil with WLE is found near the serration root ($x/c = 0.15$), although it is shifted to $x/c = 0.1$ at higher frequencies. The concentration of noise sources at the serration root has also been observed in other studies [35, 44].

The plots for 5406 airfoils also exhibit similar trends as the 0012 ones. Both PLE and SPLE configurations show the dominant source location in the middle of the porous LE ($0.12 < x/c < 0.03$) although the latter is located slightly upstream than the former at the primary tone frequency ($St_D = 0.2$). The discrepancy can be attributed to the smaller porous extent in the case of SPLE due to the protruding shape of its solid-porous junction. For the WLE variant, the dominant source corresponding to the primary tone is also found near the serration root. The upstream shift of the source location at higher frequencies, previously observed in the 0012-WLE case, is also present. When the porous extension is applied at the serration root (WPLE), the dominant source moves upstream, which implies that the acoustic scattering takes place on the porous medium instead of at the serration root.

4.2.4. CHARACTERISTICS OF UNSTEADY SURFACE PRESSURE FIELD

Following the acoustic analogy of Curle [5] and the LE noise model of Amiet [23], far-field noise level is known to be proportional to the intensity and spatial coherence of the fluctuating forces acting on the airfoil. Consequently, noise attenuation can be achieved by either (1) suppressing the intensity of surface pressure fluctuations at the airfoil LE, or (2) decreasing the spatial coherence between scattering locations along the LE span. Both mechanisms will be referred to as the source-reduction and spanwise-interference effects respectively. The role of each mechanism for the porous LE and LE serrations will

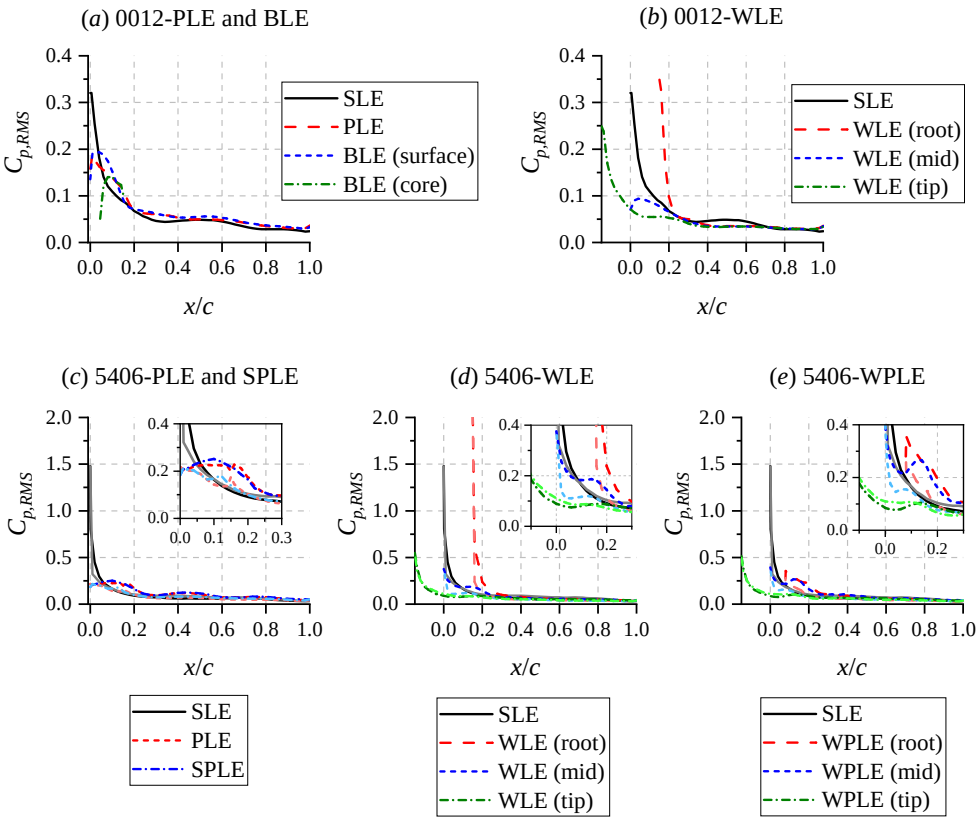

Figure 4.18: Root-mean-square of surface pressure fluctuations $C_{p,\mathrm{RMS}} = p_{\mathrm{RMS}}/0.5\rho_\infty U_\infty^2$ distribution along the airfoil chord. For the 5406 airfoils, the values on the pressure side are plotted using lighter colour.

be examined closer in this subsection.

The chordwise distribution of surface pressure fluctuations intensity is depicted in figure 4.18. In each plot, the RMS values of surface pressure fluctuations (p_{RMS}) have been normalised with the freestream dynamic pressure $q_\infty = 0.5\rho_\infty U_\infty^2$. 0012 airfoils with porous treatments are examined in plot (*a*). It is evident that the $C_{p,\mathrm{RMS}}$ intensity for the baseline (SLE) case is the highest near the LE, which is expected. The PLE and BLE treatments decrease the peak $C_{p,\mathrm{RMS}}$ level significantly, but further downstream, pressure fluctuations intensity for both porous treatments remains higher than the SLE one. The sum of $C_{p,\mathrm{RMS}}$ between $0 < x/c < 0.15$ for the PLE case is only 6 % lower than that of the SLE, whereas there is almost no difference for the BLE. The BLE case also shows a downstream shift of the peak $C_{p,\mathrm{RMS}}$ location to around $x/c = 0.1$, which is close to the edge of solid core inside the porous medium, suggesting that the solid core behaves as an additional scattering location. These behaviors could explain the relatively small noise attenuation level of the PLE and BLE configurations.

The plot for 0012 with LE serrations (WLE) is shown in (*b*), where $C_{p,\mathrm{RMS}}$ distributions

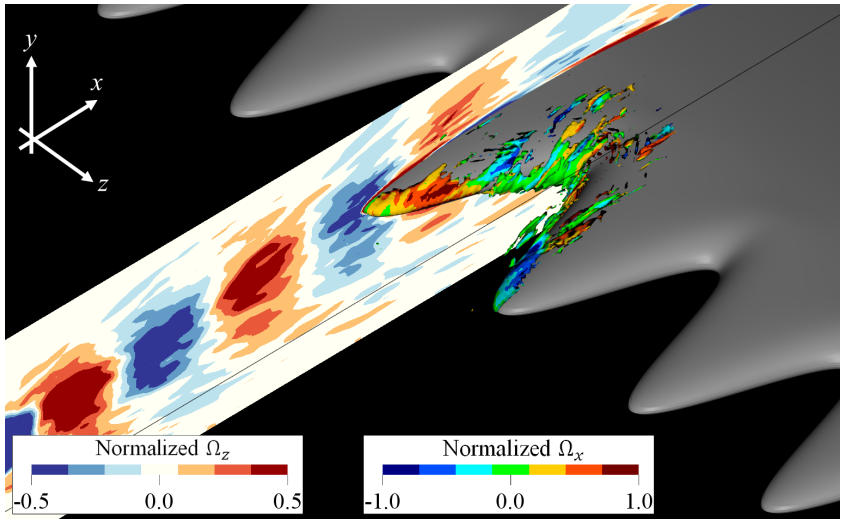

Figure 4.19: Instantaneous flow visualization for the 5406-WLE, bandpassed at $0.19 < St_D < 0.21$. The cut plane shows the contour of spanwise vorticity Ω_z. The iso-surface corresponds to $\lambda_2 = -3 \times 10^7\,\mathrm{s}^{-2}$, colored with streamwise vorticity Ω_x values. Vorticity is normalized against the characteristic time scale D/U_∞.

have been sampled at three different spanwise locations along the serrations. The serration root and tip show very similar trends as the SLE one, but the peak $C_{p,\mathrm{RMS}}$ level at the serration tip is lower than the SLE one whereas the root still exhibits comparable intensity. Nonetheless, the surface pressure fluctuations are substantially suppressed at the mid region, in line with the observation of Turner and Kim [35], and thus, the main sources at the LE serrations are mainly located at the root and tip. As a result, the spanwise average of the $C_{p,\mathrm{RMS}}$ distribution on the WLE configuration is smaller than that on the SLE, which contributes towards noise attenuation. The $C_{p,\mathrm{RMS}}$ at the serration mid is much lower than at the other locations due to it being at an oblique angle relative to the incoming vortex street [23, 32, 64]. Differently, the $C_{p,\mathrm{RMS}}$ reduction at the serration tip can be attributed to the secondary vortex system generated by the serrations [35]. This is shown using the flow visualization in figure 4.19. The figure depicts a clockwise-rotating vortex impinging the serration tip, which induces downwash throughout the LE. However, this also leads to the production of clockwise-rotating streamwise vorticity along the serration mid, such that the serration tip experiences additional upwash while at the serration root, a downwash. Due to the influence of this secondary vortex system, the induced aerodynamic fluctuations at the serration tip are partially cancelled out, while they are enhanced at the serration root.

Figure 4.18 (*c*) shows the $C_{p,\mathrm{RMS}}$ distribution for the 5406 profiles with porous treatments. The 5406-SLE clearly shows a substantially higher pressure fluctuations when compared to its 0012 counterpart, which corresponds to the stronger noise radiation of the former. The peak $C_{p,\mathrm{RMS}}$ levels of both 5406-PLE and 5406-SPLE are much lower than the SLE one. Further downstream, however, high $C_{p,\mathrm{RMS}}$ intensity can still be found near the solid-porous junctions for each porous treatment (i.e., $x/c = 0.15$

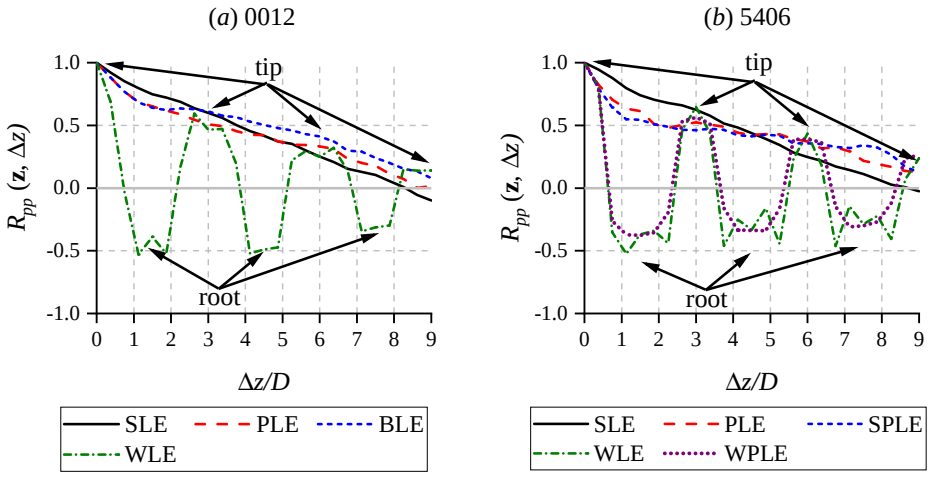

Figure 4.20: The spanwise correlation R_{pp} of the surface pressure fluctuations for the different LE treatments. The locations of serration tips and roots for the WLE are indicated in the plots.

for PLE and $x/c = 0.1$ for SPLE). This location is expected to scatter noise as well given that it represents an impedance discontinuity (i.e., a sudden change in permeability) [65]. The 5406-WLE behaves almost identically to the 0012-WLE. The $C_{p,\mathrm{RMS}}$ at the serration tip and mid is substantially smaller than that of the SLE although the intensity at the root is higher. Pressure fluctuations level downstream of the LE serrations (i.e., $x/c > 0.15$) decreases rapidly and matches that of the SLE, implying that noise sources are still concentrated near the serration root. The $C_{p,\mathrm{RMS}}$ distributions at the serration tip and mid of the 5406-WPLE remain similar to the WLE ones. However, the sharp peak previously found at the serration root of 5406-WLE has been replaced by a wider one with a lower peak intensity, similar to that of the 5406-PLE. Nevertheless, the total $C_{p,\mathrm{RMS}}$ between $0.08 < x/c < 0.3$ (i.e., between the edge of the porous extension and the location where the WPLE trend converges to the SLE one) is $\approx 10\,\%$ higher compared to that of the WLE, which can be linked to the smaller noise reduction of the WPLE. Moreover, the $C_{p,\mathrm{RMS}}$ along the serration root of the WPLE is the highest near the edge of the porous extension. This suggests that the porous extension reduces the effective amplitude of the serrations, which in turn hampers its overall noise reduction capability.

Following figure 4.18, the current implementation of porous LE is not very effective at suppressing the overall surface pressure fluctuations, and the LE serrations are only slightly better in this regard, considering that the pressure fluctuations at the serration root are enhanced. Regardless, the LE serrations have been able to produce significantly higher noise attenuation level compared to the porous LE. This might be attributed to difference in the spanwise coherence of the noise sources along the span of the different LE treatments. To verify this, two-point cross-correlation coefficients of surface pressure fluctuations are examined at different spanwise positions, as defined in the following:

$$R_{pp}(z,\Delta z)=\frac{\langle p'(z,t)\ p'(z+\Delta z,t)\rangle}{\sqrt{\langle p'^2(z,t)\rangle}\sqrt{\langle p'^2(z+\Delta z,t)\rangle}} \tag{4.5}$$

where $p'(z,t)$ is the time series of surface pressure fluctuations at a reference spanwise location z, $\langle\cdot\rangle$ is the temporal-average operator, and Δz is the spanwise separation from z. For computing R_{pp}, surface pressure fluctuations are sampled for 135 vortex shedding cycles with an acquisition rate of 15 kHz. The spanwise separation is $0.375D$ and thus, there are 9 sampling points per serration wavelength. The reference spanwise location is at the airfoil midspan ($z/D=0$), while the chordwise coordinate varies for different LE treatments depending on where $C_{p,\mathrm{RMS}}$ is the highest (see figure 4.18).

The spanwise R_{pp} trends for the different cases are shown in figure 4.20, in which the spanwise coordinate has been normalized with the rod diameter. The plot is shown within the range of $0<z/D<9$, which is equivalent to 3 serration wavelengths for WLE and WPLE configurations. For the baseline airfoil, the correlation level reduces to zero at a distance of around 8-9 times the rod diameter. In plot (*a*), the PLE and BLE configurations exhibit faster decorrelation rate than the SLE up to $z/D=3$, which suggests that the porous LE enhances the breakdown of the smaller eddies whereas the larger ones still persist. Differently, the R_{pp} trend for the WLE varies significantly along the span, even reaching negative values at locations near the serration root. This indicates that the phase of the noise sources at the serration root is the opposite of that at the tip, resulting in destructive interference. Such phenomenon can be attributed to the chordwise separation between the two locations, which leads to a phase delay between turbulence impingement at serration tip and root. Correspondingly, the serration tips show positive R_{pp} values since they are located at the same streamwise position. However, their peak R_{pp} values also follow the same downward trend along the span that can be found in other types of LE treatments. Similar behaviors can be observed for 5406 airfoils in (*b*). The spanwise decorrelation in the cases of PLE and SPLE initially outpaces that of SLE up to $z/D=4$, but the trend is reversed further away. The alternating positive and negative R_{pp} distribution is present for WLE and WPLE. However, near the serration root of the WPLE, which is covered by the porous medium, the R_{pp} values are slightly higher than the WLE ones. This further supports the argument that the porous medium reduces the effective amplitude of the serration in the case of WPLE, resulting in a smaller noise attenuation.

The correlation analysis is extended into frequency domain in the following. The cross-spectral density of the surface pressure fluctuations $G_{pp}(f)$ is defined as in equation 4.6, where $r_{pp}(z,\Delta z,t)$ is the temporal cross-correlation function between a reference location z and another one located Δz away, $\mathrm{j}=\sqrt{-1}$, and T equals the sampling length. The complex cross-spectral density can be expressed in term of its magnitude $|G_{pp}|$ and the phase angle A_{pp}.

$$\begin{aligned} G_{pp}(z,\Delta z,f)&=\int_0^T r_{pp}(z,\Delta z,t)e^{-\mathrm{j}\,2\pi f t}\mathrm{d}t \\ &=|G_{pp}(z,\Delta z,f)|\left[\cos A_{pp}(z,\Delta z,f)+\mathrm{j}\sin A_{pp}(z,\Delta z,f)\right] \end{aligned} \tag{4.6}$$

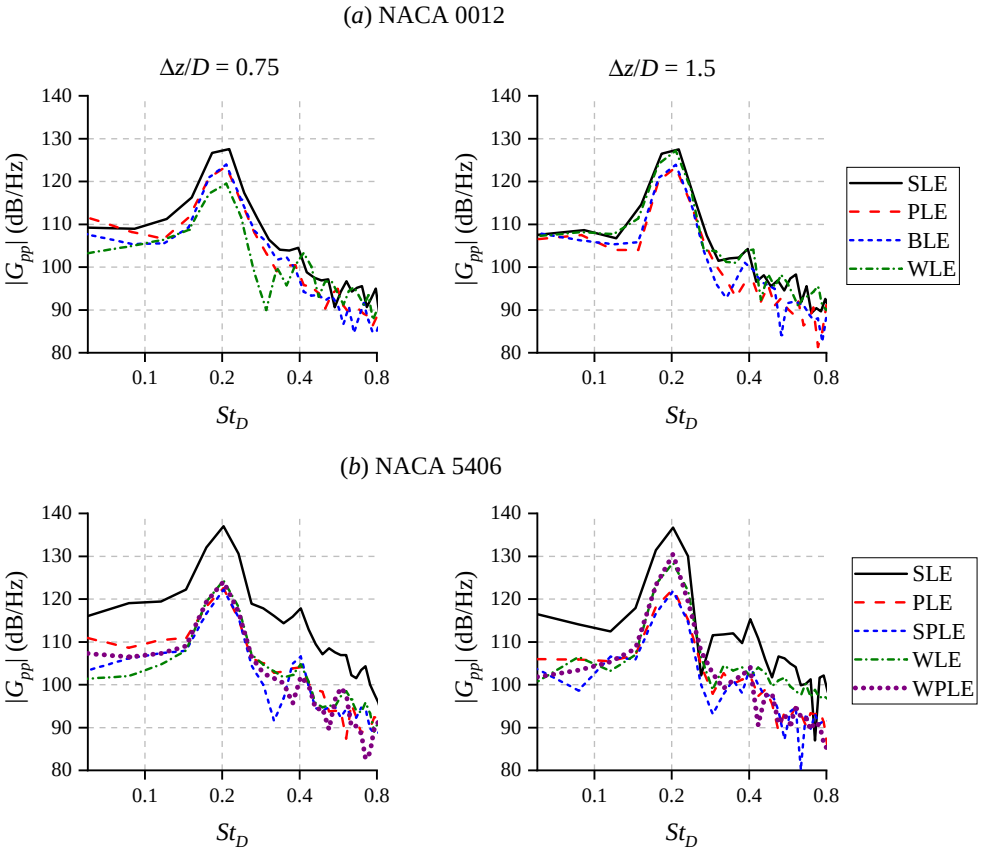

Figure 4.21: The magnitude of cross-spectral density $|G_{pp}|$ at two locations separated by $\Delta z/D = 0.75$ (left column) and $\Delta z/D = 1.5$ (right column) from the airfoil midspan. The top row (*a*) corresponds to 0012 airfoils, while the 5406 ones are at the bottom (*b*) .

The magnitude of the complex cross-spectral density $|G_{pp}|$ is plotted in figure 4.21. Note that the $|G_{pp}|$ has been normalised with the reference pressure of 20 µPa. It is computed based on a reference point at the airfoil midspan against two other locations, $\Delta z/D = 0.75$ and $\Delta z/D = 1.5$. For WLE and WPLE configurations, these locations correspond to the serration mid and root respectively. In all plots, the narrowband peak can be found at the vortex shedding frequency, which is expected since the turbulence in the rod wake is dominated by the coherent spanwise vortices as illustrated in figure 4.19 previously. For the 0012 airfoils, the porous treatments (PLE and BLE) can be observed to produce slightly lower coherence level at both $\Delta z/D$ positions. Differently, the coherence level for the 0012-WLE is noticeably lower than the SLE one at the serration mid, but it increases at the serration root. This behaviour is attributable to the suppressed or enhanced surface pressure fluctuations intensity at the serration mid and root respectively. The same behavior can be observed in figure 4.21 (*b*) for 5406-WLE and 5406-WPLE. Meanwhile the average coherence level of the PLE and SPLE configurations

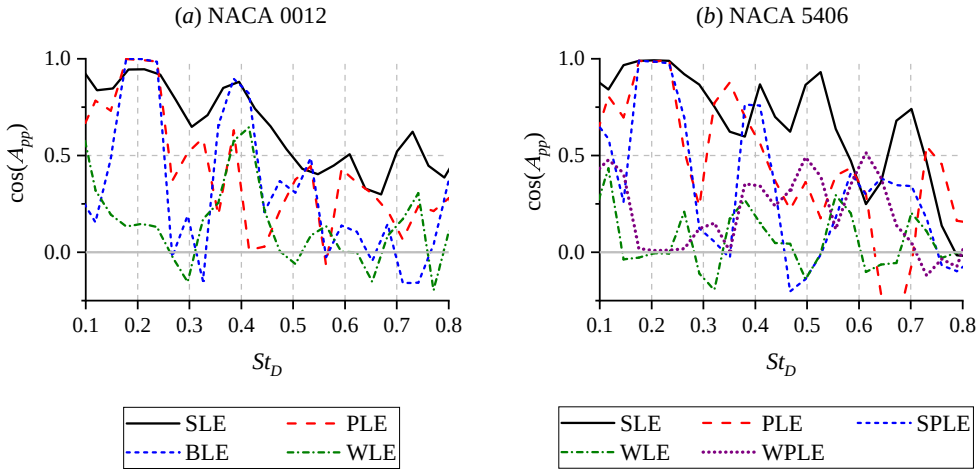

Figure 4.22: The spanwise-averaged ($0 < z/D < 3$) phase angle of the cross-power-spectra of surface pressure fluctuations A_{pp} for the different LE treatments.

Table 4.3: The comparison between the reduction in lift fluctuations and noise mitigation for airfoils with LE treatments relative to the solid ones; LET: leading edge treatment.

	$20\log\left(\frac{C_{l,\mathrm{RMS,LET}}}{C_{l,\mathrm{RMS,SLE}}}\right)$	$\Delta\mathrm{OSPL}_{\mathrm{LET,SLE}}$ (dB)
0012-WLE	−3.71	−10.25
0012-PLE	−1.38	−1.17
0012-BLE	−0.94	−0.80
5406-WLE	−3.69	−7.78
5406-PLE	−1.45	−1.10
5406-SPLE	−2.06	−2.42
5406-WPLE	−3.43	−4.43

remains lower than that of the SLE.

The phase angle information are provided in figure 4.22, where they are spanwise-averaged along a distance that is equal to the serration wavelength ($0 < z/D < 3$). Furthermore, the phase angle has been expressed in term of its cosine value. For the baseline airfoils (0012-SLE and 5406-SLE), the phase angle tends to become lower towards the higher frequencies, as eddies in the high frequency range are typically smaller than the low frequency ones. At the vortex shedding frequency ($St_D = 0.195$), it is evident that only WLE and WPLE configurations exhibit a relatively small phase angle, unlike the porous treatments. This can be related to the fact that the serrations are highly effective at mitigating the tonal noise component compared to the porous LE. In the higher frequency range, all of the different treatments appear to perform similarly; the phase angles are generally lower than those of the SLE.

Based on the results presented up to this point, the LE serrations appear to have an advantage over the porous LE in term of the spanwise-interference effect, whereas the porous LE relies mainly on the source-reduction effect as the noise mitigation mechanism.

To verify this argument, the noise attenuation level will be compared to the reduction in lift fluctuations. This comparison follows the formulation of Curle's analogy for a compact dipole source (i.e., where the characteristic length of the source is much smaller than the acoustic wavelengths), which relates the far-field sound pressure p'_a with the unsteady force $F(t)$ on a body, as the following:

$$\langle p_a'^2 \rangle = \left(\frac{1}{4\pi a_\infty}\right)^2 \frac{\cos^2(\theta)}{r^2} \left\langle \left(\frac{\partial F(t)}{\partial t}\right)^2 \right\rangle \tag{4.7}$$

where a_∞ is the freestream speed of sound, θ and r are the observer angle and distance relative to the source respectively, and $\langle\cdot\rangle$ is the temporal average operator. Although this analysis is expected to be valid only for frequencies below $St_D < 0.5$ (following the compactness criterion $M_\infty St_c < 1$ [66]), it is still useful for examining the noise reduction near the vortex shedding frequency.

Table 4.3 presents two quantities: (1) the OSPL attenuation level based on the average values between $60° < \theta < 130°$ in figure 4.14 (i.e., along the main dipole lobe), and (2) the reduction in the RMS of lift fluctuations $C_{l,\mathrm{RMS}}$ that represents the averaged of the values computed for each spanwise section of the airfoil. The latter is expressed in logarithmic value to allow for comparison with the former. It is expected that both quantities would be similar if the noise attenuation for a particular LE treatment is mainly due to the suppression of the lift fluctuations. This appears to be true for the porous treatments (0012-PLE/BLE and 5406-PLE/SPLE), implying that they mainly mitigate the sound source intensity. On the other hand, the $C_{l,\mathrm{RMS}}$ reduction is smaller than the ΔOSPL for the airfoils with LE serrations (0012-WLE and 5406-WLE/WPLE). It can be inferred that the difference is due to the spanwise-interference effect. Moreover, the table implies that the porous extension at the serration root decreases the efficacy of the spanwise-interference effect of the serrations given that the amount of $C_{l,\mathrm{RMS}}$ reduction of both 5406-WLE and 5406-WPLE is rather similar, as discussed earlier in this subsection.

4.2.5. THE AERODYNAMIC EFFECTS OF LE TREATMENTS

This subsection examines the impact of the LE treatments on the flow field surrounding the airfoil as well as its aerodynamic performance. Firstly, figure 4.23 shows the time-averaged surface pressure distribution. It is also accompanied with the velocity magnitude contours and pathline plots in figure 4.24 to elucidate the flow behaviours inside the porous medium.

In figure 4.23 (*a*), the porous medium causes a stronger suction (i.e., lower $C_{p,\mathrm{mean}}$ values) at locations upstream of $x/c = 0.15$, which is associated to the flow transpiration into the porous medium [36]. This behavior is evident in figure 4.24 (*c*) and (*e*), where some pathlines are shown to penetrate into the porous medium from the LE tip, and those are later ejected near the solid-porous junction. Downstream of the porous LE extent (i.e., $x/c > 0.15$), the $C_{p,\mathrm{mean}}$ distributions for both PLE and BLE cases recover to that of the SLE, although this indicates a stronger adverse pressure gradient (APG) near the solid-porous junction. The results are a faster boundary layer growth and larger displacement thickness as illustrated in figure 4.25 (*a*). The surface pressure distribution

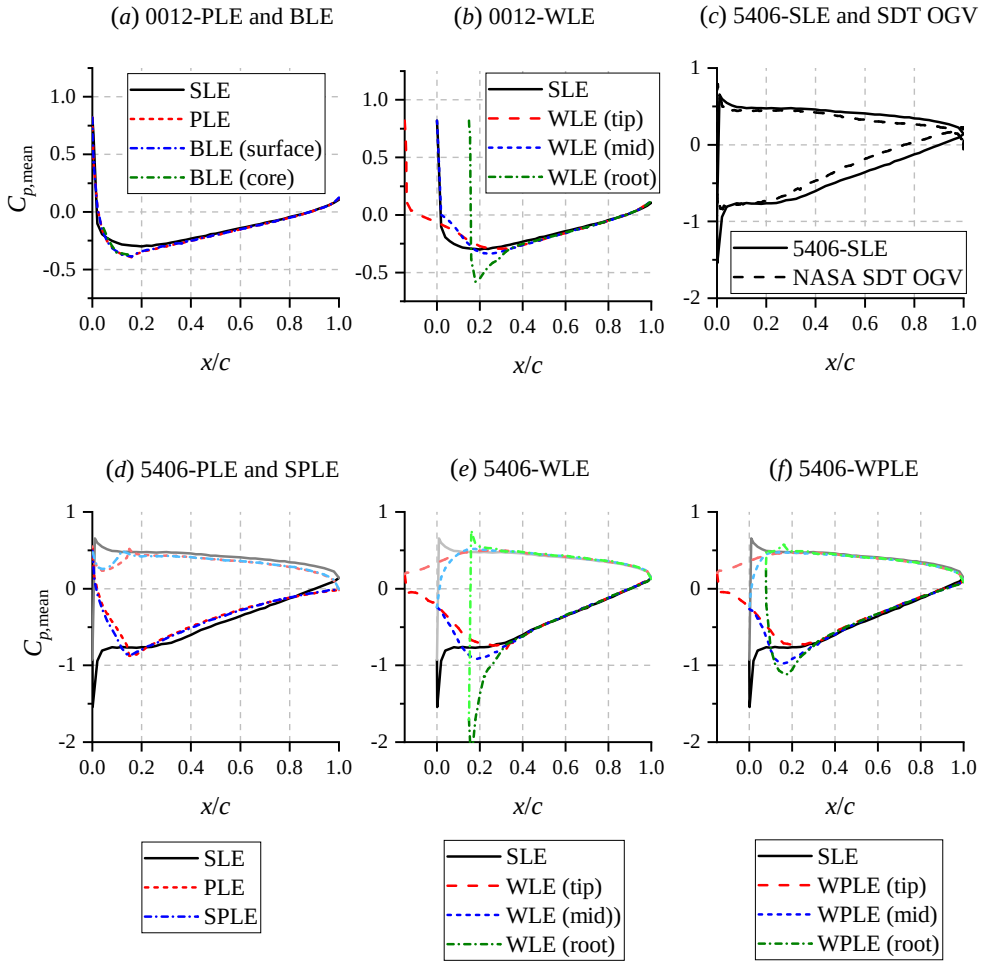

Figure 4.23: Time-averaged surface pressure distribution $C_{p,\mathrm{mean}}$ for the different LE treatments. For the 5406 airfoils, the pressure distribution at the pressure side is plotted in lighter shade.

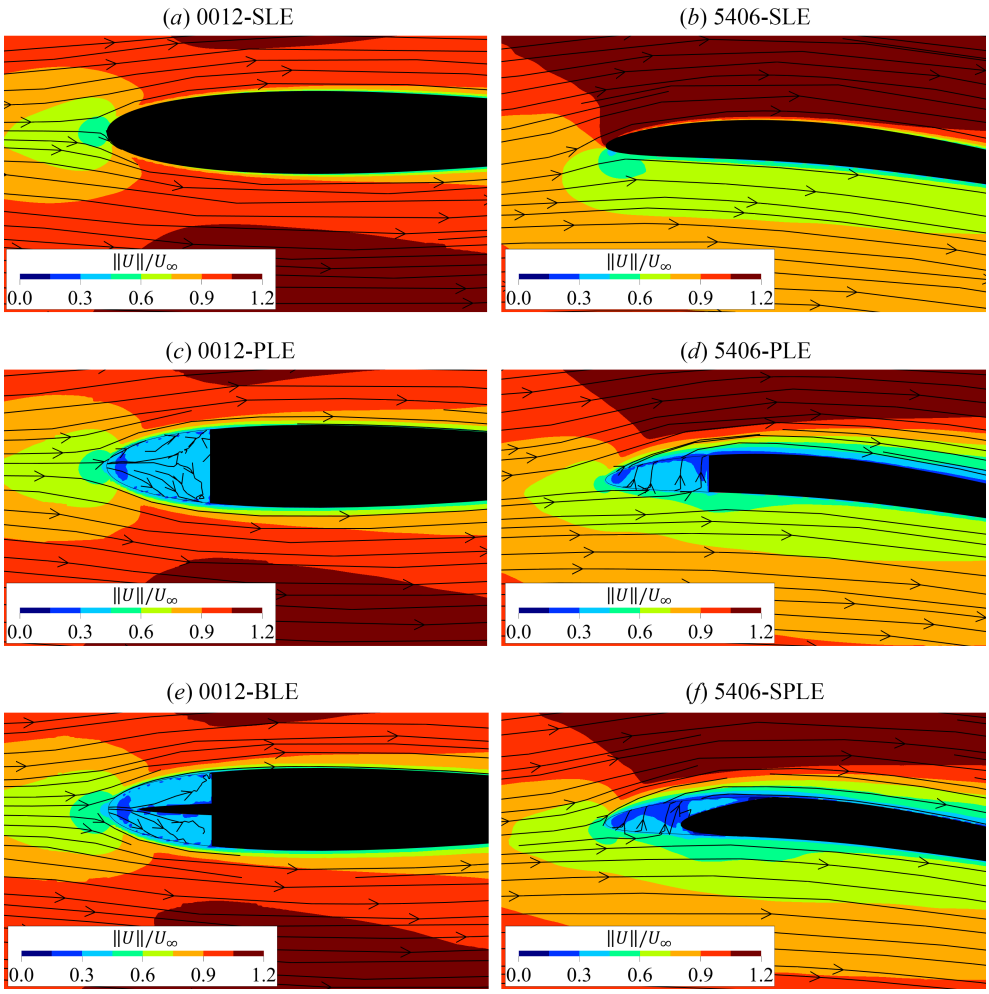

Figure 4.24: Pathline plots and contours of time-averaged velocity magnitude $||U||/U_\infty$ at the midspan of airfoils with porous LE (*c* to *f*) in comparison to the SLE (*a* to *b*). Note that some pathlines may enter or leave the sampling plane in the direction normal to this page.

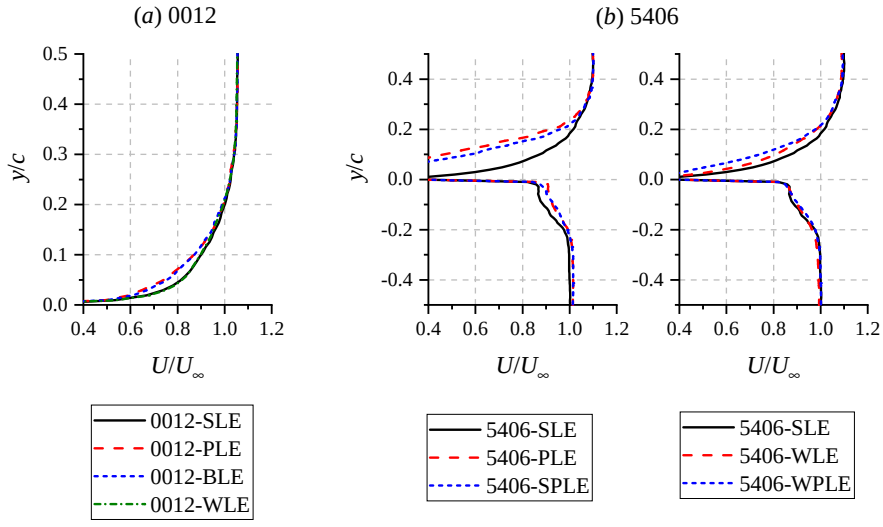

Figure 4.25: The time-averaged streamwise velocity profile at $x/c = 1$ for each LE treatment. The plots are sampled at the midspan ($z/c = 0$), except for WLE and WPLE configurations, where the values are averaged over a serration wavelength.

on the 0012 with LE serrations (WLE) varies along the span as depicted in figure 4.23 (*b*). Rapid flow acceleration can be observed near the edge at each spanwise location, but the locations of the suction peaks are still the same as in the SLE case (i.e., around $x/c = 0.2$). Due to this, the flow acceleration at the serration peak and mid is milder compared to at the serration root. Additionally, the suction peak at the serration root is also noticeably higher than that at the other locations. The stronger flow gradients at the serration root can be considered to be responsible for generating more intense noise sources [49] as indicated in the previous subsection. Nonetheless, as in the PLE and BLE cases, the $C_{p,\text{mean}}$ distribution downstream of the serrations is similar to that in the baseline (SLE) case. Referring to figure 4.25 (*a*), the boundary layer at the TE of the WLE airfoil is almost identical to the SLE one, indicating that the aerodynamic impact of the serrations is quite minimal, at least for this airfoil profile.

A comparison between the pressure distribution on the baseline 5406 with that on the outlet-guide-vane (OGV) of the NASA SDT test rig is plotted in figure 4.23 (*c*), and the similarity between both is the reason why the 5406 profile has been selected in this investigation. The effects of the porous treatments on the 5406 profile is shown in plot (*d*). The suction peak that is located near the LE tip at the suction side of the SLE configuration has disappeared in the both PLE and SPLE case. Simultaneously, the $C_{p,\text{mean}}$ values along the pressure side of the porous LE decrease, which indicates a pressure balancing process that has led to a cross-flow from the pressure side to the suction side of the porous LE. This process is illustrated in figure 4.24 (*d*) and (*f*), where pathlines enter the porous medium from the pressure side and they are ejected along the suction side. Due to its streamlined solid-porous junction, the flow ejection angle in the SPLE case appears to be shallower than in the PLE case. Nevertheless, the pressure balancing process causes the boundary

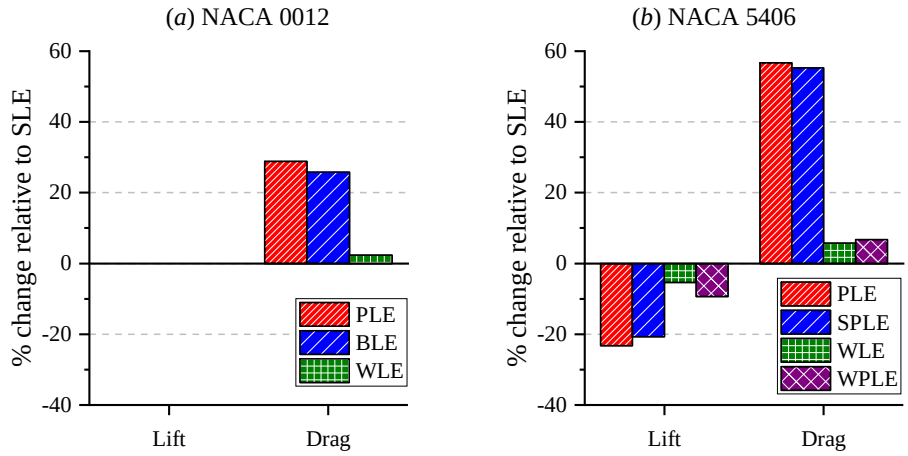

Figure 4.26: Time-averaged aerodynamic forces of the airfoils with LE treatments expressed in term of the relative difference to those of the baseline configurations (SLE).

layer at the suction side to become significantly thicker, which is reflected in the large velocity deficit shown in figure 4.25 (*b*). Conversely, the plot shows that the boundary layer at the pressure side experiences a more favorable condition. In addition, two distinct layers can be identified: (1) the inner layer where the mean velocity first converges to $U \approx 0.85U_\infty$, and (2) the outer layer where the mean velocity eventually reaches $U \approx U_\infty$. The former can be considered the "true" boundary layer that is embedded inside the latter, which is the rod wake.

The pressure distribution for the 5406-WLE is provided in figure 4.23 (*d*). While the SLE case has a noticeable suction peak near the LE tip, the serration tip and mid behave differently. The pressure differences between the upper and lower sides at these locations are relatively small, and thus, the protruding segment of the serrations contributes less to the total airfoil lift. This is comparable to the situation for a delta wing where the pressure difference between both sides of the wing causes tip leakage, resulting in the generation of streamwise-oriented vortices. Nevertheless, the smaller aerodynamic loading at the serration tip and mid is compensated by the large suction peak at the serration root. However, this also implies that the adverse pressure gradient is also more intense downstream of the serration root, leading to a faster boundary layer growth at the suction side of the airfoil as depicted in figure 4.25 (*b*). The WPLE configuration exhibits identical behaviors as the WLE at the serration tip and mid. The porous extension the serration root of the WPLE results in a lower suction peak, due to the pressure balancing process across the porous medium, similar to that in PLE and SPLE cases. Consequently, it is expected that the lift penalty of the WPLE configuration is greater than that of the WLE. Additionally, the pressure balancing process also causes a more noticeable velocity deficit in the boundary layer at the airfoil suction side, implying a more substantial drag penalty.

The aerodynamic forces on the airfoils with the various LE treatments are summarised in figure 4.26. The time-averaged lift and drag in the figure have been expressed in term of relative difference to those for the SLE configurations for each airfoil profile. It has

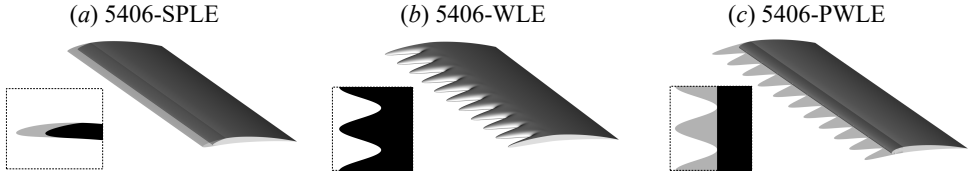

Figure 4.27: The isometric view of 5406-SPLE, 5406-WLE, and 5406-PWLE. The porous section of the airfoil is shown with lower opacity. The inset for SPLE shows a lateral view of the airfoil; for WLE/PWLE configurations, the insets show the top-down view of the planform.

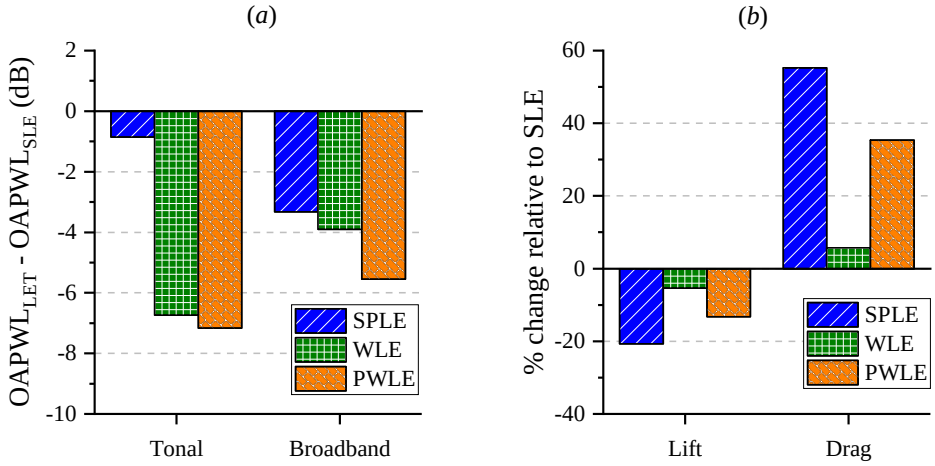

Figure 4.28: Comparisons of (*a*) source power level and (*b*) time-averaged lift and drag coefficients between the 5406-PWLE and those with different LE treatments. The values are relative to the 5406-SLE.

been verified that the mean drag coefficient of the rod is ≈ 1 in all cases, which is almost identical to that of an isolated rod [41, 67] in the subcritical Reynolds number regime. For the 0012 airfoils, only the drag information are relevant, which are shown in plot (*a*). The PLE treatment cause a drag penalty of almost 30 %, with that of the blocked variant (BLE) being slightly lower at 26 %. On the other hand, the LE serrations (WLE) only incur a drag penalty of below 5 %. Similar conclusion can be made for the 5406 series in plot (*b*), where the PLE and SPLE increase drag by an average of 55 % while the drag penalties for WLE and WPLE configurations remain below 8 %. In terms of lift generation, the PLE and SPLE also exhibit worse performance compared to either WLE or WPLE treatments. From this figure, it is possible to conclude that the application of porous treatments at the LE can be quite detrimental unless they are properly optimised. One apparent issue with the porous treatments is related to the pressure balancing process near the LE as this is where large aerodynamic loading is usually produced.

Table 4.4: The comparison between the lift fluctuations reduction and noise mitigation for 5406-SPLE, WLE, and PWLE relative to the SLE; LET: leading edge treatment.

	$20\log(\frac{C_{l,\mathrm{RMS,LET}}}{C_{l,\mathrm{RMS,SLE}}})$ (dB)	$\Delta\mathrm{OSPL}_{\mathrm{LET,SLE}}$ (dB)
5406-SPLE	−2.06	−2.42
5406-WLE	−3.69	−7.78
5406-PWLE	−3.50	−8.30

4.2.6. POSSIBLE IMPROVEMENTS ON THE CURRENT POROUS LE CONCEPTS

In the previous subsections, it has been demonstrated that the porous LE is capable of decreasing the intensity of unsteady pressure fluctuations at its surface. However, the LE serrations have the additional advantage of being able to lower the coherence of the noise sources along the airfoil span. Due to this characteristic, LE serrations are more effective at mitigating tonal noise component than the porous LE. In terms of aerodynamics, porous treatments are generally at a disadvantage due to the pressure balancing process between the pressure and suction sides of the airfoil, which leads to a larger aerodynamic penalty compared to that of LE serrations. A combination of LE serrations and porous LE has been considered previously in the form of 5406-WPLE, which porous material has been added at the recessed segments of the existing serrations, but this implementation has also been found to be detrimental to both acoustic and aerodynamic aspects.

In this subsection, a different combination of porous-serration treatment is proposed such that the LE is modified to include a serration-like planform, but it is made entirely of porous material. The serration planform is necessary to promote the spanwise-interference effect, which is beneficial for addressing the large, coherent spanwise vortices that are responsible for the tonal noise component. Concurrently, the porous medium would impose less blockage onto the impinging turbulence, while also being useful to dissipate the smaller eddies [29, 46], potentially resulting in larger broadband noise reduction. Such treatment is hereby referred to as the poro-serrated LE, or PWLE for short. A comparison between the geometries of 5406-SPLE, WLE, and PWLE airfoils is provided in figure 4.27.

The acoustic and aerodynamic characteristics of the PWLE configuration are compared with the other two in figure 4.28. In plot (*a*), the PWLE is shown to produce similar tonal noise reduction as the WLE, but the broadband noise reduction is almost 2 dB higher. However, the PWLE is still noticeably worse compared to the regular serrations in term of aerodynamic performance, but it is still significantly better compared to that of the SPLE configuration. In table 4.4, the PWLE is shown to produce similar amount of $C_{l,\mathrm{RMS}}$ reduction as the WLE one, but since the former generates larger noise reduction, it is possible to infer that the spanwise-interference effect has also been enhanced by the porous material.

4.3. SUMMARY

This chapter discusses about the applications of LE serrations and metal-foam-based porous LE concepts on a rod-airfoil configuration. Due to the spectral characteristics of the turbulent fluctuations in the rod wake, the rod-airfoil configuration generates sound

that contains both broadband and narrowband components, similar to those observed from the fan stage of a turbofan. Aside from the classical NACA 0012 airfoil, the present study also considers a thin and cambered NACA 5406 profile that possesses typical features of a turbomachinery blade. The simulation setup replicates the experiments of Jacob *et al.* [40], in which a full-span model, side plates, and wind tunnel contraction are taken into account. Furthermore, the LE treatments modify the first 15 % of the airfoil chord.

The present study focuses on examining two possible LE noise mitigation mechanism: 1) the suppression of noise source intensity by reducing the fluctuating forces induced by the impinging turbulence (source-reduction effect), and 2) the destructive interference between noise sources that are distributed along the airfoil span (spanwise-interference effect). The results show that the LE serrations realise both mechanisms, whereas the porous LE generally promotes only the first one. Nevertheless, it is found that the spanwise-interference effect is highly effective for mitigating the tonal noise component, which is why the LE serrations are able to produce large noise reduction at the vortex shedding frequency, unlike the various porous LE concepts. Conversely, the porous LE appears to be effective only at mitigating the broadband noise component at higher frequencies.

Increasing the permeable extent of the porous LE can lead to a better noise reduction level, but these would also cause a worse aerodynamic penalty. In general, airfoils with porous treatments produce higher drag than those with LE serrations. The aerodynamics on a porous LE is exacerbated further when the airfoil is at lifting conditions (i.e., in the case of NACA 5406) due to the cross-flow from the pressure side towards the suction side. By combining the serration planform with porous material, it is found out that a larger broadband noise reduction level could be achieved at high frequencies with a similar low-frequency narrowband noise attenuation as the solid serrations. Regardless, the aerodynamic penalty of the new LE concept remains substantial although it is smaller compared to that of the regular porous LE.

Although this investigation suggests that the LE serrations are preferable over the porous LE, there are several aspects of the present study that deserve further attention. Firstly, the LE serrations perform very well in the rod-airfoil setup since the rod wake impingement takes place uniformly along the airfoil span, enhancing the efficacy of the spanwise-interference effect. Such ideal condition does not always represent the flow field in an actual turbofan fan stage, where the turbulence intensity, length scales, and convection velocity in the fan wake could vary significantly along the radial direction. Consequently, the performance of LE serrations could be impeded when applied in such environment [68]. Since serrations also increase the overall axial length of a blade, their applications in future ultra-high-bypass turbofans might be subject to dimension constraints due to the shorter axial distance between the fan and the outlet-guide vanes. An optimised permeable LE treatment might be more suitable for such applications, although further investigations are still necessary.

REFERENCES

[1] C. Teruna, F. Avallone, D. Casalino, and D. Ragni, *Numerical investigation of leading edge noise reduction on a rod-airfoil configuration using porous materials and*

serrations, Journal of Sound and Vibration **494**, 115880 (2021).

[2] S. Moreau and M. Roger, *Effect of angle of attack and airfoil shape on turbulence-interaction noise,* in *11th AIAA/CEAS aeroacoustics conference* (2005) p. 2973.

[3] P. Migliore and S. Oerlemans, *Wind tunnel aeroacoustic tests of six airfoils for use on small wind turbines,* J. Sol. Energy Eng. **126**, 974 (2004).

[4] D. Casalino, F. Avallone, I. Gonzalez-Martino, and D. Ragni, *Aeroacoustic study of a wavy stator leading edge in a realistic fan/ogv stage,* Journal of Sound and Vibration **442**, 138 (2019).

[5] N. Curle, *The influence of solid boundaries upon aerodynamic sound,* Proceedings of the Royal Society of London. Series A. Mathematical and Physical Sciences **231**, 505 (1955).

[6] R. K. Amiet, *Noise due to turbulent flow past a trailing edge,* Journal of sound and vibration **47**, 387 (1976).

[7] W. R. Sears, *Some aspects of non-stationary airfoil theory and its practical application,* Journal of the Aeronautical Sciences **8**, 104 (1941).

[8] R. W. Paterson and R. K. Amiet, *Noise and surface pressure response of an airfoil to incident turbulence,* Journal of Aircraft **14**, 729 (1977).

[9] J. Marshall and J. Grant, *Penetration of a blade into a vortex core: vorticity response and unsteady blade forces,* Journal of Fluid Mechanics **306**, 83 (1996).

[10] S. E. Widnall and T. L. Wolf, *Effect of tip vortex structure on helicopter noise due to blade-vortex interaction,* Journal of Aircraft **17**, 705 (1980).

[11] A. Betz, *Behavior of vortex systems,* NACA Technical Memorandum (1933).

[12] E. R. Booth Jr, *Experimental observations of two-dimensional blade-vortex interaction,* AIAA journal **28**, 1353 (1990).

[13] M. Lowson, *Focusing of helicopter bvi noise,* Journal of sound and vibration **190**, 477 (1996).

[14] W. J. Devenport, J. K. Staubs, and S. A. Glegg, *Sound radiation from real airfoils in turbulence,* Journal of Sound and Vibration **329**, 3470 (2010).

[15] J. R. Gill, X. Zhang, and P. Joseph, *Effects of real airfoil geometry on leading edge gust interaction noise,* in *19th AIAA/CEAS Aeroacoustics Conference* (2013) p. 2203.

[16] S. Kaji and T. Okazaki, *Generation of sound by rotor-stator interaction,* Journal of Sound and Vibration **13**, 281 (1970).

[17] J. C. Hardin and S. L. Lamkin, *Concepts for reduction of blade/vortex interaction noise,* Journal of Aircraft **24**, 120 (1987).

[18] T. F. Brooks and E. R. Booth, *The effects of higher harmonic control on blade-vortex interaction noise and vibration,* Journal of the American Helicopter Society **38**, 45 (1993).

[19] K. Nguyen, M. Betzina, and C. Kitaplioglu, *Full-scale demonstration of higher harmonic control for noise and vibration reduction on the xv-15 rotor,* Journal of the American Helicopter Society **46**, 182 (2001).

[20] C. Weiland and P. P. Vlachos, *A mechanism for mitigation of blade–vortex interaction using leading edge blowing flow control,* Experiments in fluids **47**, 411 (2009).

[21] J. M. Tyler and T. G. Sofrin, *Axial flow compressor noise studies*, Tech. Rep. (SAE Technical Paper, 1962).

[22] J. B. Schulten, *Vane sweep effects on rotor/stator interaction noise,* AIAA journal **35**, 945 (1997).

[23] R. K. Amiet, *Acoustic radiation from an airfoil in a turbulent stream,* Journal of Sound and vibration **41**, 407 (1975).

[24] R. Woodward, C. Hughes, R. Jeracki, and C. Miller, *Fan noise source diagnostic test–far-field acoustic results,* in *8th AIAA/CEAS Aeroacoustics Conference & Exhibit* (2002) p. 2427.

[25] F. E. Fish and J. M. Battle, *Hydrodynamic design of the humpback whale flipper,* Journal of morphology **225**, 51 (1995).

[26] H. Johari, C. Henoch, D. Custodio, and A. Levshin, *Effects of leading-edge protuberances on airfoil performance,* AIAA journal **45**, 2634 (2007).

[27] R. Graham, *The silent flight of owls,* The Aeronautical Journal **38**, 837 (1934).

[28] A. S. Hersh, P. T. Soderman, and R. E. Hayden, *Investigation of acoustic effects of leading-edge serrations on airfoils,* Journal of Aircraft **11**, 197 (1974).

[29] M. Roger, C. Schram, and L. De Santana, *Reduction of airfoil turbulence-impingement noise by means of leading-edge serrations and/or porous material,* in *19th AIAA/CEAS aeroacoustics conference* (2013) p. 2108.

[30] S. Narayanan, P. Chaitanya, S. Haeri, P. Joseph, J. Kim, and C. Polacsek, *Airfoil noise reductions through leading edge serrations,* Physics of Fluids **27**, 025109 (2015).

[31] G. Bampanis, M. Roger, D. Ragni, F. Avallone, and C. Teruna, *Airfoil-turbulence interaction noise source identification and its reduction by means of leading edge serrations,* in *25th AIAA/CEAS Aeroacoustics Conference* (2019) p. 2741.

[32] J. W. Kim, S. Haeri, and P. F. Joseph, *On the reduction of aerofoil–turbulence interaction noise associated with wavy leading edges,* Journal of Fluid Mechanics **792**, 526 (2016).

[33] F. Gea Aguilera, J. R. Gill, D. Angland, and X. Zhang, *Wavy leading edge airfoils interacting with anisotropic turbulence,* in *23rd AIAA/CEAS Aeroacoustics Conference* (2017) p. 3370.

[34] P. Chaitanya, P. Joseph, S. Narayanan, C. Vanderwel, J. Turner, J.-W. Kim, and B. Ganapathisubramani, *Performance and mechanism of sinusoidal leading edge serrations for the reduction of turbulence–aerofoil interaction noise,* Journal of Fluid Mechanics **818**, 435 (2017).

[35] J. M. Turner and J. W. Kim, *Aeroacoustic source mechanisms of a wavy leading edge undergoing vortical disturbances,* Journal of Fluid Mechanics **811**, 582 (2017).

[36] S. Lee, *Reduction of blade-vortex interaction noise through porous leading edge,* AIAA journal **32**, 480 (1994).

[37] E. Sarradj and T. Geyer, *Noise generation by porous airfoils,* in *13th AIAA/CEAS Aeroacoustics Conference (28th AIAA Aeroacoustics Conference)* (2007) p. 3719.

[38] T. F. Geyer, A. Lucius, M. Schrödter, M. Schneider, and E. Sarradj, *Reduction of turbulence interaction noise through airfoils with perforated leading edges,* Acta Acustica united with Acustica **105**, 109 (2019).

[39] P. Chaitanya, P. Joseph, T. P. Chong, M. Priddin, and L. Ayton, *On the noise reduction mechanisms of porous aerofoil leading edges,* Journal of Sound and Vibration **485**, 115574 (2020).

[40] M. C. Jacob, J. Boudet, D. Casalino, and M. Michard, *A rod-airfoil experiment as a benchmark for broadband noise modeling,* Theoretical and Computational Fluid Dynamics **19**, 171 (2005).

[41] J. H. Lienhard *et al., Synopsis of lift, drag, and vortex frequency data for rigid circular cylinders*, Vol. 300 (Technical Extension Service, Washington State University, 1966).

[42] D. Casalino, A. Hazir, and A. Mann, *Turbofan broadband noise prediction using the lattice boltzmann method,* AIAA Journal **56**, 609 (2018).

[43] J.-C. Giret, A. Sengissen, S. Moreau, M. Sanjosé, and J.-C. Jouhaud, *Prediction of the sound generated by a rod-airfoil configuration using a compressible unstructured les solver and a fw-h analogy,* in *18th AIAA/CEAS Aeroacoustics Conference (33rd AIAA Aeroacoustics Conference)* (2012) p. 2058.

[44] W. Chen, W. Qiao, F. Tong, L. Wang, and X. Wang, *Numerical investigation of wavy leading edges on rod–airfoil interaction noise,* AIAA Journal **56**, 2553 (2018).

[45] B. R. Agrawal and A. Sharma, *Numerical analysis of aerodynamic noise mitigation via leading edge serrations for a rod–airfoil configuration,* International Journal of Aeroacoustics **15**, 734 (2016).

[46] R. Zamponi, S. Satcunanathan, S. Moreau, D. Ragni, M. Meinke, W. Schröder, and C. Schram, *On the role of turbulence distortion on leading-edge noise reduction by means of porosity,* Journal of Sound and Vibration **485**, 115561 (2020).

[47] C. Kato, A. Iida, Y. Takano, H. Fujita, and M. Ikegawa, *Numerical prediction of aerodynamic noise radiated from low mach number turbulent wake,* in *31st Aerospace Sciences Meeting* (1993) p. 145.

[48] J. H. Seo and Y. J. Moon, *Aerodynamic noise prediction for long-span bodies,* Journal of Sound and Vibration **306**, 564 (2007).

[49] J. Gill, X. Zhang, and P. Joseph, *Symmetric airfoil geometry effects on leading edge noise,* The Journal of the Acoustical Society of America **134**, 2669 (2013).

[50] P. Chaitanya, P. Joseph, S. Narayanan, and J. Kim, *Aerofoil broadband noise reductions through double-wavelength leading-edge serrations: a new control concept,* Journal of Fluid Mechanics **855**, 131 (2018).

[51] D. M. Freed, *Lattice-boltzmann method for macroscopic porous media modeling,* International Journal of Modern Physics C **9**, 1491 (1998).

[52] C. Sun, F. Pérot, R. Zhang, P.-T. Lew, A. Mann, V. Gupta, D. M. Freed, I. Staroselsky, and H. Chen, *Lattice boltzmann formulation for flows with acoustic porous media,* Comptes Rendus Mécanique **343**, 533 (2015).

[53] P. Welch, *The use of fast fourier transform for the estimation of power spectra: a method based on time averaging over short, modified periodograms,* IEEE Transactions on audio and electroacoustics **15**, 70 (1967).

[54] R. Satti, P.-T. Lew, Y. Li, R. Shock, and S. Noelting, *Unsteady flow computations and noise predictions on rod-airfoil using lattice boltzmann method,* in *47th AIAA Aerospace Sciences Meeting including The New Horizons Forum and Aerospace Exposition* (2009) p. 497.

[55] Y. Jiang, M.-L. Mao, X.-G. Deng, and H.-Y. Liu, *Numerical investigation on body-wake flow interaction over rod–airfoil configuration,* Journal of Fluid Mechanics **779**, 1 (2015).

[56] J.-C. Giret, A. Sengissen, S. Moreau, M. Sanjosé, and J.-C. Jouhaud, *Noise source analysis of a rod–airfoil configuration using unstructured large-eddy simulation,* AIAA Journal **53**, 1062 (2015).

[57] A. Eltaweel and M. Wang, *Numerical simulation of broadband noise from airfoil-wake interaction,* in *17th AIAA/CEAS Aeroacoustics Conference (32nd AIAA Aeroacoustics Conference)* (2011) p. 2802.

[58] B. Greschner, F. Thiele, M. C. Jacob, and D. Casalino, *Prediction of sound generated by a rod–airfoil configuration using easm des and the generalised lighthill/fw-h analogy,* Computers & fluids **37**, 402 (2008).

[59] C. Apelt, G. West, and A. A. Szewczyk, *The effects of wake splitter plates on the flow past a circular cylinder in the range* $10^4 < \mathrm{Re} < 5 \times 10^4$, Journal of Fluid Mechanics **61**, 187 (1973).

[60] S. Szepessy and P. Bearman, *Aspect ratio and end plate effects on vortex shedding from a circular cylinder,* Journal of Fluid Mechanics **234**, 191 (1992).

[61] S. B. Pope, *Turbulent flows* (IOP Publishing, 2001).

[62] P. J. Roache, *Verification and validation in computational science and engineering,* Vol. 895 (Hermosa Albuquerque, NM, 1998).

[63] J. R. Underbrink, *Circularly symmetric, zero redundancy, planar array having broad frequency range applications,* (2001), uS Patent 6,205,224.

[64] M. Roger and A. Carazo, *Blade-geometry considerations in analytical gust-airfoil interaction noise models,* in *16th AIAA/CEAS Aeroacoustics Conference* (2010) p. 3799.

[65] D. M. Chase, *Noise radiated from an edge in turbulent flow,* AIAA journal **13**, 1041 (1975).

[66] P. R. Spalart, *On the precise implications of acoustic analogies for aerodynamic noise at low mach numbers,* Journal of Sound and Vibration **332**, 2808 (2013).

[67] E. Achenbach, *Distribution of local pressure and skin friction around a circular cylinder in cross-flow up to* $\mathrm{Re} = 5 \times 10^6$, Journal of Fluid Mechanics **34**, 625 (1968).

[68] F. Avallone, D. Casalino, and D. Ragni, *Impingement of a propeller-slipstream on a leading edge with a flow-permeable insert: A computational aeroacoustic study,* International Journal of Aeroacoustics **17**, 687 (2018).

5

PROOF-OF-CONCEPTS

To some people, there is no noise on earth as exciting as the sound of three or four big fan-jet engines rising in pitch, as the plane they are sitting in swivels at the end of the runway and, straining against its brakes, prepares for takeoff.

David Lodge

This chapter presents two numerical investigations on the application of permeable leading-edge treatments in test setups with higher complexity than those in the previous chapters. Firstly, a rod-linear cascade (RLC) model is investigated as an extension to the rod-airfoil configuration (RAC) in a high-solidity environment, similar to that in an actual turbomachinery. In the RLC, the rod is positioned upstream of a 7-blade cascade such that the rod wake impinges the central blade. A resonant mode has been identified close to the vortex-shedding frequency, which enhances the tonal noise emission of the RLC. The central blade is subsequently modified using a metal-foam based permeable leading edge, although this only achieves broadband noise reduction in the high-frequency range. A poro-serrated blade concept is also tested in a full-scale airframe and fan stage models to mitigate rotor-stator interaction noise. Compared to the RLC, turbulent wake impingement takes place simultaneously at multiple blades, and the resulting sound waves are forced to propagate through an annulus. The porous treatment induces flow separation at the suction side of the stator blades. Consequently, the thrust generated by the modified fan stage becomes smaller and broadband noise emission at low frequencies is enhanced. The flow separation is also responsible for enhancing broadband noise emission through a stall-noise mechanism at the blade trailing edge. Nevertheless, the porous treatment substantially mitigates the tonal noise component at the blade-passage frequency and its harmonics.

Parts of this chapter have been published in Teruna *et al.* [1, 2].

5.1. ROD-LINEAR CASCADE CONFIGURATION

In chapter 4, the usage of permeable treatments for aerodynamic noise mitigation has been demonstrated using the rod-airfoil configuration (RAC). The RAC has been recognised as a suitable setup for emulating the turbulence-impingement noise (TIN) generated by a rotor-stator interaction mechanism (e.g., in a turbofan fan stage) [3], but it also lacks some important aspects due to its simplified setup. Stator vanes in a fan stage are generally designed with a large camber and a relatively small thickness, and both features have been known to enhance TIN level as previously discussed in subsection 4.2.3. These features were taken into account in chapter 4, where the classical NACA 0012 profile has been replaced with a NACA 5406. Nevertheless, the stators in a fan stage are arranged in a cascade with high solidity (i.e., c/s where s is the inter-blade separation) that enables each blade to achieve a large flow deflection without causing flow separation [4]. In turn, sound propagation will be affected by the presence of multiple blades in close proximity [5, 6], and the resulting phenomena are collectively referred to as the cascade effects.

The relevance of the cascade effect has been demonstrated by Finez *et al.* [7] who studied the trailing-edge (TE) noise of a linear cascade setup. It is worth mentioning that a linear cascade is a two-dimensional representation of an annular cascade at a given radial position. The authors attempted to predict the TE noise using two approaches: (1) by adapting Amiet's [8] model for an isolated airfoil and (2) by using Glegg's model [5] that is intended for a blade row. Unsurprisingly, the latter was found to produce better agreement against the experimental measurements. The authors concluded that the cascade effect is more prominent at low frequencies where the acoustic wavelength is larger than the inter-blade separation. More recently, de Laborderie *et al.* [9] looked into the influence of airfoil camber on the tonal noise generation generated in a rotor-stator setup. In this study, the authors employed the analytical model of Posson *et al.* [10] for a cascade of flat-plates and extended it to include the camber effects using the two-stagger-angle approach. The inclusion of camber effect into the analytical model results in a better noise prediction when compared to the results of a high-fidelity CAA simulation [11].

Following the literature, replacing the isolated airfoil of the RAC with a linear cascade (blade row) would realise a setup that better represents the environment in a turbomachinery. This new setup is referred to as the rod-linear cascade (RLC) configuration, and it is compared to other models with various level of complexity in figure 5.1. The RLC occupies a spot in between the RAC and the more complex rotor-stator cascade configuration. The table at the lower part of the figure compares the aerodynamic and acoustic features of each configuration. Compared to the RAC, the RLC takes into account the influence of a high-solidity blade row on its aerodynamic and acoustic characteristics. However, since the RLC still uses a single rod, only one of the blade will be subjected to rod-wake impingement in the present configuration. It is possible to tilt the rod to achieve wake interaction at multiple blades, but this configuration is not considered in the present study. The design of a RLC setup will be discussed in the upcoming subsection, and afterward, its aerodynamic and acoustic characteristics will be examined numerically.

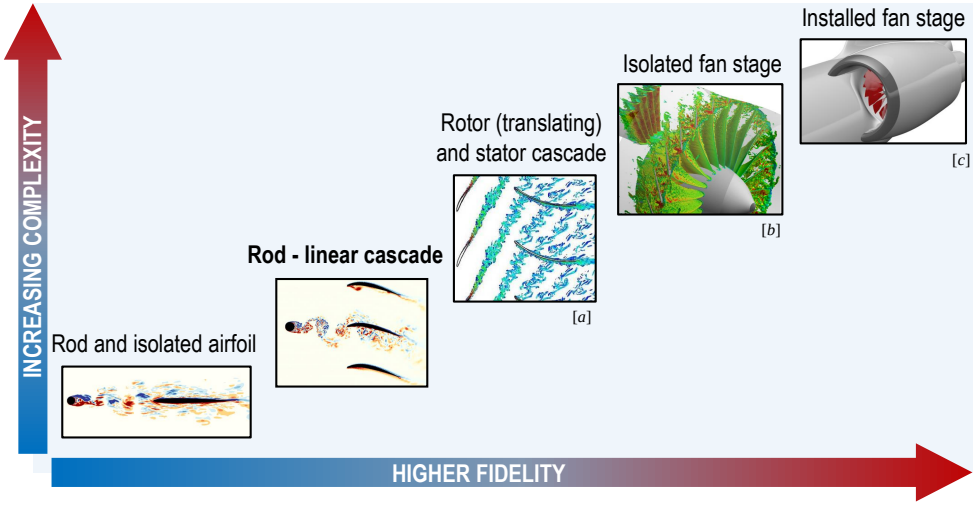

Features				
Tonal and broadband noise emission	✓	✓	✓	✓
Cascade aerodynamics and acoustic effects	✗	✓	✓	✓
Wake interaction on multiple blades	✗	✗	✓	✓
Annular flow and duct effects	✗	✗	✗	✓

Figure 5.1: A general comparison between computational cost and the level of realism (top) and the features (bottom) between different setups for studying rotor-stator interaction noise in a fan stage. The following images were obtained from external sources: [*a*][12], [*b*][13], and [*c*][14].

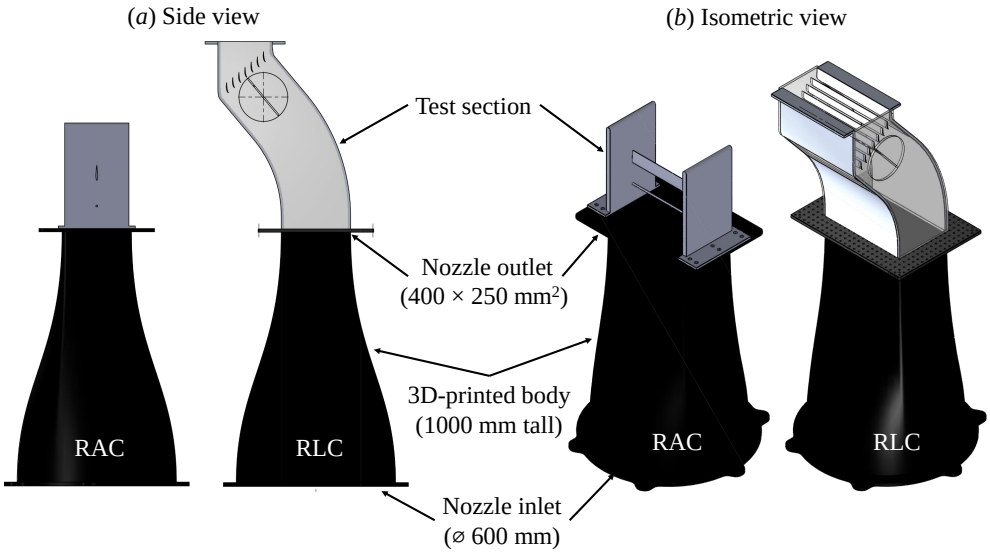

Figure 5.2: A comparison between a rod-airfoil configuration (RAC) setup and the rod-linear cascade (RLC) one when mounted in the vertical wind tunnel of TU Delft.

5.1.1. SIMULATION SETUP

The RAC experiment of Jacob *et al.* [3] was carried out using an open jet test section. When adapted to the vertical wind tunnel facility of TU Delft, the RAC configuration would appear as in figure 5.2. Differently, the RLC is mounted inside a closed test section as shown in figure 5.2 such that the flow surrounding the linear cascade remains bounded by a physical wall. This design is chosen to approximate the periodicity of the flow field in the cascade blade passage. Nevertheless, the integration of the linear cascade setup into the wind tunnel facility could become more complicated than that of the RAC. This is partly due to the fact that the anechoic chamber where the RLC is mounted has a relatively narrow opening on the ceiling where the flow from the test section can be extracted. Hence, the flow exiting the cascade should be aligned against this opening after taking into account the flow deflection induced by the linear cascade itself.

Figure 5.3 illustrates several earlier concepts of the RLC setup, which are referred after the location where flow alignment takes place, e.g., upstream (BEFORE) or downstream (AFTER) of the linear cascade. In the latter, the flow coming out from the contraction immediately encounters the blade row, and it is realigned at the test section outlet using curved walls. As shown in the lower half of figure 5.3, the flow acceleration/deceleration at the upper/lower curved wall significantly affects the uniformity of the flow field in the inter-blade channels. This could be alleviated by placing the curved segment of the wall further away from the cascade, but this results in a longer test section. Differently, the BEFORE configuration introduces the flow turning upstream of the linear cascade, and subsequently, the blade row redirects the flow towards the collector. This configuration has a closer resemblance to an actual fan stage, where the stators recover the swirl in the fan wake. Thus, the BEFORE configuration has been chosen as the flow field in the inter-

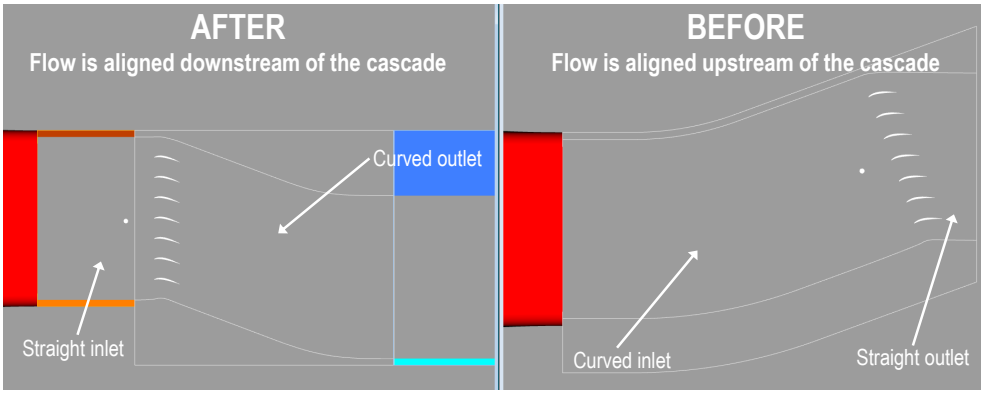

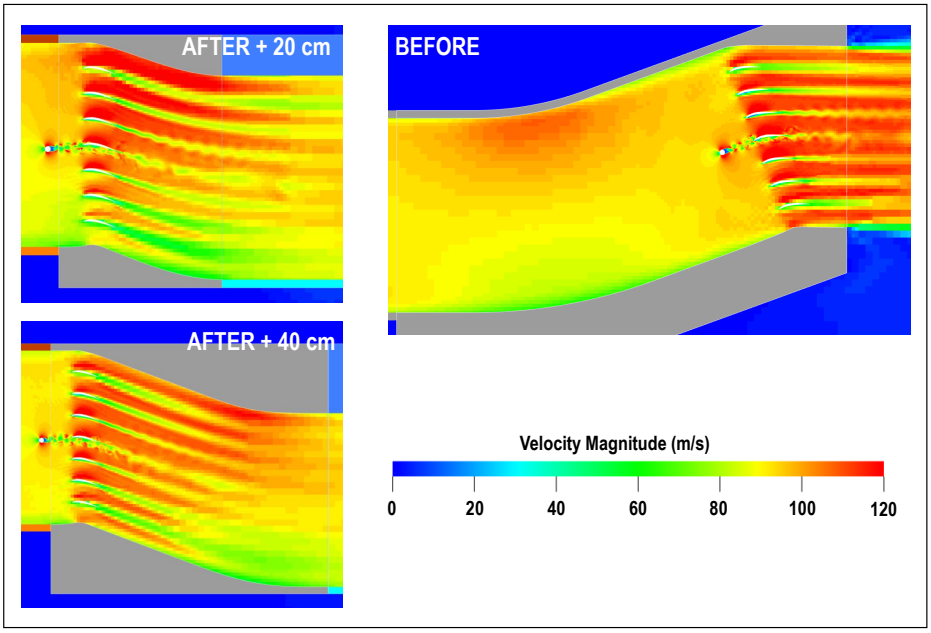

Figure 5.3: A comparison of the model arrangement and flow field inside the test section between a setup with flow turning downstream (AFTER) and upstream (BEFORE) of the cascade. The velocity magnitude contours have been obtained using PowerFLOW simulations with a coarse grid resolution level.

blade channels appears to be less sensitive against the curved wall near the test section inlet.

The selected RLC configuration is sketched in figure 5.4 (*a*), consisting of a test section that is mounted downstream of a 1 m-long nozzle. The nozzle has a circular inlet with a diameter of 0.6 m and a rectangular outlet that is 0.4 m wide and 0.25 m high. The test section has a similar cross section as the nozzle outlet such that its walls are flushed on all sides against the nozzle. The curved segment of the test section has a radius of curvature of 650 mm, and it is located in between 50 mm downstream of the nozzle outlet and 180 mm upstream of the rod center. It has been verified that the curved test section wall does not cause a flow separation. The rod is located upstream of the cascade with the rod base being separated by 41 mm from the leading-edges of the OGV blades. The rod diameter has been scaled to $D = 5.2\,\text{mm}$ to achieve a vortex-shedding frequency that matches the first blade-passage-frequency (BPF_1) of the SDT ($\approx 2.87\,\text{kHz}$ [15]) at the freestream velocity $U_\infty = 75\,\text{m/s}$. This corresponds to the Reynolds number based on the rod diameter $\text{Re}_D = 26,600$, which falls into the regime where the turbulent transition takes place in the rod wake.

The blade profile of the linear cascade has been extracted from the OGV of the NASA Glenn - Source Diagnostics Test (SDT) rig [15], at the 90 % of the outer radius. This location has been selected as the fan wake-OGV interaction is expected to be relatively intense due to the large local tangential velocity, while the aerodynamic interference from the blade tip remains negligible [16]. The OGV profile is scaled at 1:1 in comparison to that of the SDT, and it is extruded into an straight blade with a span $b = 400\,\text{mm}$. The solidity (i.e., the ratio between the blade chord and the blade-to-blade separation) of the linear cascade is also based on that of the SDT, which is 1.22. This corresponds to a blade-to-blade separation of 32.5 mm and thus, the test section accommodates 7 blades in total. In order to achieve the same blade outlet angle as in the SDT, while ensuring that the blade leading-edges have identical streamwise separation from the upstream rod, a stagger angle of 29° has been chosen instead of the 11° in the SDT. Nevertheless, it will be shown that the surface pressure distributions on the OGV blades in the RLC and in the SDT are still comparable. To ensure that a turbulent boundary layer develops on the blades that are not immersed in the rod wake, zig-zag tripping devices have been installed on both the pressure and suction sides of the blades at 10 % of the chord.

The detailed schematic of the RLC is shown in figure 5.4 (*b*). This study uses two coordinate systems, the local one (x - y) that is aligned with the test section walls adjacent to the RLC and a global one (x' - y') that is aligned with the test section outlet. Relative to the global coordinate system, the local one is rotated in the counterclockwise direction by $\gamma = 40°$, which equals to the flow deflection angle of the linear cascade. The spanwise direction is defined by the z axis that applies identically for both coordinate systems. Note that the simulation results will be presented using the local coordinate system unless specified otherwise. Figure 5.4 (*b*) also provides the nomenclature system to identify the position of each blade in the cascade. The blade that is directly downstream of the rod is referred to as the central blade with its leading edge located at $y/D = 0$. The other blades are indicated with a letter (T - top, B - bottom) that corresponds to the their position relative to the central blade, and a number (1, 2, and 3) in ascending order for blades further away from the central blade.

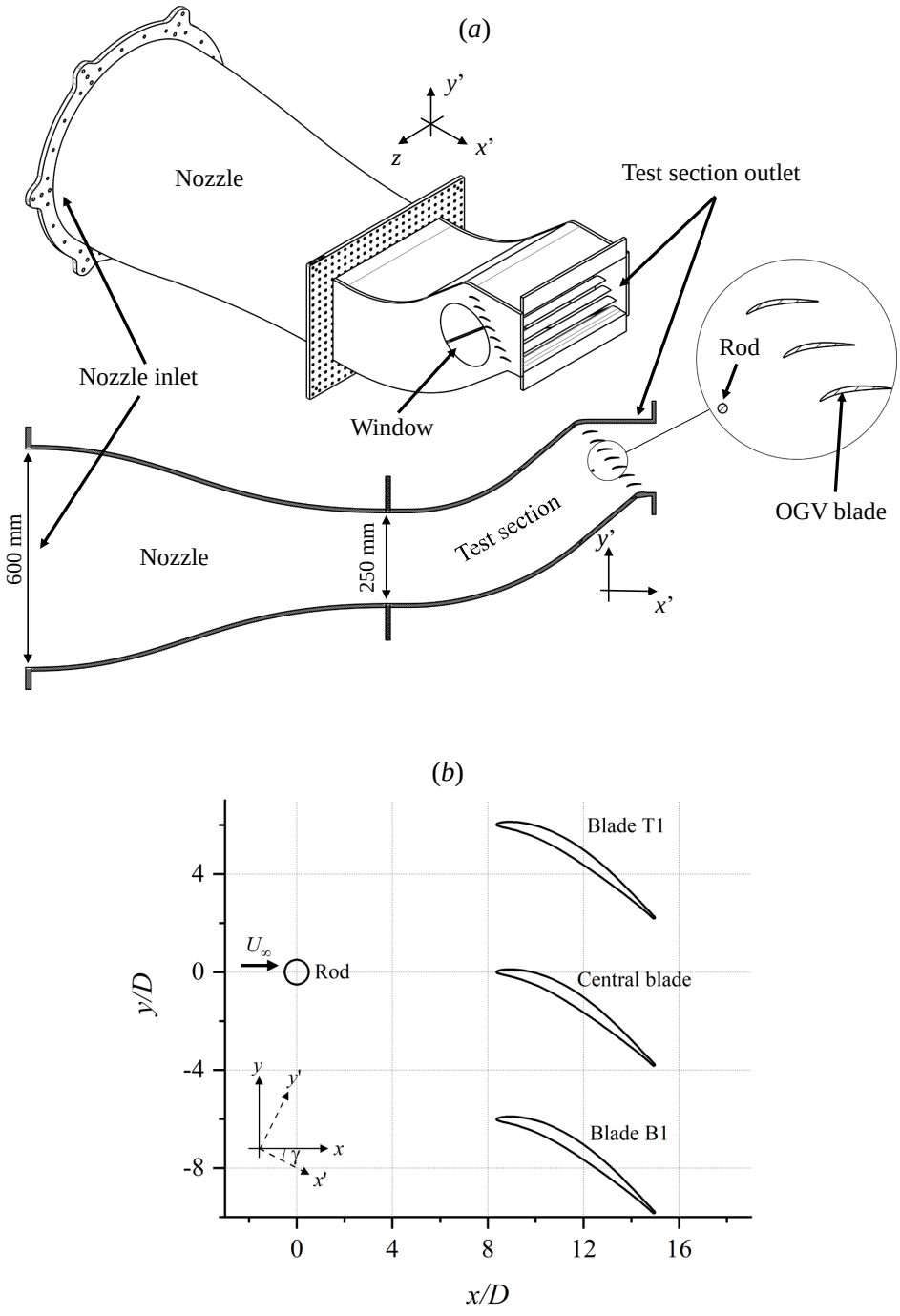

Figure 5.4: (*a*) A sketch of the RLC test rig revealing the rod and the OGV blade-row arrangement. (*b*) Closer detail of the rod-linear cascade components, showing 3 out of the 7 OGV blades.

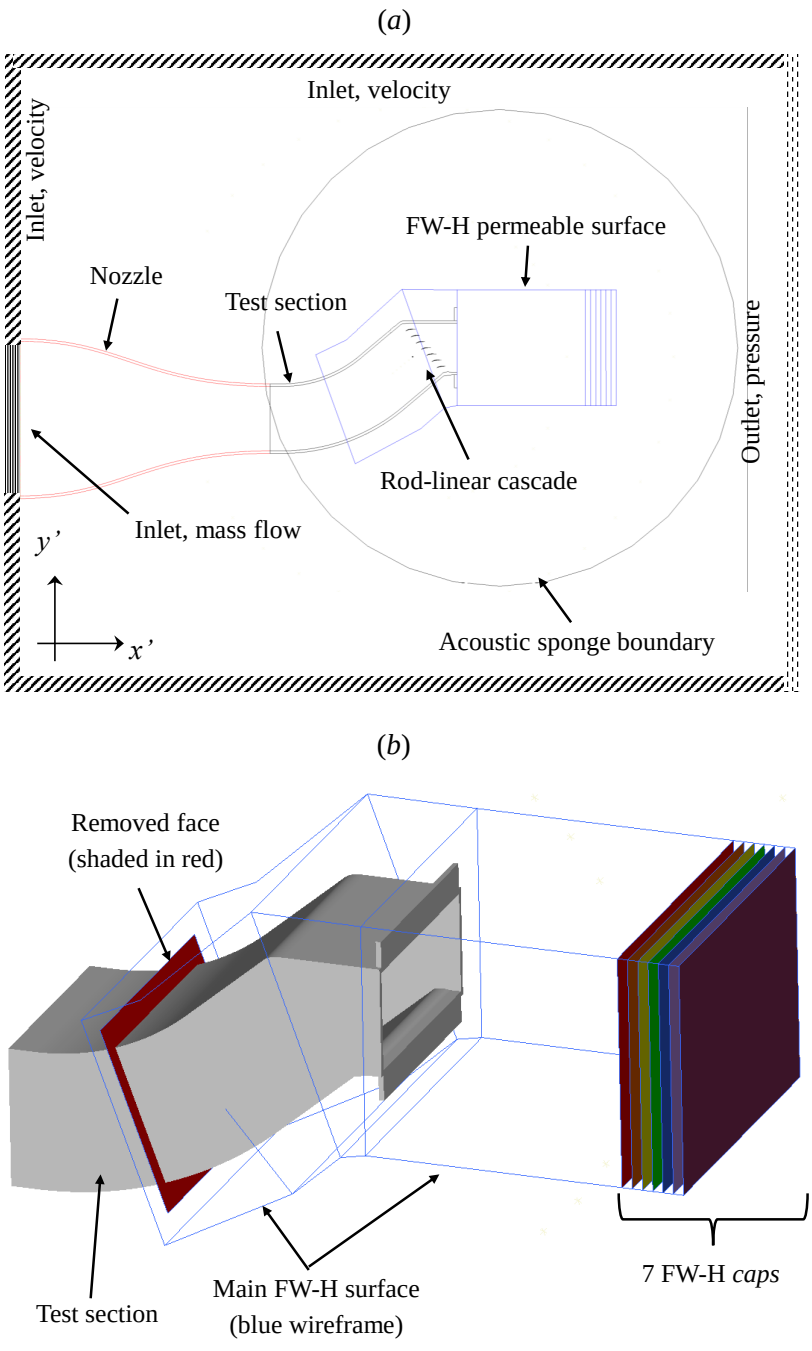

Figure 5.5: (*a*) A (not-to-scale) lateral view of of the simulation domain. (*b*) A closer view the FW-H permeable surface setup, revealing the 7 *caps*. The nozzle is hidden in this view and the edges of the main FW-H surface are drawn as a wireframe.

Figure 5.5 (*a*) shows a lateral cutaway of the simulation domain. The domain boundaries form a box that is 3.85 m long in the x' direction (i.e., more than twice the combined length of the test section and the nozzle), and 2.6 m in both y' and z directions. In the figure, the nozzle inlet is shown to coincide with the upstream boundary of the domain. A mass-flow inlet of 9.8 kg/s is set at the nozzle inlet such that an average velocity of $U_\infty = 75$ m/s is achieved at the contraction exit (i.e., test section inlet). The downstream boundary is modelled as an outlet that is specified with ambient pressure $p_\infty = 1$ atm. The other boundaries are specified as inlets with zero velocity. Solid bodies, including the contraction, test section, rod, cascade blades, and zig-zag trips, are no-slip walls. To realise an anechoic far-field region in the simulation domain, an acoustic sponge region is defined starting from a radius of $100D$, with its center located at $60D$ downstream of the central blade.

The simulation domain contains a total of 12 grid refinement regions with the highest grid resolution level applied at regions adjacent to the rod and the blades. At the finest grid resolution setting, the smallest grid size equals to $0.016D$, which corresponds to an average y^+ of the first wall-adjacent cell of 8 on the rod and the leading edges of the central blade, blade T1, and blade B1; the other blades are enveloped inside coarser grid refinement regions. Additional grid refinement regions are applied along the nozzle wall to resolve the boundary layer development upstream of the test section. The grid arrangement in the simulation domain corresponding to the finest grid resolution setting is shown in figure 5.6. The simulation is carried out for 56.7 ms, which is roughly equal to 162 vortex shedding cycles. The simulation length allows for reliable acoustic measurement for frequencies as low as 300 Hz or $St_D = 0.021$. The simulations have been carried out at TU Delft's parallel computing facility running 200-core of Intel-Sandybridge Xeon E5-2660. The computational cost will be reported in the subsequent section where a grid independence study will be discussed.

For far-field noise computation, a permeable surface has been prepared, enclosing the test section exterior as shown in figure 5.5 (*b*). Pressure and velocity fluctuations are sampled on the permeable surface with a rate of 56.5 kHz for 160 vortex shedding cycles (i.e., 56 ms). Nevertheless, several parts of the permeable surface would intersect with regions of the flow field where vortical perturbations are present, leading to pseudo-sound contamination [17]. These regions can be found at the upstream face where the permeable surface intersects with the test section and at the downstream face that stands in the path of the jet coming from the test section outlet. To mitigate the pseudo-sound effect, a portion of the upstream face is removed, but this strategy cannot be applied to the downstream face as its removal would reduce the accuracy of noise computations at shallow angles in the downstream direction [18]. Instead, multiple *caps* are added to the downstream face, which are separated by 20 mm ($3.85D$) between each other. This solution exploits the difference in convection velocity (and consequently, characteristic scales) between the slow-moving turbulence (small scales) and the fast-moving sound waves (large scales/wavelengths), such that the former's contribution is recorded at each cap with larger phase variation compared to the latter's [19, 20]. Once the far-field noise contribution at each cap is summed, the effect of pseudo-sound would be averaged out while the acoustic wave perturbations are preserved.

In this study, noise computations using the FW-H analogy will be carried out using

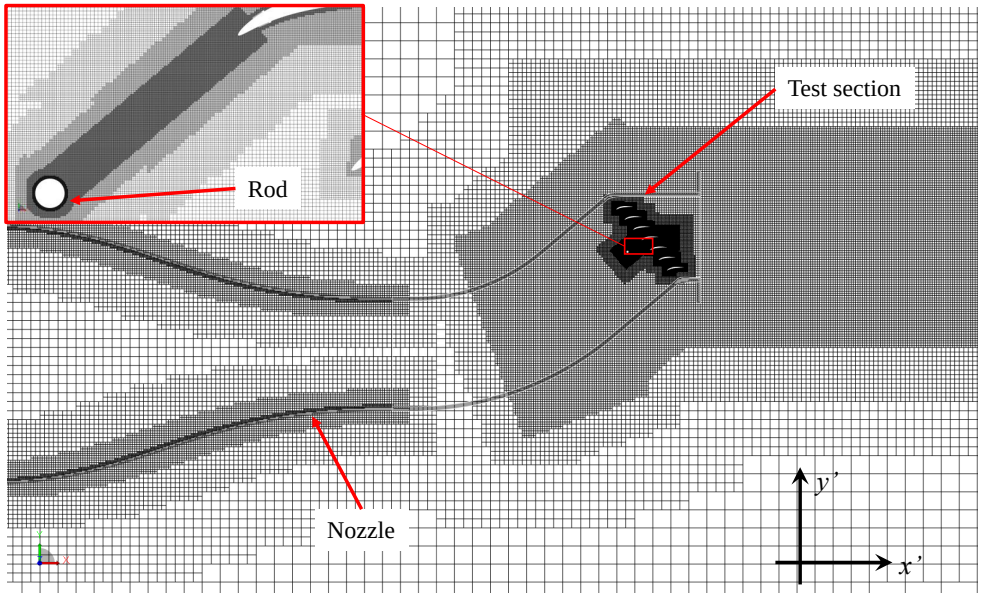

Figure 5.6: A cut plane showing the grid arrangement at the domain midspan for the finest grid resolution setting. The inset shows a close-up view on the region bounded by the red box.

several integration "paths", as shown in figure 5.7. A closed integration surface can be formed by combining the main surface and one of the cap. For caps that are not directly connected to the main surface (e.g., caps 2 to 7), "connector" surfaces will be added to the integration path. These connectors are denoted as SC_{ab} in the figure, where a and b are indices corresponding to the caps that are adjacent to the connector. In the instance of "path 1", the integration surface consists of only the main surface and cap 1, while the contributions of the other surfaces are neglected. In another example, the integration surface following "path 4" also includes multiple connectors (i.e., SC12, SC23, and SC34) in addition to cap 4 and the main surface. Subsequently, acoustic pressure signals are computed for each integration path (i.e., 7 in the present case following the number of caps). They are averaged afterward following equation 5.1, where p refers to the acoustic pressure contribution from a particular surface, and N equals the number of caps. The same approach has also been applied for the rod-airfoil configuration study in chapter 4.

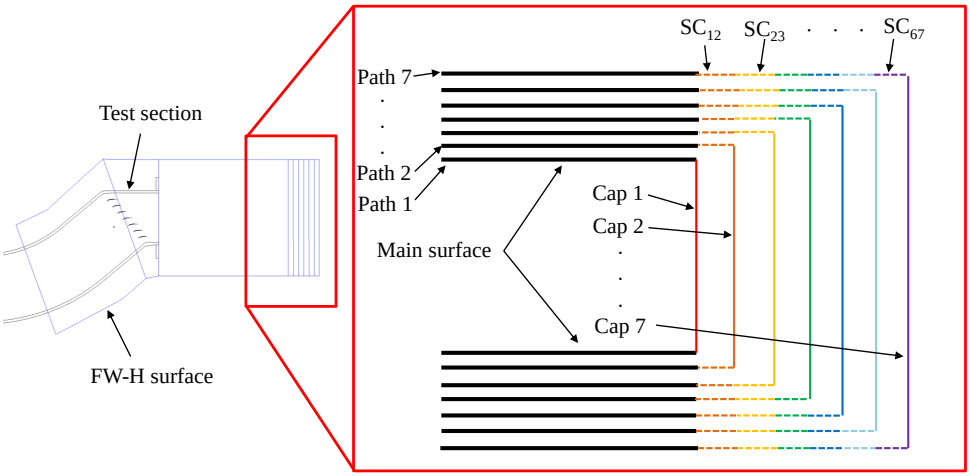

Figure 5.7: The nomenclature of integration paths on the FW-H permeable surface with cap and connector surfaces.

$$
\begin{aligned}
p_{\text{total}} &= \frac{1}{N}\sum_{n=1}^{N} p_{\text{path(n)}} \\
&= \frac{1}{N}\left[\overbrace{p_{\text{main}} + p_{\text{cap1}}}^{p_{\text{path(1)}}} + \overbrace{p_{\text{main}} + p_{\text{SC12}} + p_{\text{cap2}}}^{p_{\text{path(2)}}} + \cdots \right. \\
&\quad \left. \cdots + \overbrace{p_{\text{main}} + p_{\text{SC12}} + \cdots + p_{\text{SC(N-1)N}} + p_{\text{cap1}} + \cdots p_{\text{capN}}}^{p_{\text{path(N)}}}\right] \\
&= p_{\text{main}} + \overbrace{\left[\frac{p_{\text{cap1}} + \cdots + p_{\text{capN}}}{N}\right]}^{\text{Cap contributions}} + \overbrace{\left[\frac{(N-1)\,p_{\text{SC12}} + \cdots + p_{\text{SC(N-1)N}}}{N}\right]}^{\text{Connector contributions}}
\end{aligned}
\tag{5.1}
$$

5.1.2. GRID INDEPENDENCE STUDY AND VERIFICATION

As listed in table 5.1, the grid independence study has been carried out for the RLC setup using three different grid resolutions with refinement ratio of $\sqrt{2}$, namely *coarse*, *medium*, and *fine*. The grid resolution is defined as the number of grid points distributed over the rod diameter D.

The turbulent wake shed by the rod is inherently three-dimensional, reflected by the spanwise correlation decay of the pressure fluctuations on the rod surface [21]. As a consequence, the turbulence in the rod wake possesses a finite correlation length, which in turn influences the phase distribution of noise sources along the span of the downstream central blade. To evaluate this aspect of the simulation, the spanwise correlation of the surface pressure fluctuations (R_{pp}) on the rod is computed as follows,

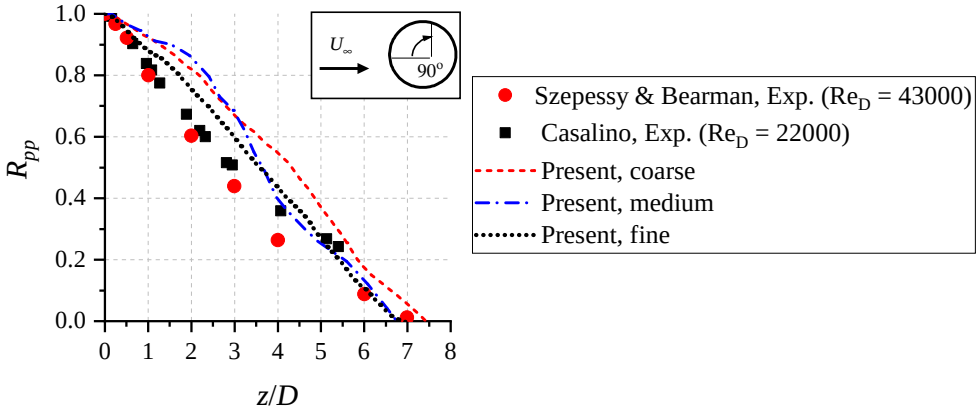

Figure 5.8: Spanwise correlation of surface pressure fluctuations on the rod surface. The rod Re_D is 26,600 in the present simulation. Reference results were obtained from Szepessy [21] and Casalino *et al.* [22].

5

Table 5.1: Comparison of domain statistics for the different grid resolution levels.

Type	Resolution (grid points/D)	Grid count (10^6)	CPU hours (10^3)
Coarse	62.5	107	7.4
Medium	88.4	300	29.4
Fine	125	645	118

$$R_{pp}(z_{\text{ref}} + \Delta z) = \frac{\langle p(z_{\text{ref}} + \Delta z)\, p(z_{\text{ref}}) \rangle}{\langle p^2(z_{\text{ref}}) \rangle} \tag{5.2}$$

where $p(z_{\text{ref}})$ is the pressure fluctuations time series at a reference spanwise location z_{ref}, Δz is the spanwise separation, and $\langle \cdot \rangle$ is the ensemble average operator. z_{ref} is located at the midspan of the rod, at an angular coordinate of 90° from the upstream stagnation point. The spanwise distributions of R_{pp} from the simulations with different grid resolution levels are compared against those from the literature [21, 22] in figure 5.8. It becomes clear that the finest grid resolution produces the best agreement with the reference, with the R_{pp} becomes zero at $z/D \approx 7$ that is expected for the present Reynolds number regime [3].

The effect of the grid resolution level on the aerodynamic response of the central blade is examined in figure 5.9 (*a*) and (*b*). The mean pressure coefficient is defined as $C_{p,\text{mean}} = (\langle p \rangle - p_\infty)/(0.5\rho_\infty U_\infty^2)$, while the RMS of the pressure fluctuations is normalized as $C_{p,\text{RMS}} = p_{\text{RMS}}/(0.5\rho_\infty U_\infty^2)$. The variation in $C_{p,\text{mean}}$ is relatively small from the coarse to the fine grid resolution setting. On the other hand, a larger discrepancy can be found in the $C_{p,\text{RMS}}$ distribution between coarse and medium results, but a converging trend is present between those of medium and fine resolution settings. The aforementioned discrepancy might be linked to the under-resolved turbulence distortion near the LE of the central blade, as depicted in figure 5.10. Plot (*c*) in figure 5.9

shows the pressure difference between the suction and pressure sides of the central blade, normalised by the maximum pressure difference value throughout the entire chord. The plot shows that the central blade of the RLC generates comparable mean aerodynamic loading as the OGV in the SDT, especially near the LE. Nevertheless, the discrepancy between $0.4 < x/c < 0.8$ might be attributable to the difference in the stagger angle between the two cases.

The acoustic aspects of the simulation are verified in the following. As described in the previous subsection, far-field noise has been obtained using the FW-H analogy in combination with a permeable surface enclosing the RLC test section. Following the end-cap-averaging approach in equation 5.1, it is expected that the results would converge as the number of caps (N) increases. Such trend is evident in figure 5.11 (a) where the noise directivity pattern is plotted in term of overall SPL (OSPL). Note that the zero angle reference is aligned with the x' direction. The figure suggests that 7 caps are already sufficient for producing converged OSPL values. The grid convergence trend for the source power level (PWL) is illustrated in figure 5.11 (b). The PWL values at the vortex-shedding frequency ($St_D \approx 0.195$) and its harmonics are almost identical among the three grid resolution levels. However, the broadband noise level is clearly underpredicted for the simulation with coarser grid, as it is unable to resolving finer turbulent structures in the rod wake that are responsible for broadband noise generation.

The reliability of the current FW-H permeable surface configuration is assessed further by comparing the prediction from direct acoustics computation (DAC). For this comparison, DAC results are obtained at a radius of 0.6 m from the rod center, which is still located outside of the acoustic sponge region. The spectra from the recorded acoustic pressure are plotted in figure 5.12 for several observer angles. The acoustic analogy predictions appear to be in good agreement with the DAC ones throughout the entire frequency range of interest, which implies that the 7 caps used on the FW-H permeable surface allows for reliable noise prediction. Nonetheless, the DAC results at large observation angles (e.g., ±60°) show the SPL values to drop sharply at high frequencies. This is an expected behavior related to the grid cutoff condition (e.g., 15 grid points per acoustic wavelength) at locations where the DAC information are sampled.

5.1.3. AERODYNAMIC CHARACTERISATION OF THE RLC

Figure 5.13 shows the mean velocity and the root-mean-square (RMS) of velocity fluctuations in the x direction at the test section midspan, sampled at multiple locations inside the test section. In addition, the spectra of streamwise velocity fluctuations are plotted in figure 5.14. Upstream of the rod ($x/D = -7$), the mean velocity profile in the test section appears to be uniform, although a region with slightly higher U values can be observed near the upper wall. The turbulence intensity remains low (< 1 %) throughout the test section height, which implies that the curved walls of the test section does not compromise the flow quality upstream of the cascade. This is also evidenced by the velocity fluctuations spectra at a location further upstream ($x/D = -10$). Nevertheless, there are several narrowband peaks that correspond to the vortex-shedding frequency and its harmonics, which can be attributed to the upstream-propagating acoustic waves. At $x/D = 4$, the trace of the rod wake can be identified by the mean velocity deficit near $y/D = 0$. The turbulent vortices in the rod wake are characterised by high u_{RMS} levels in

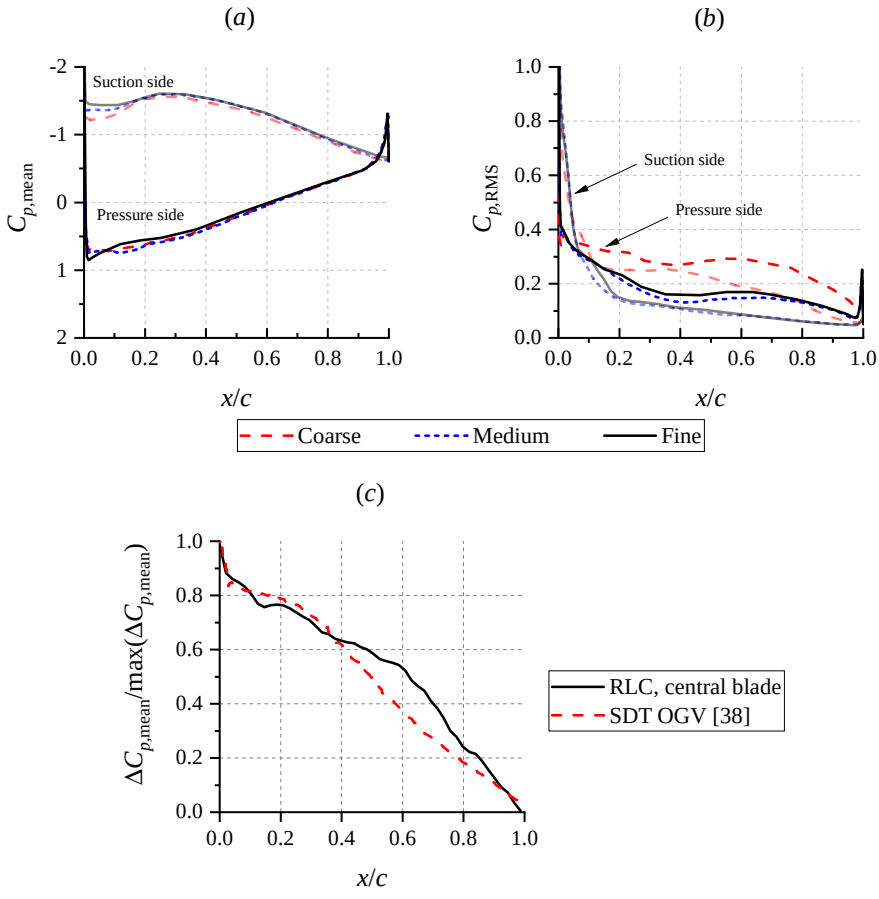

Figure 5.9: The mean surface pressure and the root-mean-square (RMS) of surface pressure fluctuations are plotted in (*a*) and (*b*) respectively. The distributions along the suction side are shown with lower opacity. Plot (*c*) compares the distribution of pressure difference between the suction and pressure sides of the RLC central blade and the SDT OGV; this plot is based on the fine grid resolution level.

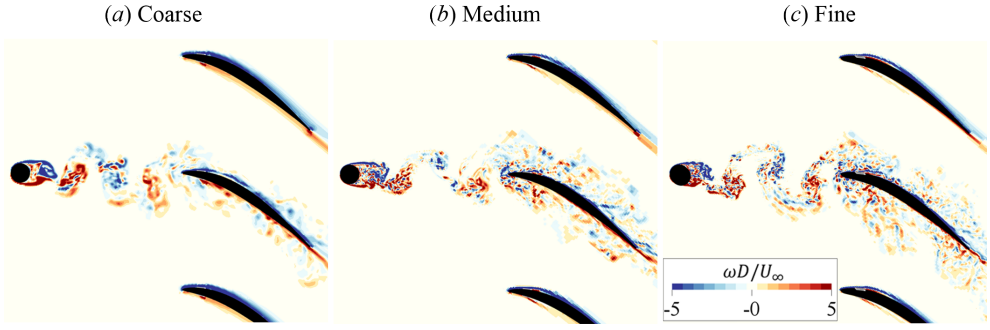

Figure 5.10: Comparison of spanwise vorticity (ω_z) contour between the different resolution settings. These instantaneous snapshots were taken at approximately the same shedding phase.

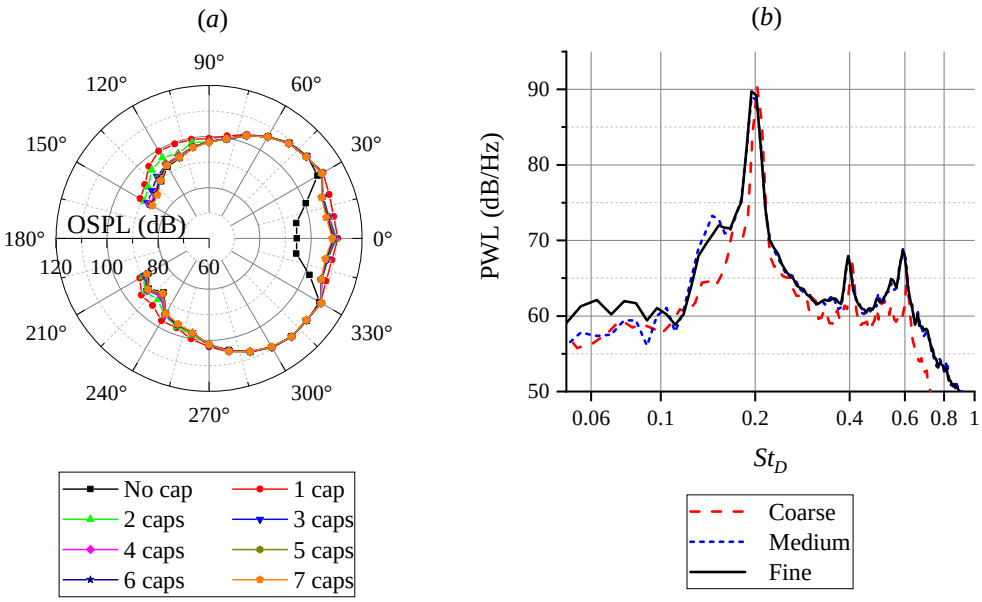

Figure 5.11: (*a*) Effect of the number of caps on the overall sound pressure level (OSPL) at different observation angles 1 m away from the rod center (fine grid resolution setting). (*b*) The convergence trend of the acoustics source power level (PWL) against various grid resolutions.

the figure, and a closer look reveals the presence of a pair of peaks corresponding to the shear layers that originate from the upper and lower sides of the rod. The turbulent nature of the rod wake is reflected in the broadband-dominated S_{uu} spectra, although a narrowband peak near the vortex-shedding frequency can still be identified. Outside of the rod wake (e.g., at $y/D = 15$), the S_{uu} amplitude drops significantly, and the spectra become more similar to those upstream of the rod wake, implying that the velocity fluctuations at this location are caused by acoustic perturbations.

The locations of each blade are indicated in the mean velocity profile plot along the cascade channel ($x/D = 10$). The channels adjacent to the central blade (C-T1 and B1-C) exhibit lower mean velocity and higher u_{RMS} levels compared to the others due to the rod wake impingement at the central blade. Thus, it is expected that all blades aside the center one are subjected to a similar aerodynamic condition. The same phenomenon is reflected in figure 5.14 where the velocity fluctuations level near the central blade ($y/D = 3$) is significantly stronger than that in the T2-T3 channel ($y/D = 15$). Due to the stagger angle setting of the cascade, the height of the test section at the outlet is smaller by almost 30 % than at the inlet. Due to the contraction of the cross-section area, the mean velocity at the outlet increases beyond U_∞, although the velocity deficit corresponding to the wake of each blade can be identified. The traces of the rod wake are still present at this location, depicted as the bump near $y/D = 0$ in the u_{RMS} profile. In figure 5.14, the velocity fluctuation spectra at the outlet center location appear to be fully broadband, implying that the coherent large vortices in the rod wake have been broken down after impinging the central blade.

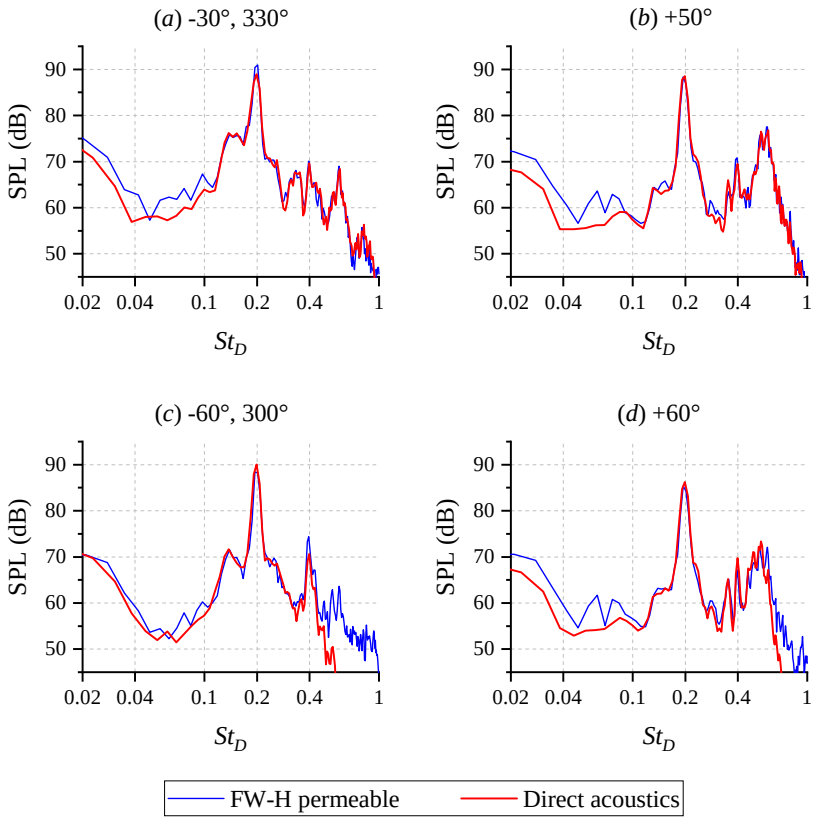

Figure 5.12: Comparison between results from FW-H analogy and direct acoustics computation for the fine grid resolution level at several observer angles and a radial distance of 0.6 m.

Turbulent structures in the rod wake and the interactions with the central blade are depicted in figure 5.15. Contour (*a*) shows the instantaneous spanwise vorticity levels at the test section midspan. The rod can be seen to periodically shed large vortices that contain finer turbulent structures. The vortices slightly grow in size as they travel downstream until they are severely deformed when impinging the central-blade leading edge. Further downstream, the large vortical structures broke down into smaller eddies with random shapes. This contour clearly shows that the rod wake only strongly affects the flow field in the channels adjacent to the central blade. Figure 5.15 (*b*) shows the topology of the rod wake along the spanwise direction. The vortex-cores are identified using the λ_2 [23] iso-surfaces. The three-dimensional nature of the rod wake becomes evident in the figure as the vortex sheets shed by the rod become less organised along the spanwise direction as they are convected downstream.

The turbulent wake impinging on the central blade leading edge can be characterised by the integral length scales L^m in m^{th} direction, using the method outlined in chapter 4, equation 4.4. The reference position for this calculation is located D upstream of the central-blade leading edge. The estimated integral length scales are reported in table 5.2,

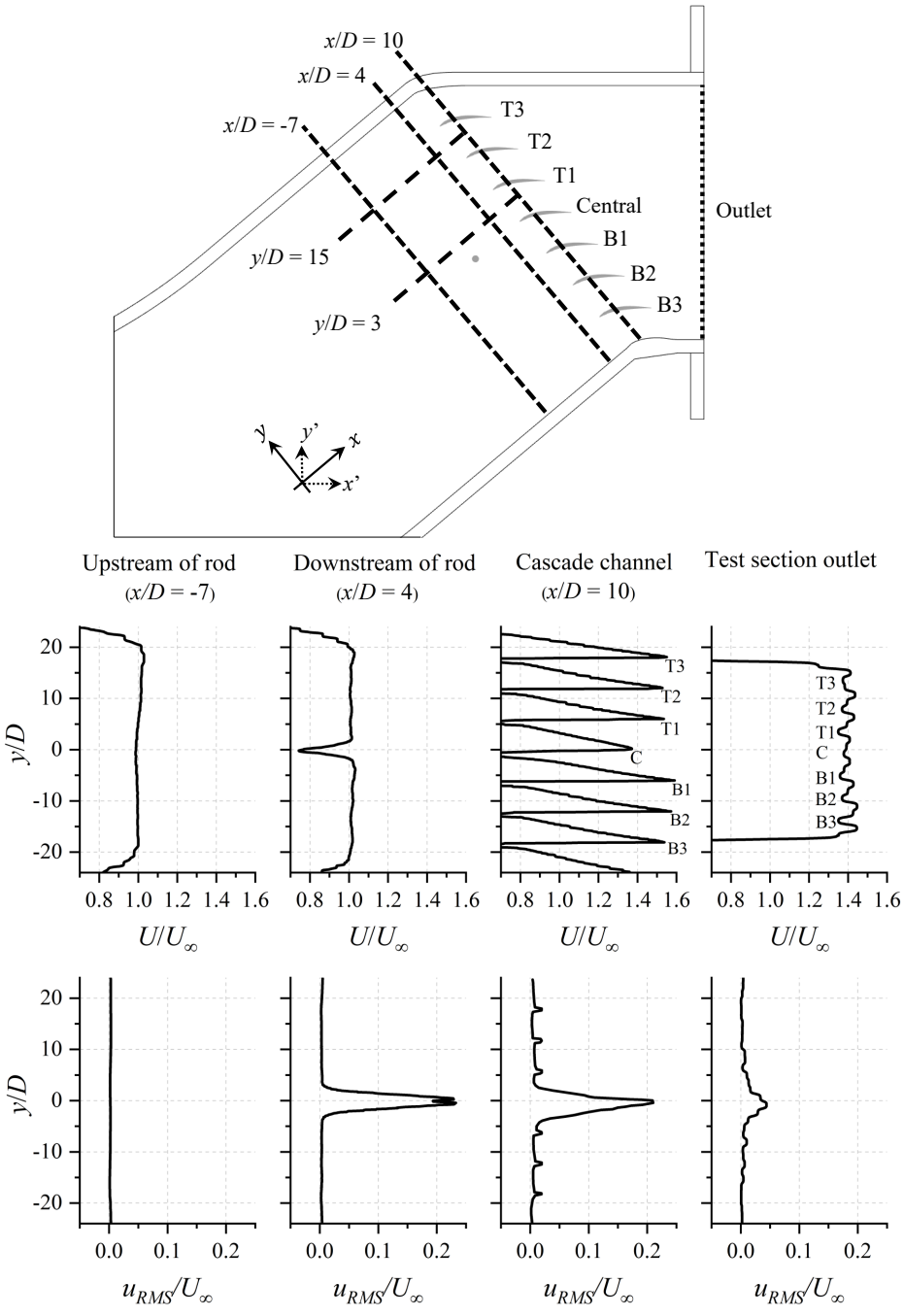

Figure 5.13: Profiles of mean velocity (U/U_∞) and root-mean-square of velocity fluctuations ($u_{\mathrm{RMS}}/U_\infty$) in the x direction, measured at different sampling lines along the test section midspan ($z/D = 0$). These lines are indicated in the sketch at the upper half of the figure. Note that the sampling line and velocity vector at the test section outlet are based on the global coordinate system (x' and y').

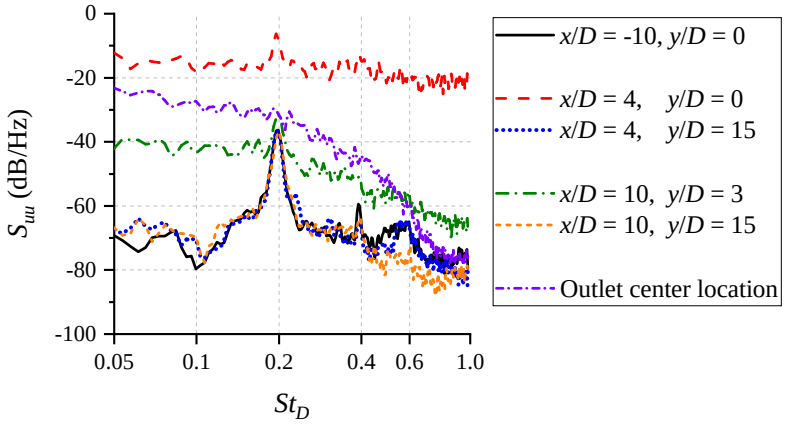

Figure 5.14: Power spectral density of streamwise velocity fluctuations S_{uu} at the midspan of the test section. S_{uu} has been normalised with a reference velocity of 1 m/s.

Table 5.2: The integral length scales of within the rod wake at D distance upstream of the central blade leading edge. The reference data have been obtained from the NASA SDT studies (hotwire anemometry from the experiment of Podboy *et al.* [16] and LBM-VLES from Casalino *et al.* [24]).

	Present	SDT, exp. [16]	SDT, LBM-VLES [24]
L^x_{uu}	4.78 mm	4.65 mm	6.50 mm
L^y_{vv}	3.78 mm	-	4.50 mm
L^z_{ww}	3.64 mm	-	6.80 mm

(*a*)

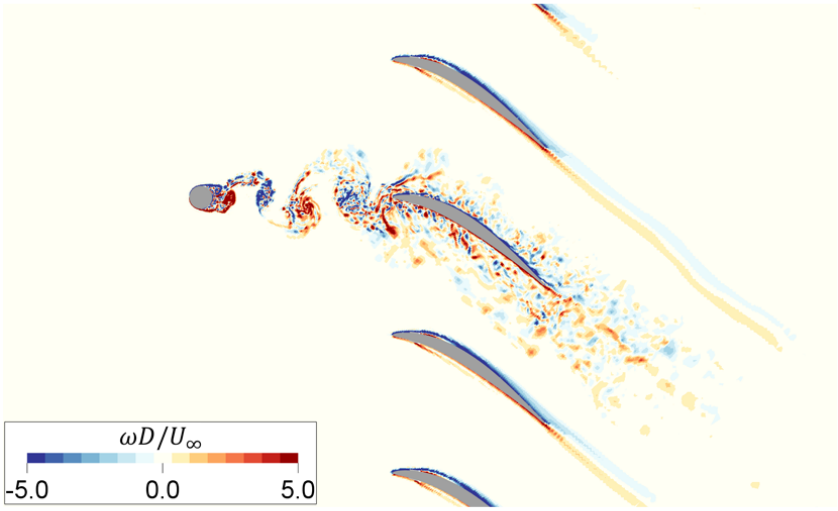

(*b*)

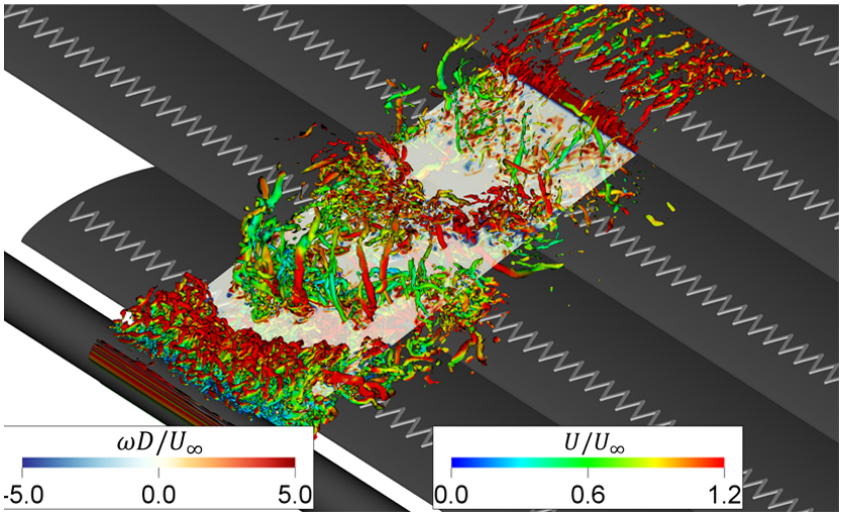

Figure 5.15: (*a*) Instantaneous contour of spanwise vorticity (ω_z) at the midspan and (*b*) lambda-2 iso-surface ($\lambda_2 = -3 \times 10^9\ s^{-2}$) with $y = 0$ plane included for highlighting the wake pattern. The iso-surface is shown up to $z = \pm 5D$ in the spanwise direction. Both contours have been extracted at the same time instance.

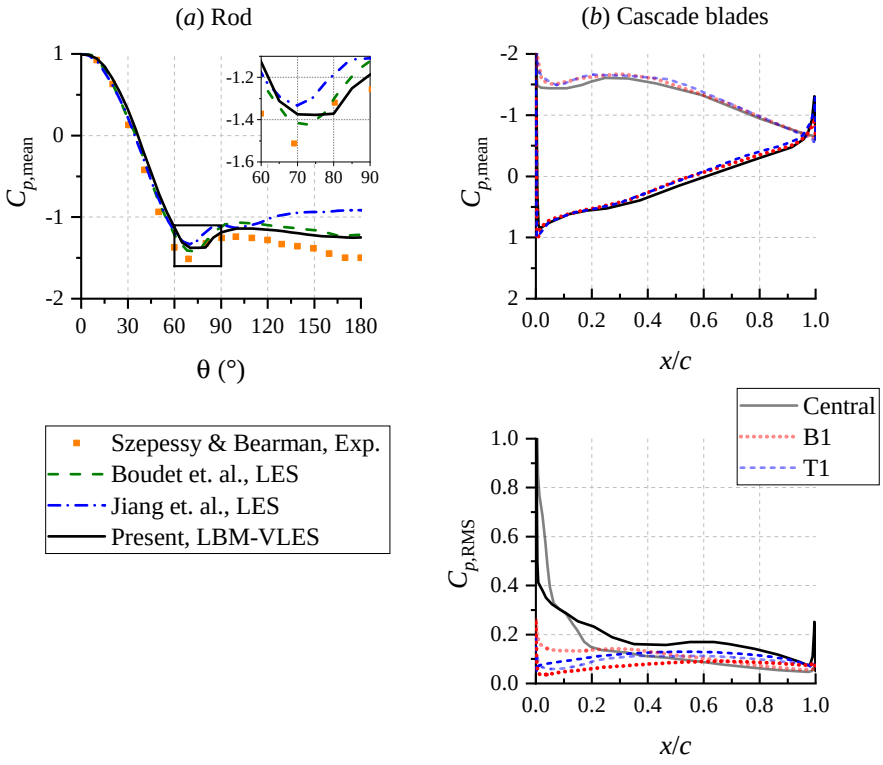

Figure 5.16: The surface pressure distribution on the rod (*a*) and on the cascade blades (*b*). Time-averaged surface pressure is normalised as pressure coefficient $C_{p,\mathrm{mean}} = (p_{\mathrm{mean}} - p_\infty)/q_\infty$, where $q_\infty = 0.5\rho_\infty U_\infty^2$. For the cascade blades, the data points at the suction side are drawn with lower opacity. In (*a*), the reference angle $\theta = 0°$ faces towards the upstream direction. In (*b*), the root-mean-square of surface pressure fluctuations is expressed as $C_{p,\mathrm{RMS}} = p_{\mathrm{RMS}}/q_\infty$. Reference data in (*a*) have been taken from Szepessy and Bearman [26], Boudet *et al.* [27], and Jiang *et al.* [28].

where they are compared against past experimental and numerical data of the SDT fan stage. Note that the length scales estimate of Podboy *et al.* [16] have been obtained using a single-probe method that requires invoking the Taylor's frozen turbulence assumption [25]. This approach is unsuitable for the present results due to short simulation time that would lead to unreliable estimate of the turbulence integral time scale. The present results reveal that the length scale in the rod wake is longer in the streamwise direction (L^x_{uu}), whereas in the simulation of Casalino *et al.* [24], the spanwise/radial length scale (L^z_{ww}) is slightly longer. Nevertheless, the present L^x_{uu} estimate is quite close to that of Podboy *et al.* [16].

The aerodynamic loading distributions on the rod and the cascade blades are provided in figure 5.16. As observed by Jiang *et al.* [28], the pressure distribution on the rod in RAC approaches that of an isolated rod when the separation between the rod base and the downstream body is larger than $6D$. This is evident in figure 5.16 (*a*) since the rod-central blade separation is slightly longer than $8D$, such that the $C_{p,\mathrm{mean}}$ distribution

Table 5.3: Mean values and RMS of fluctuations of lift and drag forces on the rod and cascade blades. Both lift and drag forces are computed based on the local coordinate system.

	$C_{l,\text{mean}}$	$C_{d,\text{mean}}$	$C_{l,\text{RMS}}$	$C_{d,\text{RMS}}$
Rod	≈ 0	1.22	0.16	0.019
Central blade	1.18	0.52	0.16	0.066
Blade T1	1.53	0.64	0.11	0.051
Blade B1	1.54	0.64	0.12	0.069
Blade T2	1.52	0.65	0.07	0.035
Blade B2	1.54	0.66	0.10	0.059

on the rod agrees well to that of Boudet *et al.* [27]. However, the mean surface pressure near the rod base overpredicts that of Szepessy and Bearman [26]. It is worth mentioning that a similar situation is also present in the RAC (see figure 4.23). In the upper half of plot (*b*), the $C_{p,\text{mean}}$ distribution on the central blade is compared with that of T1 and B1 blades. Note that the dynamic pressure used for normalising the surface pressure on the central blade is based on a velocity $U = 0.9U_\infty$ that is slightly lower than the freestream, since the central blade is immersed in the rod wake. The plot shows that once the velocity deficit in the rod wake is accounted for, the mean loading characteristic on the central blade is still comparable to that of T1 and B1 blades that are not directly affected by the rod wake. More noticeable discrepancies between blades are present in the surface pressure fluctuations $C_{p,\text{RMS}}$ plot. As expected, the rod wake impingement induces a substantial increase in surface pressure fluctuations intensity near the leading edge of the central blade. The $C_{p,\text{RMS}}$ level drops immediately further downstream, implying that the noise source region is localised at the leading edge. An additional spike in the surface pressure fluctuations can be observed near $x/c = 1$, which might be due to the interaction between the remaining turbulent structures with the trailing edge. The $C_{p,\text{RMS}}$ distributions on the T1 and B1 blades are on average lower compared to that on the central one. Nevertheless, upon closer inspection, the suction side of the B1 blade and the pressure side of the T1 blade, which are directly facing the central blade, exhibit stronger pressure fluctuations than their opposite sides.

The aerodynamic forces on the RLC components are summarised in table 5.3, where they have been expressed as lift and drag coefficients with respect to the local coordinate system. The mean drag coefficient on the rod is found to be within the range for an isolated rod [21, 29]; similar value has been reported for the RAC [28]. The mean drag coefficients on all blades are almost identical except that for the central blade due to the influence of the rod wake. Nevertheless, once the drag coefficient normalisation takes the lower mean velocity in the rod wake into account, the $C_{d,\text{mean}}$ of the central blade is comparable to that of the others. As expected, the rod wake impingement induces larger lift and drag fluctuations on the central blade. Nevertheless, it is also evident that the inner blades (T1 and B1) experience stronger aerodynamic fluctuations compared to the outer ones (T2 and B2), implying that the rod wake influence is limited to only the channels adjacent to the central blade.

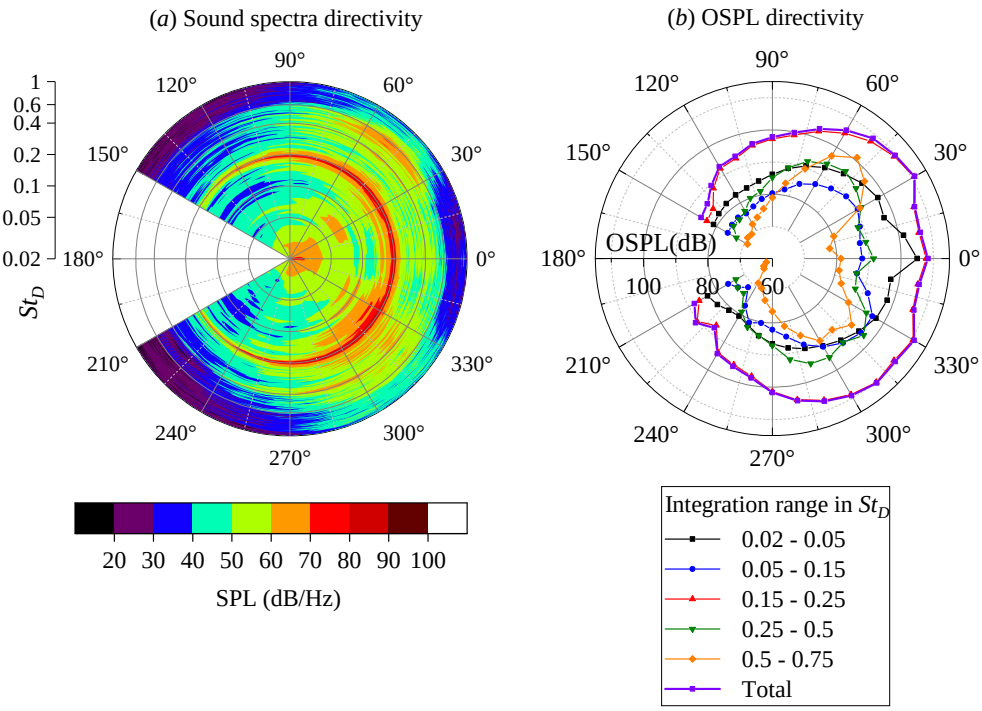

Figure 5.17: Far-field sound spectra and OSPL directivity pattern along an arc in the x' - y' plane. The arc has a radius of 1 m centered at the rod midspan.

5.1.4. ACOUSTIC CHARACTERISATION OF THE RLC

Using the FW-H analogy, the predicted far-field noise at a radius of 1 m from the rod midspan is shown in figure 5.17, in which the noise spectra contours are given in (*a*), and the narrowband-integrated OSPL (overall sound pressure level) directivity patterns in (*b*). To assist with the interpretation of this figure, the dilatation field ($\nabla \cdot \boldsymbol{u}$) and near-field pressure fluctuations (p_{RMS}) contours at the test section midspan are provided in figure 5.18. The dilatation field is expressed in term of time derivative of pressure [30] following this relationship:

$$\nabla \cdot \boldsymbol{u} = -\frac{1}{\rho_\infty c_\infty^2} \frac{\partial p}{\partial t} \tag{5.3}$$

where ρ_∞ and c_∞ are the freestream density and speed of sound respectively. Subsequently, $\frac{\partial p}{\partial t}$ is normalized using the freestream dynamic pressure ($q_\infty = 0.5\rho_\infty U_\infty^2$) and a characteristic time (D/U_∞).

The sound waves at the lowest frequency band (i.e., $0.02 < St_D < 0.05$) radiate predominantly in the downstream direction, aligned with the flow. As shown in the corresponding dilatation field and near-field pressure contours, sound waves in this frequency range propagate inside the test section as plane waves. The acoustic behaviour

(*a*) St_D= 0.02 - 0.05

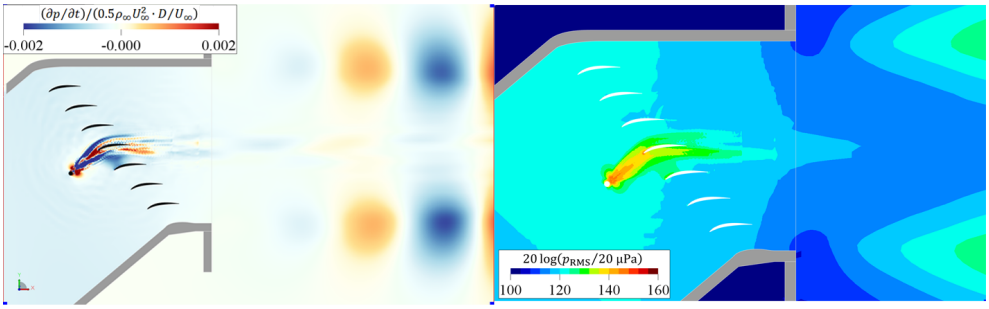

(*b*) St_D= 0.15 - 0.25

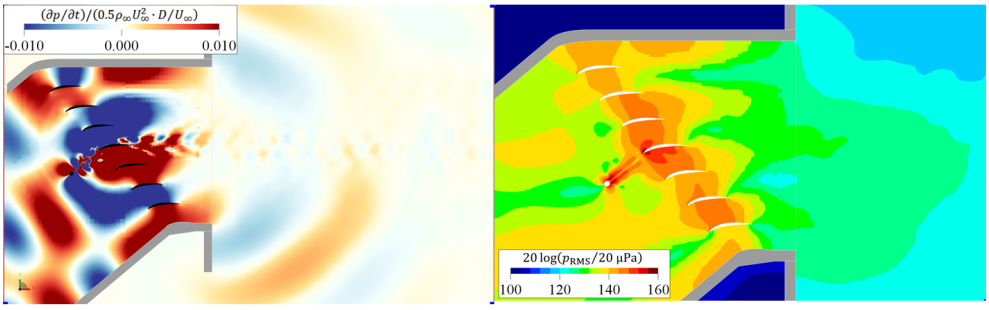

(*c*) St_D= 0.50 - 0.75

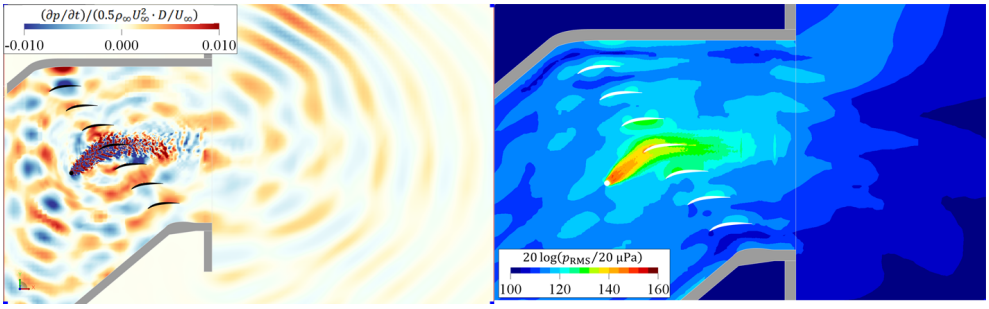

Figure 5.18: Bandpass-filtered contours of instantaneous dilatation field as time derivative of pressure $\frac{\partial p}{\partial t}$ (left column) and the near-field pressure fluctuations p_{RMS} in decibel scale (right column).

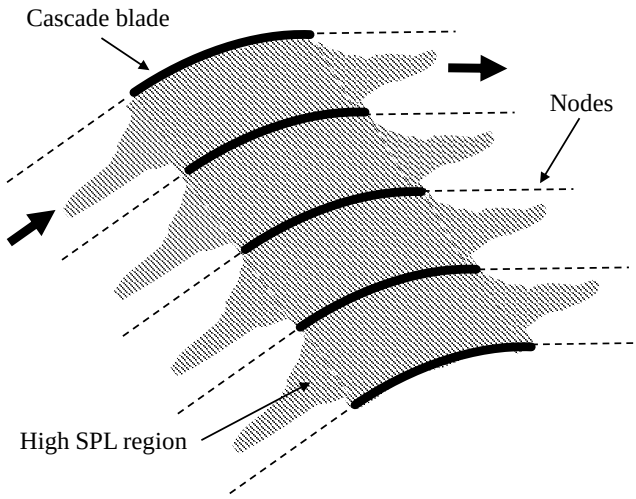

Figure 5.19: The resonant mode β (i.e., half-wavelength mode) in a linear cascade as reported by Parker [32].

at this frequency band can be associated with the blockage inside the test section caused by the rod wake, in addition to the turbulent eddies in the shear layer forming downstream of the test section outlet. The latter, however, is not strongly present in the dilatation field contours at higher frequency bands, implying that the sound contribution from the shear layer is only significant in the low frequency range.

Figure 5.17 (*b*) clearly shows that the majority of the acoustic energy is concentrated in the narrowband surrounding the vortex-shedding frequency (i.e., $0.15 < St_D < 0.25$), which is linked to the quasi-periodic upwash/downwash induced by the vortices impinging the leading edge of the central blade. The sound waves produced by the central blade propagate towards the adjacent inter-blade channels. Nevertheless, related to the cascade configuration, it is also possible to consider that the unsteady ae rodynamic forcing at the central blade also indirectly influences the other blades, which could trigger a resonance-like phenomenon [31]. In fact, the near-field pressure contours in figure 5.18 at this Strouhal range suggest that Parker's [32] β-mode (half-wavelength) resonance might be present, for which the resonant frequency f_r is predicted using the following empricial formula:

$$f_\mathrm{r} = 0.5\left(\frac{a_\infty}{c}\right)\Big/\left(1+\alpha\left(\frac{s}{c}\right)^{\beta}\right) \tag{5.4}$$

where a_∞ is the freestream speed of sound, $\alpha = 0.7$, and $\beta = 0.84$. Using this formula, f_r is predicted to be approximately 2.7 kHz or $St_{D,\mathrm{r}} \approx 0.19$, which is quite close to the vortex-shedding frequency ($St_D = 0.195$). A sketch of the expected high SPL region due to the resonant mode is provided in figure 5.19. The sound at this Strouhal range is predominantly radiated towards the shallow angles on the upper and lower arc with the highest intensity found at 30° and 330°, which is likely to be due to the diffraction by the edge of the test section walls at the outlet.

Finer turbulent structures in the rod wake are responsible for generating sound in the high frequency range. The sound directivity at these Strouhal ranges (i.e., $0.5 < St_D < 0.75$) is more directional than the lower frequency ones, with the main lobes directed towards 50° and 310°. However, the noise intensity towards the upper arc is higher than in the opposite direction. This behaviour is clearly depicted in figure 5.18, but the reason is not entirely clear. It is possible that such asymmetry is the result of interference between sound waves that are diffracted at the trailing edge of each blade, which in turn is influenced by the geometrical aspects of the cascade itself (e.g., blade camber and stagger angle) [33–35]. The dilatation field contour shows an alternating variation in intensity along each wavefront at locations downstream of the test section outlet. Regardless, these are interesting aspects of the RLC that can be studied further in future experimental studies.

5.1.5. NOISE MITIGATION TREATMENTS AT THE CENTRAL BLADE

In this subsection, porous LE and serrations are implemented in the RLC as proof-of-concepts, as shown in the upper half of figure 5.20, although only the central blade is modified. This is intended for isolating the noise reduction contribution due to the mitigation of noise sources on the central blade while minimising the overall changes to the steady aerodynamic characteristics of the system. Although the sound propagation phenomenon in the cascade would be affected as the geometrical periodicity of the cascade is altered, it would still be interesting to evaluate the changes in source power level caused by the LE treatment at the central blade.

The porous LE implementation is similar to the PLE treatment for the RAC in chapter 4, with the modified chordwise extent equals to 15 % of the chord. It is also modelled as an equivalent fluid region (depicted in dark blue colour in the figure) where the transport properties of the 800-µm Ni-Cr-Al metal foam have been imposed. The serrations are designed according to the turbulence length scales that are reported in table 5.2, such that the serration amplitude equals to $0.2c$ and the wavelength to $0.64c$. The design procedure is the same as that described in equation 4.2 and 4.3, but the extension of the airfoil chord follows the camber line in order to preserve the camber curvature.

As evidenced in the polar plot of figure 5.20 (*a*), the modification of the central blade has altered the far-field sound intensity. The plot illustrates the noise reduction in term of the difference in OSPL between the baseline RLC and those with LE treatments. In general, higher noise reduction level can be observed towards the upper and lower downstream directions, which are also the observer angles where the OSPL is the largest (see figure 5.17 (*b*)). On average, the ΔOSPL values for the serrated case are higher than those for the porous one, which has also been observed with the RAC in chapter 4. The same behavior is reflected by the PWL spectra in figure 5.20 (*b*). Both LE treatments clearly affect the frequency range where turbulence-impingement noise dominates the spectra, e.g., $St_c > 0.13$. However, the present porous LE implementation barely attenuates the tonal noise component, but a substantial broadband noise reduction above $St_c = 0.4$ can be found. On the other hand, the serrated blade achieves a 6 dB reduction at both the fundamental tone frequency and its first harmonic, in addition to the reduction of the low-frequency broadband noise component between $0.15 < St_c < 0.4$. Above $St_c = 0.4$, the noise reduction levels of both porous and serrated

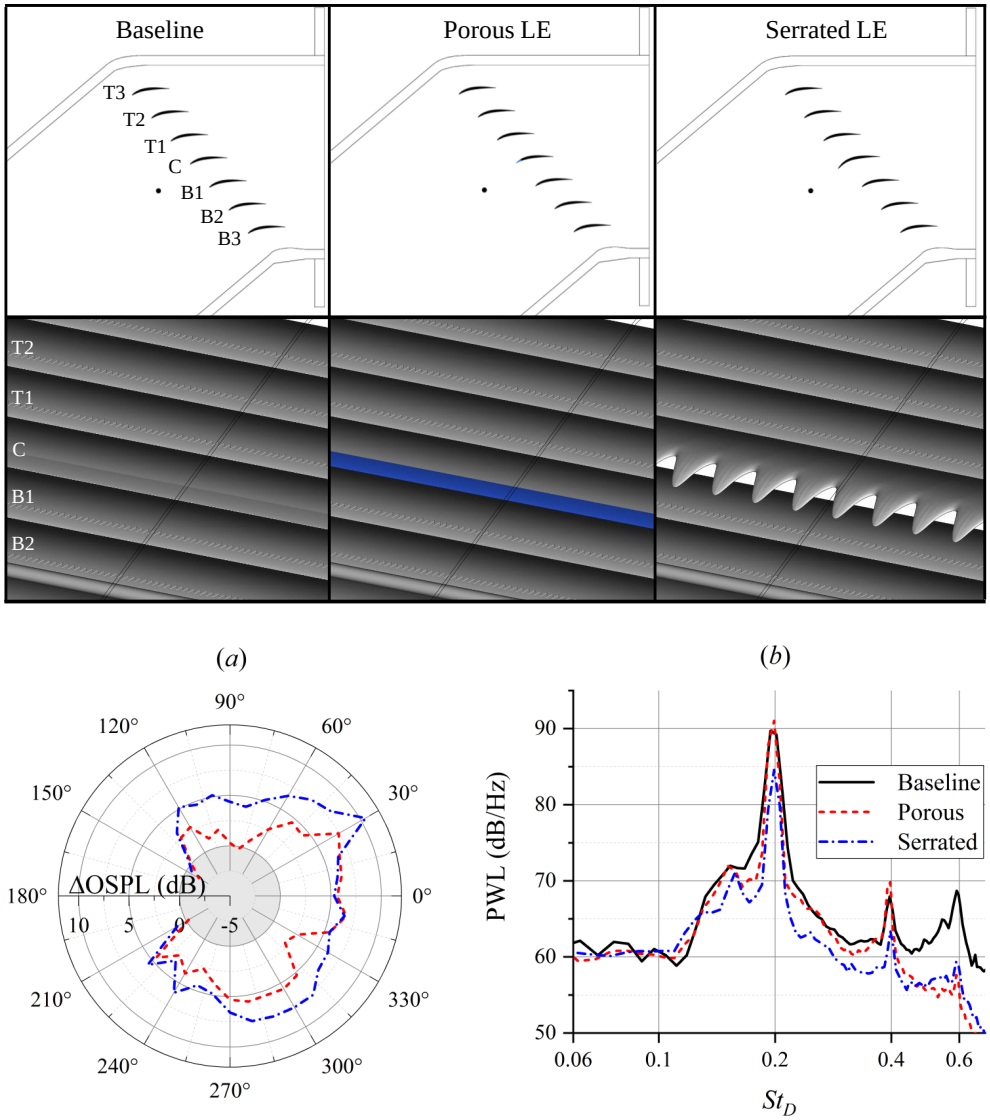

Figure 5.20: The upper half shows the computer drawings of the RLC configurations, including those with porous and serrated LE. The lower half shows (*a*) the noise reduction directivity pattern given as $\Delta\text{OSPL} = \text{OSPL}_{\text{baseline}} - \text{OSPL}_{\text{porous,serrated}}$, and (*b*) the comparison of the sound power level.

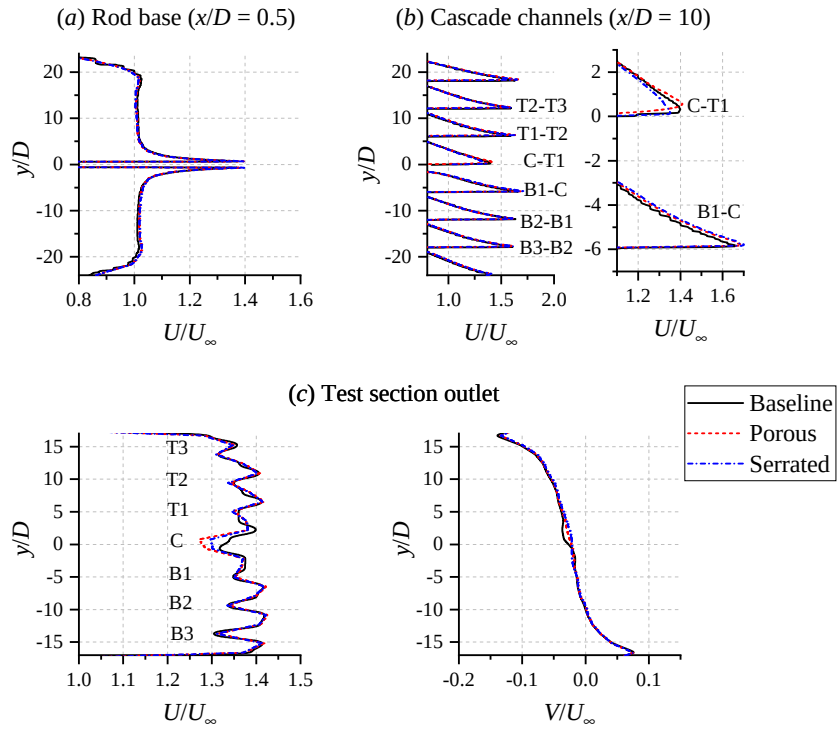

Figure 5.21: Velocity profiles sampled at various segments in the test section for the RLC with different central blade configurations.

blades are comparable.

The aerodynamic effects of the central blade modifications are examined in the following. Figure 5.21 (*a*) evidences that the porous or serrated LE do not influence the inflow, and the rod wake profile remains the same for all cases. Along the cascade channels, in plot (*b*), the velocity profile in each channel is practically identical regardless of the LE type. Nevertheless, a closer look at channel C-T1 (i.e., the one adjacent to the suction side of the central blade) reveals that the porous LE causes the local peak in the velocity profile to be shifted slightly upward, indicating a smaller amount of flow deflection that can be attributed to the lower aerodynamic loading at the porous LE. For the serrated LE, this peak remains at roughly at the same position as the baseline one. The velocity profiles at the test section outlet are shown in (*c*). In the streamwise velocity component (U) plot, it is apparent that the velocity deficit corresponding to the wake of the central blade is more significant in the porous LE case, rather than in the serrated one. Following this, the drag increase caused by the central blade modification is estimated to be 9.3 % and 6.8 % for the porous and serrated cases respectively. This is an interesting finding considering that when the PLE is implemented in the RAC, the drag penalty is significantly higher due to the cross-flow from the pressure side to the suction side. It is likely that the influence of the unsteady transpiration at the suction side of the

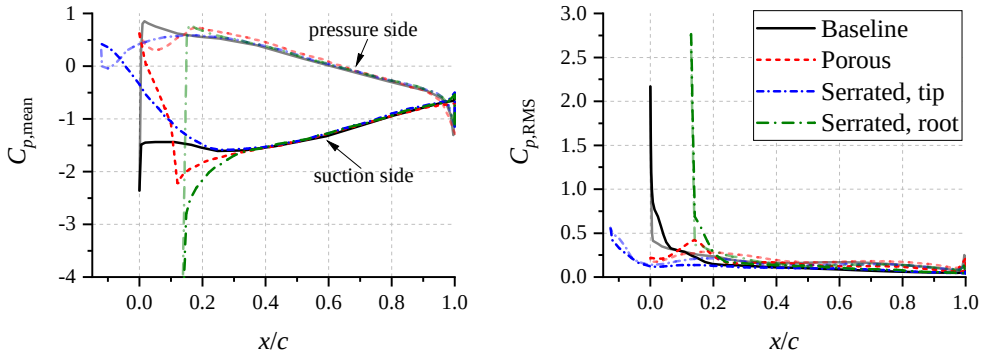

Figure 5.22: The comparisons of surface pressure statistics for the RLC with different central blade configurations. The pressure side distributions are plotted with lower opacity.

central blade is mitigated by the adjacent ones whose aerodynamic loading remains relatively unmodified. Moreover, as shown by the profile of vertical velocity component (V) at the outlet, the central blade modification does not cause any major alternation to the flow turning produced by the linear cascade.

The alterations in aerodynamic loading on the central blade are depicted in figure 5.22. The permeability of the porous LE causes the suction peak near the LE tip to vanish, indicating that the cross-flow from the pressure side to the suction side is present in this case. Despite this, a secondary suction peak appears near the solid-porous junction ($x/c = 0.15$), unlike what previously observed with the PLE configuration of the RAC (see figure 4.23). Further downstream, the $C_{p,\mathrm{mean}}$ distribution for the porous LE case becomes almost identical to the baseline one. The serrations on the central blade produce similar behaviours as the WLE configuration of the RAC. The serration tip also exhibits a reduced aerodynamic loading, and the cross-over of the $C_{p,\mathrm{mean}}$ distribution near $x/c = -0.02$ is an indication that the serration tip is installed with a negative incidence relative to the incoming flow. The serration root shows a significantly stronger suction peak compared to the baseline one, which also realises a stronger adverse pressure gradient further downstream. This would enhance boundary layer growth downstream that eventually contributes to an increased drag as discussed earlier.

The flow field surrounding the rod and the nearest three blades is visualised in figure 5.23 (a). Flow vectors are added to the contour to emphasise the flow turning induced by the linear cascade. It is evident that the flow entering the cascade is deflected with a relatively similar outlet angle for all three cases, although there are some noticeable differences. In the porous case, the boundary layer on the suction side of the central blade grows noticeably thicker compared to the baseline one, resulting in a wider wake region. Additionally, the location on the central blade surface, where large flow acceleration can be found, has been shifted slightly downstream to the location of the solid-porous junction; the same behavior is also present for the PLE configuration in the RAC case. For the blade with LE serrations, the wake region is also slightly wider than the baseline one, but it is not as prominent as in the porous case. The shift of the flow acceleration region at the suction side is also present here, specifically towards the

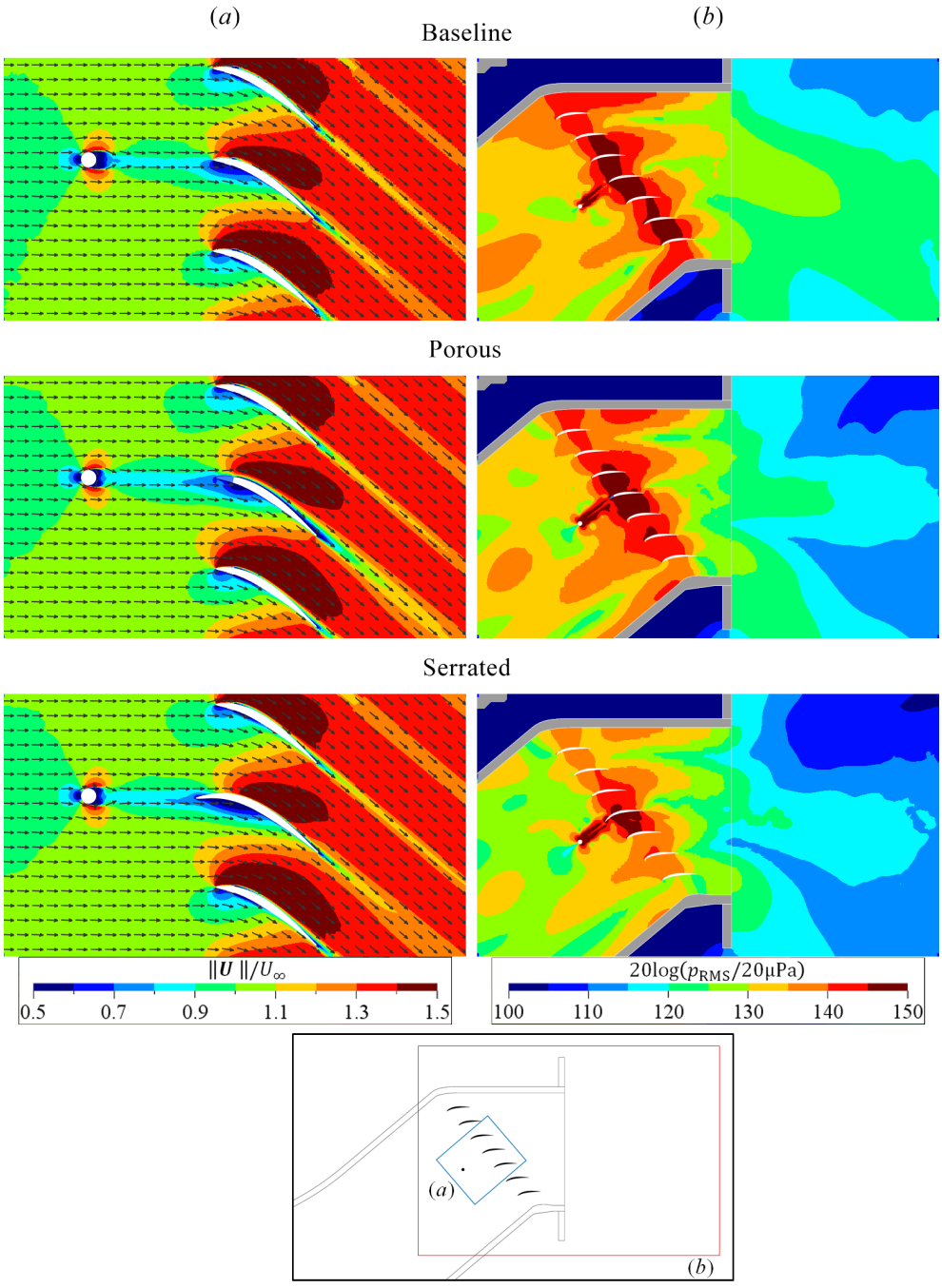

Figure 5.23: (*a*) Contours of time-averaged and normalised velocity magnitude, with the velocity contours plotted on top. (*b*) The contours of near-field pressure fluctuations, bandpassed between $0.15 < St_c < 0.25$, presented in decibel. The field of view of each contour is indicated in the inset at the lower part of the figure.

location of the serration root.

The effects of the LE treatments on the unsteady pressure field in the test section are illustrated in figure 5.23 (*b*). The contour for the baseline case has been taken from figure 5.18 (*b*), which corresponds to the Strouhal band centered at the vortex-shedding frequency. In both porous and serrated cases, the high-SPL regions within each inter-blade channels are still present, albeit with lower intensities. The reduction of the pressure fluctuations is more substantial in the serrated case than the porous one, reflecting the noise attenuation that was previously shown in figure 5.20. Nonetheless, the figure also corroborates that the β-mode-like resonance phenomenon in the RLC originates from the rod wake impingement at the central blade.

In summary, the present investigation has demonstrated that the noise emission of the RLC can be mitigated using LE modifications at the central blade. Nevertheless, the porous LE concept would require further improvements, such as by incorporating a serration-like planform as suggested in chapter 4. Aerodynamic optimisation is also necessary once the porous LE is applied on all blades to minimise the impact of cross-flow in the porous medium on the overall aerodynamic performance of the linear cascade. There are also caveats related to the fact that the current RLC realises rod wake impingement only at one blade, while in an actual fan stage, fan wake impingement would take place on multiple blades depending on the number of fan and OGV blades. In the RLC, this phenomenon can be emulated to a certain extent by inclining the rod along the cross-section plane of the test section. Future investigations on such configuration will become necessary to elucidate the efficacy of the porous and serrated LE when they are applied on all blades of the RLC.

5.2. POROUS STATOR IN A FULL-SCALE AIRCRAFT MODEL

In chapter 4, the poro-serrated serrations have been found to be the most effective at mitigating TIN in the rod-airfoil configuration. Nevertheless, it remains to be seen whether the same concept would result a similar amount of noise reduction in an actual aircraft engine. Hence, this section looks into the application porous edge treatments on a full-scale aircraft model in order to obtain additional insights beyond those achievable using the rod-airfoil or the rod-linear cascade configuration.

5.2.1. SIMULATION DESCRIPTION

The present full-scale aircraft model consists of two main elements, both of which were developed by NASA. The airframe is referred to as the Common Research Model (CRM), which bears a resemblance to a typical transonic wide-body airliner. The CRM is equipped with flow-through (empty) nacelles, and thus, the port nacelle is replaced with the fan stage model from the Source Diagnostic Test (SDT) rig. The combined CRM/SDT configuration is illustrated in figure 5.24. Identical to the original CRM geometry, some components, such as horizontal and vertical stabilisers, are missing, although the details of high-lift devices on the wings, including flaps and slats, are retained. Considering in chapter 1 that the aircraft noise emission during the approach phase is more crucial, the present study considers a subvariant of the CRM geometry that is referred to as the CRM-HL (High-Lift), such that the slats and flaps are in a fully-extended state. While the

	NASA-CRM (37:1 scale)	Airbus A330-300
Fuselage length (m)	62.8	63.6
Wing span (m)	58.7	60.3

	NASA-SDT (11:2 scale)	Rolls-Royce Trent 1000
Fan diameter (m)	2.93	2.85
Bypass ratio	-	10.8 - 11.0
Fan blade count	22	20
OGV blade count	26	46

Table 5.4: Comparisons between the up-scaled NASA-CRM/SDT geometries against their closest real-life counterparts.

Type	d_p (µm)	ϕ(%)	K (m^2)	C (m^{-1})
Metal foam (M800; as in chapter 3)	800	91.65	2.7×10^{-9}	2613
Metal foam (M450)	450	89.28	6.11×10^{-10}	9758

Table 5.5: The properties of porous materials employed for the poro-serrated OGVs.

original CRM and SDT geometries are scaled models for laboratory tests, they have been up-scaled in the present study to better resemble an actual wide-body airliner. Consequently, the CRM airframe haas been up-scaled by 37 times, such that the wing span equals to 58.7 m. The SDT fan stage has been up-scaled by 5.5 times, leading to a fan diameter of 2.93 m. The fan operates at a constant rotational speed of 1420 RPM, at which the expected fan tip speed is $U_{\text{ref}} = 237.57\,\text{m/s}$, corresponding to the *approach* thrust setting in the original SDT study [16]. The dimensions of the up-scaled NASA-CRM/SDT geometries are compared against their closest real-life counterparts in table 5.4.

Current study focuses on the mitigation of the fan wake-OGV interaction mechanism inside the fan stage. For this purpose, the OGVs have been modified to incorporate poro-serrated LE extensions. The serrated blade planform is intended to attenuate the tonal noise component at low-frequencies, and the material porosity for the broadband one in the higher frequency range. The porous treatment has been modelled after a Ni-Cr-Al metal foam with two different mean pore diameters: 800 µm and 450 µm; the former has been employed in chapters 3 and 4. The properties of the metal foam are reported in table 5.5. In the subsequent sections, the setups with modified OGVs will be referred to as the "M800" and "M450" configurations respectively, emphasising the mean pore size. A closer view of the poro-serrated OGV in the fan stage is provided in figure 5.25. The serrated planform of the permeable treatment is characterised by a sinusoidal shape with a wavelength $\Lambda = 0.76c$ and amplitude $H = 0.38c$, where c is the average chord length of the OGV. Although the porous serrations modify the OGV planform only at the first 20 % of the OGV chord, the porous medium region wraps around a streamlined solid-porous junction that extends in between 35 % to 60 % of the OGV chord.

As shown at the top of figure 5.26, the CRM/SDT model is enclosed in a cubic simulation domain whose sides are 1400 m long, or roughly 24 times the aircraft wingspan. All domain boundaries are specified with a freestream velocity of 68 m/s and a

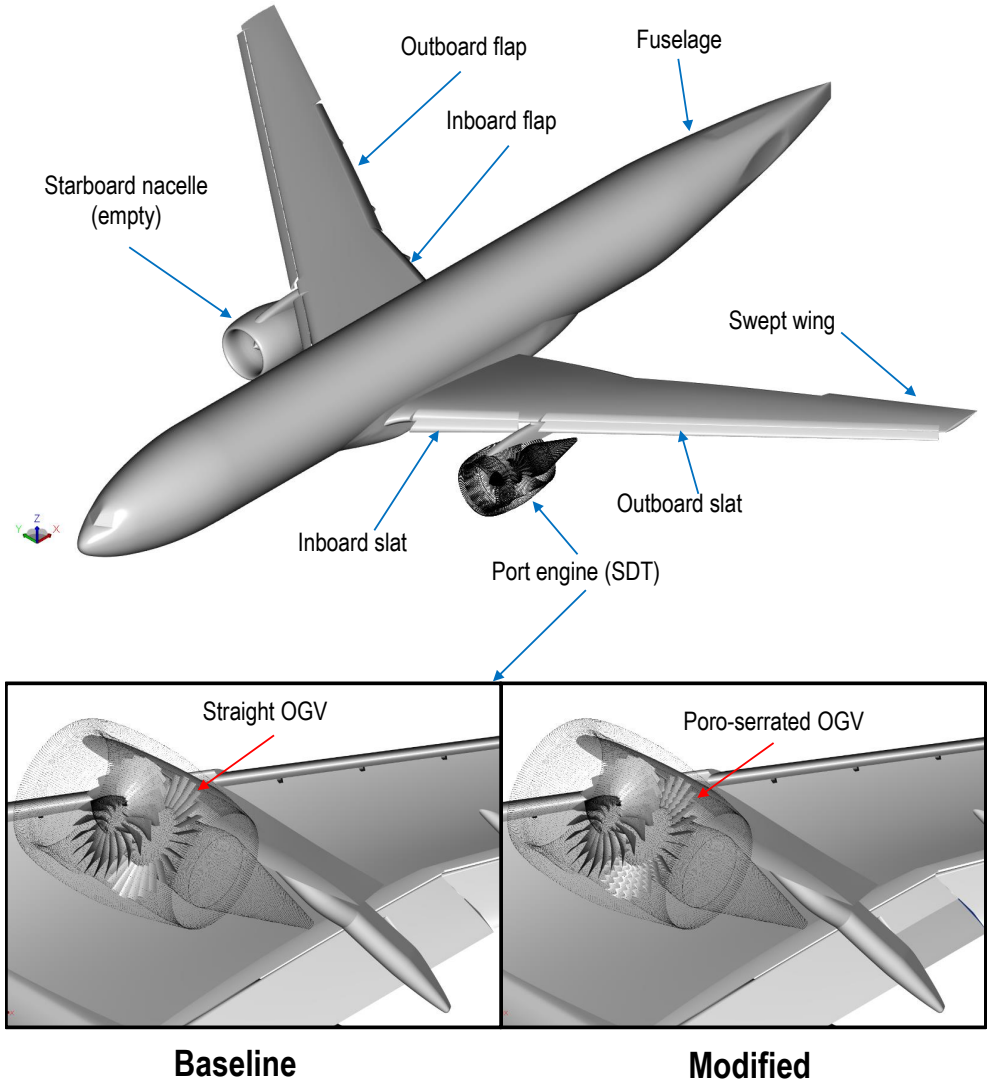

Figure 5.24: The NASA-CRM/SDT configuration in the present study. The lower part of the figures shows a comparison between the baseline configuration and another with porous treatments.

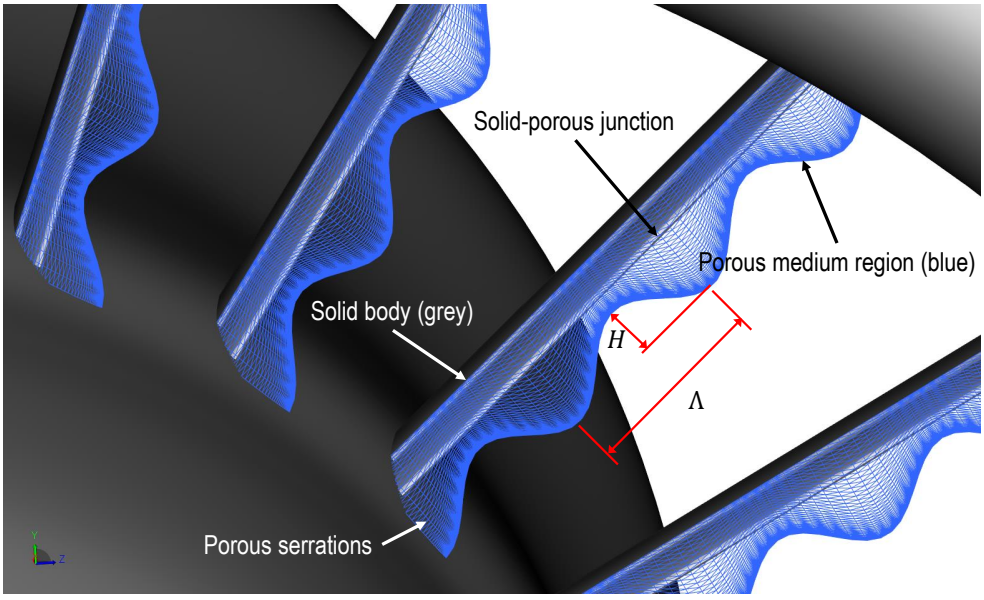

Figure 5.25: A closer view on the modified OGV in the fan stage, highlighting the amplitude H and wavelength Λ of the serration planform.

static pressure of 101,325 Pa. The aircraft is installed at an incidence of 7 deg relative to the inflow, which is equal to the sum between an angle-of-attack of 4 deg and the angle of a standard descent profile of 3 deg [36]. For far-field noise computation, a permeable surface has been specified at the exterior of the turbofan and an inboard segment of the port wing as in figure 5.26. Pressure and velocity fluctuations are sampled on the permeable surface at 5.93 kHz, resulting in a Nyquist frequency that equals to 5.7 times the expected blade-passing frequency (BPF_1). Data sampling has been carried out for 1.32 s, which is roughly equivalent to 31 fan rotational cycles. 6 end caps are added at the downstream end of the permeable surface to filter pseudo-sound contamination from the jet plume. The usage of the caps is identical to that of RLC case in the previous section. To prevent acoustic reflection at the domain boundaries, a sponge region has been defined starting from a radius of 258 m from the aircraft's nose.

The simulation domain contains a total of 16 grid refinement regions, where the finest one can be found inside the fan stage and in the region surrounding the jet plume. The smallest grid size in the simulation domain is equal to 2.54 mm or $0.012c$, which corresponds to an average y^+ of the first wall-adjacent voxel of 500 on the OGV surface for the baseline configuration. A snapshot of the voxel distribution in the simulation domain is shown in figure 5.27. The simulation is carried out for a total of 2.56 s with an initial transient of 1.24 s, which is intended to capture acoustic information at frequencies as low as 50 Hz (≈ 0.1 BPF_1). The simulations have been carried out at the Dutch National Supercomputer facility (Cartesius), employing 720 cores of Intel-Haswell Xeon E5-2690 v3. For the present grid configuration, the computational cost is approximately 95,000 CPU hours for the configuration with poro-serrated OGVs.

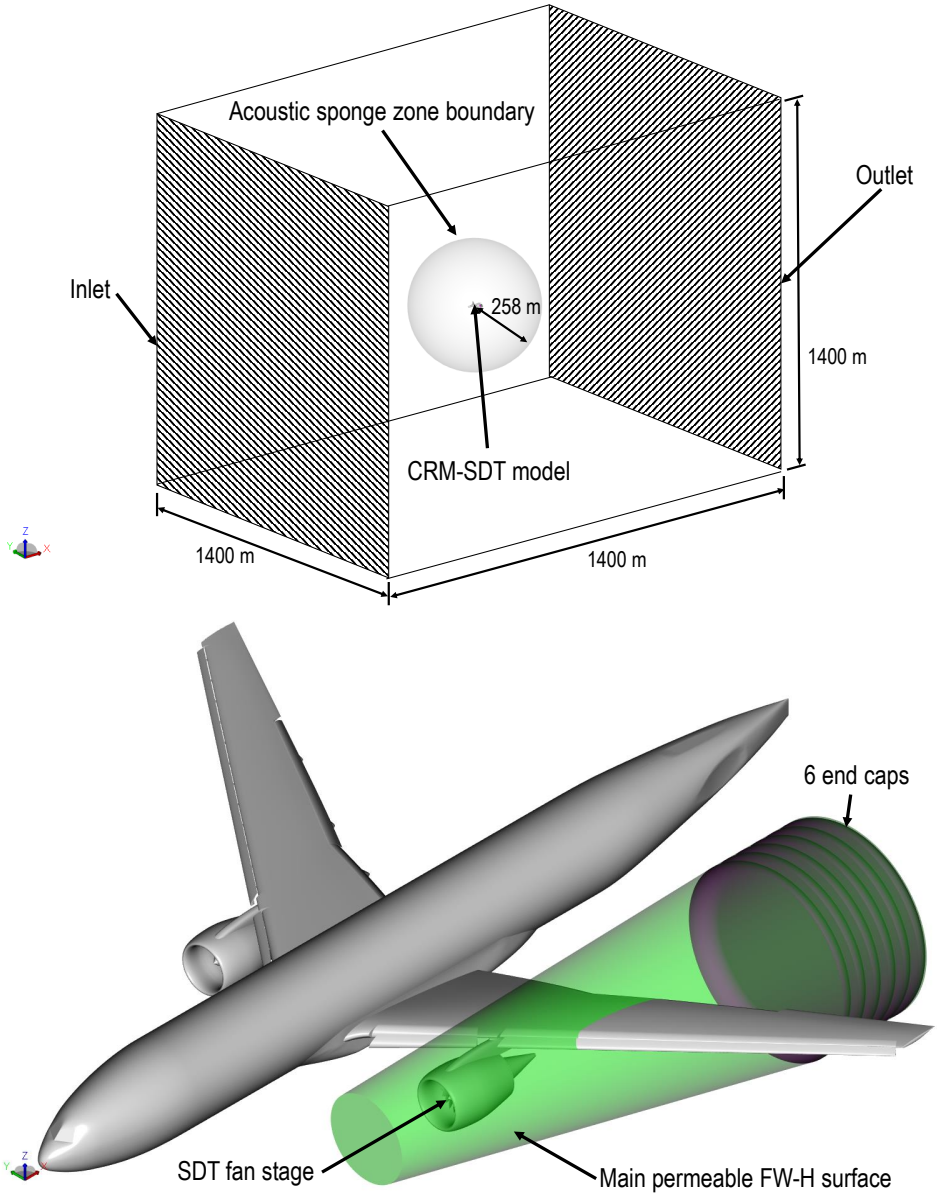

Figure 5.26: (Top) The simulation domain enclosing the CRM/SDT model. (Bottom) The configuration of permeable FW-H surface for noise analyses.

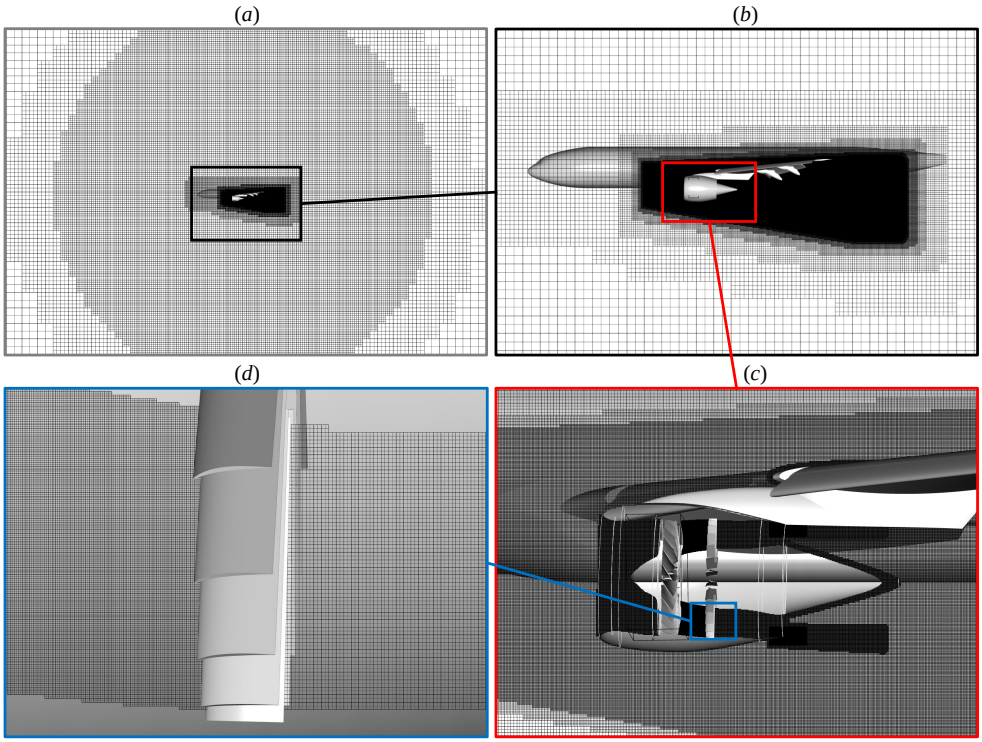

Figure 5.27: The voxel distribution in the simulation domain: (*a*) near the borders of the acoustic sponge boundary; (*b*) surrounding the airframe; (*c*) surrounding the SDT fan stage; (*d*) near the OGVs.

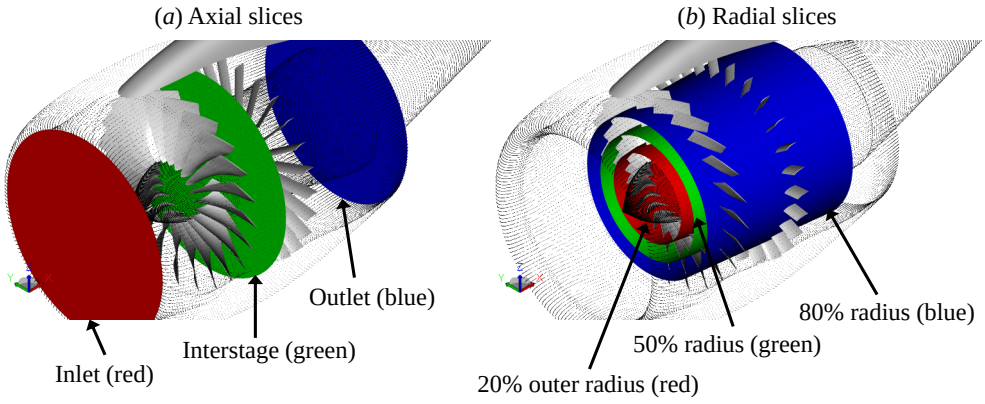

Figure 5.28: A sketch of the slice planes that will be used for plotting contours in the subsequent figures.

5.2.2. FLOW FIELD STATISTICS AND AERODYNAMIC PERFORMANCE

The effects of the porous treatments on the aerodynamics in the fan stage are discussed in this subsection. Flow information have been sampled inside the fan stage using several slice planes that are introduced in figure 5.28. Figure (*a*) shows 3 axial slices corresponding to the locations of the turbofan intake, the interstage, and the turbofan outlet. The interstage slice is located halfway between the fan and the OGVs. Aside from the axial slices, radial slices are positioned at 10 %, 45 %, and 80 % of the outer radius of the fan stage, as shown in figure (*b*).

Firstly, phase-locked velocity statistics at the turbofan inlet, interstage, and outlet are shown in figures 5.29 and 5.31. The velocity values have been normalised against the reference velocity $U_{\text{ref}} = 237.57\,\text{m/s}$ (i.e., fan tip velocity). Due to the aircraft's incidence relative to the freestream, the velocity at the fan-stage inlet is not uniform. The flow at the lower side of the inlet has a higher velocity than the upper side. Compared to the baseline, the average inlet velocity for the modified case is slightly lower, suggesting that the air throughput of the fan stage decreases due to the poro-serrated OGVs. The spiral patterns associated with the radial variation of velocity in the fan wake can be clearly observed in the contours at the interstage. Expectedly, the average velocity for both modified configurations at this location is also slightly lower than the baseline one. A more noticeable discrepancy can be found at the outlet of the turbofan, where the velocity magnitude near the hub for the M800 case is around 10 % lower than that of its baseline counterpart. A similar trend can be found for the M450 case although the velocity reduction is slightly less severe. Since the fan RPM remains the same in all configurations, it is likely that the poro-serrations have introduced an additional aerodynamic resistance inside the fan stage, which would impose a penalty on the overall fan stage performance.

The thrust produced by the fan stage has been computed using the following general thrust equation.

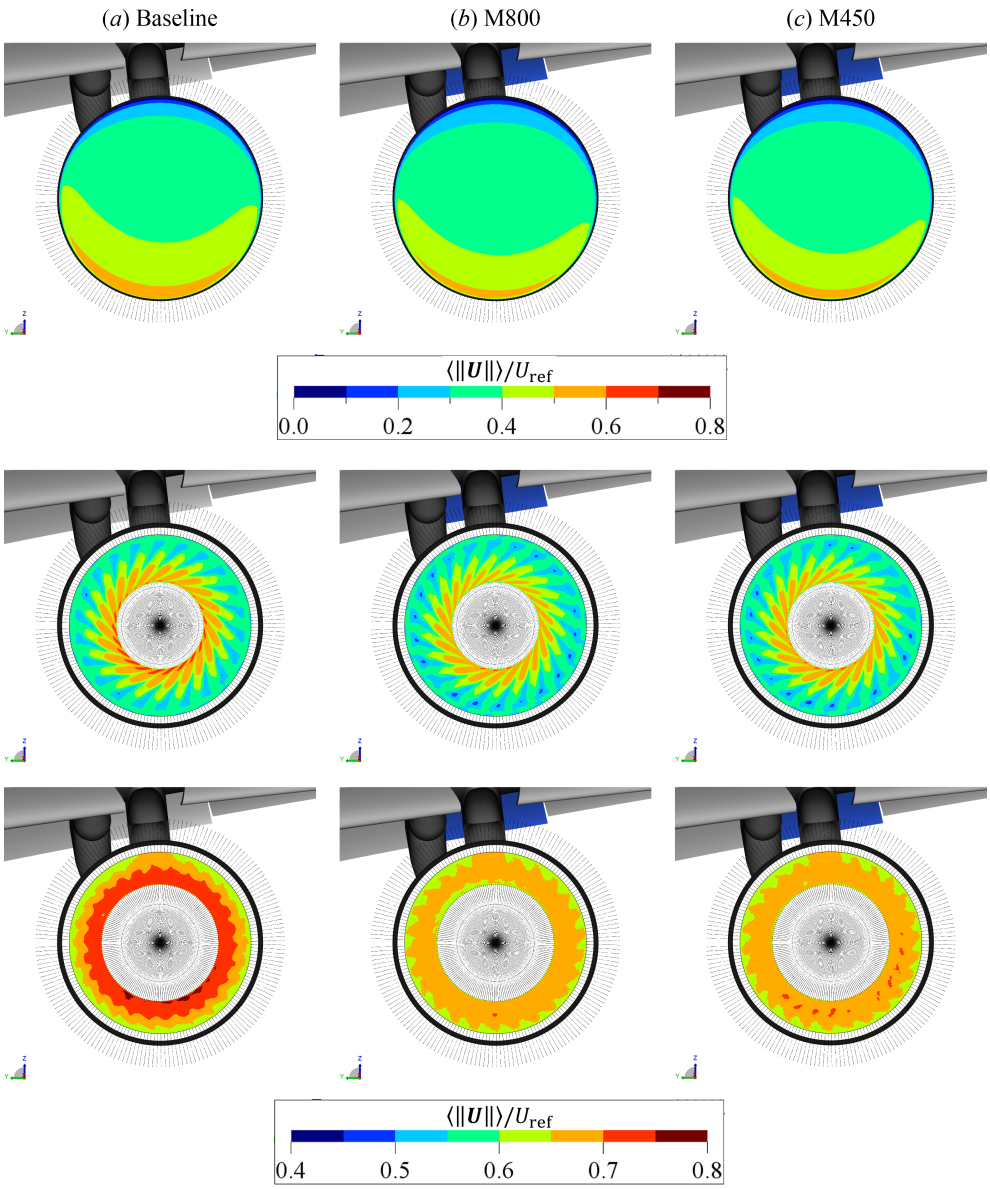

Figure 5.29: (Front view) Contours of phase-locked average of velocity magnitude $||\boldsymbol{U}||$ at the SDT inlet (top row), interstage (middle row), and outlet (bottom row).

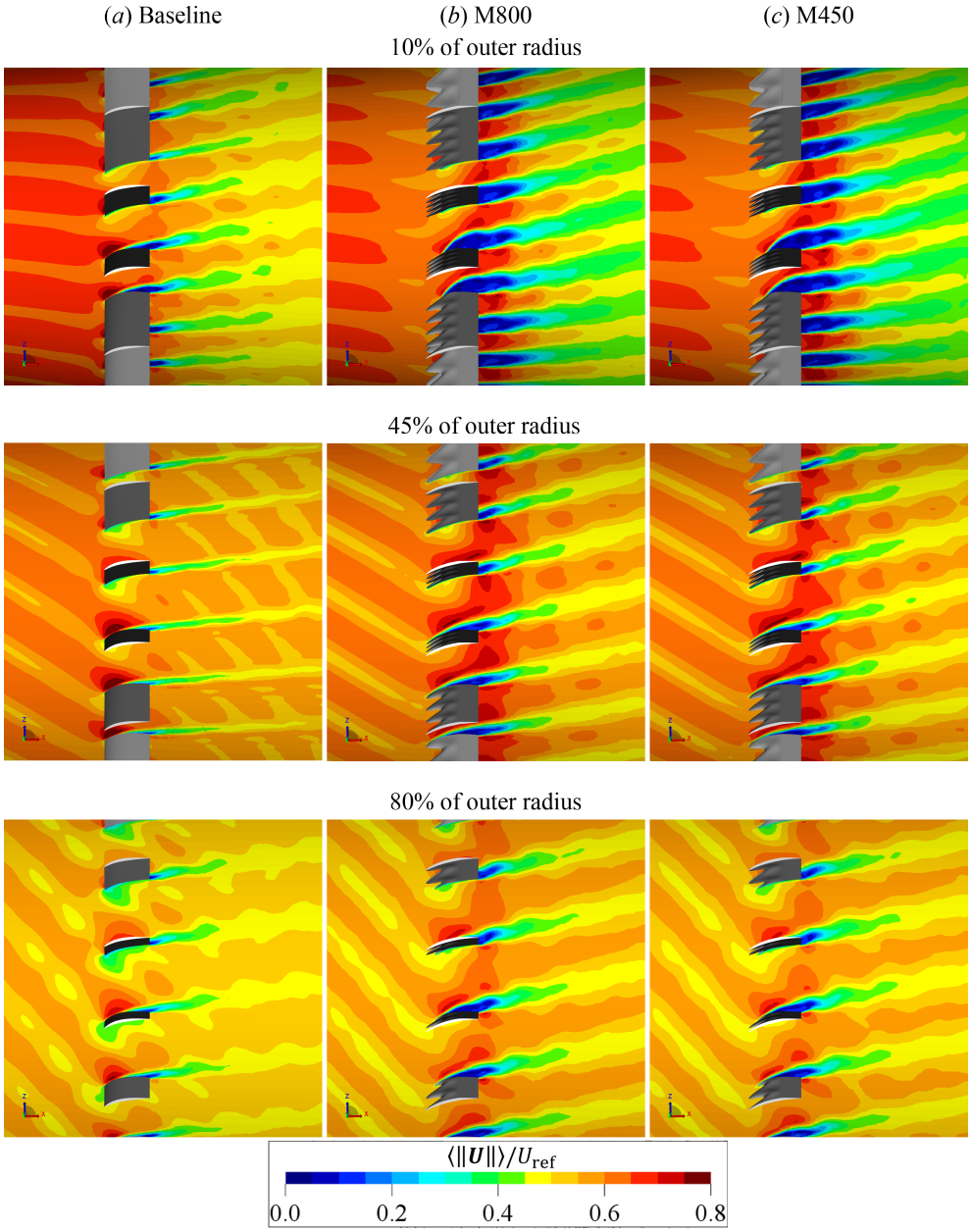

Figure 5.30: (Side view) Contours of phase-locked average of velocity magnitude $||\boldsymbol{U}||$ at the different radial sections in the fan stage.

$$\text{Thrust} = \left(\dot{m}_{\text{outlet}} U_{x,\text{outlet}} - \dot{m}_{\text{inlet}} U_{x,\text{inlet}}\right) + \left(p_{\text{outlet}} - p_{\text{inlet}}\right) A_{\text{outlet}} \tag{5.5}$$

The mass flow at the inlet $\dot{m}_{\text{inlet}}$ is equal to that at the outlet $\dot{m}_{\text{outlet}}$ as the SDT configuration lacks a core stage, and thus the thrust contribution from the first term of equation 5.5 is only due to the average axial velocity (U_x) difference between the fan-stage inlet and outlet. The second term in equation 5.5 refers to the pressure-area term, with A_{outlet} being the cross-section area of the fan-stage outlet.

In the present study, the baseline configuration is found to generate 70.64 kN of thrust from which 12.7 % comes from the pressure-area term. Given that the fan currently operates at 61.7 % of the maximum rotational speed [15], it is estimated that the maximum thrust of the fan stage is 325 kN following a typical RPM-thrust curve for a turbofan engine [37]. This amount is comparable to the take-off thrust rating of Trent 1000 turbofan [38]. In comparison, the thrust produced by the M800 configuration is smaller at 64.22 kN, where the pressure-area term has a contribution of 11.6 % out of the total thrust amount. Consequently, the usage of the poro-serrated OGVs has lead to a 9 % thrust penalty, which is rather substantial. Assuming that the thrust penalty does not change for a small increase in fan RPM and the RPM-thrust relations of both the baseline and the modified fan stages remain identical, it is estimated that the fan of the M800 configuration should operate at 1462 RPM (i.e., an increase of 1.8 % over that of the baseline) to retain the same thrust level as that of the baseline. By using the modified OGVs with lower porosity (M450), the thrust reduction is milder at 7.5 %, which can be compensated by increasing the fan rotational speed by 1.5 % to 1454 RPM.

Contours depicting the phase-locked average flow field are also plotted at the radial slices in figure 5.30. In the contours, the swirling wake patterns downstream of the fan blades can be clearly seen, especially at the outermost radial section. At the top row of the figure (the slice at 10 % of the outer radius), it is evident that the wake region downstream of the poro-serrated (modified) OGVs has a lower average velocity compared to that of the baseline. This behaviour is due to the flow separation at the suction side of the OGVs. Consequently, the recovery of swirl in the fan wake is less efficient in the modified configurations, as illustrated by the larger inclination of the OGV wake relative to the axial direction. Since the separation originates above the porous-medium region, it is likely to be driven by a mean cross-flow through the poro-serrations (see also the velocity contour for 5406-PLE configuration in figure 4.7). The same phenomenon can still be found at other radial positions, although the flow separation on the OGVs becomes less severe further away from the hub. At 45 % of the outer radius (the middle row of figure 5.30), the width of the wake behind the poro-serrated OGV is only slightly larger than that of the baseline. Nevertheless, the wider wake downstream of the poro-serrated OGVs still leads to an overall reduction in the axial velocity component at the fan stage outlet as previously shown in figure 5.29.

The impact of the poro-serrations on the fluctuating components of the flow field can be examined using the contours of mean-removed RMS (standard deviation) of velocity magnitude $||\boldsymbol{U}_{\text{RMS}}||$ in figures 5.31 and 5.32. The first figure shows the contours for the axial slice planes at the interstage and outlet locations. The contours at the interstage of the three configurations are relatively similar, suggesting that the turbulence in the fan

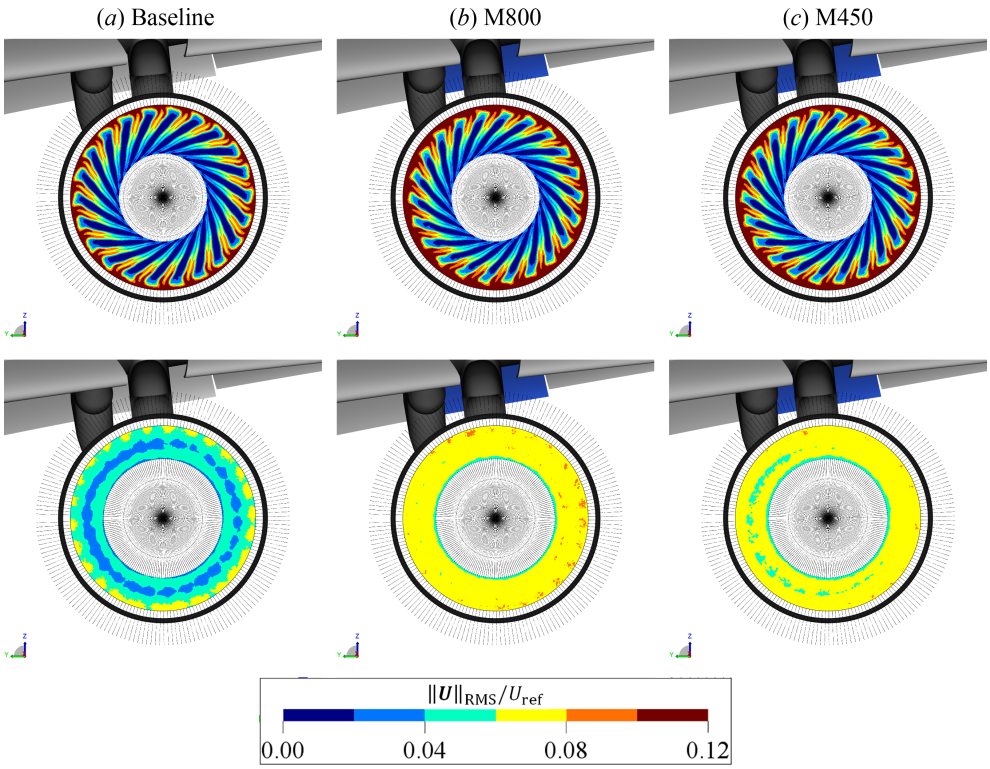

Figure 5.31: (Front view) Contours of phase-locked standard deviation of velocity magnitude $||\boldsymbol{U}_{\mathrm{RMS}}||$ at the SDT interstage (top row) and outlet (bottom row).

wake is not significantly affected by the installation of the porous treatment. Stronger velocity fluctuations are generally found further away from the hub where the local tangential velocity, and in turn the local Reynolds number, is higher. Nonetheless, the contours at the fan stage outlet clearly shows that the flow leaving the OGVs contains higher turbulence intensity. Interestingly, the $||\boldsymbol{U}_{\mathrm{RMS}}||$ levels in both configurations are slightly higher towards the right side of the figure (e.g., port side of the aircraft). This non-uniformity seems to be the consequence of the flow condition at the inlet (see figure 5.29), which is related to the aircraft incidence relative to the freestream.

Figure 5.32 illustrates the $||\boldsymbol{U}_{\mathrm{RMS}}||$ contours at the radial slices. The contour at 10 % of the outer radius depicts the flow separation originating from the poro-serrations of the M800 and M450 configurations, which results in a dramatic increase in velocity fluctuations level downstream of the OGVs. Similar situations can be found at other radial locations, which are also associated with the mean cross-flow through the poro-serrations. In comparison to the M800 configuration, the flow separation on the poro-serrations with lower porosity (M450) is slightly milder, indicated by the lower $||\boldsymbol{U}_{\mathrm{RMS}}||$ levels at the downstream end of the contours. Nonetheless, both types of poro-serrated OGVs enhance the velocity fluctuations at locations slightly upstream of

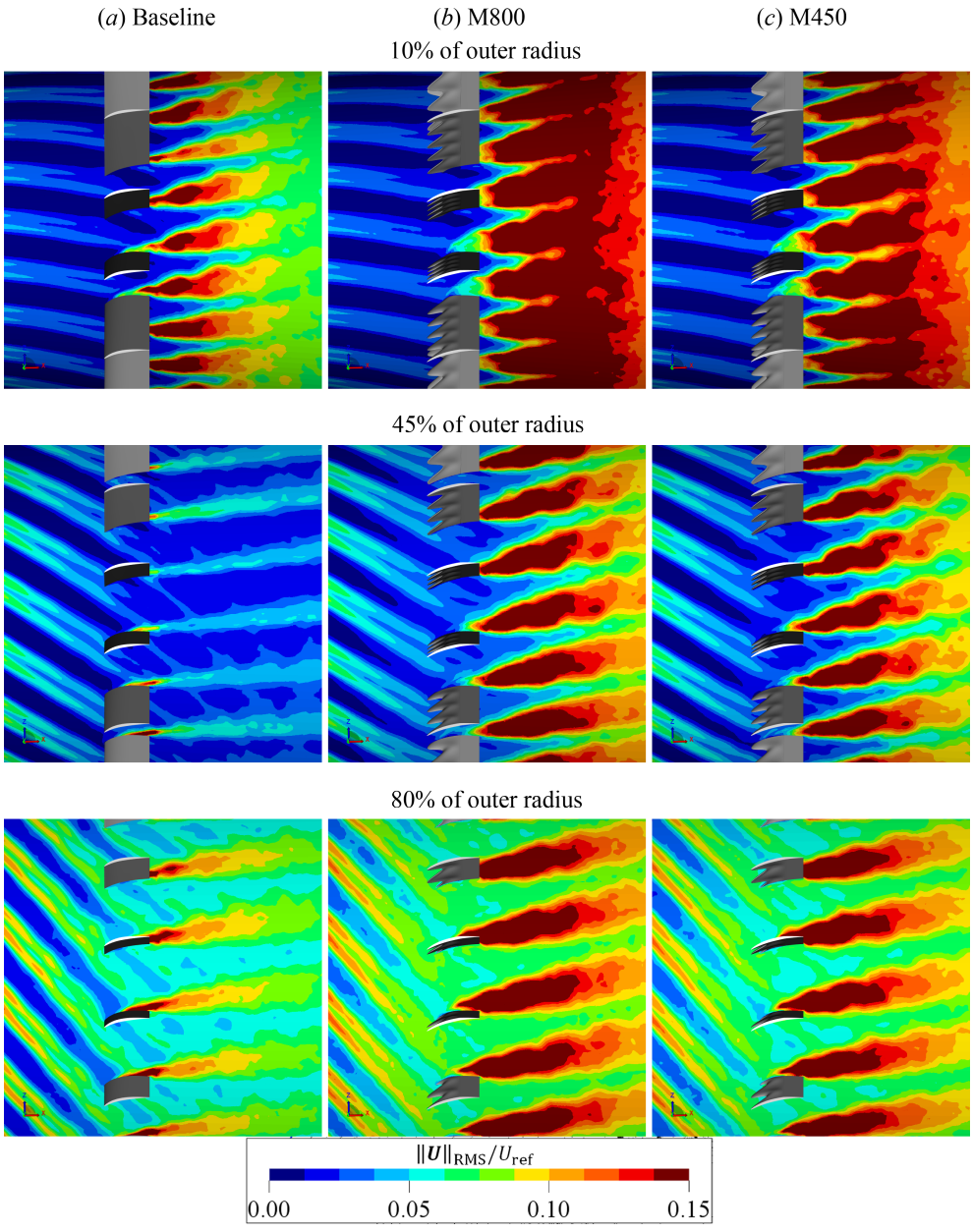

Figure 5.32: (Side view) Contours of phase-locked standard deviation of velocity magnitude $||\boldsymbol{U}_{\mathrm{RMS}}||$ at the different radial sections in the fan stage.

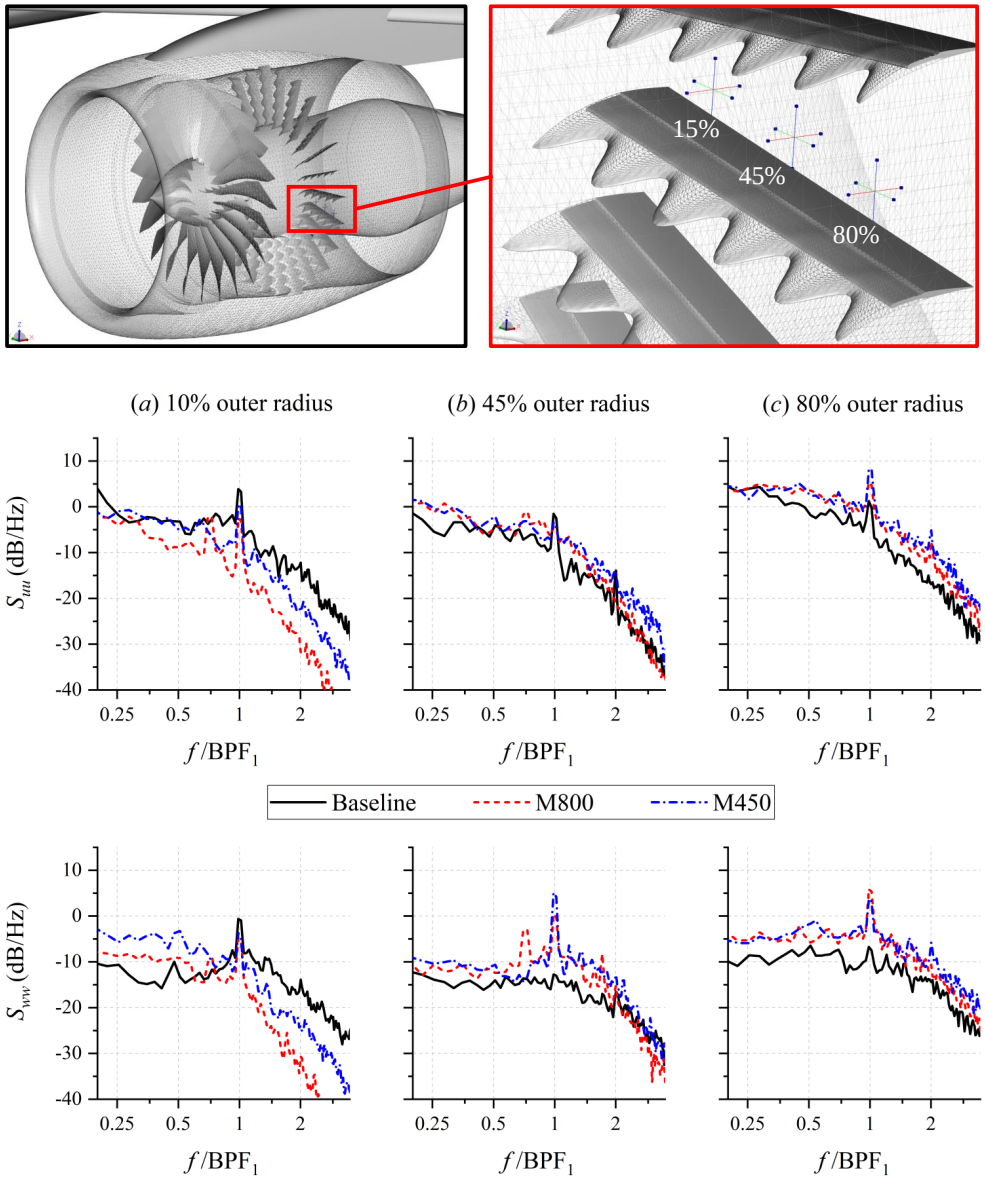

Figure 5.33: Plots of axial (S_{uu}) and tangential (S_{ww}) velocity fluctuations spectra at a height of 50 mm (0.23c) above the OGV TE. The power spectral density is normalised against a reference velocity of 1 m/s.

the poro-serrations (i.e., the interstage), especially at the outer radius of the fan stage.

The spectral contents of the flow field near the OGV surface are examined in figure 5.33. Velocity fluctuations spectra in the figure have been sampled at a distance of 50 mm above the OGV TE. At 10 % of the outer radius, there appears to be a shift in the turbulent kinetic energy from the higher frequencies to lower ones in the M800 and M450 cases. This behaviour is particularly noticeable for the S_{ww} component, which can be associated with the unsteady upwash due to the flow injection at the suction side of the poro-serrations. The M450 configuration also exhibits higher axial and tangential velocity fluctuations compared to those in the M800 case at this radial position, reflecting the contours in figure 5.32. However, both S_{uu} and S_{ww} spectra of the M800 case show a tonal peak at $f/\mathrm{BPF}_1 = 0.71$. The same peak is still present in the S_{ww} plot at 45 % of the outer radius, but for the M450 one, the tonal peak is completely absent. It is worth mentioning that the frequency of the tonal peak corresponds to a Strouhal number of approximately 0.1 when it is normalised with the mean velocity magnitude upstream of the poro-serrated OGV and the maximum blade thickness. Thus, it is likely that the peak is linked to a vortex shedding phenomenon at a solid-porous junction, similar to that previously reported by Carpio *et al.* [39]. Both M800 and M450 configurations exhibit almost identical spectra at 80 % of the outer radius, whose levels are generally higher than those of the baseline, particularly for the tangential velocity component. At 80 % of the outer radius (plot *c*), both M800 and M450 configurations exhibit almost identical spectra, although the velocity fluctuations are generally stronger in the latter at frequencies above BPF_1.

The effect of the porous treatments on the OGV's loading characteristics can be examined using figure 5.34 that shows the distributions of time-averaged surface pressure ($C_{p,\mathrm{mean}}$) and the RMS of surface pressure fluctuations $C_{p,\mathrm{RMS}}$ at different radial positions. The time-averaged surface pressure is expressed as $C_{p,\mathrm{mean}} = (\langle p \rangle - p_\infty)/(0.5\rho_\infty U_{\mathrm{ref}}^2)$, where $p_\infty = 101{,}325\,\mathrm{Pa}$. Meanwhile the RMS of surface pressure fluctuations is expressed as $C_{p,\mathrm{RMS}} = p_{\mathrm{RMS}}/(0.5\rho_\infty U_{\mathrm{ref}}^2)$.

For the baseline case, it is evident that the largest aerodynamic loading is generated at the LE region of the blade. At 10 % of the outer radius, the flat $C_{p,\mathrm{mean}}$ distribution on the aft segment at the suction side of the baseline OGV ($0.6 < x/c < 1$) indicates flow separation, although it appears to be absent at other radial locations. On the modified OGV, flow separation takes place at a location further upstream (near $x/c = 0.4$), which is closer to the solid-porous junction. Although this radial position roughly coincides with the serration root of the modified OGV, its suction peak is weaker compared to that of the baseline. This is caused by a pressure balancing process across the porous medium, which has been previously observed in the porous LE application for the rod-airfoil configuration (see figure 4.23). At 45 % of the outer radius, the $C_{p,\mathrm{mean}}$ distribution at the suction side of the baseline OGV is no longer showing any indication of flow separation, which is in contrast to the flat pressure distribution of the poro-serrated OGV at $x/c > 0.4$. This radial location is also where a serration tip can be found. As expected, the pressure difference between the suction and pressure sides of the poro-serrated LE is smaller for the M800 case, which has a higher porosity than the M450 one. The $C_{p,\mathrm{mean}}$ distribution at the pressure side of the poro-serrated OGV also evidences stronger flow acceleration with respect to that of the baseline, which is caused by the constriction of the inter-OGV

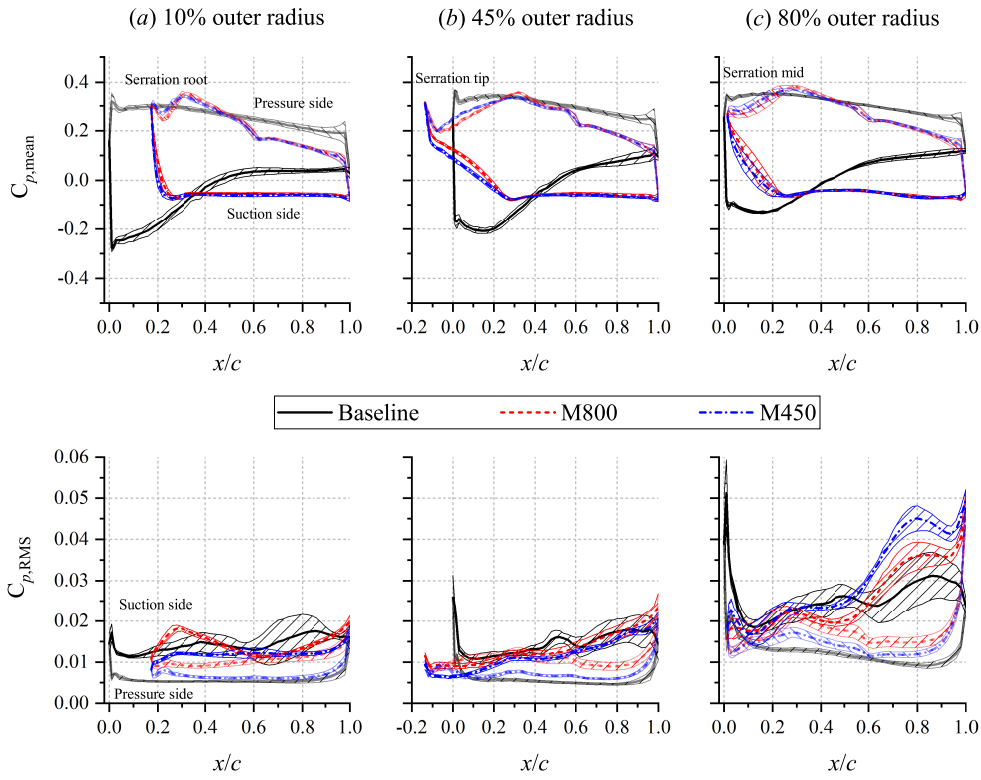

Figure 5.34: Plots of (top row) time-averaged surface pressure coefficient and (middle row) RMS of surface pressure fluctuations. The pressure distributions at the pressure side are plotted with lower opacity. The standard deviation of the pressure distributions on the different OGV blades is indicated by the shaded region.

channel due to the separated-flow region. The surface pressure distributions at 80 % of the outer radius also show similar trends as the previous ones.

The lower half of figure 5.34 shows the intensity of surface pressure fluctuations on the OGV in the baseline case, a noticeable peak can be found near the OGV LE, but it is absent in configurations with poro-serrated OGVs; this resembles the behavior observed in the rod-airfoil configuration (see figure 4.18). However, the $C_{p,\mathrm{RMS}}$ levels on the suction side of the poro-serrated OGVs tend to be stronger than the baseline ones near the TE, and such discrepancies are the most noticeable towards at the outer radius of the fan stage. This phenomenon can be attributed to the flow separation, which would induce a stall-noise mechanism [40] that results in the enhanced broadband noise generation in the low-frequency range. Comparing the $C_{p,\mathrm{RMS}}$ distributions between the M800 and M450 configurations, the former tends to induce stronger surface pressure fluctuations at the inner radial positions. However, the situation is reversed closer to the tip of the OGV blade, and thus, it is conjectured that the permeability of the poro-serrations should increase with the outer radius in order to minimise the intensity of the surface pressure fluctuations across the OGV span.

5.2.3. FAR-FIELD NOISE CHARACTERISTICS

The effects of the porous treatments on the noise emission characteristics of the CRM/SDT configuration are discussed in this subsection. Figure 5.35 provides the far-field noise spectra measured at two reference locations, namely *approach* and *lateral*, following the noise certification procedures outlined in ICAO Annex 16 [41]. On average, the sound intensity at the *approach* location is 12 dB higher than the *lateral* one, which is roughly equal to the difference following the spherical-spreading assumption. A closer look at the spectra reveals that the porous treatments manage to substantially mitigate the tones at BPF_1, BPF_2, and BPF_3. However, the modified configurations also enhance the broadband noise component, mainly at frequencies below BPF_2.

Similar conclusions can be made using the source power (PWL) spectra plots in figure 5.36 (*a*). The OPWL (overall-PWL) discrepancies between the modified configurations and the baseline are relatively small, but as shown in figure 5.36 (*b*), this is due to the fact that the reduction of PWL at the BPFs has been counteracted by the increased broadband PWL. The plot also indicates that the changes in the PWL components are proportional to the porosity of the poro-serrations. In figure 5.36 (*a*), the PWL values for both M800 and M450 configurations are higher than the baseline by up to 5 dB at frequencies around $0.3 < f/BPF_2 < 0.7$ and $1 < f/BPF_2 < 1.3$. On the other hand, the intensity of tonal peaks at BPF_1, BPF_2, and BPF_3 have been reduced significantly. Following the discussions in the previous subsection, the enhanced broadband noise emission of the modified configuration is linked to the flow separation at the suction side of the poro-serrated OGV [42]. The M800 configuration exhibits additional tones that do not fall under the harmonics or subharmonics of BPF_1. These can be found at $f/BPF_1 = 0.71$, 1.33, 1.48, and 1.71; the last one has a peak intensity that is similar to that of BPF_2 of the baseline configuration. These additional tones are absent in the M450 configuration, which leads to a lower OPWL value relative to that of the M800 configuration. Based on the analysis in figure 5.33, these tones are associated with the vortex shedding at the solid-porous junction of the poro-serrated OGV. Above BPF_2, both modified setups have very similar PWL distributions, which show an average of 1 dB reduction compared to that of the baseline.

The far-field directivity of the CRM/SDT setup is shown in figure 5.37, where the OSPL values at a distance corresponding to the *approach* reference location have been computed along an arc on the lateral plane of the aircraft. In the plot, the aircraft nose is aligned with the 180° angle. The noise coming from the aircraft is predominantly radiated towards the upstream and downward directions, which can be attributed to the shielding effect from the wing since the engine is mounted underneath it [43]. The plot evidences that the M800 and M450 configurations produces 1 to 2 dB of OSPL increase relative to the baseline configuration, except at angles in between 310° and 330° where up to 2.5 dB of noise reduction can be observed.

The noise directivity analysis is expanded in the lower part of figure 5.37 where the directivity patterns have been plotted at frequency bands that have been denoted in figure 5.36 (*a*). In plot A, which corresponds to the frequency band $0.35 < f/BPF_1 < 0.75$, the M800 case is found to cause a substantial noise increase ($\approx$ 2.5 dB) in almost all observer directions. Similar behaviour is present in plot B, but the excess noise is present only in directions normal to the fan stage axis. The M450 also exhibits comparable

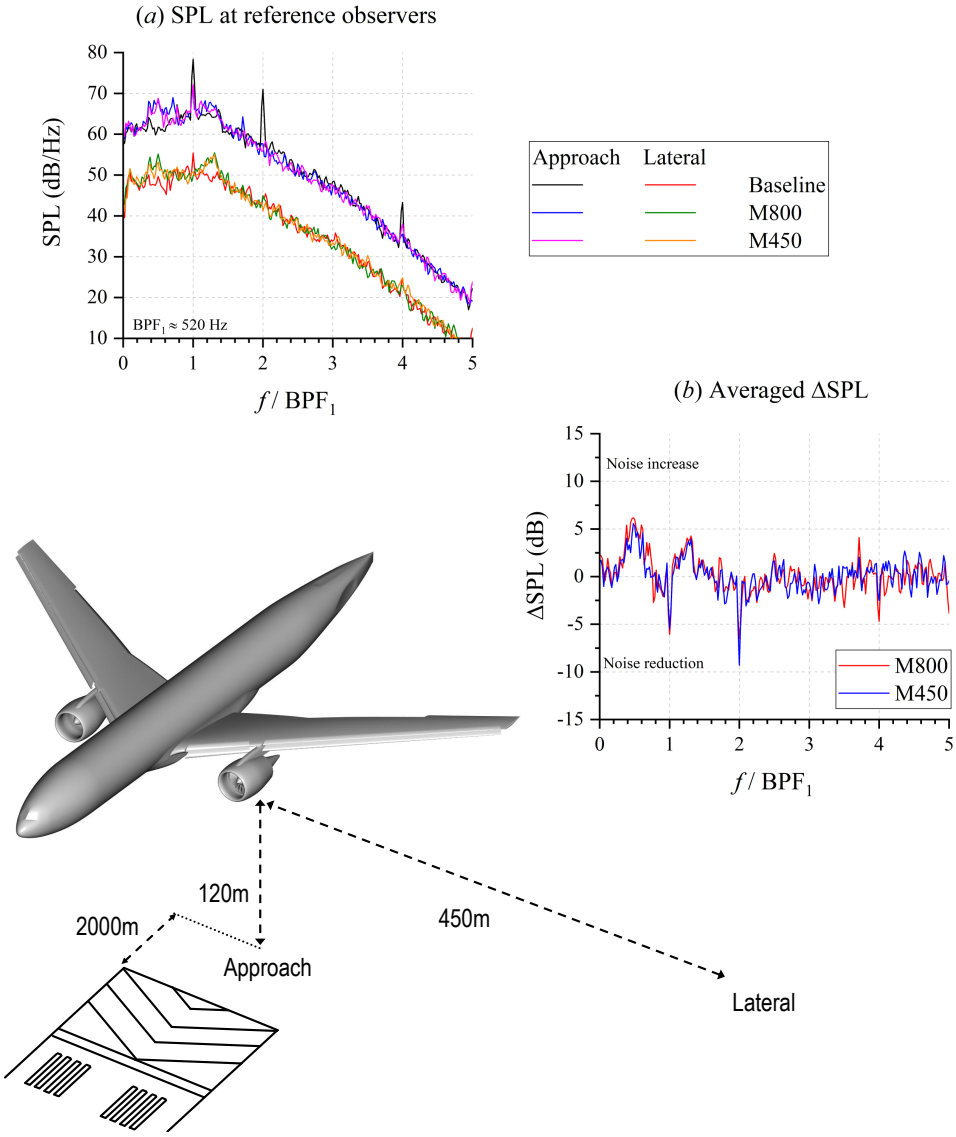

Figure 5.35: (*a*) The sound pressure level (SPL) at reference noise measurement distances following ICAO Annex 16 [41] and (*b*) the SPL difference between the baseline and the two modified cases. Note that the dimensions in the illustration at the lower right of the figure are not to scale.

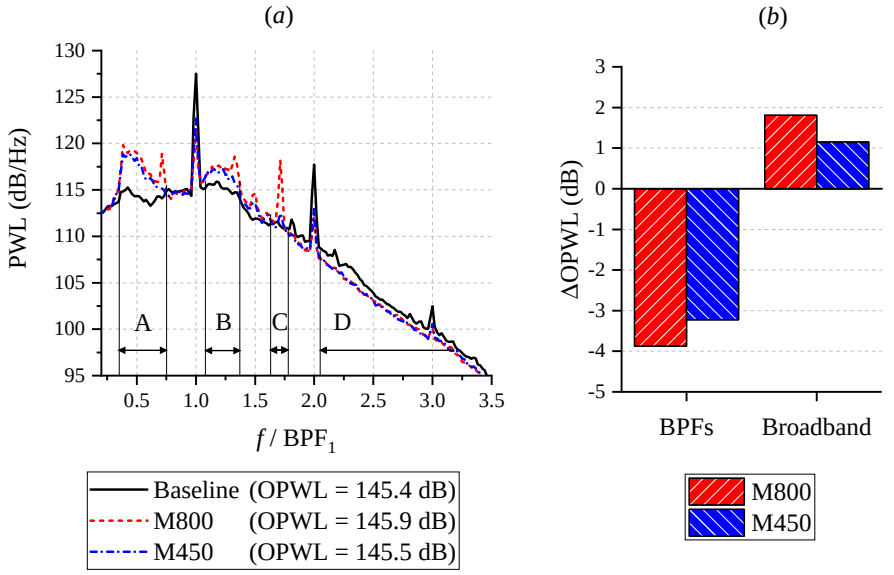

Figure 5.36: (*a*) Source power level (PWL) of the CRM/SDT configuration. The capital letters denote the frequency ranges where the directivity patterns are plotted in figure 5.37. Plot (*b*) shows the OPWL difference between the modified configurations and the baseline, divided into two categories: BPFs (the tonal peaks BPF_1 to BPF_3) and broadband (the broadband noise component and other tones up to $f/BPF_1 = 3.5$).

directivity patterns as the M800 one, but the noise increase relative to the baseline is milder. The frequency range in plot C is associated with the additional tone near f/BPF_2 that is present in the case of M800 configuration. This tonal noise component is mainly radiated towards the upper- and lower-upstream directions, similar to the trends in plot B. Unlike the others, plot D corresponds to the broadband noise reduction in the high-frequency range, which is concentrated in the lower downstream direction.

It is also interesting to evaluate the impact of the porous treatments on the noise footprint of the aircraft, taking the response of human hearing system into account. As a matter of fact, normal human hearing is generally the most sensitive to sound in the frequency range in between 2 and 4 kHz [41]. Additionally, the tonal noise component usually induces a stronger annoyance than the broadband one. Aside from the spectral features, the directivity of the noise source and the flight path of an aircraft can affect the perceived noise at different observers on the ground. All of these aspects have been considered in the process of aircraft noise certification using the effective perceived noise level (EPNL) metric. For a given aircraft flyover trajectory, the EPNL is computed following several steps that are briefly outlined in the following:

1. The recorded noise signal is split into multiple segments, each of which has a duration of 0.5 s.

2. The sound pressure spectra (in SPL) are computed for each segment, and the SPL values are converted into perceived noise level (PNL) by applying an equal-loudness weighting.

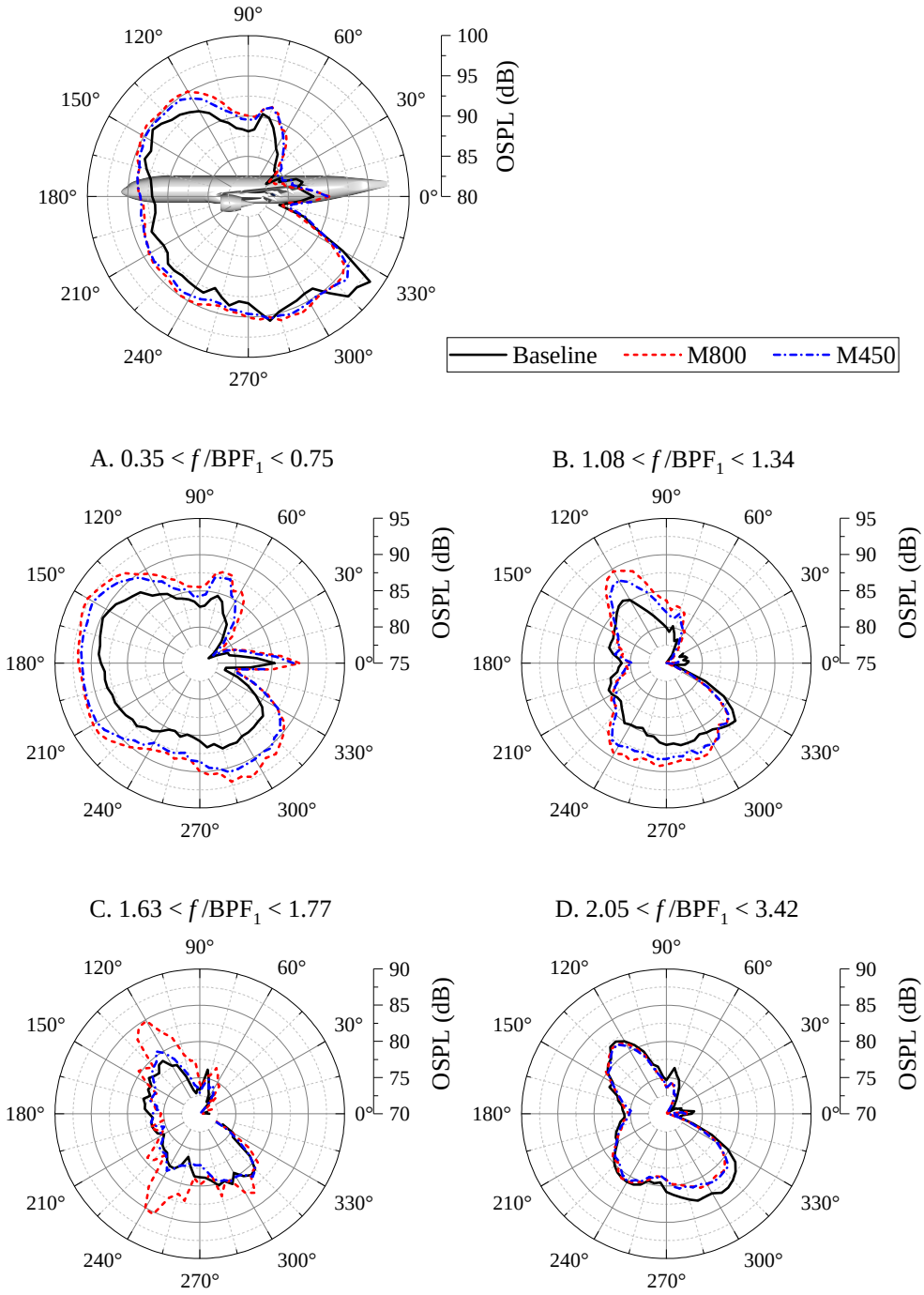

Figure 5.37: The noise directivity pattern along the lateral axis. Directivity plots are also provided at frequency bands where notable discrepancies between the modified and baseline configurations are present in figure 5.36.

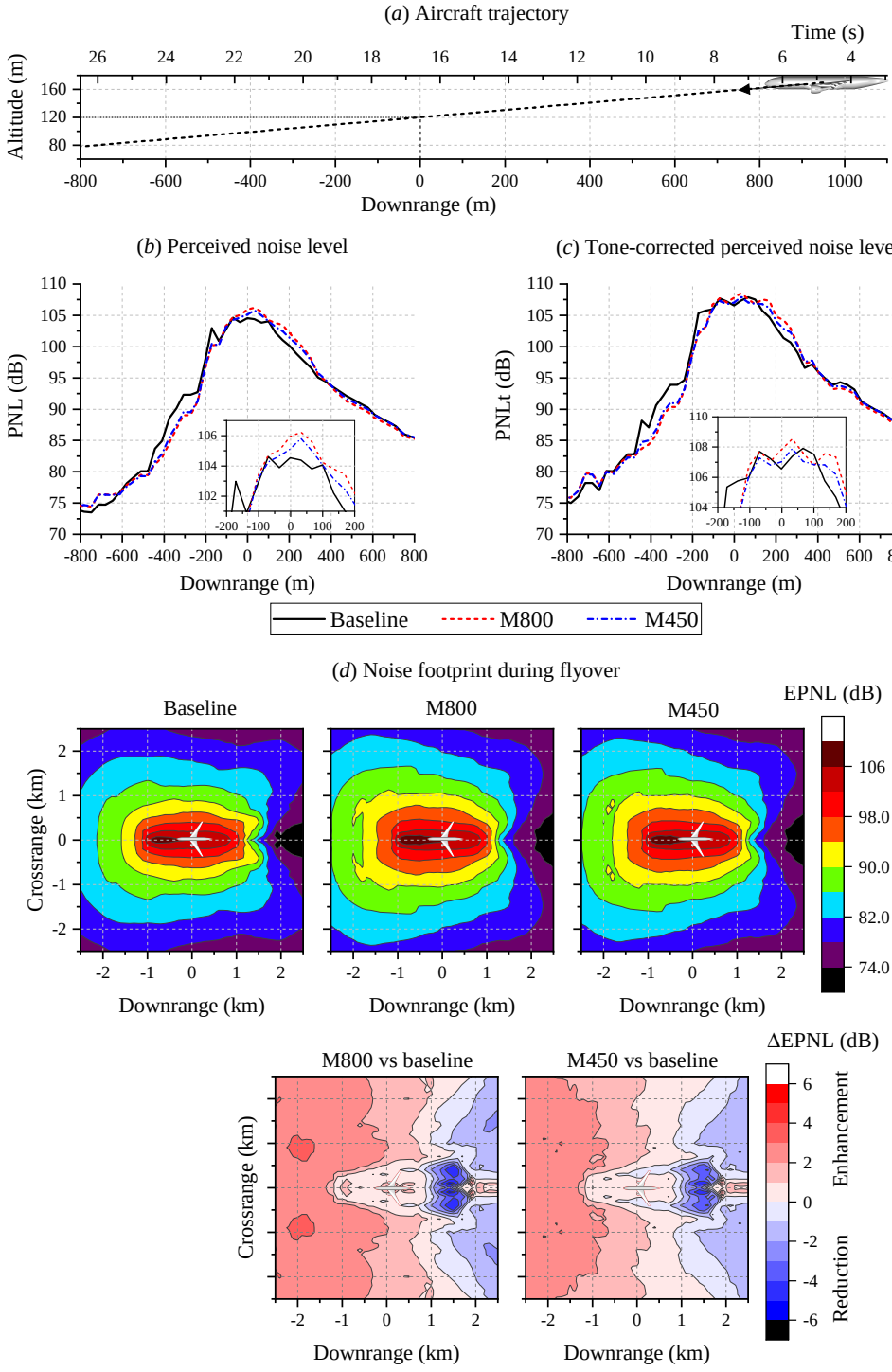

Figure 5.38: (*a*) The aircraft trajectory for noise footprint analysis. (*b*) The variation of perceived noise level (PNL) and (*c*) the tone-corrected PNL (PNLt) for a reference aircraft approach scenario. The noise footprints during the flyover are given in (*d*). The reference flyover microphone is located at the origin of the downrange axis, where the aircraft altitude is 120 m.

3. A penalty is applied into the PNL values for each tone that is present in the spectra, resulting in tone-corrected PNL (PNLt).

4. The EPNL (effective PNL) is obtained by applying a duration correction based on the length of time during which the recorded PNLt value is within 10 dB from the maximum level (i.e., 10-dB-downtime).

In the present analysis, the aircraft assumes an approach trajectory as illustrated in figure 5.38 (*a*). The aircraft is on a standard descending flight path with a glide slope of 3 degrees, which translates into a rate-of-descend of 3.56 m/s. Although there is only a single SDT fan stage installed on the CRM model, the overall aircraft noise is estimated by mirroring the noise contribution from the SDT along the longitudinal axis of the fuselage. This is equivalent to assuming that the CRM model is equipped with two fan stages. The aircraft noise emission is evaluated with respect to the "approach" reference location, where the aircraft altitude is 120 m during the flyover. The microphone location is indicated as the zero downrange position in figure 5.38.

The PNL and PNLt values measured at the reference microphone as the aircraft travels along its trajectory are shown in figure 5.38 (*b*) and (*c*) respectively. As the aircraft approaches the microphone (e.g., at positive downrange coordinates), the M800 and M450 configurations produce higher PNL and PNLt values than the baseline one. This behaviour is related to the low-frequency broadband noise increase with a relatively uniform directivity (see figure 5.36 A.). In plot (*b*), the PNL of the M450 case is slightly lower than the M800 one where the difference is ≈ 1 dB, but the discrepancies between the two are more noticeable in terms of PNLt (plot (*c*)), since the M800 configuration generates extra tones that are absent in the M450 case. The peak of the PNL and PNLt curves is located near the flyover position. Although the peak PNL intensities of the modified configurations are up to 2 dB higher than the baseline one, the peak PNLt values of the three are relatively similar. The difference between the PNL and PNLt values is due to the reduction of the tonal noise component at BPF_1 and its harmonics by the poro-serrations. Once the aircraft travels further away from the reference location, a substantial reduction in the PNL can be observed between the downrange coordinates of -200 m and -500 m. This is related to the far-field directivity patterns in figure 5.36 (*b*), where noise reduction of the can be observed in the lower downstream direction.

The noise footprint of the aircraft (e.g., the noise level measured on the ground surrounding the aircraft flight path) is plotted in figure 5.38 (*d*) in term of EPNL. While the footprint has been computed on a square grid of 2.5 km by 2.5 km, note that the simulation only considers a downrange distance in between -850 m to 850 m. It is evident that the noise radiation in the upstream direction becomes more intense in both modified cases (M800 and M450), while EPNL reduction is present only in the downstream direction. The noise contours also show that the noise increase is more severe in the M800 case than the M450 one, which is expected based on the comparison of the source power spectra in figure 5.36. Based on the contours, the EPNL values at the *approach* reference location are 105.9 dB, 106.8 dB, and 106.2 dB for the baseline, M800, and M450 configurations respectively. These values are comparatively higher than the *approach* EPNL of a similar class of aircraft, such as a Boeing 777-300ER, which has an EPNL of 100.5 dB [44].

5.3. SUMMARY

This chapter has presented the applications of porous treatments in more complex setups than those in earlier parts of this dissertation. The first half of the chapter revolves around the numerical characterisation of a rod-linear cascade (RLC) model as an extension to the RAC. The usage of a blade row instead of an isolated airfoil is necessary to realise a high-solidity environment that is typical in turbomachinery. Similar as in the RAC, the rod in the RLC sheds turbulent wake that impinged onto the leading edge of the central blade, leading to noise scattering. However, the cascade arrangement is found to significantly influence the sound propagation to the far field. Furthermore, it may have been responsible for inducing acoustic resonance at a frequency that is relatively close to the vortex-shedding frequency, evidenced by the high pressure fluctuations levels in all inter-blade channels, even though only the central blade is subjected to the rod wake impingement. When a porous treatment, which is modelled after a metal foam with a mean pore diameter of 800 µm, is employed at the leading edge of the central blade, a noticeable noise reduction is achieved only in the high-frequency range. However, it also lowers the aerodynamic loading produced at the leading edge of the central blade, similar to the previous observations using the RAC.

A porous leading-edge treatment is subsequently applied in a full-scale aircraft simulation. The aircraft model is equipped with a fan stage that is based on the NASA-Glenn Source Diagnostic Test (SDT) rig. The outlet-guide-vanes (OGV) of the fan stage are modified to include poro-serrations to mitigate the fan wake-OGV interaction noise. The poro-serrations are modelled after a metal foam with two different mean pore diameters, namely 800 µm (M800) and 450 µm (M450). The modified OGVs are found to mitigate the intensity of tones at the blade-passage frequency (BPF) and its harmonics. However, they also cause a substantial increase in broadband noise level, and in the case of M800 configuration, additional tones associated with a vortex-shedding phenomenon are generated. As a consequence, the overall source power level of the modified fan stage is relatively unchanged from the baseline. The pressure balancing process at the poro-serrations causes a severe flow separation at the suction side of the modified OGVs. As a result, the thrust generated by the modified fan stage is slightly decreased relative to that of the baseline. Interestingly, the M450 configuration, despite having a lower porosity compared to the M800 one, exhibits a more favourable trade-off between acoustic and aerodynamic characteristics.

In conclusion, this chapter has demonstrated that the integration of porous leading-edge treatments on a more complex test setup is not straightforward. As a matter of fact, current results have shown that the porous LE modifications have significantly altered the aerodynamic characteristics of the system, undoing the noise reduction benefits as a consequence. Hence, it is likely that the integration of LE modifications will have to be carefully considered from the early stages of design. Nevertheless, it is still worth noting that there are several physical mechanisms that are present in a full-scale aircraft simulation that can be observed using simpler configurations, such as the RLC and RAC. Therefore, these setups are still useful in a parametric study to obtain preliminary insights on the applications of various noise reduction technology.

REFERENCES

[1] C. Teruna, D. Ragni, F. Avallone, and D. Casalino, *A rod-linear cascade model for emulating rotor-stator interaction noise in turbofans: a numerical study,* Aerospace Science and Technology **90**, 275 (2019).

[2] C. Teruna, L. Rego, D. Casalino, D. Ragni, and F. Avallone, *A numerical study on aircraft noise mitigation using porous stator concepts,* Aerospace **9** (2022), 10.3390/aerospace9020070.

[3] M. C. Jacob, J. Boudet, D. Casalino, and M. Michard, *A rod-airfoil experiment as a benchmark for broadband noise modeling,* Theoretical and Computational Fluid Dynamics **19**, 171 (2005).

[4] R. A. Spurr and H. J. Allen, *A theory of unstaggered airfoil cascades in compressible flow*, Tech. Rep. (NASA Ames Research Center, 1947).

[5] S. A. L. Glegg, *Airfoil self-noise generated in a cascade,* AIAA journal **36**, 1575 (1998).

[6] H. H. Hubbard, *Aeroacoustics of flight vehicles: Theory and practice. volume 1. noise sources*, Tech. Rep. (NASA Langley Research Center, Hampton, VA, 1991).

[7] A. Finez, M. Jacob, E. Jondeau, and M. Roger, *Experimental investigation of trailing-edge noise from a linear cascade of cambered airfoils,* in *17th AIAA/CEAS Aeroacoustics Conference (32nd AIAA Aeroacoustics Conference)* (2011) p. 2876.

[8] R. K. Amiet, *Noise due to turbulent flow past a trailing edge,* Journal of sound and vibration **47**, 387 (1976).

[9] J. de Laborderie, V. Blandeau, T. Node-Langlois, and S. Moreau, *Extension of a fan tonal noise cascade model for camber effects,* AIAA Journal **53**, 863 (2014).

[10] H. Posson, S. Moreau, and M. Roger, *On the use of a uniformly valid analytical cascade response function for fan broadband noise predictions,* Journal of sound and vibration **329**, 3721 (2010).

[11] L. Soulat, S. Moreau, and H. Posson, *Wake model effects on the prediction of turbulence-interaction broadband noise in a realistic compressor stage,* in *41st AIAA Fluid Dynamics Conference and Exhibit* (2011) p. 3900.

[12] L. Enghardt, *Improvement of fan broadband noise prediction: Experimental investigation and computational modelling,* Final Project Report: Proband-DLR-WP1-Task **1** (2008).

[13] S. Moreau, *Turbomachinery noise predictions: present and future,* in *Acoustics*, Vol. 1 (Multidisciplinary Digital Publishing Institute, 2019) pp. 92–116.

[14] G. Romani, Q. Ye, F. Avallone, D. Ragni, and D. Casalino, *Fan noise boundary-layer ingestion installation effects for nova aircraft configuration,* in *25th AIAA/CEAS Aeroacoustics Conference* (2019) p. 2429.

[15] R. Woodward, C. Hughes, R. Jeracki, and C. Miller, *Fan noise source diagnostic test–far-field acoustic results,* in *8th AIAA/CEAS Aeroacoustics Conference & Exhibit* (2002) p. 2427.

[16] G. Podboy, M. Krupar, S. Helland, and C. Hughes, *Steady and unsteady flow field measurements within a nasa 22 inch fan model,* in *40th AIAA Aerospace Sciences Meeting & Exhibit* (2002) p. 1033.

[17] D. Lockard and J. Casper, *Permeable surface corrections for ffowcs williams and hawkings integrals,* in *11th AIAA/CEAS Aeroacoustics Conference* (2005) p. 2995.

[18] M. L. Shur, P. R. Spalart, and M. K. Strelets, *Noise prediction for increasingly complex jets. part i: Methods and tests,* International journal of aeroacoustics **4**, 213 (2005).

[19] S. Mendez, M. Shoeybi, S. Lele, and P. Moin, *On the use of the ffowcs williams-hawkings equation to predict far-field jet noise from large-eddy simulations,* International Journal of Aeroacoustics **12**, 1 (2013).

[20] M. R. Khorrami, P. A. Ravetta, D. P. Lockard, B. M. Duda, and R. Ferris, *Comparison of measured and simulated acoustic signatures for a full-scale aircraft with and without airframe noise abatement,* in *2018 AIAA/CEAS Aeroacoustics Conference* (2018) p. 2975.

[21] S. Szepessy, *On the spanwise correlation of vortex shedding from a circular cylinder at high subcritical reynolds number,* Physics of Fluids **6**, 2406 (1994).

[22] D. Casalino, M. Jacob, and M. Roger, *Prediction of rod-airfoil interaction noise using the ffowcs-williams-hawkings analogy,* AIAA journal **41**, 182 (2003).

[23] J. Jeong and F. Hussain, *On the identification of a vortex,* Journal of fluid mechanics **285**, 69 (1995).

[24] D. Casalino, F. Avallone, I. Gonzalez-Martino, and D. Ragni, *Aeroacoustic study of a wavy stator leading edge in a realistic fan/ogv stage,* Journal of Sound and Vibration **442**, 138 (2019).

[25] S. Grace, I. Gonzalez-Martino, and D. Casalino, *Analysis of fan-stage gap-flow data to inform simulation of fan broadband noise,* Philosophical Transactions of the Royal Society A **377**, 20190080 (2019).

[26] S. Szepessy and P. Bearman, *Aspect ratio and end plate effects on vortex shedding from a circular cylinder,* Journal of Fluid Mechanics **234**, 191 (1992).

[27] J. Boudet, N. Grosjean, and M. C. Jacob, *Wake-airfoil interaction as broadband noise source: a large-eddy simulation study,* International Journal of Aeroacoustics **4**, 93 (2005).

[28] Y. Jiang, M.-L. Mao, X.-G. Deng, and H.-Y. Liu, *Numerical investigation on body-wake flow interaction over rod–airfoil configuration,* Journal of Fluid Mechanics **779**, 1 (2015).

[29] J. H. Lienhard *et al.*, *Synopsis of lift, drag, and vortex frequency data for rigid circular cylinders*, Vol. 300 (Technical Extension Service, Washington State University, 1966).

[30] C. Bogey, C. Bailly, and D. Juve, *Noise computation using lighthill's equation with inclusion of mean flow-acoustics interactions,* in *7th AIAA/CEAS Aeroacoustics Conference and Exhibit* (2001) p. 2255.

[31] H. Yokoyama, K. Kitamiya, and A. Iida, *Flows around a cascade of flat plates with acoustic resonance,* Physics of Fluids **25**, 106104 (2013).

[32] R. Parker, *Resonance effects in wake shedding from parallel plates: calculation of resonant frequencies,* Journal of Sound and Vibration **5**, 330 (1967).

[33] I. Evers and N. Peake, *On sound generation by the interaction between turbulence and a cascade of airfoils with non-uniform mean flow,* Journal of Fluid Mechanics **463**, 25 (2002).

[34] N. Peake and E. Kerschen, *Influence of mean loading on noise generated by the interaction of gusts with a cascade: downstream radiation,* Journal of Fluid Mechanics **515**, 99 (2004).

[35] K. A. Kousen and J. M. Verdon, *Aeroacoustics of real blade cascades,* in *Unsteady aerodynamics, aeroacoustics, and aeroelasticity of turbomachines and propellers* (Springer, 1993) pp. 725–742.

[36] F. A. Regulations, *Noise Standards: Aircraft Type and Airworthiness Certification*, Tech. Rep. (Technical Report 14 CFR Part 36, United States Federal Aviation Administration, 2009).

[37] FAA, *Airplane Flying Handbook (FAA-H-8083-3A)* (Skyhorse Publishing Inc., 2011).

[38] EASA, *Type-Certificate Data Sheet for Trent 1000 series engines (EASA.E.036)* (European Union Aviation Safety Agency, 2019).

[39] A. R. Carpio, F. Avallone, D. Ragni, M. Snellen, and S. van der Zwaag, *Quantitative criteria to design optimal permeable trailing edges for noise abatement,* Journal of Sound and Vibration **485**, 115596 (2020).

[40] T. F. Brooks, D. S. Pope, and M. A. Marcolini, *Airfoil self-noise and prediction,* NASA Reference Publication, NASA-RP-1218 (1989).

[41] J. Boettcher, *Noise certification workshop,* in *Session 2: Aircraft Noise Certification* (2006).

[42] J. M. Turner and J. W. Kim, *Aerofoil dipole noise due to flow separation and stall at a low reynolds number,* International Journal of Heat and Fluid Flow **86**, 108715 (2020).

[43] L. Bertsch, W. Heinze, S. Guérin, M. Lummer, and J. W. Delfs, *10 years of joint research at dlr and tu braunschweig toward low-noise aircraft design-what did we achieve?* Aeronautics and Aerospace Open Access Journal **3**, 89 (2019).

[44] U. Michel, *Correlation of aircraft certification noise levels epnl with controlling physical parameters,* in *19th AIAA/CEAS Aeroacoustics Conference* (2013) p. 2014.

6

Conclusion and Outlook

Noise pollution is a relative thing. In a city, it's a jet plane taking off.
In a monastery, it's a pen that scratches.

Robert Orben

Without looking back, without admiration for the circumstances, ...
... we aim to walk towards the future.

Hideaki Anno

6.1. SUMMARY OF FINDINGS

OVER the previous 4 chapters, this dissertation has presented various numerical investigations on the applications of porous inserts (chapter 2) for trailing-edge noise (chapter 3) and leading-edge noise (chapter 4) abatement, followed by two proof-of-concepts (chapter 5). In the following, key findings of the aforementioned investigations will be summarised:

1. **The multi-layer porous medium modelling approach that simplifies the implementation of resistivity for thin geometries.**

   In subsection 2.3.2, the entrance effect has been shown to influence the thickness dependency of porous material resistivity, especially for samples with small thicknesses. Since slender bodies are commonplace in aerospace applications, it is often necessary to take the entrance effect into account when performing numerical analyses using porous medium models. The entrance effect is limited to a region beneath the porous medium surface, which is referred to as the entrance length. Nevertheless, the present estimate of the entrance length is still qualitative, i.e., 1 pore diameter from the surface for foam-like material. The multi-layer porous medium modelling approach isolates the entrance length from the rest of the porous medium volume. In other words, this approach aims to divide the porous material sample into two regions with different resistivity-thickness relationships.

   The multi-layer porous medium modelling approach has been successfully employed for predicting the pressure drop in a porous material characterisation test rig (subsection 2.3.2) and for emulating the metal-foam trailing edge of a NACA 0018 airfoil. In the latter, it has also been confirmed that the entrance length is indeed equal to approximately one pore diameter based on the variation of velocity and pressure fluctuations intensity. Nevertheless, in a fully-resolved simulation of a trailing edge insert based on a synthetic porous-cell geometry, the entrance length is found to be slightly larger than its mean pore size. Thus, further studies are warranted to obtain a more universal description of entrance length for different types of porous materials.

2. **Noise scattering descriptions of a porous trailing edge and the role of the pressure release process in noise abatement.**

   The experimental studies of Rubio Carpio *et al.* [1] have revealed several key traits of the application of metal-foam inserts on a NACA 0018 airfoil. They found that noise reduction can only be achieved by enabling an interactivity between the unsteady pressure fields at the upper and lower sides of the porous insert. Additionally, a relatively small segment of the permeable insert near the trailing-edge tip contributes the most to the noise reduction level. To better understand the underlying physical mechanisms for the aforementioned phenomena, several numerical simulations are performed and reported in chapter 3. The first one aims at elucidating the differences in sound source behaviours between the porous and solid inserts. The dipole sources on a solid trailing edge are distributed along the airfoil chord with strong in-phase relation, particularly at

low frequencies where the insert is acoustically compact, as expected. The dipole sources are distributed on the porous insert with out-of-phase relations with respect to each other, which effectively reduces the intensity of far-field noise. Adding a thin solid partition along the center of the porous insert completely removes the noise reduction benefit, consistent with the observation in the experiment.

Another numerical investigation considers a fully-resolved porous insert made using synthetic porous-cell geometry. The results support the conclusion that the noise reduction of the permeable insert can be attributed to the destructive interference caused by the out-of-phase distribution of the noise sources and the suppression of noise source intensity near the tip of the trailing edge. In this study, a partially-blocked insert is obtained by adding a thin solid partition between 20 % to 80 % of its chordwise extent. The noise reduction level at low frequencies of the partially-blocked insert is slightly smaller compared to that of a fully-permeable insert, but the noise intensities at higher frequencies are relatively unaffected. This implies that the permeable extent of the insert influences not only influence the overall noise reduction level, but also the frequency range where noise reduction is present. Subsequently the pressure release process is characterised as the gradual phase equalisation between the surface pressure fluctuations on the opposite sides of the porous insert. High level of coherence is found near the trailing-edge tip where the local thickness is equal to or smaller than twice the entrance length. As a consequence, the improvement in noise reduction level diminishes as the chordwise extent of the porous insert is increased further away from the trailing edge.

3. **The differences in noise reduction mechanisms between permeable treatment and serrations for mitigating leading-edge noise.**

   Chapter 4 examines the potential of leading-edge (LE) noise mitigation using permeable material in a rod-airfoil configuration (RAC). The RAC has been selected for this study as it emulates the noise emission from a rotor-stator interaction mechanism. The present study includes a thin-cambered profile, NACA 5406, that better represents the geometrical features of typical turbomachinery blades. The airfoil LE is modified with a permeable insert or with serrations; the latter is designed following the state-of-the-art optimisation strategies in literature [2, 3]. The permeable insert is modelled after the same metal-foam that has been used in the earlier porous TE study. The rest of the setup and flow conditions remain identical to those of the classical RAC experiment of Jacob *et al.* [4].

   The serrations are able to mitigate the scattered noise level by weakening the coherence of the noise source distribution along the span. Additionally, the local source intensity at the serration tip is suppressed due to the generation of secondary streamwise vortex systems in a similar manner as on a delta wing. Conversely, the porous LE simply redistributes the sound sources over the its entire chordwise extent. Hence, while the peak surface pressure fluctuations near the porous LE tip is significantly smaller than on a solid one, the overall far-field noise attenuation is relatively small, particularly in the low-frequency range that

contains the tone associated with the vortex-shedding process. Introducing permeability at the LE also leads to a more severe aerodynamic penalty compared to that of the serrations. This consequence becomes more apparent when the airfoil is installed at a lifting condition as the mean pressure imbalance between the upper and lower sides of the airfoil drives a cross-flow through the porous medium. In the case of serrations, the loss in aerodynamic performance is associated with the reduced lift contribution at the serration tip, and the enhanced adverse pressure gradient downstream of the serration root. The chapter also looks into a LE treatment combining the porous material with serration-like planform, which has been found to achieve higher broadband noise reduction when compared to the regular serrations, although the tonal one remains similar. The aerodynamic penalty is also substantially less than that of the porous LE with a straight planform. Nevertheless, it can also be argued that the metal-foam, which is a homogeneous and isotropic porous material, is not optimal for this application, and thus, future investigations are still necessary.

4. **The rod-linear cascade model as a platform for emulating turbulence-impingement mechanism in turbomachinery.**

   The rod-linear cascade (RLC) model has been proposed as an extension to the RAC by incorporating a high-solidity environment, which is typical in turbomachinery. The RLC is designed to be installed in the vertical wind tunnel facility of TU Delft, for which an appropriate test section has been developed. The blade profile in the RLC is based on the outlet-guide-vane (OGV) of a scaled turbofan model (NASA Source Diagnostics Test - SDT), and a total of 7 blades can be installed in the test section. The rod diameter has been scaled to achieve a vortex shedding frequency that equals the blade-passage frequency of the SDT, and it is installed parallel to the central blade. Subsequently, a numerical study is performed in order to gain insights into the aerodynamic and acoustic characteristics of the RLC prior to manufacturing, and the results are discussed in the first half of chapter 5. The far-field noise emitted by the RLC contains both tonal and broadband components, similar to that of the RAC, but sound propagation from the LE of the central blade is heavily influenced by the surrounding installation effects. The majority of the acoustic energy is concentrated in a narrowband surrounding the vortex shedding frequency. This is associated with a resonance-like behaviour referred to as Parker's half-wavelength mode that is expected to occur at a frequency that is close to that of the vortex shedding. The resonance phenomenon is also indicated by strong pressure fluctuations in each inter-blade channel, including the ones that are not directly adjacent to the central blade. The aerodynamic loading distribution on each cascade blade has been found to be comparable to that of the SDT OGV despite the difference in stagger angle. Furthermore, the mean surface pressure distribution on the rod is almost identical to that of an isolated rod, implying the absence of a strong feedback mechanism between the rod and the linear cascade. The rod wake is confirmed to directly impinge the leading-edge of the central blade. However, the mean surface pressure characteristics on all blades are relatively similar after accounting for the lower mean velocity in the rod wake

encountered by the central blade. This suggests that the rod wake impingement on the central blade has a minor impact on the overall steady flow characteristics of the RLC. The RLC can be considered as a suitable platform for evaluating the effects of various LE treatments on the turbulence-impingement noise in a blade row.

5. **The application of a permeable treatments in a full-scale aircraft model.**

   The second half of chapter 5 serves as a proof-of-concept to the poro-serrated LE concept previously discussed in chapter 4. The numerical simulation considers an up-scaled NASA Common Research Model (CRM) fuselage combined with the SDT fan stage. The poro-serrated treatment is employed at the LE of the SDT outlet-guide vane (OGV), and it is modelled after the same metal foam as in the previous chapters, where two configurations with different porosity values have been prepared. The LE treatment reduces the tonal noise emission associated with the blade passage frequency and its harmonics. However, the pressure balancing process across the porous medium region induces a severe flow separation at the suction side of the OGV, enhancing the broadband noise emission in the process. Due to this, the overall source power level of the modified fan stage is relatively unchanged in comparison to the baseline. The flow separation on the OGV also worsens the recovery of swirl in the fan wake, while decreasing the mass flow rate in the fan stage. As a result, the thrust produced by the modified fan stage is up to 9 % lower relative to the baseline. Interestingly, the lower-porosity LE treatment exhibits better acoustic and aerodynamic trade-off. While the implementation of the poro-serrations treatment is evidently not optimised, the present study also suggests that increasing the porosity of the leading edge along the radial direction, from the hub to the OGV tip, could minimise the total lift fluctuations at the OGV, which promotes higher noise attenuation.

   It is worth mentioning that many phenomena found in the full-scale CRM/SDT simulation can be linked to those observed in less-complex setups, such as the RLC and RAC. Hence, the simple, laboratory-scale, configurations are still useful for studying specific physical mechanisms in a controlled manner. The findings from the low-complexity test configurations can be utilised for designing and optimising different solutions, which is eventually verified using the test setups with higher complexity.

In conclusion, the chapters presented in this dissertation have fulfilled the objectives that are outlined in section 1. These studies have demonstrated the promising capability of permeable treatments for mitigating leading-edge and trailing-edge noise while providing additional insights into their working principles. Despite this, there are still several aspects of the present study that deserve to be investigated further, which are listed in the next section.

6.2. OUTLOOK AND RECOMMENDATIONS

This section provides a list of recommendations that could stimulate future investigations. These include the extension of the studies that have been carried out in this dissertation as well as several other practical aspects.

- **The extended verification on the multi-layer porous medium modelling approach.**

  The multi-layer porous medium modelling approach has been proposed in chapter 2, and its usage has been demonstrated for homogeneous and isotropic porous materials, such as a metal-foam. Nevertheless, more extensive verification of this methodology is still necessary to determine its suitability for other types of porous materials. The present multi-layer approach is grounded in the isolation of the *entrance length*, which is still defined qualitatively based on the pore geometry of the porous material. In particular, there is a need to define the entrance length using a quantitative parameter that does not only relate itself to the material parameters (e.g., pore size or permeability), but also to the flow quantities (statistics), such as the correlation distance of the pressure field from the surface into the porous material.

- **The quantitative relationship between the entrance length, porous trailing-edge geometry, and trailing-edge noise reduction level.**

  Chapter 3 has shown that the interaction between pressure fluctuations at the opposite sides of the porous trailing edge weakens the scattering intensity at the trailing-edge tip, which is referred to as the pressure release process. This happens at locations where the local thickness of the porous material is less than the combined length of the entrance length at both sides of the porous trailing edge. Hence, it is hypothesised that the ratio between the entrance length and the local thickness of the porous trailing edge, combined with the surface pressure jump spectra across the porous trailing edge could be used to predict the noise reduction contribution of the pressure release process.

- **A modular porous flat-plate model as a parametric study platform instead of an airfoil profile.**

  A simplified laboratory model is generally more advantageous for isolating and studying a particular physical phenomenon. For instance, the NACA 0018 airfoil that has been used for the TE noise study might not be ideal for this purpose. Instead, a flat-plate model is proposed, as shown in figure 6.1, consisting of a solid leading edge piece attached to a series of permeable plates. Tripping devices are added at the leading edge piece to trigger boundary layer transition. The porous plates are designed to be modular such that the total length of the porous segment can be adjusted. A porous wedge is added to the downstream end of the model to ensure that the trailing-edge profile remains sharp. This flat-plate model can be used for different types of investigations. For instance, by increasing the separation between the solid-porous junction and the porous trailing-edge tip, it would be easier for an existing beamforming array for distinguishing noise sources at each location. By instrumenting the modular porous plates with small pressure probes, it would be possible to determine the trend of the correlation between the pressure fluctuations at the upper and lower sides of the plate and the local boundary layer statistics (e.g., displacement thickness).

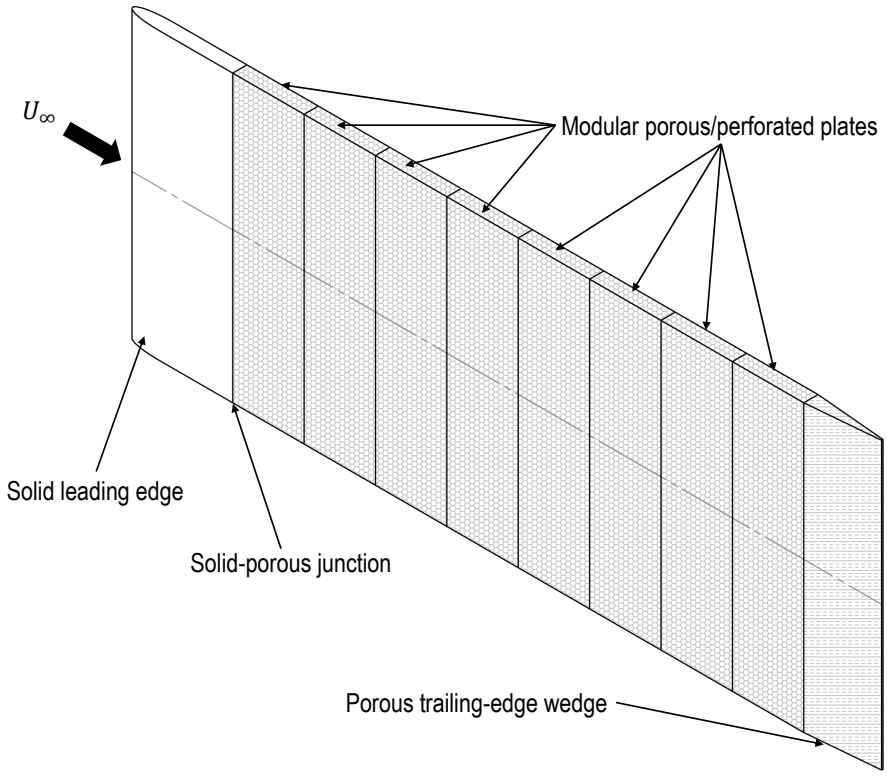

Figure 6.1: A flat-plate model consisting of a solid leading-edge and modular porous plates to investigation sound generation of a porous body.

- **Advanced porous leading edge concepts for noise mitigation beyond the metal foam.**

  The metal foam has been chosen for the majority of investigations in this dissertation due to several reasons. One of these is its homogeneous and isotropic properties, thanks to which, the metal foam is relatively simple to model in simulations. However, based on the results shown in chapter 4, the porous treatments based on the metal-foam have been found to be quite underwhelming considering that the noise reduction level is substantially smaller than that of the serrations. Nevertheless, the present study is not the only one that has presented the challenges related to porous leading edge applications. Very recently, Bowen *et al.* [5] performed a study on NACA 0012 airfoil with its first 10 % of the chord replaced by metal-foam leading edge; the metal-foam has comparable porosity as that in the present study. The impinging turbulence length scale is of the same order of magnitude as the airfoil thickness and the chordwise extent of the porous leading-edge, which is similar to the conditions of the rod-airfoil setup in chapter 4. The authors observed that the metal-foam leading edge produced a noise reduction of < 2 dB in the low frequency range followed by up to 5 dB of excess

noise at high frequencies. These findings reflect those in this dissertation, except that the excess noise cannot be fully replicated by the simulation due to the lack of surface-roughness modelling. They also demonstrated that a more permeable material could achieve a slightly higher noise reduction level, but simultaneously the degradation of aerodynamic performance became more significant. Following this, the porous leading-edge might be considered unsuitable against inflow turbulence with large length scales, especially in applications where aerodynamic performance is crucial. Despite this, it is still likely that more advanced types of porous inserts, such as those with spatially-varying permeability could achieve better acoustics and aerodynamics behaviours.

6.3. A FINAL REMARK

Aerodynamic noise mitigation using permeable treatments is quite promising, and it can be argued that they possess greater versatility than what has been shown in literature. Unfortunately, the underlying design and integration principles are still not fully understood, and while this dissertation has provided additional insights, current findings are still far from being exhaustive. As a consequence, optimising permeable treatments would remain challenging and industrial adoption is unlikely in the near future. These challenges can be partly attributed to the multidisciplinary nature behind the porous treatments (e.g., fluid dynamics, acoustics, solid mechanics, material science, etc.). Given that the expertise of many scientists and engineers are often limited to a relatively narrow domain, they might overlook the perspectives from the others, and thus, a closer collaboration between the different research fields is strongly encouraged. In addition, there are other practical aspects relevant to the industrial applications of permeable treatments beside the more fundamental ones, such as potential financial costs, ease of manufacturing, and maintenance or refurbishment procedures.

REFERENCES

[1] A. Rubio Carpio, F. Avallone, D. Ragni, M. Snellen, and S. van der Zwaag, *Mechanisms of broadband noise generation on metal foam edges,* Physics of Fluids **31**, 105110 (2019).

[2] F. Gea Aguilera, J. R. Gill, D. Angland, and X. Zhang, *Wavy leading edge airfoils interacting with anisotropic turbulence,* in *23rd AIAA/CEAS Aeroacoustics Conference* (2017) p. 3370.

[3] P. Chaitanya, P. Joseph, S. Narayanan, C. Vanderwel, J. Turner, J.-W. Kim, and B. Ganapathisubramani, *Performance and mechanism of sinusoidal leading edge serrations for the reduction of turbulence–aerofoil interaction noise,* Journal of Fluid Mechanics **818**, 435 (2017).

[4] M. C. Jacob, J. Boudet, D. Casalino, and M. Michard, *A rod-airfoil experiment as a benchmark for broadband noise modeling,* Theoretical and Computational Fluid Dynamics **19**, 171 (2005).

[5] L. Bowen, A. Celik, M. Azarpeyvand, and C. R. Ilario da Silva, *On the use of tailored*

permeable surfaces for turbulence interaction noise control, in *AIAA AVIATION 2020 FORUM* (2020) p. 2530.

ACKNOWLEDGEMENT

To conclude this dissertation, I would like to acknowledge all parties whose contributions have ensured that this 4-year-long PhD project finally fulfilled its objectives. I would like to begin by disclosing that this study has been supported by the project **SmartANSWER** (Smart Mitigation of flow-induced Acoustic Radiation and Transmission for reduced Aircraft, surface traNSport, Workplaces and wind enERgy noise) which has received funding from the European Union's Horizon 2020 research and innovation program under the Marie Skłodowska-Curie grant agreement No. 722401. More information about this project and its beneficiaries can be found on https://www.h2020-smartanswer.eu/. Therefore, I would like to thank the European Commission for sponsoring this project and to remain committed in promoting scientific researches at independent institutions. Furthermore, I also would like to acknowledge the project coordinator of SmartANSWER, Christophe Schram, and the project liaison, Julien Christophe, from the Von Karman Institute (VKI) for helping realising and organising the project.

I would like to highlight the roles of the three members of my supervision committee, although it would not be possible to list all of their contributions in a short paragraph. I want to express my sincere gratitude to my promotor, Prof. Damiano Casalino, for all of the conversations and suggestions related to both scientific and practical aspects of aeroacoustic studies. He developed several post-processing tools that have been indispensable for generating various plots and contours in this dissertation. He also provided me with the motivation to look into the multi-layer porous medium modelling approach, without which, the present numerical works would have been significantly more challenging. My first co-promotor is Dr. Daniele Ragni, who is specialised in various experimental techniques, from oil-flow visualisation to particle-image-velocimetry. I understand that supervising tens of PhDs while simultaneously fulfilling administrative duties would not be an easy task, but I am grateful that he is generally available to support my daily activities. He has also pushed me to work efficiently during the early years of the PhD, especially on the presentation and reporting aspects. As a result, I managed to the meet the expectation to "Hand-In-1-Paper-Per-Year" (H1PPY). The second co-promotor is Dr. Francesco Avallone, who works more closely with numerical approach. He brought me up-to-speed on the operation of the high-performance-computing (HPC) facilities at TU Delft. I have also learned a lot from him on how to stay organised in the busy environment of academia.

I also greatly appreciate the friendship and support from the rest of the aeroacoustics research group members. I started my PhD together with Javed who was also working under SmartANSWER. On different occassions, I was under the impression that some people jokingly saw us like Chris Tucker and Jackie Chan in *Rush Hour* while we traveled across Europe. Regardless, Javed had been a great buddy to work and to have discussions

with; although your stay in the Netherlands was cut short, I will always wish you the best. Then, there was Pranav, my desk neighbour and probably the friendliest person in the office for the longest time. Special thanks for inviting me to your home-cooking sessions and I hope that Siemens-Gamesa would invest further into a hardworking guy like you. Leandro and Gabriel joined the research group next, and you have shown me that life should be a roller-coaster ride filled with alcohol, barbeque, and sarcasm. I also truly enjoyed our trip together in Atlanta, 2018. Edoardo, I am amazed at your perseverance working on such a challenging projects with the industrial partners; I believe that you will get employed as soon as you complete your PhD programme. After Javed left SmartANSWER, his position was assumed by Lourenço, who is the most resourceful tinkerer I have ever met. You have taught me to have the right motivation (and the right stuff) to carry out scientific research, but I hope you will forgive me for not being able to forget about the H1PPY concept. Similarly, Pranav's position was assumed by Hugo, who later became my desk neighbour until the end of my PhD programme; I really appreciated the thought-provoking questions regarding PowerFLOW simulations and flow physics in general. Manoel and Fernanda joined the research group later during the COVID pandemic, and I was very happy to be able to spend coffee break together with all of you. I also would like to acknowledge Salil from the ANCE department. Towards the end of our PhD programme, you have formulated a method to quantify and predict the trailing-edge noise reduction contribution from the pressure release process, which I could not accomplish before. There are many more research group members whom I do not have much opportunity to interact with: Yunusi, Colin, Cornelius, Umberto, Hasse, and Ruben; I wish all of you a smooth PhD journey.

As a member of the Wind Energy department, I cannot understate the support provided by the secretary, Sylvia. I would like to thank you personally for arranging the paperwork and providing with essential information ever since I received my PhD contract. I also would like to mention my office colleagues. In room 06.15, there were Delphine, Tom, Chihoon, and Sharif. Then after moving to 06.08, I also met Johannes, Mark, Julia, Ming, and Dylan. Needless to say, I truly enjoyed the moments we spent in office and at the coffee corner. I also would like to acknowledge the rest of the members of our pre-COVID card club: Sebastian, Miko, Bedassa, Mihir, and Jingna.

While working with PowerFLOW, it goes without saying that technical support from colleagues at Dassault Systèmes is needed sometimes. Firstly, I would like to acknowledge the outstanding support from Wouter, such as with the preparation of the automated trailing-edge noise workflow. I want to thank Gianluca as well who was always ready to reply to my sudden email related to PowerDELTA and PowerVIZ. Should I remain in the aerospace industry in the near future, I hope to see both of you in some conferences again.

During the PhD programme, I have also spent thousands of Euros to create an abomination known as the rod-linear cascade test rig, and I would not be able to make a return on this investment without the awesome collaborations with a couple of my MSc students, Sidharth and Sarah. It might not have been easy working with a test setup as complex as the rod-linear cascade configuration, but I truly appreciated your patience during each 2-week experimental campaign. I apologise as a supervisor for not always having sastisfying answer to every trend that we observed, but this is why we perform

research, right? These experiments would also not be possible without the manufacturing experts at DEMO (Ed, Rob, and Peter) and the support of technicians at the low-speed lab (Stefan and Emiel).

This PhD programme would not be as special as it is without the people behind the SmartANSWER activities. Through the project, I got to befriend 15 other PhD candidates from different institutions. Riccardo (VKI), whom later became my role model in research; Alessandro (VKI) who usually throws some jokes in his presentations; Niloofar (KTH), the kind and caring one; Massimo (LAUM) and his fancy laser-doppler velocimetry experiment; Thomas (EPFL) who is very knowledgeable with beers; Thanu (IMP-PAN) who has very pragmatic view on work-life balance; Sergi (Southampton), the youngest of us all; Felipe (KU Leuven), with whom I could always discuss about the project duties; Giorgos (ECL), the brother in arms in leading-edge noise mitigation research; Emanuele (ECL) who surprised me with his hand-drawn animations; Morteza (NTUA), the lucky one to have stayed in Athens; Chaitanya (Siemens PLM), the first one to graduate among us all; Ignacio (CETIAT), from whom I have learned plenty about the history and culture of various parts of Europe; and Simone (VKI), who helped us organising the preparation of SmartANSWER demonstrator during the chaotic period of the project. I will not be able to forget any of the SmartANSWER meetings, through which we have learned a lot about each other's research projects, while also enjoying the social events. While the project ended in a mundane manner, I wish all of you a great career up ahead.

Needless to say that I am indebted to my family who has been supporting me up to this point. I understand that pursuing a career in aerospace engineering had not been very convincing to my parents, but I am glad that I could demonstrate my commitment with the completion of this PhD programme. Nonetheless, I know that all of this was only possible with your sincerest prayers. I am also happy that my grandmother will be able to witness her first grandson receiving his doctorate. Although I might stay far away from Indonesia for the time being, I will regularly report on my status.

On this occasion, I also would like to thank International Christian Fellowship (ICF) Delft which has allowed me to find a place in a Christian community. I am very pleased to be entrusted with the responsibility to organise the "beamer & PPT" department, and I will continue serving the congregation while I am still staying in Delft. Big thanks as well to the members of the "life group" where I belong: Adam, Grace, the family of Speeder and Kiki, the family of Ilyas and Huma, the family of Gerard and Riet, and the family of Arjan. Special thanks to David and Fera that I have considered as my foster family during my stay in Delft. Both of you have become role models for me to continue pursuing a career overseas.

Last but not least, allow me to thank my readers for making it this far into the dissertation. I sincerely hope the information contained in the past few chapters have been particularly interesting and thought-provoking for you. If you have any question about the content of this dissertation, please do not hesitate to send me a message to my LinkedIn account (https://nl.linkedin.com/in/cteruna).

CURRICULUM VITÆ

Christopher TERUNA

17-11-1993 Born in Medan, Indonesia.

EDUCATION

2010–2014 Bachelor of Science in Aeronautics & Astronautics
Institut Teknologi Bandung (Bandung Institute of Technology)
Bandung, Indonesia
GPA : 3.76/4.0
Thesis: Aero/Aerothermo-dynamic Design of Parabolic-based/Cone-derived Waverider as a Hypersonic Cruise Vehicle
Supervisor: Dr. R. O. Bura

2015–2017 Master of Science in Aerospace Engineering
Korea Advanced Institute of Science & Technology (KAIST)
GPA : 3.88/4.3
Thesis: Supersonic Partially-Covered Cavity Flow Frequency Estimation with Proper Orthogonal Decomposition on Schlieren Photography
Supervisor: Prof. D. J. Lee

2017–2021 Doctor of Philosophy in Aeroacoustics
Technische Universiteit Delft (Delft University of Technology)
Thesis: Aerodynamic Noise Reduction with Porous Materials
Promotor: Prof. Dr. D. Casalino
Co-promotor: Dr. D. Ragni & Dr. F. Avallone

List of Publications

Journal Papers

8. **C. Teruna**, L. Rego, D. Casalino, D. Ragni, & F. Avallone, *A numerical study on aircraft noise mitigation using porous stator concepts*, MDPI Aerospace **9**(2), 70 (2022).

7. **C. Teruna**, F. Avallone, D. Ragni, & D. Casalino, *Numerical analysis of a 3D-printed porous trailing edge for broadband noise reduction*, Journal of Fluid Mechanics **926**, A17 (2021).

6. **C. Teruna**, L. Rego, F. Avallone, D. Ragni, & D. Casalino, *Applications of the multi-layer porous medium modelling approach for noise mitigation*, Journal of Aerospace Engineering **34**(6), 04021074 (2021).

5. **C. Teruna**, F. Avallone, D. Ragni, A. Rubio-Carpio & D. Casalino, *On the noise reduction of a porous trailing edge applied to an airfoil at lifting condition*, Physics of Fluids **33**, 055132 (2021).

4. S. Tamaro, R. Zamponi, D. Ragni, **C. Teruna**, & C. Schram, *Experimental investigation of turbulent coherent structures interacting with a porous airfoil*, Experiments in Fluids **62**, 94 (2021).

3. **C. Teruna**, L. Rego, F. Avallone, D. Ragni, & D. Casalino, *Numerical investigation of leading edge noise reduction on a rod-airfoil configuration using porous materials and serrations*, Journal of Sound and Vibration **494**, 115880 (2021).

2. **C. Teruna**, F. Manegar, F. Avallone, D. Ragni, D. Casalino & , T. Carolus *Noise reduction mechanisms of an open-cell metal-foam trailing edge*, Journal of Fluid Mechanics **898**, A18 (2020).

1. **C. Teruna**, F. Avallone, D. Ragni, & D. Casalino, *A rod-linear cascade model for emulating rotor-stator interaction noise in turbofans: a numerical study*, Aerospace Science and Technology **90**, 275-288 (2019).

Conference Papers

3. G. Bampanis, M. Roger, D. Ragni, F. Avallone, & **C. Teruna**, *Airfoil-turbulence interaction noise source identification and its reduction by means of leading edge serrations*, 25th AIAA/CEAS Aeroacoustics Conference, (2019).

2. **C. Teruna**, F. Manegar, F. Avallone, D. Casalino, D. Ragni, A. Rubio-Carpio, & T. Carolus, *Numerical analysis of metal-foam application for trailing edge noise reduction*, 25th AIAA/CEAS Aeroacoustics Conference, (2019).

1. **C. Teruna**, D. Casalino, F. Avallone, & D. Ragni, *Numerical analysis of a linear cascade model for rotor-stator interaction aeroacoustics*, 24th AIAA/CEAS Aeroacoustics Conference, (2018).

OTHER CONTRIBUTIONS

3. **C. Teruna**, F. Avallone, D. Ragni, & D. Casalino, *Modelling of porous metamaterials*, Noise Reduction Technologies with Meta-materials, 10-14 February 2020.

2. **C. Teruna**, F. Avallone, D. Ragni, D. Casalino, & A. Rubio-Carpio, *Trailing Edge Noise Reduction with Permeable Materials: Description of Noise Scattering Mechanism*, 23rd Workshop of the Aeroacoustics Specialists Committee of the CEAS, 26-27 September 2019.

1. **C. Teruna**, L. Rego, P. Manjunath, D. Casalino, F. Avallone & D. Ragni, *How to reduce aero-engine noise: researching wake/stator interaction noise, jet installation noise and acoustic liners using PowerFLOW*, 2018 SIMULIA BeNeLux Regional User Meeting, 7-8 November 2018.

Who has seen the wind? Neither I nor you: But when the leaves hang trembling, **The wind is passing through**.

Jiro Horikoshi in "*The Wind Rises*" (2013)

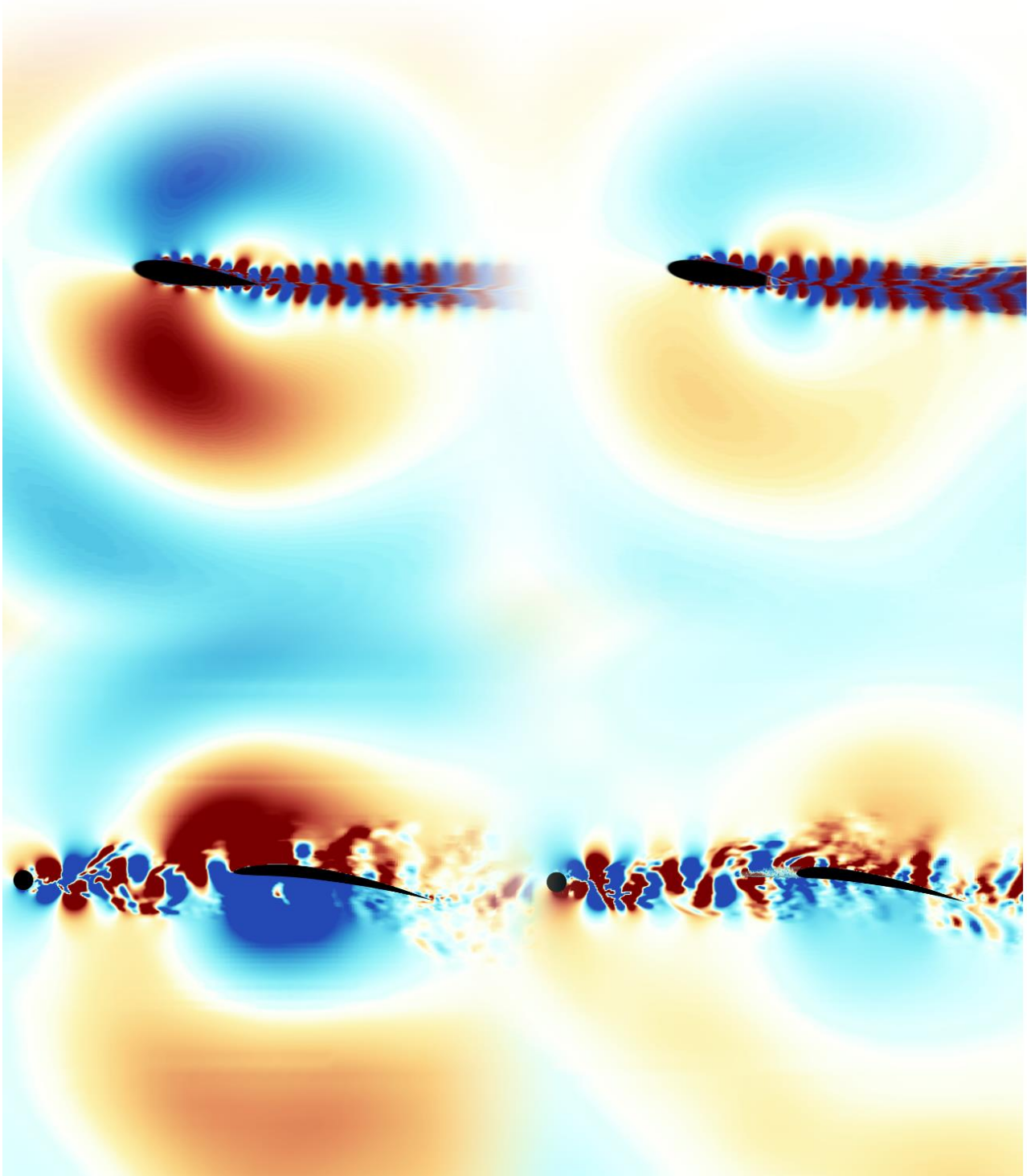


Eneco

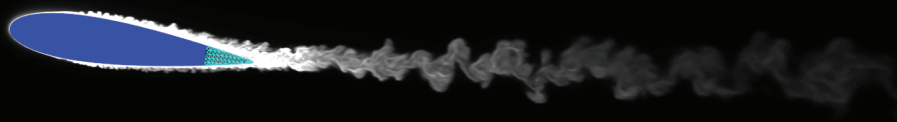

TU Delft

Smart ANSWER

Marie Skłodowska-Curie Actions

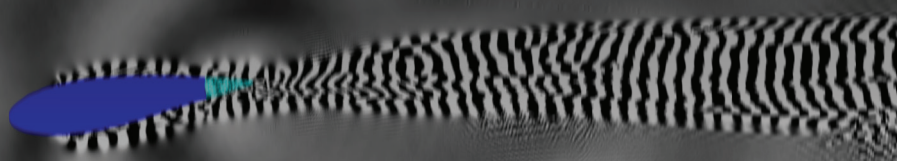

AERODYNAMIC NOISE REDUCTION WITH POROUS MATERIALS

Christopher Teruna

TUDelft